In presenting the dissertation as a partial fulfillment of the requirements for an advanced degree from the Georgia Institute of Technology, I agree that the Library of the Institute shall make it available for inspection and circulation in accordance with its regulations governing materials of this type. I agree that permission to copy from, or to publish from, this dissertation may be granted by the professor under whose direction it was written, or, in his absence, by the Dean of the Graduate Division when such copying or publication is solely for scholarly purposes and does not involve potential financial gain. It is understood that any copying from, or publication of, this dissertation which involves potential financial gain will not be allowed without written permission.

7/25/68

AN EXPERIMENTAL STUDY OF SKIN FRICTION ON A STATIONARY FLAT SURFACE IN CONTACT WITH VORTEX FLOW

A THESIS

Presented to

The Faculty of the Division of Graduate

Studies and Research

by

James Richard Huntley, Jr.

In Partial Fulfillment

of the Requirements for the Degree

Master of Science in Mechanical Engineering

Georgia Institute of Technology

June, 1972

AN EXPERIMENTAL STUDY OF SKIN FRICTION ON A STATIONARY FLAT SURFACE IN CONTACT WITH VORTEX FLOW

Approved:

Chairman

Date approved by Chairman: 5/31/72

ACKNOWLEDGEMENTS

I extend my sincere appreciation to my advisor, Dr. Wolfgang Wulff, who was a source of much helpful technical advice. His ideas were instrumental in developing this project.

I thank the National Science Foundation for funding this research under Grant GK-5525.

I thank the members of the technical staff of the Mechanical Engineering Department at Georgia Institute of Technology, all of whom contributed to this project at one time or another.

I thank Mr. C. L. Williams and Mr. W. W. Carr for their continued interest and helpful suggestions.

Especially, I thank my wife, Loretta, who has stood by me in this work.

TABLE OF CONTENTS

TABLE OF CONTENTS (CONTINUED)

TABLE OF CONTENTS (CONTINUED)

TABLE OF CONTENTS (CONCLUDED)

LIST OF TABLES

LIST OF FIGURES

LIST OF FIGURES (CONTINUED)

LIST OF FIGURES (CONTINUED)

LIST OF FIGURES (CONTINUED)

LIST OF FIGURES (CONTINUED)

LIST OF FIGURES (CONCLUDED)

SUMMARY

The surface boundary layer of the buoyancy driven atmospheric vortex was simulated in a laboratory model, and a quantitative description of the boundary layer was obtained. A large vortex generator, eight feet in diameter by sixteen feet tall, was constructed to simulate the boundary layer. The vortex was driven by a variable speed fan mounted in the top. Circulation was imparted to the flow by adjustable vertically mounted vanes around the circumference. A table mounted horizontally in the lower half of the vortex generator formed the boundary surface. Mean velocity profiles were measured by a V-probe hot wire anemometer designed and built for the purpose. The tangential velocity profile was well developed, and demonstrated similarity. The radial velocity profile developed fully over one-fourth of the plate radius; similarity was shown not to exist. A Preston tube was used to measure the surface shear, from which empirical shear laws were derived. A momentum integral analysis of the data was performed; but measured, local momentum did not balance as a result of experimental difficulties caused by flow instability.

NOMENCLATURE*

C	Capacitance
d	Local plate diameter Preston tube diameter
D	Plate diameter
E	Voltage
g	Gravity acceleration
Gr	Grashof number
h	Convection heat transfer coefficient
I	Current
k	Thermal conductivity
L	Reference length
Nu	Nusselt number
p	Pressure
Pr	Prandtl number
q	Heat transfer
Q	Radial volumetric flow rate
r	Radial coordinate position
R	Plate radius Resistance
Re	Reynolds number

*Appendix D contains a separate supplemental nomenclature section for its own use.

T	Temperature
u	Velocity
U	Voltage
v	Velocity
V	Velocity magnitude
x	Horizontal coordinate position
y	Horizontal coordinate position
z	Vertical coordinate position above plate

GREEK SYMBOLS

α	Temperature coefficient of resistance
Γ	Freestream circulation
δ	Boundary layer thickness
δ^*	Velocity displacement thickness
Δ	Difference
ζ	Hot wire conduction heat loss fraction
η	Non-dimensional wire length
θ	Excess hot wire temperature
μ	Dynamic viscosity
ν	Kinematic viscosity
ξ	Hot wire damping coefficient
ρ	Density Resistivity
σ	Stefan-Boltzmann constant

τ	Shear stress Time constant
Φ	Velocity direction, angle in the horizontal plane between the plate radius and the velocity vector
Ψ	Velocity direction with respect to the "V" probe
ω	Vorticity Angular rotation Excitation frequency
$\otimes$	Vector cross product

SUBSCRIPTS

f	Film
n	Normal, perpendicular
o	Reference
p	Probe
r	Radial
s	Shunt
t	Tangential
w	Wall Wire
z	Vertical
$\perp$	Perpendicular
∞	Freestream Ambient

SUPERSCRIPTS

-	Vector Average

CHAPTER I

INTRODUCTION

Relevance of Work

This research contributes to the quantitative description of the buoyancy-driven atmospheric vortices such as fire whirls, tornados, dust devils, and waterspouts. It is designed to ultimately help predict the occurrence and strength of storm wind disasters, and it may help to design tornado resistant structures.

Objective

The primary objective of this research is to provide a quantitative description of the vortex ground boundary layer by measuring velocity profiles and surface shear. This knowledge in turn will contribute to the prediction of storm wind disasters in terms of atmospheric lapse rate and circulation, and to the design criteria of storm resistant structures.

The ground boundary layer of the quasi-steady state, buoyancy-driven atmospheric vortex supplies the mass to the core and oxygen to the fire whirl, it causes the ground destruction, and it produces most of the vorticity.

Originally, when this work was proposed in 1969 by Dr. Wolfgang Wulff at the Georgia Institute of Technology, the quantitative description of the ground boundary layer did not exist. Laboratory simulation seemed to be necessary to obtain the desired description. This research was proposed to the National Science

Foundation and funded. In January, 1970, Ying and Chang (23)* published mean velocity profiles measured in a model tornado boundary layer. Consequently, the emphasis of this thesis then shifted to checking Ying and Chang's results and measuring the surface shear stress to verify the laws used by Rott and Lewellen (20) in their momentum integral analysis of the boundary layer. Later in the research, because of the existence of measured freestream radial velocity, the Rott and Lewellen laws were replaced by the momentum integral equations derived by Dr. Wolfgang Wulff to include this velocity.

A more detailed description of the vortex, the ground boundary layer, the thesis background, and the direction of the experiment is in the following sections.

Description of the Vortex

The vortex is driven by a strong buoyant force causing vertical axial flow in the center of the plume. The buoyant force may be caused for example: by combustion in a fire storm, by condensation and sublimation in a cumulus tower in tornados, and by ground heated air in a dust devil.

The fully developed tornado has three main parts, shown in Figure 1:

1) a strongly rotating plume with a low pressure center and vertical axial flow;
2) a potential vortex surrounding the core, balancing the radial pressure gradient with centrifugal acceleration, and supplying air to both the ground boundary layer and the vertical core; and
3) the ground boundary layer which supplies mass and vorticity to the core.

---

*Numbers in parenthesis refer to bibliography.

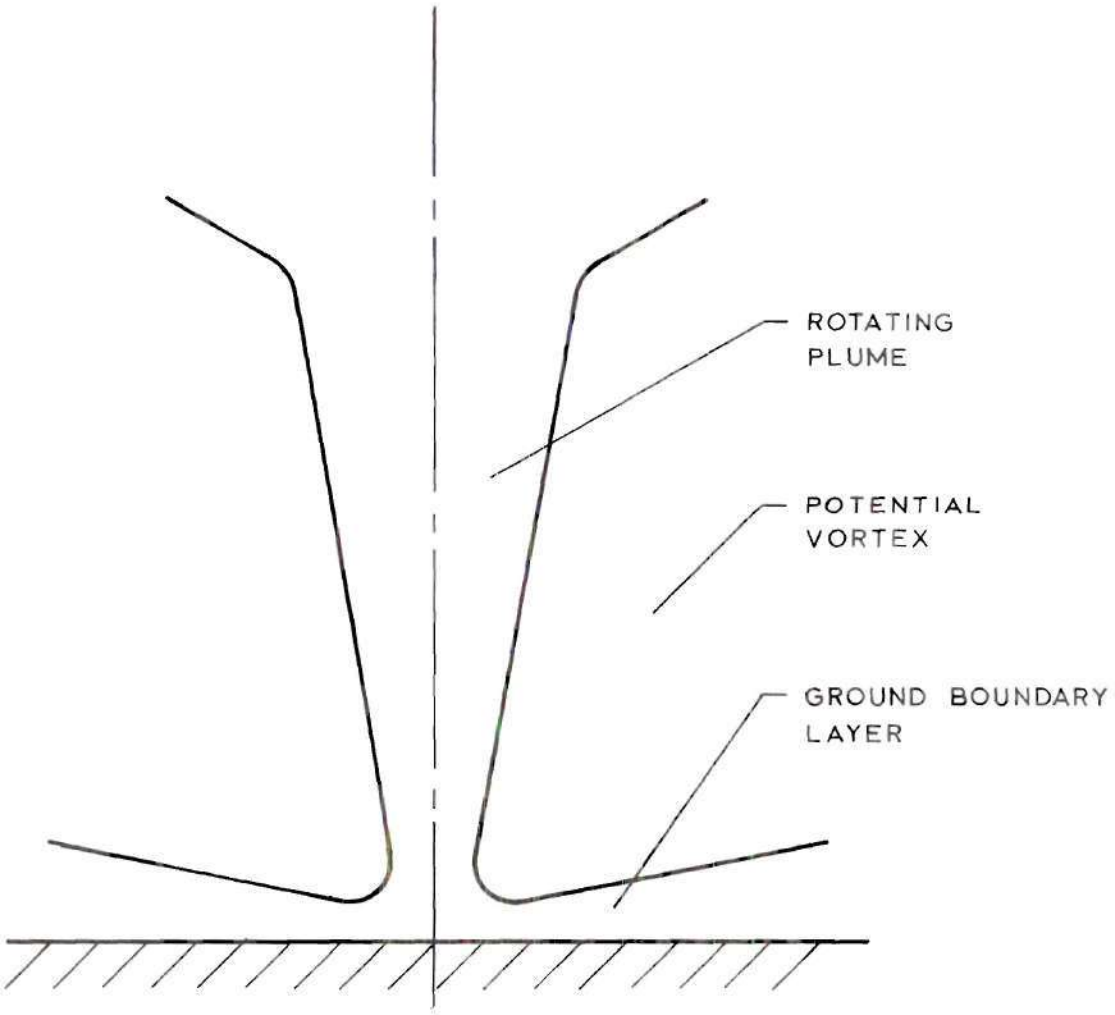

Figure 1. Vortex Regions.

Shear at the ground retards the tangential flow, creating an imbalance of radial forces. Air is accelerated into the core, but surface shear also slows the radial flow, thus the ground boundary layer forms a "leaky stopper" for air supplied at the ground end of the vortex "tube." This radial inflow in the boundary layer supplies mass for the vertical flow in the core. The effect of the boundary layer on the strength of the vortex is significant since the axial and azimuthal velocity

fields in a strongly rotating core are closely coupled (14).

Three sources of vorticity may contribute to the vertical rotating core:

1) vertical circulation originating in the atmosphere as a result of the earth's rotation, not usually significant in tornados;
2) vorticity from stretching and tilting of vortex lines, significant when cross wind accompanies a tornado;
3) vorticity created by non-symmetric pressure-density variations in the horizontal plane, caused by mixing of hot and cold air masses.

The last two sources deserve more attention. Examine the incompressible, constant viscosity, vorticity equation (4, 15)

$$\frac{D\bar{\omega}}{Dt} = \bar{\omega} \cdot \nabla \bar{u} - \frac{1}{\rho^2} \nabla \rho \otimes \nabla p + \nu \nabla^2 \bar{\omega}, \qquad (1)$$

where $\bar{\omega} = \nabla \otimes \bar{u}$.

The first term on the left hand side is the material rate of change of the vorticity with reference to an inertial axis. It includes vorticity convection.

The first term on the right hand side is the vorticity producing stretching and tilting of vortex lines. The significant contribution to a tornado vorticity comes when a cross wind creates vorticity lines in the ground boundary layer. Morton (14) showed this effect in Figure 2.

The second term on the right hand side is the creation of vorticity by density and pressure variations. Production of the vorticity depends on the inclination of the surfaces of constant pressure to the surfaces of constant density. Nielson (15)

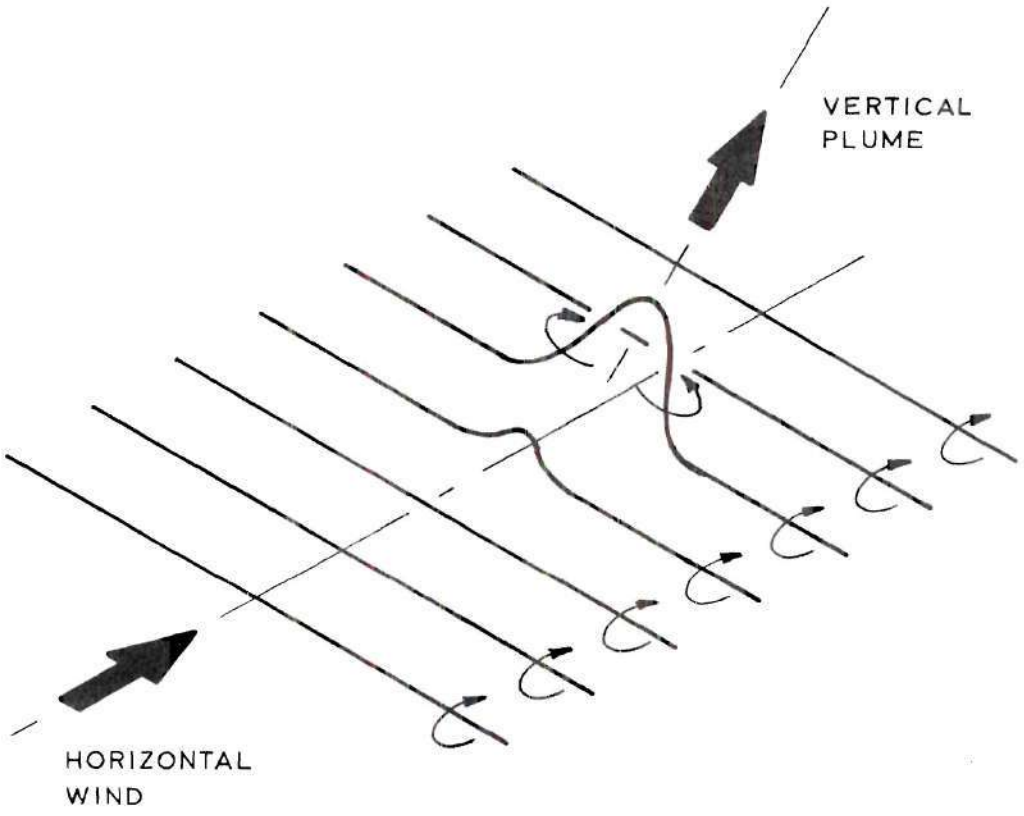

Figure 2. Vorticity from Tilting Vortex Lines.

shows how this mechanism may produce weak vertical vorticity in a fire whirl. Vorticity is also produced in this manner when hot and cold weather fronts move together.

The third term on the right hand side is the diffusive transport of vorticity to and from the surrounding elements.

Background and Previous Work

In 1969 a quantitative description of the turbulent boundary layer of a vortex in contact with a stationary flat surface appeared not to exist.

Mathematical solutions to the Navier-Stokes equations for the laminar boundary layer were available, first from Boedewadt (21) in 1940, and later from Schwiderski (22), Kidd, and Farris (8). Rott and Lewellen (20) dealt with the turbulent boundary layer using the momentum integral equations. Assuming self-similar velocity profiles and flat plate shear laws they arrived at an estimated solution of air supplied to the core by the boundary layer. They did not allow for back flow in their velocity profiles as King and Lewellen (9) had earlier indicated. Further progress in studying the boundary layer appeared to require the experimental simulation.

The importance of the work of Ying and Chang was discussed in the objective.

In 1971 H. L. Kuo (10) published a detailed analysis of the vortex-surface boundary layer by solving the Navier-Stokes equations with semi-empirical shear laws allowing for turbulent flow. His work did not eliminate the need for the experimental description sought by this thesis.

Advances Required

The advances required in this research are a quantitative description of the vortex-surface turbulent boundary layer, including velocity profiles and surface shear stress.

Scope

The scope of this thesis in pursuit of the quantitative description of the boundary layer is an experimental and analytical investigation, with emphasis on

mean velocity profiles, boundary layer thickness, surface shear stress, and mass supply to the core.

In the experimental investigation the turbulent boundary layer is simulated using a large vortex generator. The velocity profiles are measured with a two-dimensional V-probe hot wire anemometer. The surface shear is measured with a Preston tube using Patel's calibration (17). These measurements are made at different radii, while varying flow and vorticity characteristics.

The analytical investigation consists of evaluating the characteristics in the momentum integral equations, i.e. the characteristics thicknesses δ_r^*, δ_t^*, θ_r, δ_1, δ_2, and testing their solution.

The boundary layer equations are tested for similarity, and the empirical shear stress laws are derived.

CHAPTER II

EXPERIMENTAL EFFORT

The purpose of the experimental effort is to obtain a quantitative description of the vortex-surface boundary layer. It consists of flow simulation, velocity profile measurement, and surface shear stress measurement.

Instrumentation and Equipment

The instrumentation and equipment discussed in this section provide the flow generation, velocity profile measurement, and surface shear measurement.

The Vortex Generator

The vortex generator, shown in Figures 3 and 4 (construction drawings in Appendix A), was constructed to generate the vortex-surface turbulent boundary layer. It consists of the following major parts.

1) An overhead 42 inch diameter, 12,600 cubic feet per minute capacity attic fan, with a variable speed direct current, one horsepower motor, drives the vortex.
2) A cylindrical array of 24 vertical vanes, each 10 inches wide and 12 feet long, whose trailing edges form a cylinder of 48 inches in diameter, are hung from the ceiling by means of a 55 inch diameter ball bearing which permits the synchronous rotation of each vane about a vertical axis near its trailing edge through the angle of ± 75 degrees from the radius.
3) The working surface, representing the stationary ground below the vortex, is

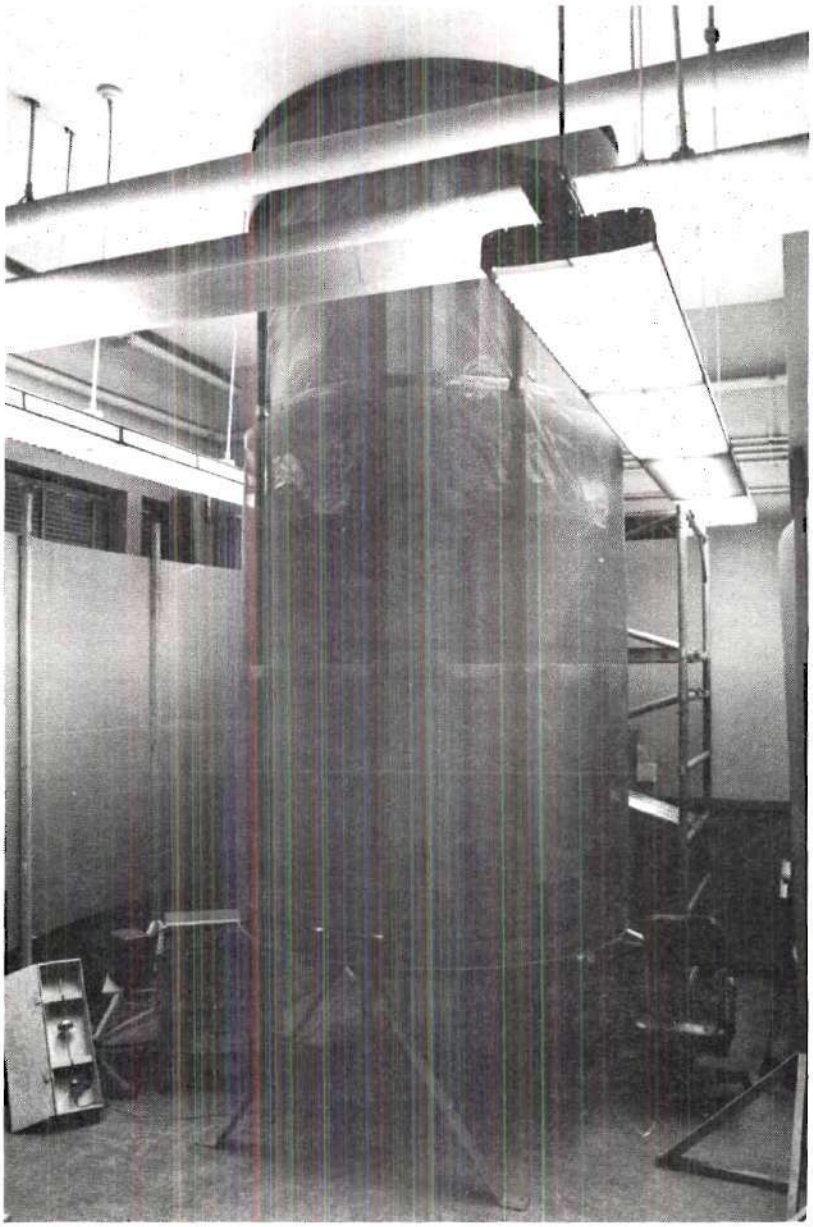

Figure 3. Vortex Generator Installed.

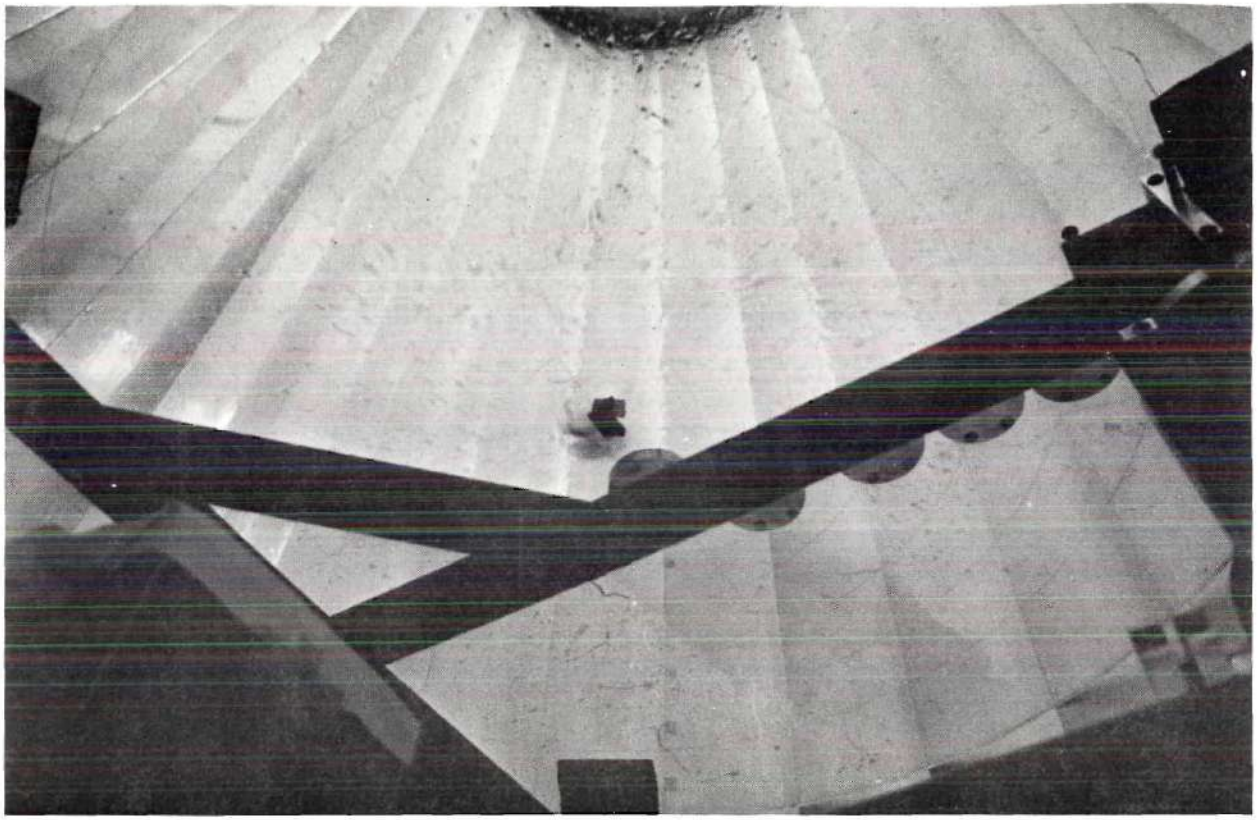

Figure 4. View Into the Vortex Generator from Below the Table During Attempted Flow Visualization.

a horizontal clear plexiglass table top, 48 inches in diameter. The surface, positioned four feet above the floor, permits visual observation of the vortex from below it. Instrumentation is accessible (inserted) from under the table.

The air is drawn through two wire mesh screens surrounding the vanes, then through the vanes at the vane angle, then upward through the fan orifice in the ceiling, and out through the fan. During operation a cardboard baffle surrounds the vortex generator to increase the vortex stability. It extends from $2\frac{1}{2}$ feet to $9\frac{1}{2}$ feet above the floor and is positioned three feet from the vortex generator outer radius. A polyvinyl plastic sheet covers the upper portion of the vortex generator down to five feet above the table top to adjust the radial air supply to the potential vortex.

The vortex generator was made large to obtain a fully developed turbulent boundary layer over a large part of the ground radius. The characteristic dimensions during operation are

a) the core length to diameter ratio

$$\frac{L}{D} \approx 20. \ ,$$

b) the boundary layer thickness to radius ratio

$$\frac{\delta}{R} \approx 0.25 \ ,$$

c) and the ratio of hot wire diameter to boundary layer thickness

$$\frac{d}{\delta} \approx 0.0002 \ .$$

The boundary layer was assumed to be turbulent for tangential Reynolds

number

$$Re_t = \frac{rv_{t\,\infty}}{\nu} > 10^4 \quad .$$

This number is thought to be conservative based on the following consideration.

Transition to turbulent boundary layer on a rotating disc begins at (21)

$$Re_t \approx 4 \times 10^4 \quad .$$

Ignoring the effect of radial flow, we see this value corresponds to the two-dimensional flat plate transition (21)

$$Re_x = \frac{xu}{\nu} \approx 3 \times 10^5 \quad ,$$

where the distance along the plate, x, corresponds to the circumference, $2\pi r$, in the tangential flow direction.

Thus it appears the transition to turbulent flow in the boundary layer will occur at

$$Re_t < 10^4 \quad .$$

The tests in this research will be run at $Re_t > 10^4$.

The operating conditions for the vortex generator may be characterized as

1) angular momentum variations corresponding to a range of tangential Reynolds numbers based on the free stream circulation of the potential vortex,

$$\Gamma = rv_{t\,\infty} \quad , \qquad 16,000 < Re_t = \frac{\Gamma}{\nu} < 47,000 \quad ,$$

2) radial inflow corresponding to the directional change of the intake velocity for vane angles of 60.0 degrees to 75.0 degrees measured from the radius.

The final configuration of the vortex generator and its operating range were established experimentally. The fan orifice size, the height of the plastic covering, and varying screen installations were tested.

Hot Wire Anemometer

To measure the two-dimensional time mean velocity profile of the boundary layer, an inexpensive, constant temperature, V-probe hot wire anemometer was selected, designed, and built. Figures 5, 6, and 7 are pictures of the probe. Appendix B contains the schematic wiring diagram in Figure 49 and the details of the design, the analysis, the construction, and the calibration of the probe.

The hot wire anemometer relation between current, velocity, wire temperature, and ambient temperature occurring when a current heated wire transfers heat to an ambient fluid environment is used.

A balanced Wheatstone bridge gives constant wire temperature. The fluid ambient temperature is measured with a mercury thermometer to ± 0.1 degree.

The V-probe has two 0.001 inch diameter wires mounted in a 90 degree "V" to operate parallel to the surface in the plane of the two-dimensional velocity field. The probe height is adjustable to the nearest 0.001 inch in a range of 0.200 inch to 6.000 inches above the surface. The direction of the velocity is indicated by rotating the probe into the velocity vector until the probe direction bridge circuit in Figure 50 is balanced. The direction bridge is sensitive to ± 0.5 degree. The velocity magnitude is determined by varying the current to balance the Wheatstone bridge

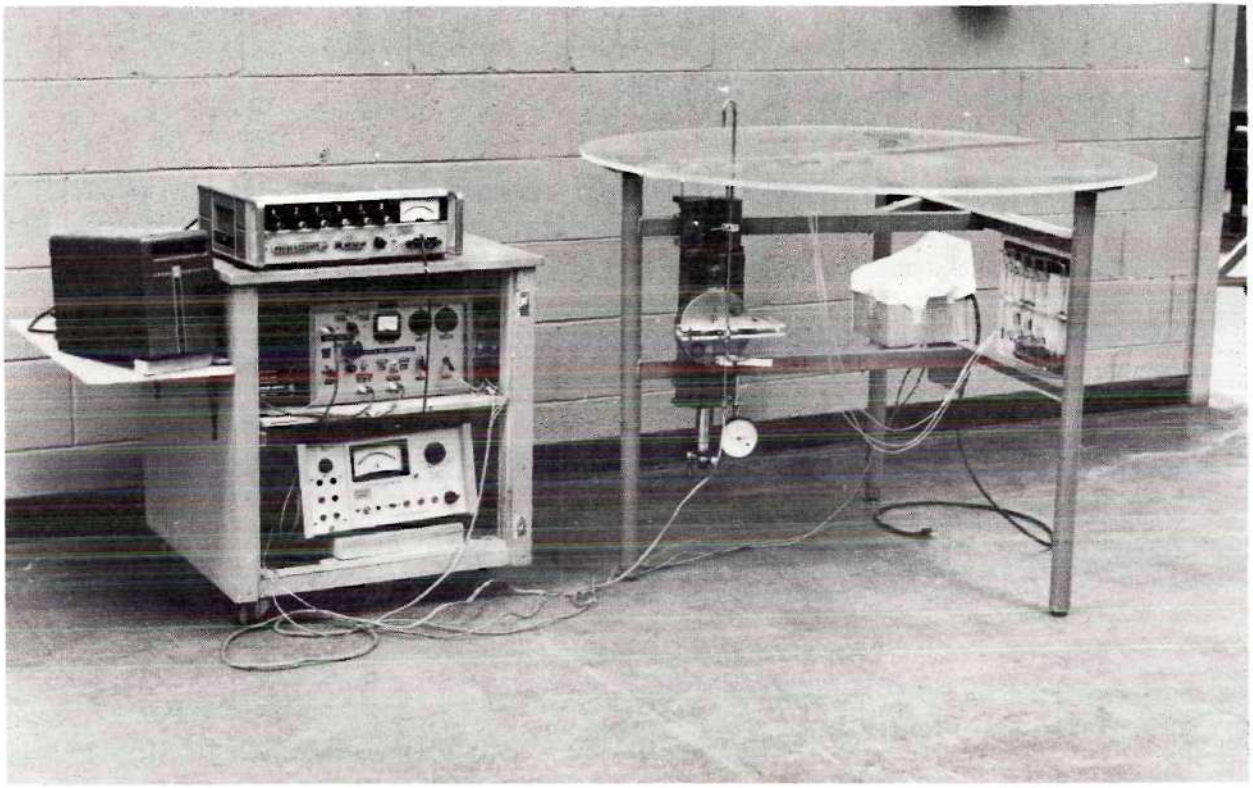

Figure 5. Vortex Generator Table with the Hot Wire Anemometer and the Preston Tube Mounted.

Figure 6. Installation of the Hot Wire Anemometer and the Preston Tube in the Table Surface.

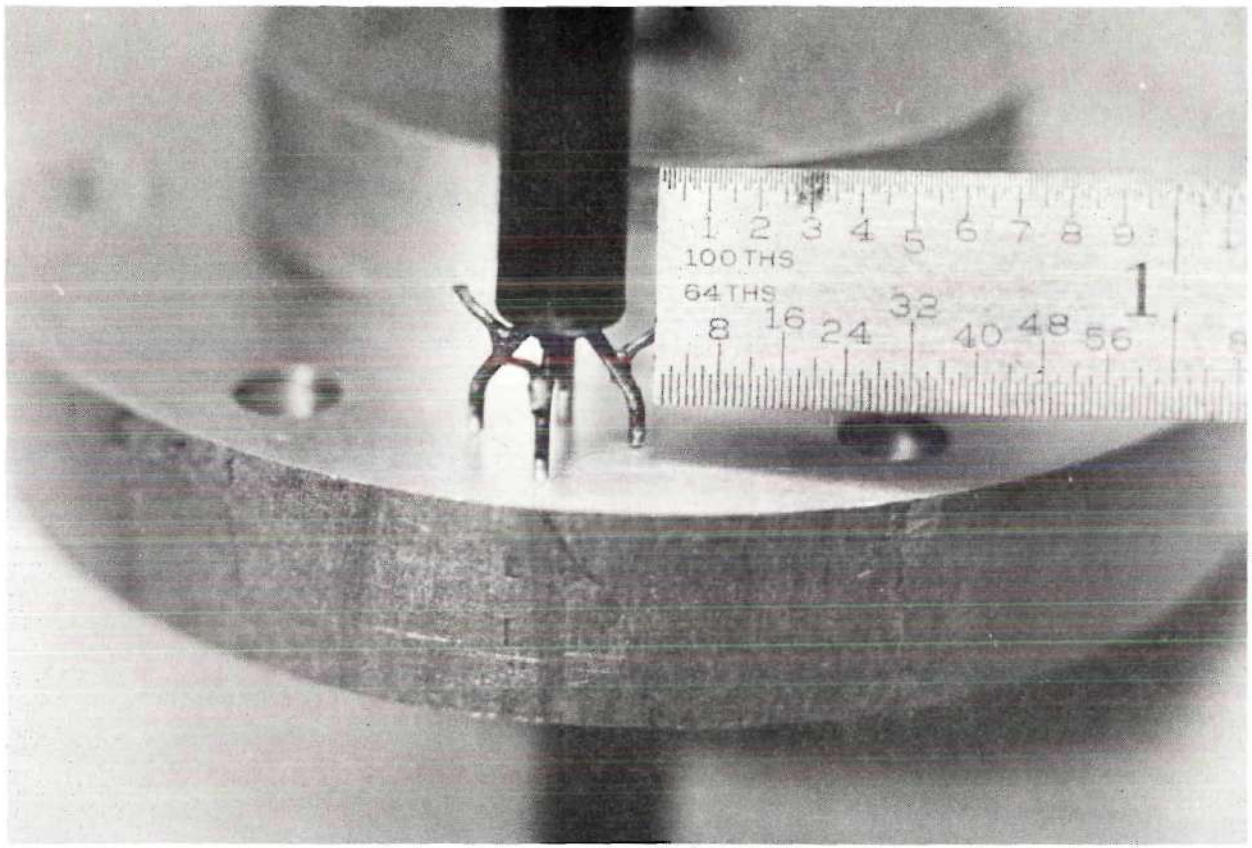

Figure 7. Hot Wire Probe Tip Close Up.

(magnitude bridge). The velocity magnitude bridge is sensitive to 0.01 foot per second. The velocity direction measurement is not affected by small changes in direction bridge current, I, in Figure 50, or by small changes in the velocity. The velocity magnitude measurement is insensitive to the probe direction for ± 5 degrees from its null position.

Calibration furnished the most dependable current-velocity-temperature relation. Analysis was used to support the calibration.

The velocity magnitude of the probe was calibrated on a variable speed rotating arm, shown in Figure 8. The velocity direction was calibrated in a small one-dimensional wind tunnel. Details are given in Appendix B, the results are presented here.

In the calibration, the shunt voltage, which is related directly to the current in a single wire, is used instead of the wire current. The shunt voltage, from the analysis in Appendix B, is about

$$E_S \simeq 2 I_W$$

Figure 9 is the plotted data from the velocity magnitude calibration. These data were then reduced to a single analytical expression for the velocity-temperature current relation. Based on the plotted ambient temperature dependence in Figure 10, and on the expected heat transfer relation expressed in equations (3), (4), and (5); the current was assumed to vary exponentially with the driving potential temperature difference, $T_W - T_\infty$, for all velocities, that is

$$I_W \sim (T_W - T_\infty)^n \quad . \tag{2}$$

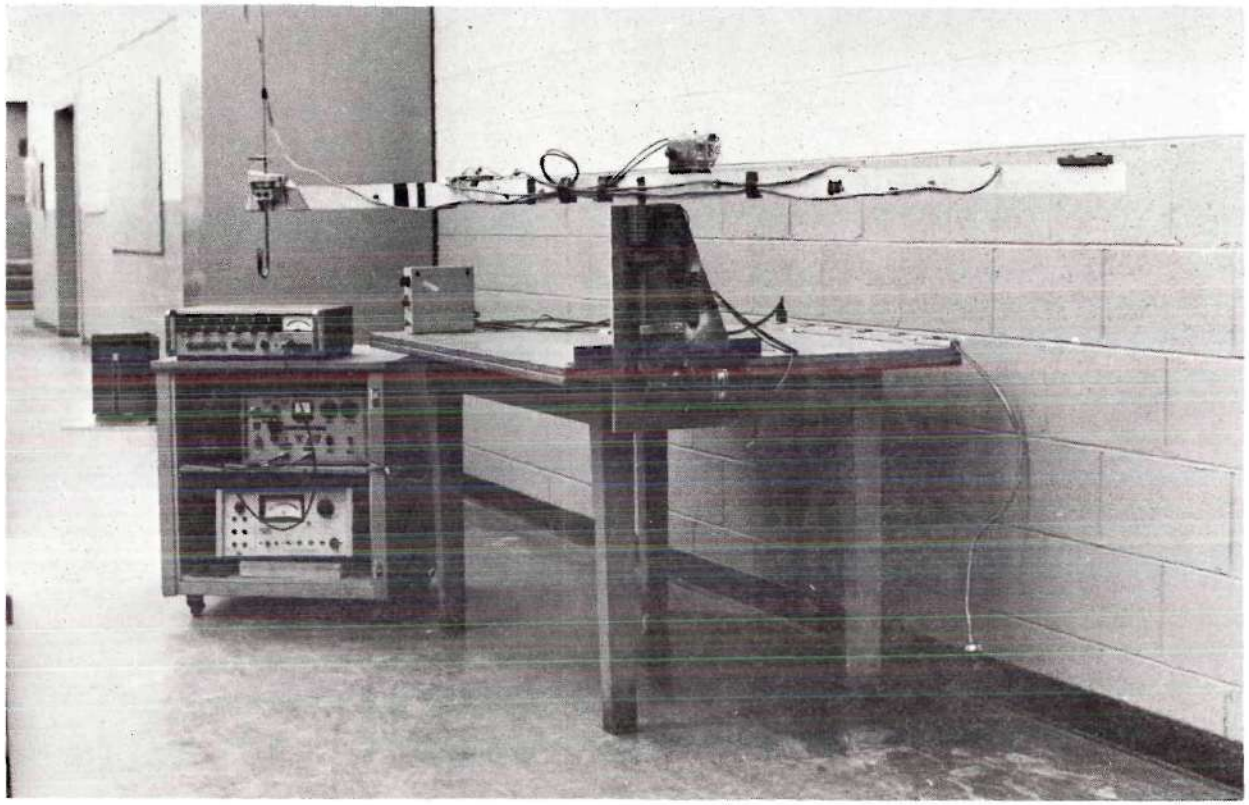

Figure 8. Hot Wire Anemometer Calibrator.

From Figure 10 the average power, n, was calculated to be n = 0.61. The data of Figure 9 were then reduced to an 80 degree ambient temperature for the known operating wire temperature, T_w = 266 degrees, and plotted in Figure 11. The results show a single current-velocity calibration curve which was fitted with a seventh order polynomial, shown in Figure 11. The calibration data then show a maximum scatter of the smaller of 0.4 foot per second or four percent in the velocity about the velocity magnitude calibration.

The probe was designed to have its reference angle point directly into the velocity vector when the direction bridge was balanced, but this result was not achieved in the construction. The error, called the velocity reference angle, was determined from calibration. The results are presented in Figure 12. The velocity reference angle was found to be, Ψ_o = -2.8 degrees. The direction calibration shows the probe sensitive to $\pm$ 0.5 degree in measuring the velocity direction. Also shown in Figure 12, from Appendix B, is the estimated response of the probe direction bridge. Further details of this calibration are in Appendix B.

The analysis of the hot wire response is now presented. The primary heat transfer mechanism is convection, giving the relation

$$I_w^2 R_w = \pi r^2 h(T_w - T_\infty) \tag{3}$$

From the analysis in Appendix B the hot wire response is calculated using the following empirical convection heat transfer relations for infinite wires:

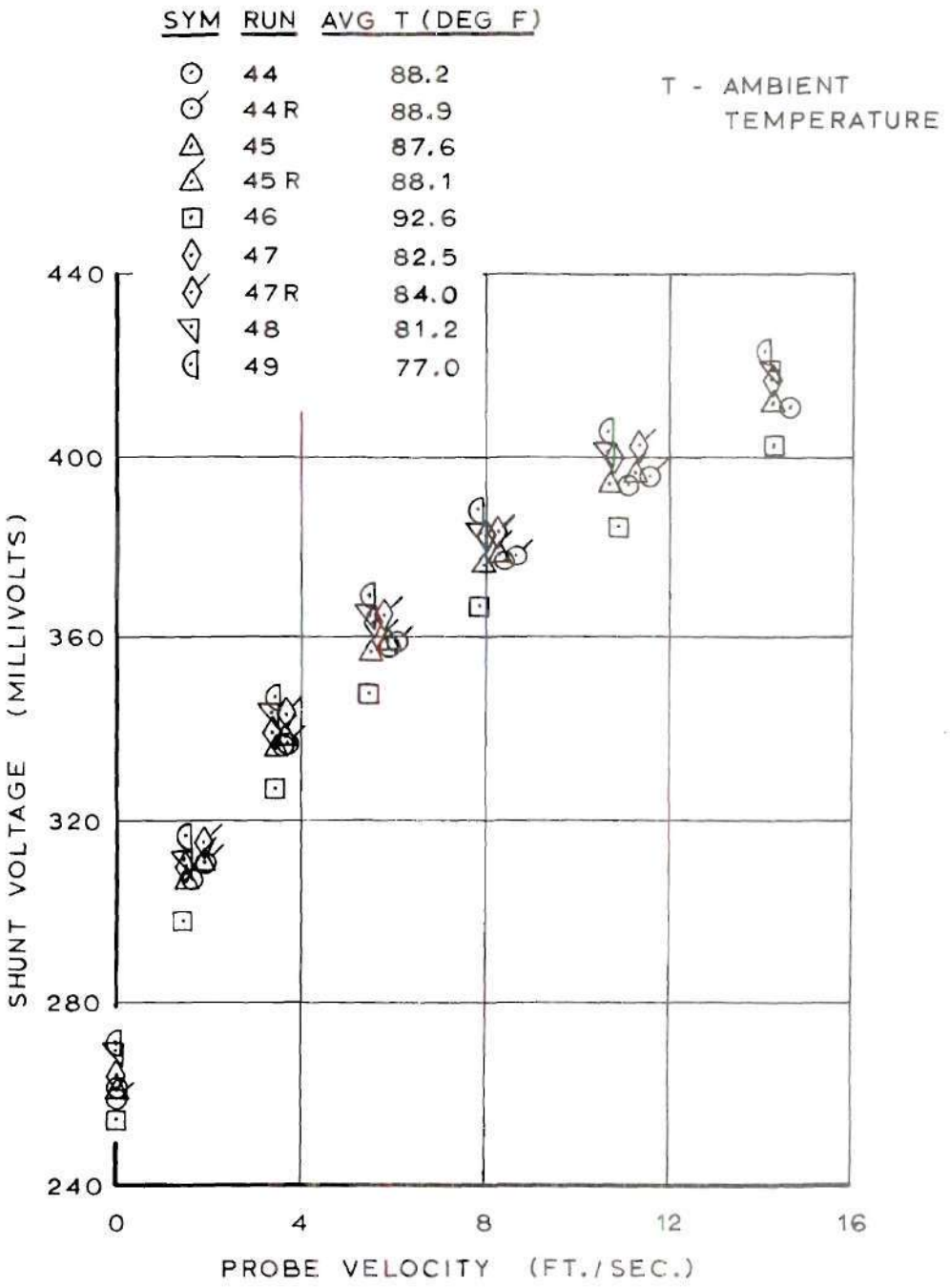

Figure 9. Hot Wire Recorded Calibration Data.

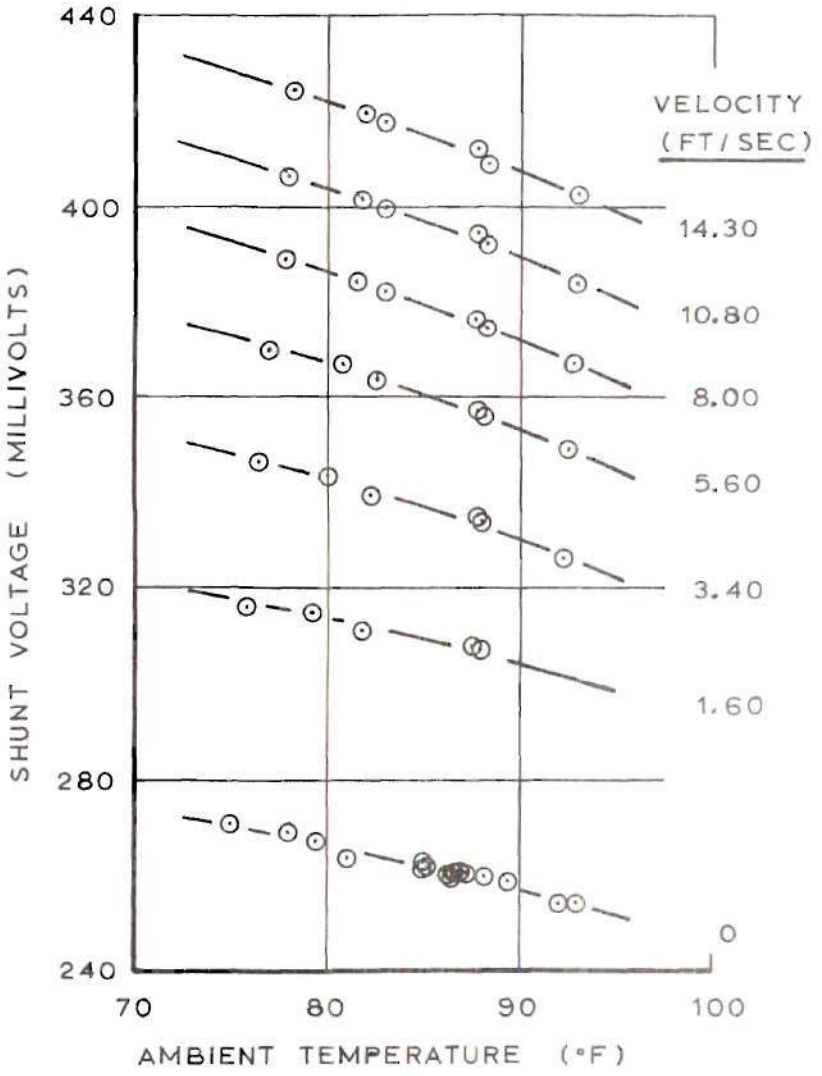

Figure 10. Hot Wire Ambient Temperature Dependence.

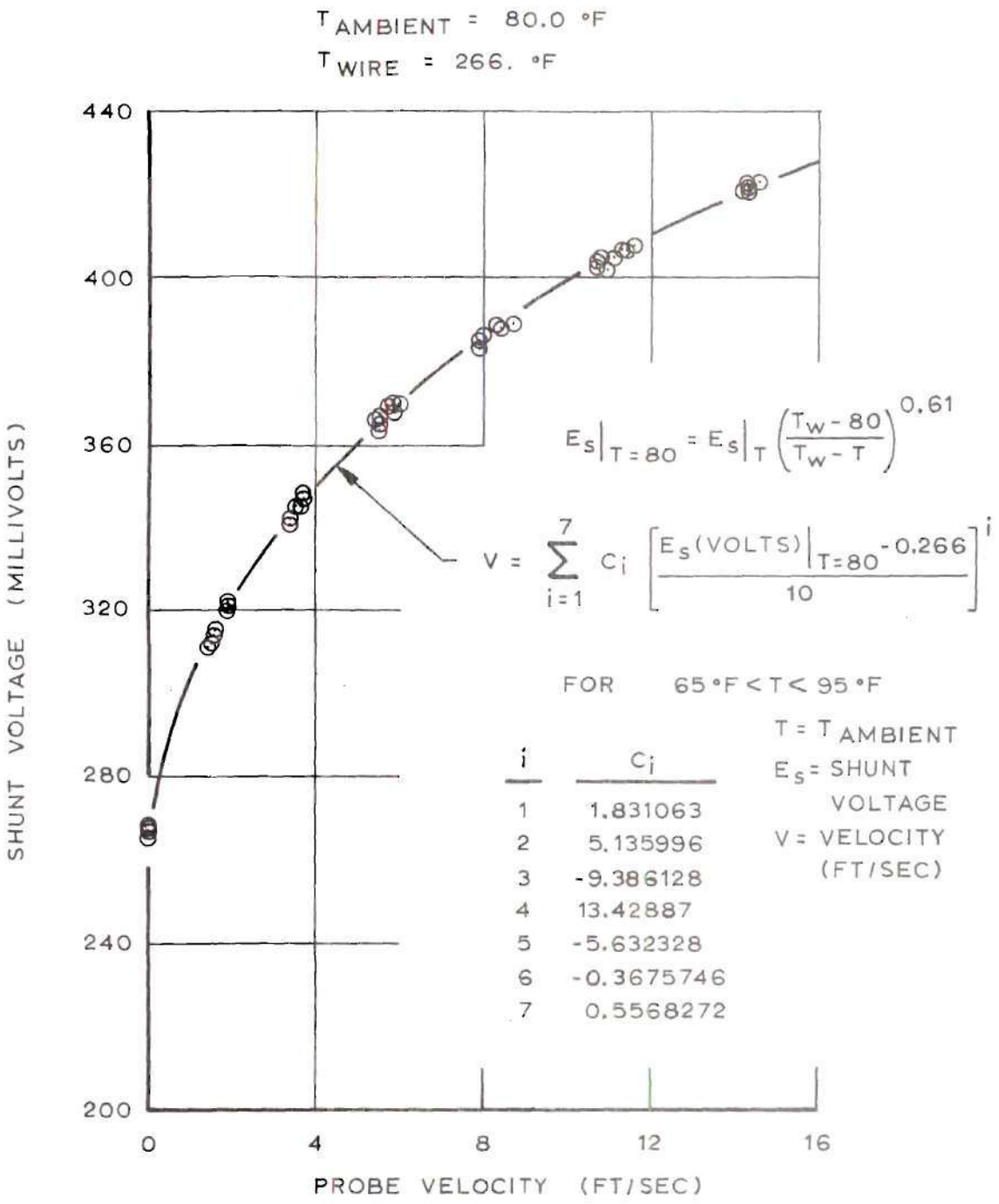

Figure 11. Velocity Magnitude Calibration Curve.

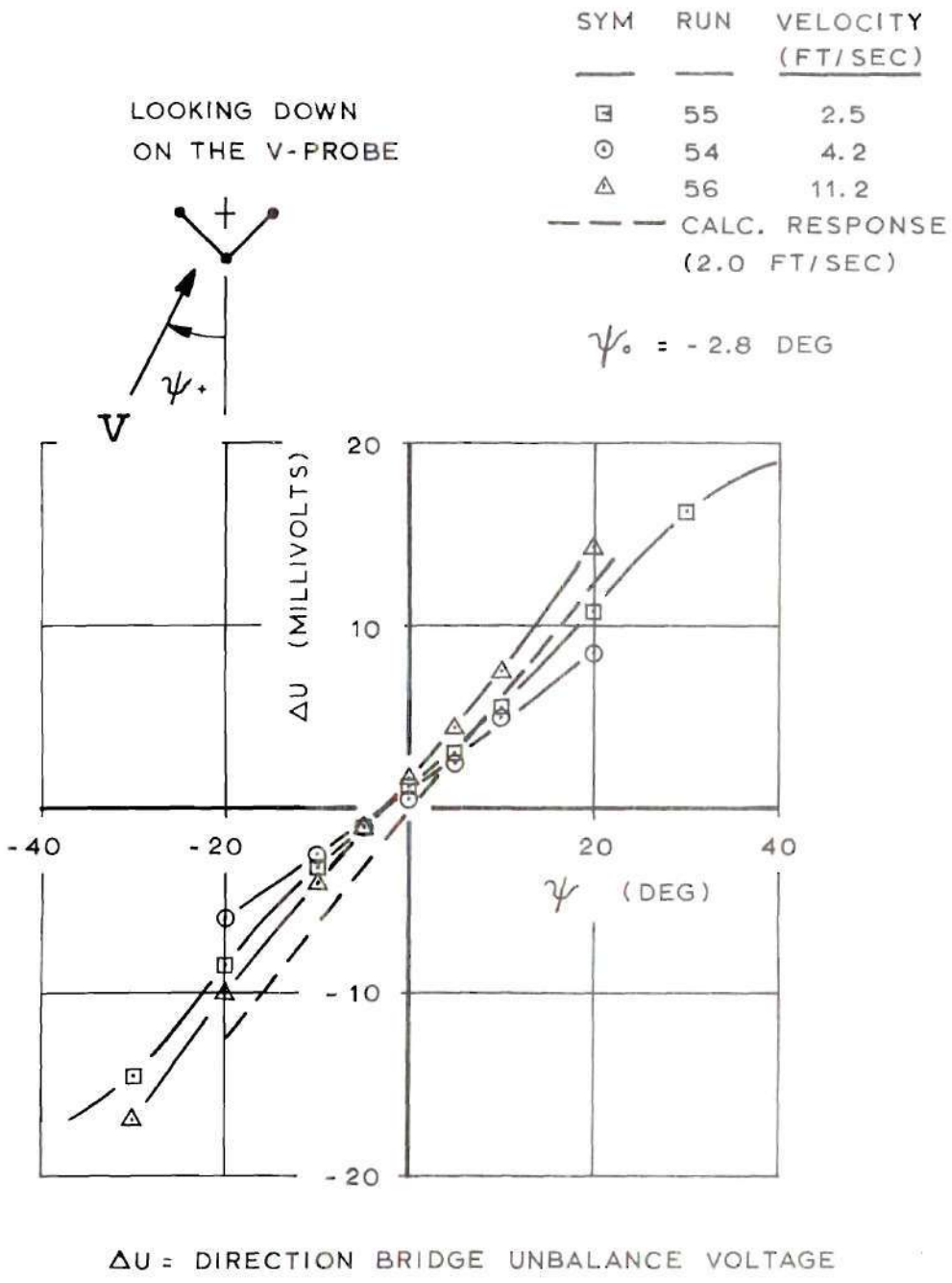

Figure 12. Probe Calibration for Velocity Direction.

a) free convection (6)

$$Nu_f = [Pr_f Gr_f]^{\frac{1}{12.5}} , \tag{4}$$

for $$10^{-5} < Pr_f Gr_f < 1 ,$$

b) forced convection (1)

$$Nu_f \left(\frac{T_f}{T_\infty}\right)^{-0.17} = 0.24 + 0.56 (Re_f)^{0.45} , \tag{5}$$

for $$0.2 < Re_f < 44,$$

where

the film temperature $$T_f = \frac{T_w + T_\infty}{2} , \tag{6}$$

the Reynolds number $$Re_f = \frac{ud}{\nu_f} , \tag{7}$$

the Nusselt number $$Nu_f = \frac{h_f d}{k_f} , \tag{8}$$

the Grashof number $$Gr_f = \frac{g}{T_f} \frac{(T_w - T_\infty)}{\nu_f^2} d^3 , \tag{9}$$

and the Prandtl number $$Pr_f = \frac{\mu_f c_p}{k_f} . \tag{10}$$

The hot wire response was calculated for convection only, and for convection with conduction end losses. The radiation heat losses were also calculated and found to

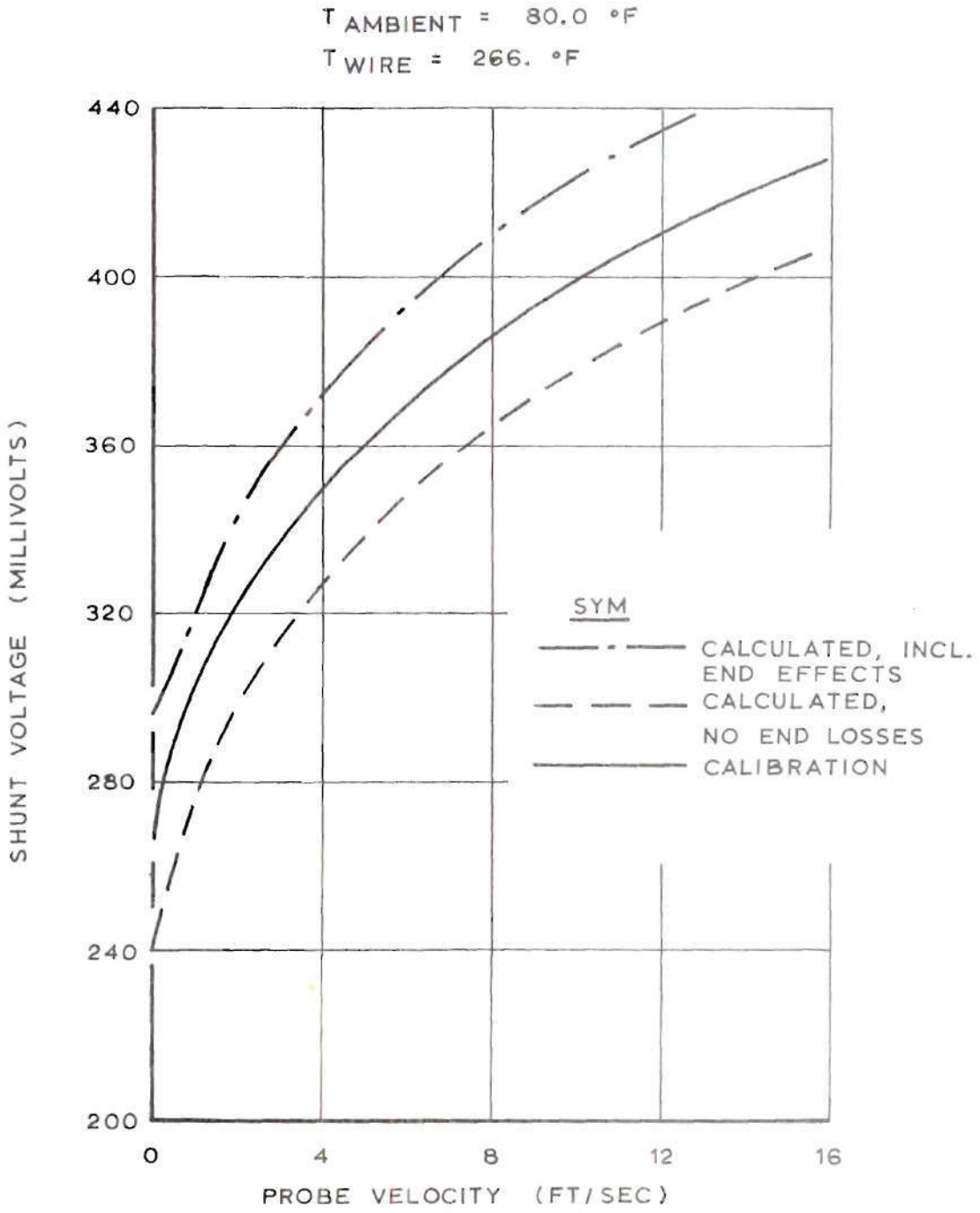

Figure 13. Calculated Hot Wire Response and Calibration Comparison.

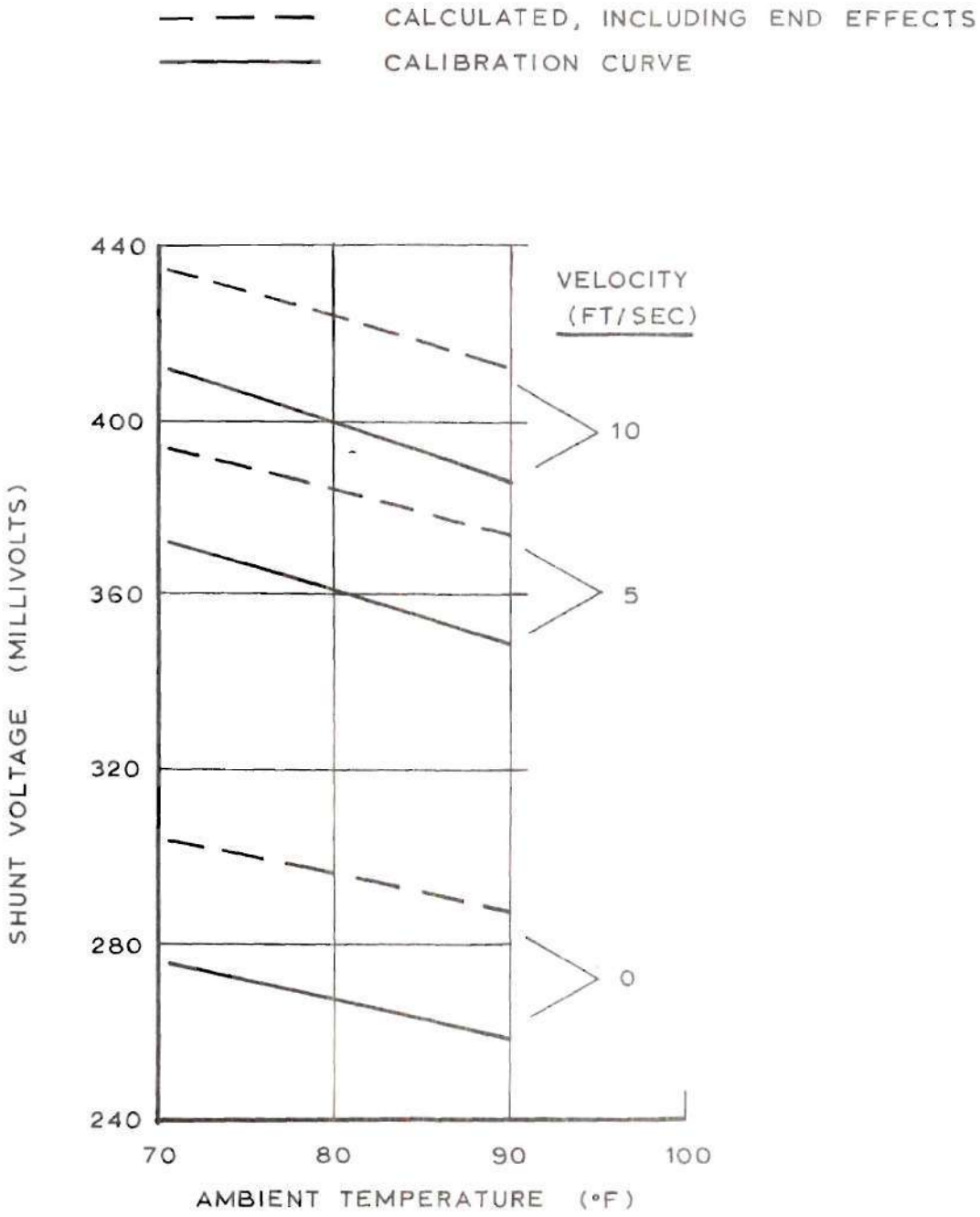

Figure 14. Calculated Hot Wire Ambient Temperature Dependence Compared to Calibration.

be about two percent of the total heat transfer, so radiation was neglected in the final calculations. Figures 13 and 14 present the results of the calculations compared to the calibration. As shown in Figure 13, the conduction end losses are significant. The calculated hot wire response may be in error ± 5 percent in the shunt voltage due to

a) uncertainties in the wire physical and electrical properties, and

b) simplification of the circuit for the analysis, for example, assuming both the wires have the same resistance.

Within the limitations of the analysis, the calibrated results are well supported.

Preston Tube

Available Techniques. The Preston tube was used to measure the wall shear stress, but in its selection the following methods were also considered.

1) A "floating element" balance (2) measures directly the shear force on an isolated element of the boundary surface. This method is presently widely used. Its chief advantage is that it gives a direct measurement. Its main disadvantages are that air may flow around the edges of the element when used in a flow with pressure gradients, and it is susceptible to erratic behavior caused by shock and vibration.

2) A "heated element" (13) works on the principal of Reynolds analogy and measures the heat transfer through an element of the boundary surface. This method requires constant Prandtl number and a small temperature difference between the free stream and the heated element.

3) The "Stanton tube" (5) used a flat sharp edged tube to measure total pressure

in the laminar sublayer next to the boundary surface. The difference between this pressure and the static pressure at the same location yields the skin friction. The Stanton tube gives much lower pressure differences than the Preston tube and must be mechanically more precise.

4) The "razor blade" (sublayer fence) technique (3, 5) uses a "razor blade" extended a few thousandths of an inch above the surface, perpendicular to it and perpendicular to the flow in the laminar sublayer next to the surface. The skin friction is a function of the difference in static pressure on each side of the blade. The pressure difference signal from the "razor blade" is larger than the Stanton tube signal but smaller than the Preston tube signal.

5) The momentum integral (wake transverse) method (16) uses the change in momentum calculated from two velocity profiles measured above two points on the boundary surface. This method is not considered very accurate or reliable due partly to inaccuracies in the measurements and partly to the fact that the flow may be slightly three-dimensional when the velocity profiles are assumed to be two-dimensional. When calculating the surface shear stress, taking the difference between the two velocity profiles of approximately the same magnitude increases existing errors.

6) The velocity profile slope method uses the velocity profile slope at the surface calculated from the measured velocity profile. It works best if velocities can be measured in the laminar sublayer. It is unreliable, differentiation compounds the errors in the measurements.

7) The Preston tube (17, 18) senses the pressure difference between the pressure

from a total pressure tube resting on the boundary surface and the pressure from a static pressure tap at the same location. It is simple to construct. It must be totally in the boundary layer where the "law of the wall" applies.

Preston Tube Considerations. From the methods considered the Preston tube offered the greatest accuracy combined with simple construction, but the vortex boundary layer presented several problems. The boundary layer is three-dimensional (The Preston tube was calibrated in a two-dimensional boundary layer.); it has a radial pressure gradient, and the Preston tube differential pressure signal is small enough to make detection difficult.

An electronic manometer solved the latter problem, allowing measurement of all but the smallest signals encountered.

To be used in rotational flow the probe, shown in Figure 15, was made to rotate into the flow, so that at impact the velocity vector was perpendicular to the face of the total pressure tube. To get the static pressure at the face of the total pressure tube, two static pressure taps were placed to each side of the face, far enough out so that the static pressure would not be affected by the presence of the tube. This effect was checked by a similar Preston tube plug with the total pressure tube removed. Two taps were used to compensate for the pressure gradient parallel to the face of the total pressure tube, the average of the pressure differences between each static tap and the total tube being used. In operation though, no significant difference between the two pressure differences could be detected except at the smallest radii. Initially, the two static taps were to correct for the pressure gradient completely. However, as later noticed, they corrected only

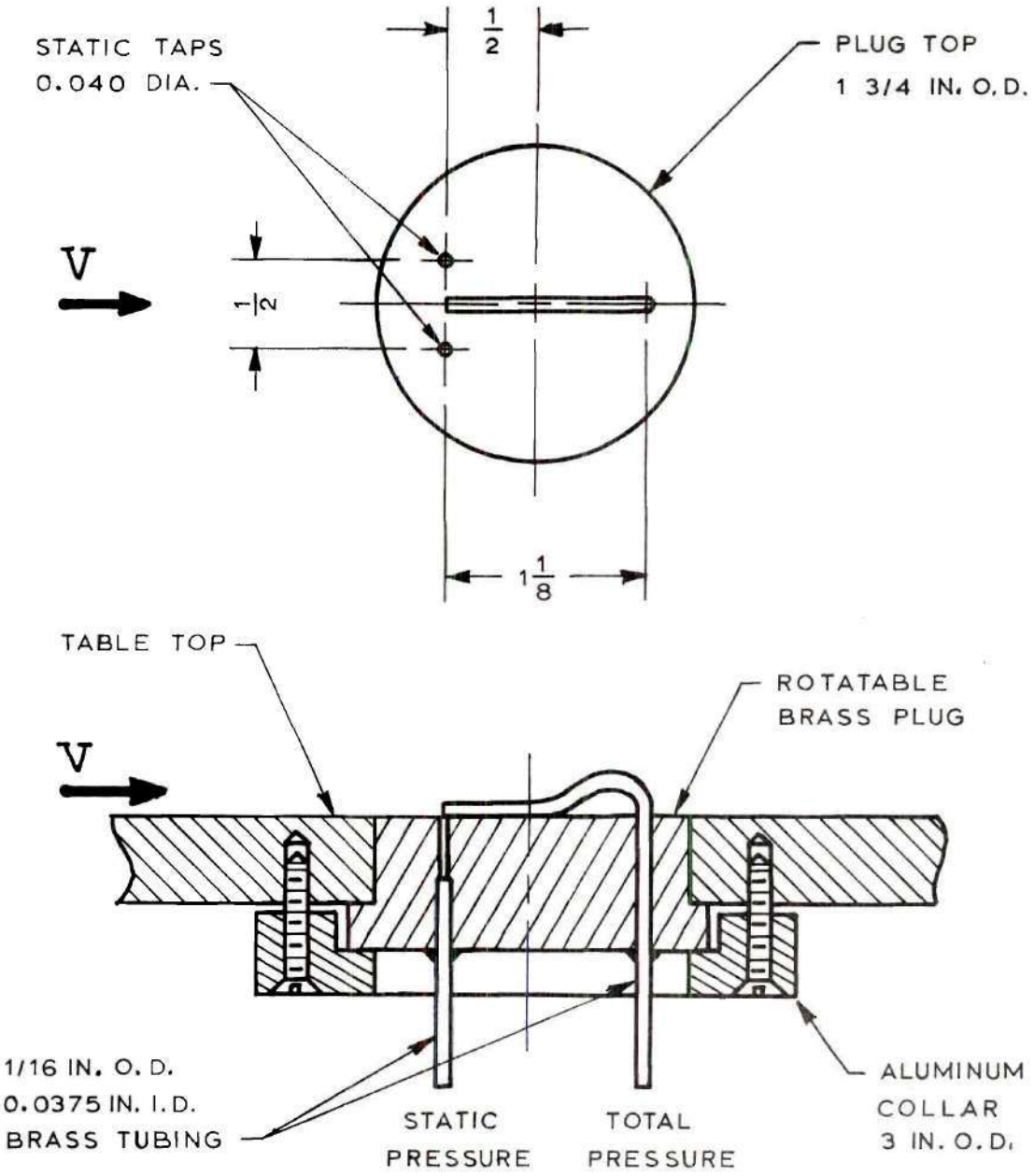

Figure 15. Preston Tube.

for the pressure gradient parallel to the face of the total pressure tube but not for the pressure gradient perpendicular to it. This effect will be considered later.

Patel's experiments supported the law of the wall for turbulent boundary layers, whether external or internal, as long as the pressure gradient on the boundary layer was within certain limits. His experiments indicated that with a symmetrical bore for round Preston tubes the ratio of inside to outside diameter has a negligible effect on the calibration for diameter ratios larger than 0.2. The Preston tube used here has a ratio of 0.6. Additionally, earlier experiments by Smith and Walker (17) suggested that the law of the wall is valid for $z/\delta < 1/6$, where δ is the boundary layer thickness. The Preston tube as used here stays well within that range.

Preston Tube Calibration. (17, 18) Von Karman (21) using Prandtl's mixing length theory in the momentum equations proposed a unique law of the wall,

$$\frac{u}{U_\tau} = F\left(y\frac{U_\tau}{\nu}\right), \tag{11}$$

where the friction velocity,

$$U_\tau = \sqrt{\frac{\tau_w}{\rho}},$$

in a region near the surface. Ludweig and Tillman (18) were able to confirm this law experimentally. Since the function is unique, the wall shear stress, $\tau_w = \mu(\partial u/\partial y)_{y=0}$, is uniquely related to the kinetic energy, ρu^2, in the flow. The Preston tube pressure difference, Δp, is caused by the kinetic energy striking the

face of the tube integrated over the tube face. Thus, Preston (18), assuming the existence of a region near the surface in which conditions are functions only of skin friction, the relevant physical properties (ρ and ν) of the fluid, and a suitable length, obtained a universal non-dimensional relation for the difference between the total pressure recorded by a round pitot tube resting on the surface and the static pressure at the wall, in terms of the skin friction. It is, using the tube diameter, d, as the reference length,

$$\frac{\Delta p d^2}{\rho \nu^2} = F\left(\frac{\tau_w d^2}{\rho \nu^2}\right) , \tag{12}$$

where Δp is the pressure difference, $\Delta p d^2/\rho\nu^2$ is the non-dimensional kinetic energy striking the tube face, $\tau_w d^2/\rho\nu^2 = (U_\tau d/\nu)^2$ is the law of the wall similarity parameter, and F is the function relation.

Patel's (17) calibration curves establishing the function, F, are used here. They are

with
$$x^* = \log\left[\Delta p \frac{d^2}{4\rho\nu^2}\right] , \tag{13}$$

and
$$y^* = \log\left[\tau_w \frac{d^2}{4\rho\nu^2}\right] , \tag{14}$$

for
$$0 < x^* \leq 2.9 ,$$

$$y^* = \tfrac{1}{2} x^* + 0.037 , \tag{15}$$

for
$$2.9 < x^* < 5.6 ,$$

$$y^* = 0.8287 - 0.1381\, x^* + 0.1437\, x^{*2} - 0.0060\, x^{*3} , \tag{16}$$

and for $5.6 \leq x^* < 7.6$,

$$x^* = y^* + 2 \log_{10}(1.95\, y^* + 4.10) . \tag{17}$$

Patel established error limitations for pressure gradients in the direction of the flow. They are

1) for adverse pressure gradients,

$$\frac{\delta(\tau_w)}{\tau_w} < 0.03 \text{ for } 0 < \Delta < 0.01 ,$$

$$\frac{\delta(\tau_w)}{\tau_w} < 0.06 \text{ for } 0 < \Delta < 0.015 ,$$

2) and for favorable pressure gradients with $d\Delta/dx < 0$,

$$\frac{\delta(\tau_w)}{\tau_w} < 0.03 \text{ for } 0 > \Delta > -0.005 ,$$

$$\frac{\delta(\tau_w)}{\tau_w} < 0.06 \text{ for } 0 > \Delta > -0.007 ,$$

where

$$\Delta = \frac{\nu}{\rho\, U_\tau^3} \frac{dp}{dx} , \tag{18}$$

and

$$U_\tau = \sqrt{\frac{\tau_w}{\rho}} . \tag{19}$$

Patel's calibrations are empirical for pipe flow, but may be extended to external flow. The pressure gradient effect is caused by a departure from the law of the wall of the velocity profile. Physically, favorable pressure gradients lead to reversion to laminar flow. Unfavorable pressure gradients lead to separation of the flow. In severe favorable and adverse pressure gradients the Preston tube was found to overestimate the skin friction.

Pressure Gradient (Δ) Limitation in Vortex Flow. An estimation of Patel's, Δ, was calculated to see what error it may cause in the measured surface shear stress. The necessary pressure gradient, dp/dx, for the Δ calculation is derived from the radial momentum equation, assuming $v_z = 0$,

$$v_r \frac{\partial v_r}{\partial r} - \frac{v_t^2}{r} = -\frac{1}{\rho}\frac{\partial p}{\partial r} + \frac{1}{\rho}\frac{\partial \tau_{rz}}{\partial z} \quad . \tag{20}$$

Integrating this equation over the boundary layer with the boundary conditions, at $z = \delta$, $v_t = v_{t\infty}$, $v_r = v_{r\infty}$, and $\tau_{rz} = 0$, and at $z = 0$, $\tau_{rz} = \tau_{rz}(0) = \tau_{w_r}$, and recognizing that the vertical pressure gradient is of the order of ρg and negligibly small through the boundary layer, gives

$$\underset{①}{\rho \int_0^{\delta_r} v_r \frac{\partial v_r}{\partial r}\, dz} - \underset{②}{\rho \int_0^{\delta_r} \frac{v_t^2}{r}\, dz} = \underset{③}{-\delta_r \frac{\partial p}{\partial r}} + \underset{④}{\tau_{w_r}} \quad . \tag{21}$$

Term ① is the radial acceleration force. Term ② is the centripedal acceleration force. Term ③ is the pressure gradient force. Term ④ is the wall

shear force. Free stream conditions are

$$v_{r\infty}\frac{\partial v_{r\infty}}{\partial r} - \frac{v_{t\infty}^2}{r} = -\frac{1}{\rho}\frac{\partial p}{\partial r} \quad . \tag{22}$$

In a two-dimensional boundary layer (where Patel made his calibrations) term (2) is absent resulting in Von Karman's momentum integral equation, and the pressure gradient term (3) serves only to accelerate the radial velocity. This is the pressure gradient used to calculate Patel's Δ in a two-dimensional boundary layer. In a three-dimensional vortex boundary layer, the radial pressure gradient primarily balances the centripedal acceleration term (2) . The difference between term (3) and term (2) remains to accelerate the radial velocity. The pressure gradient for Patel's Δ in the three-dimensional vortex boundary layer is the component in the flow direction of the difference just mentioned. It is, using equation (22) and neglecting $v_{r\infty}\frac{dv_{r\infty}}{dr}$, which is small compared to $v_{t\infty}^2/r$,

$$\frac{dp}{dx} = -\rho\frac{v_{t\infty}^2}{r}\left\{\int_0^1\left[1-\left(\frac{v_t}{v_{t\infty}}\right)^2\right]d\eta\right\}\cos\Phi \tag{23}$$

where $\eta = z/\delta_r$.

Using the above equation and evaluating Δ from several sample test conditions gave, generally, $\Delta \approx -0.002$. Thus the error in τ_w, measured by the Preston tube, due to the pressure gradient is less than three percent.

Experimental Procedure

Flow Generation

The vortex-surface boundary layer was produced by the vortex generator. The vanes were set at angles of 60.0, 67.5, and 75.0 degrees measured from the radius to produce rotating flows in the clockwise direction, when viewed in the direction of increasing height. At each angle three fan speeds were used to produce the variation of freestream circulation, Γ, shown in Table 1. A pitot tube installed directly above the fan was used to monitor the flow through the fan, which varied, based on the pitot readings, from approximately 6,000 to 12,000 cubic feet per minute for the three fan speeds.

At each vane angle and fan speed, measurements of height, indicated angle, shunt voltage, and ambient boundary layer temperature were made at each of five radial positions, 6.00, 9.00, 12.00, 15.00, and 18.00 inches (sample data shown in data reduction program in Appendix C). Additional radial positions of 3.00 and 21.00 inches were available, but they were not used because the first was too close to the core and the second was too close to the edge of the developing boundary layer. Water was injected through a small hole at the center of the table to check the position of the center of the vortex core with respect to the center of the table.

Velocity Profile Measurement

The V-probe was inserted through the table at a radial position to measure velocity magnitude and direction versus height. The probe reference angle was established by aligning the probe pointer (mentioned in the calibration in Appendix B), which was below the table and coincident with the probe reference angle, with

the line of centers of the plug positions at each radius, shown in Figure 16. The reference height of the probe V above the surface was established with a finely honed stop, mounted to the probe and extending 0.021 inch below the mean wire "V" plane. The probe was then adjusted to the desired height to within $\pm$0.0005 inch with a modified lathe cross feed bed. Close to the surface a dial indicator permitted changes in the probe height to within $\pm$0.0001 inch.

After the angle referencing and height adjustment, the V was pointed approximately into the velocity direction using a small pennant mounted three inches above the probe V. Then the magnitude bridge was balanced to provide the proper voltage to the direction bridge. The direction bridge was then balanced by rotating the probe, and the indicated angle was recorded from a protractor and pointer mounted below the table, the first to the probe and the second to the feed bed. With the probe pointing into the velocity direction, the magnitude bridge was rebalanced and the shunt voltage recorded. The room temperature was read from a mercury thermometer, to $\pm$0.1 degree Fahrenheit accuracy, mounted at the edge of the table and extending into the boundary layer air supply. Initially a thermocouple installed in the probe tip was to be used to measure the ambient temperature, however, the heated wire interfered with the thermocouple readings. Attempts to eliminate or work around this problem by moving the thermocouple away from the wire and by calibration of the thermocouple with the heating effect included failed, so the mercury thermometer was used.

Surface Shear Stress Measurement

For the surface shear stress measurement the Preston tube was mounted

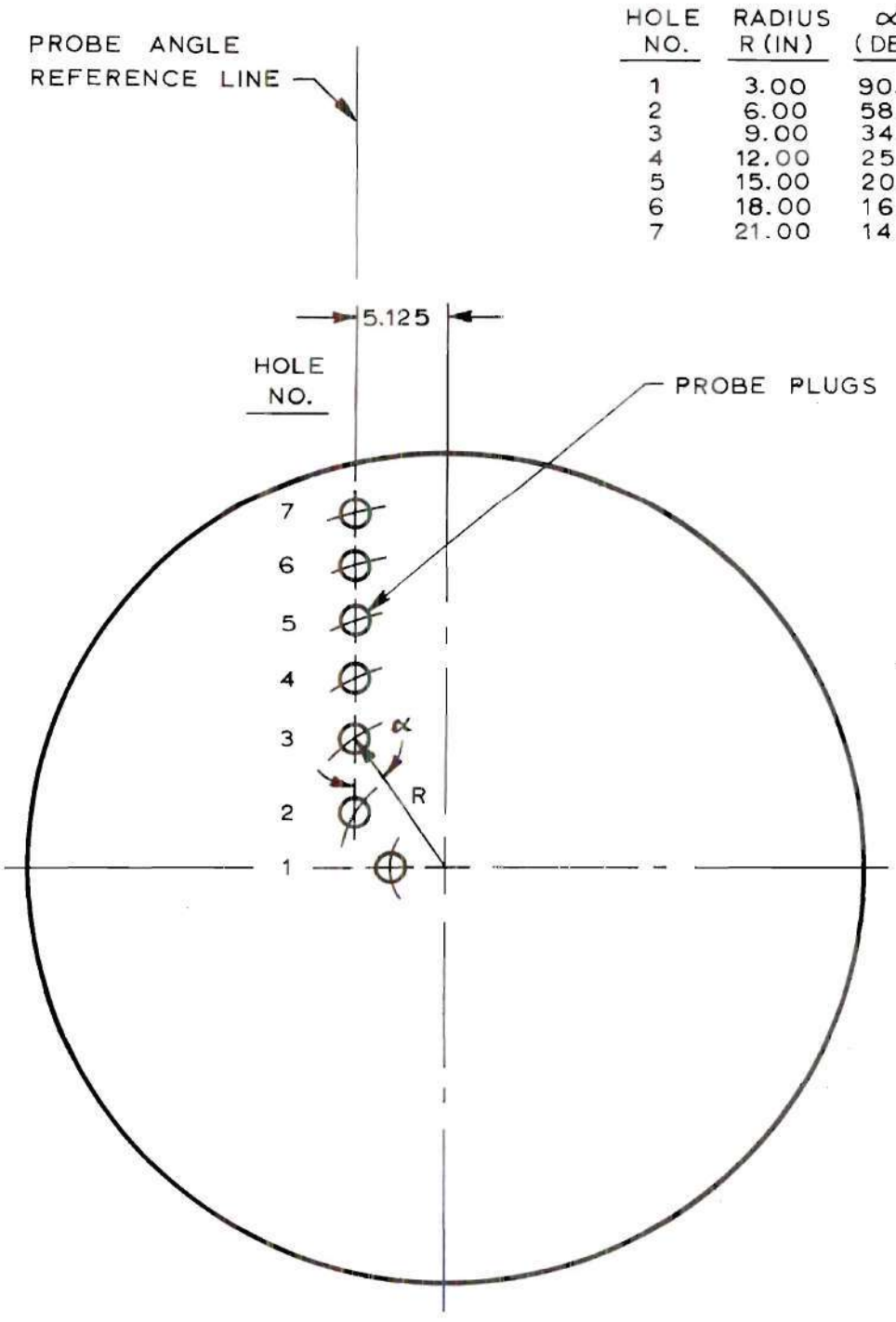

Figure 16. Probe Installation Positions in Table Top.

in the same plug positions as the hot wire probe. It was then rotated into the velocity direction until a maximum pressure differential between the tube total pressure and the surface static pressure was noted and recorded.

Data Reduction

The recorded data were fed into a digital computer program, shown in Appendix C, which reduced the data, tabulated the results, and plotted the velocity profiles.

Velocity Profile Reference Height Correction

The reference height was corrected to bring the surface shear calculated from the slope of the measured velocity profile into agreement with the measured Preston tube surface shear. The slope of the measured velocity profile was calculated by inserting the velocity at $z = 0$ equal to zero and fitting a third order least squares curve through the lowest five heights of the velocity profile.

The height correction was made to correct for

1) variations in the wire height in the V-probe of 0.030 to 0.040 inch, and

2) the surface influence on measurements.

Figure 17 shows the results of this correction. Scatter in the data was caused by errors in the measurements and the compounding effect on errors of taking the derivative when calculating the velocity profile slope. The latter effect was minimized by using the least squares curve fitting technique.

The resulting reference height correction used was

$$\Delta z = 0.047 \text{ inches.} \tag{24}$$

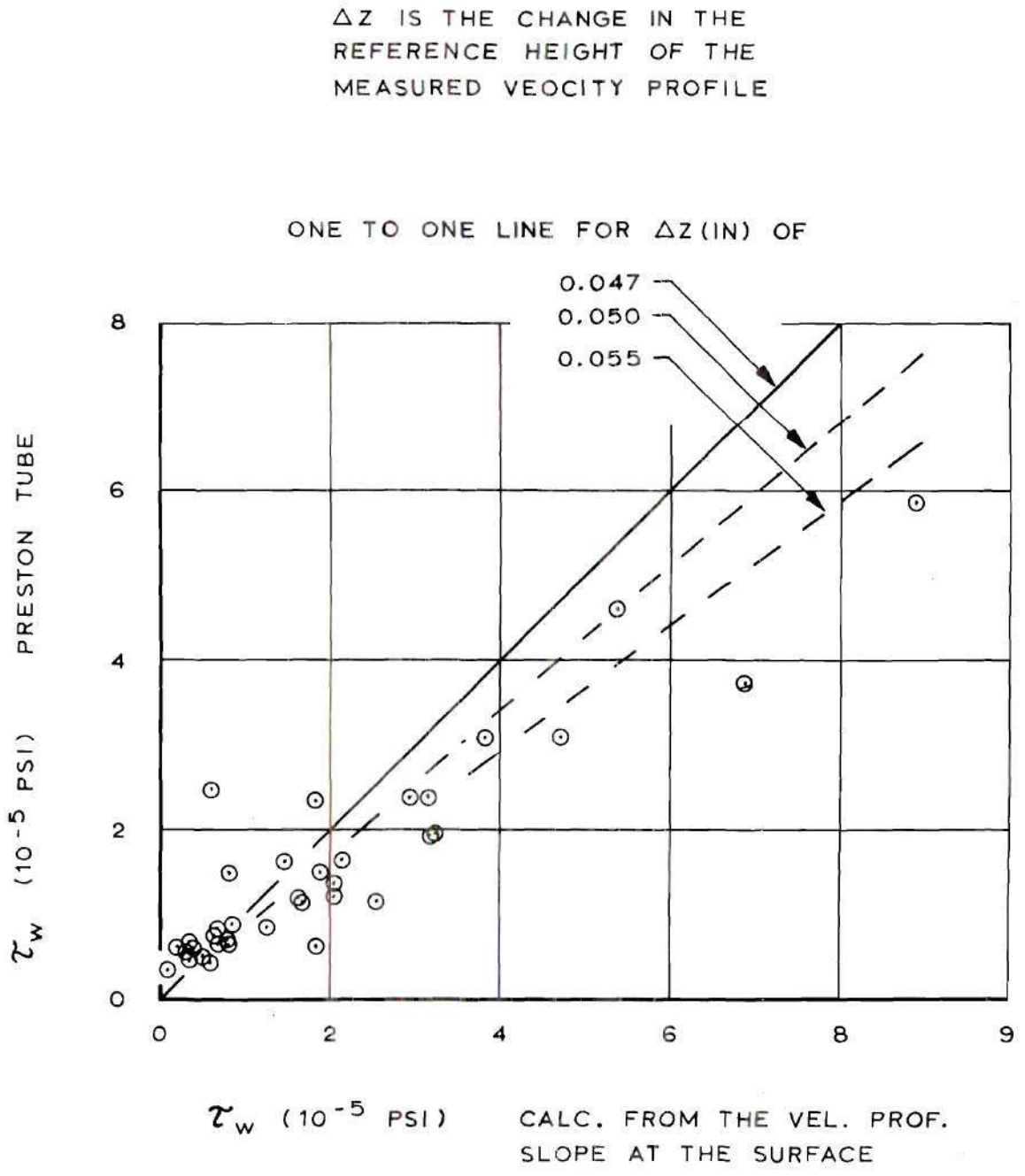

Figure 17. Surface Shear Comparison.

Data Recording Difficulties

Two major problems, flow instabilities, and the limitations of the instruments to record steady state data in unstable flow conditions hampered data taking. The flow instabilities could be seen as oscillations of the vortex core center in a three inch diameter circle about its mean center position, and as variations in the intensity (circulation strength) of the vortex. Two wire screens and one cardboard baffle, described in the vortex generator section, were mounted around the vortex generator to minimize flow instabilities. To further minimize the effect of this problem on the hot wire, an averaging filter (see Appendix B) was added to the galvanometer used to balance the magnitude and direction bridges. Still, small oscillations were present in the instrument indications, so a visual estimation of the mean indicated data was made. Generally, the method for establishing the mean data readout was to observe the band width of the oscillation and take its midpoint as the recorded value.

Table 1. Test Conditions

Test	Vane (deg.)	$\Gamma(ft^2/sec)$
1	60.0	2.6
2	60.0	3.7
3	60.0	4.5
4	67.5	3.0
5	67.5	5.2
6	67.5	6.3
7	75.0	4.2
8	75.0	6.5
9	75.0	7.8

Results and Discussion

The surface shear and velocity profiles were measured at the test conditions of Table 1.

The data reduction program and a sample of its output are included in Appendix C.

In this section, the results are presented for a typical sample of the tests with the remainder of the test results presented in Appendix C.

Velocity Profiles

Velocity profiles at the typical test condition of $\Gamma = 4.5$ ft^2/sec and vane angle = 60.0 degrees are presented in Figures 18 and 19. Following the velocity profiles are plots of the tangential velocity ratio, the radial velocity ratio, the local circulation, and the local radial inflow, presented in Figures 20 to 23. The representative freestream velocities and boundary layer thicknesses at the vane angle = 60.0 degrees are presented in Figures 24 to 26. Finally, Figures 27, 28, and 29 show a typical maximum radial velocity variation with circulation, and comparison of the results obtained in this work with those obtained by Ying and Chang (23).

The tangential velocity profiles are similar, as shown in Figure 20, having the flat plate two-dimensional turbulent velocity profile law

$$\frac{v_t}{v_{t\,\infty}} = \left(\frac{z}{\delta_t}\right)^{\frac{1}{7}} \quad . \tag{25}$$

The difference between equation (25) and the data points at the low z/δ_t ($z/\delta_t < 0.15$)

is caused by the laminar sublayer. The radial velocity profiles demonstrate no similarity as shown in Figures 21 and 23.

In the freestream above the boundary layer the tangential velocities have a constant circulation,

$$\Gamma = r v_{t\,\infty} \quad , \tag{26}$$

as shown in Figures 22 and 24, except at the six inch radius where the flow is beginning transition to solid rotational flow,

$$\omega_z = \frac{v_{t\,\infty}}{r} = \text{constant}, \tag{27}$$

in the core. This constant freestream circulation means the freestream potential vortex has been achieved in the boundary layer simulation. The radial freestream velocities approach a constant local inflow,

$$\frac{1}{2\pi}\frac{dQ}{dz} = r v_{r\,\infty} = \text{constant} \quad , \tag{28}$$

over the center section of the plate local radius, as shown in Figure 25. The outer radii greater than or equal to 15 inches are in the developing radial boundary layer, and the local radial inflow is decreasing, indicating a vertical flow to the potential vortex. In the inner radii less than or equal to six inches, the flow turns up into the core. Thus the fully developed radial boundary layer covers a relatively small portion of the plate radius between six and 14 inches, generally.

The boundary layer thicknesses shown in Figure 26 were measured from

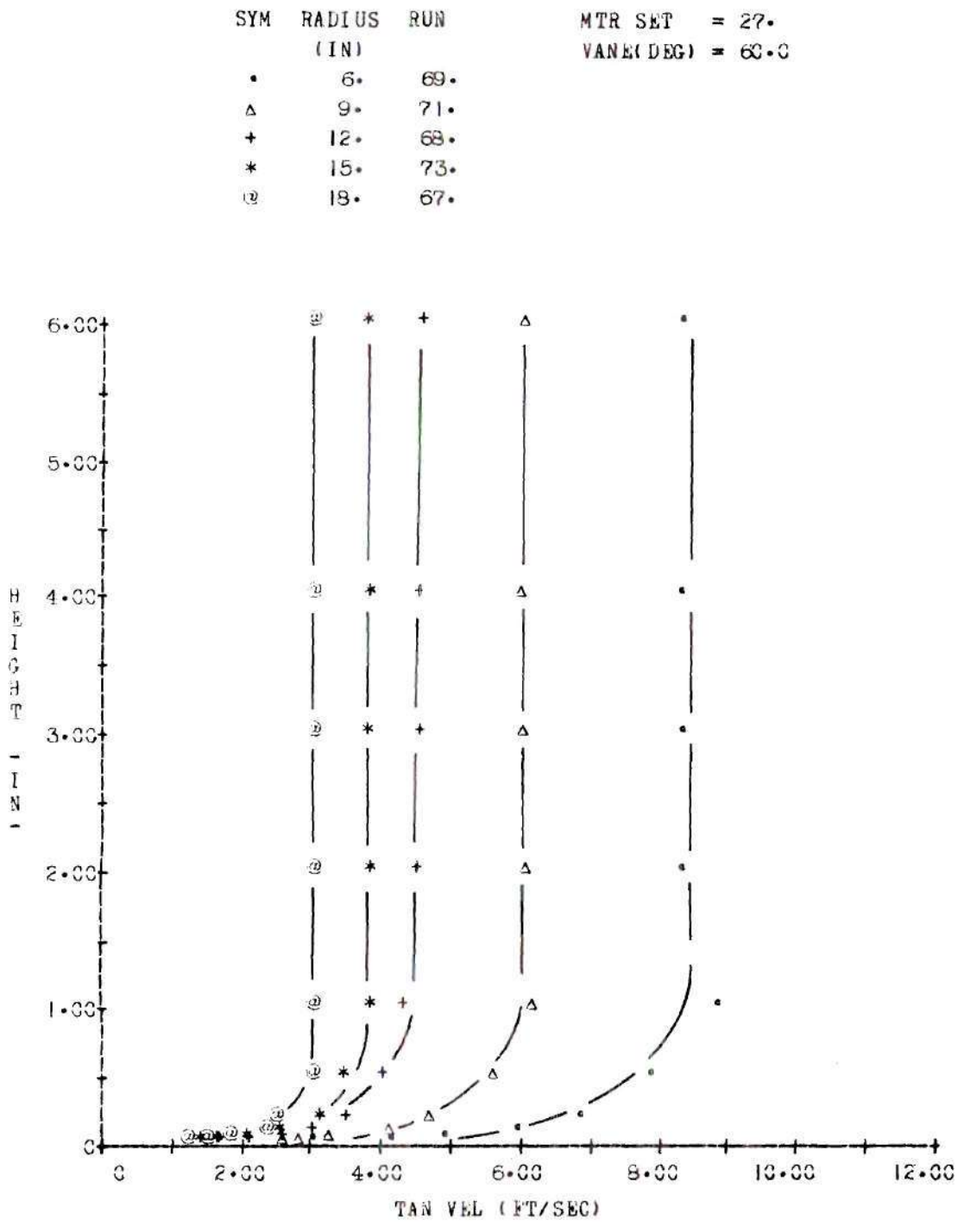

Figure 18. Tangential Velocity Profiles

Vane = 60.0^{o}, $\Gamma = 4.5\ ft^2/sec.$

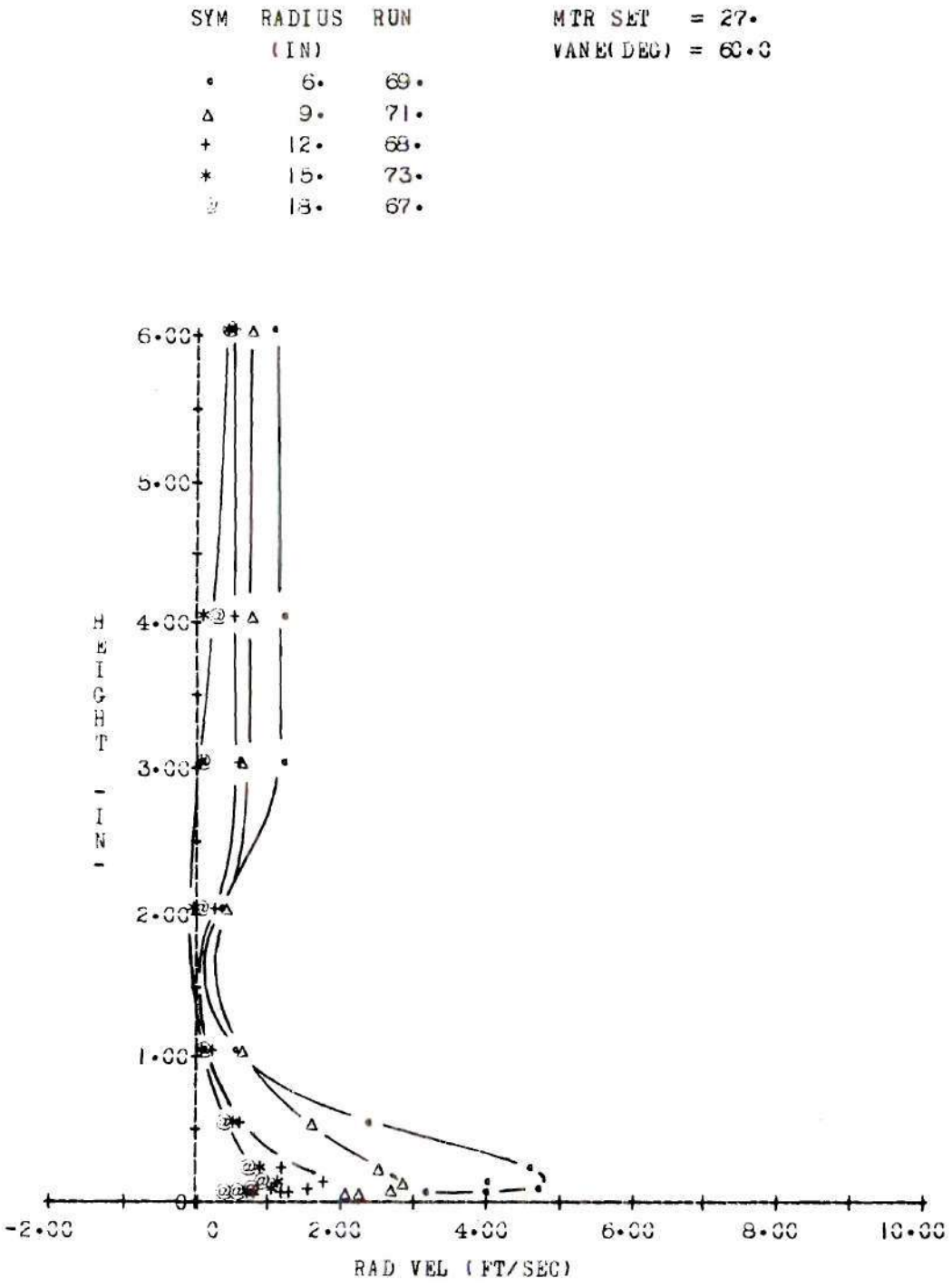

Figure 19. Radial Velocity Profiles (Inflow)

Vane = 60.0°, Γ = 4.5 ft^2/sec.

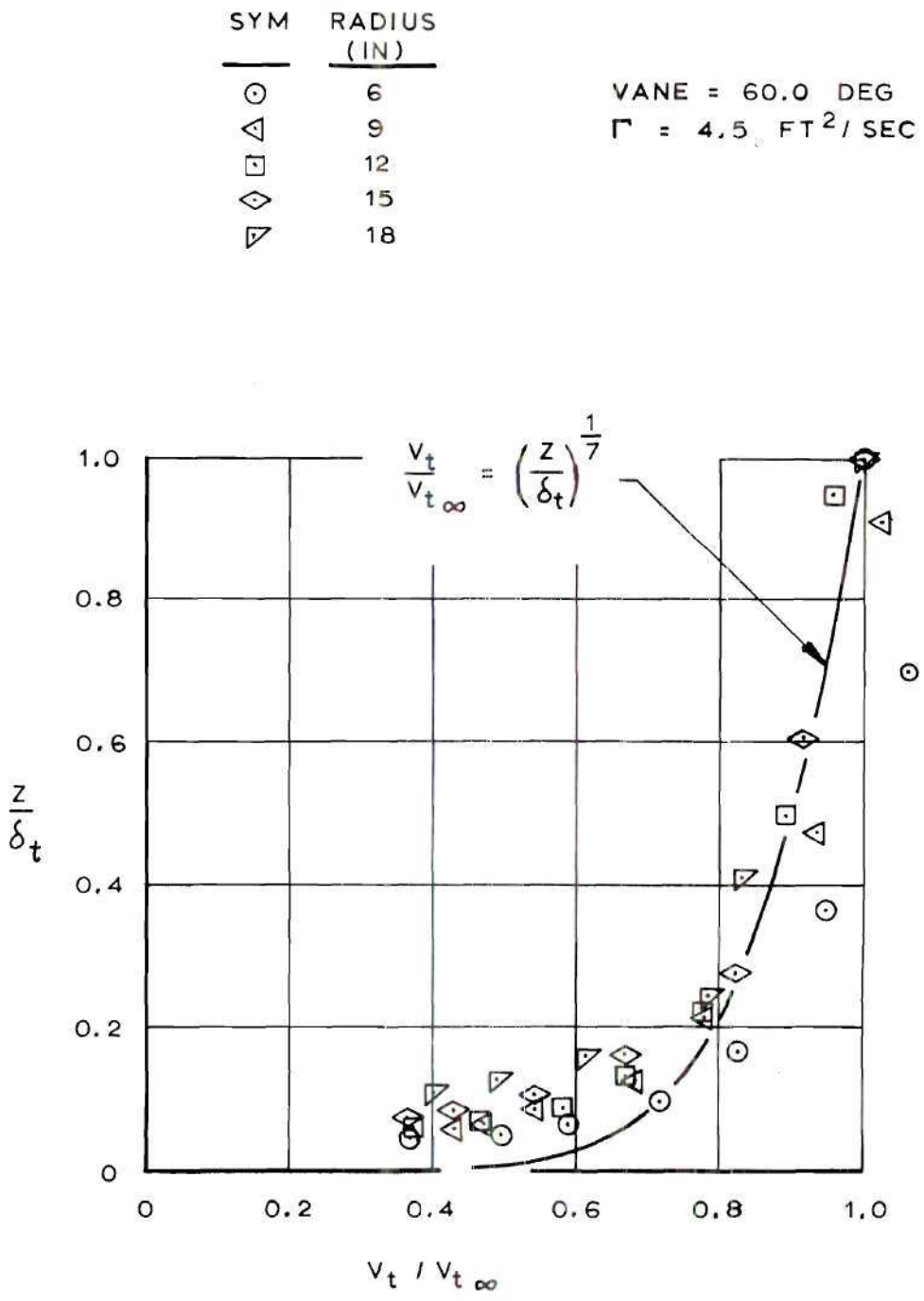

Figure 20. Tangential Velocity Ratio

Vane = 60.0 Deg, Γ = 4.5 ft^2/sec.

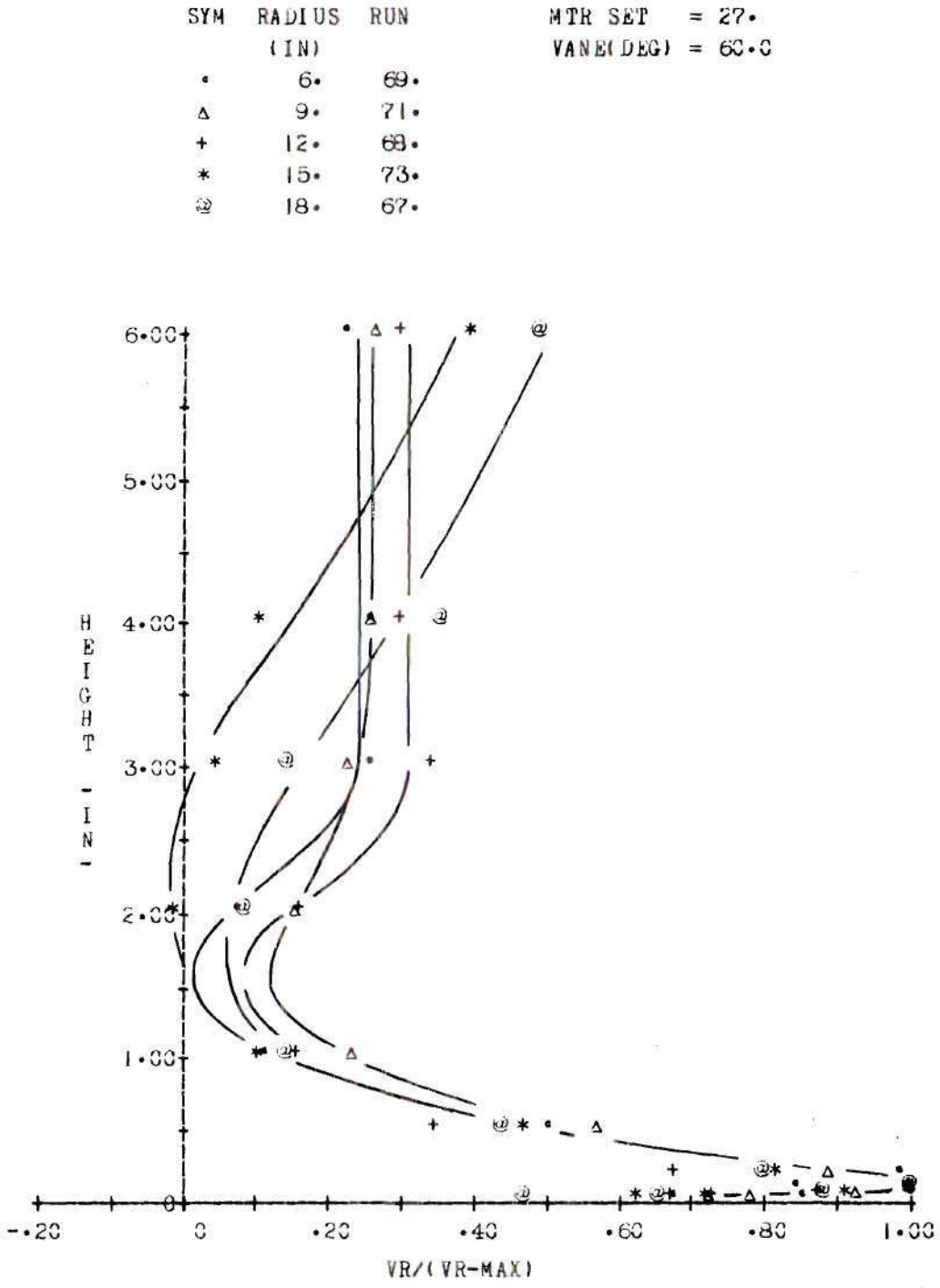

Figure 21. Radial Velocity Ratio

Vane = 60.0°, $\Gamma = 4.5$ ft^2/sec.

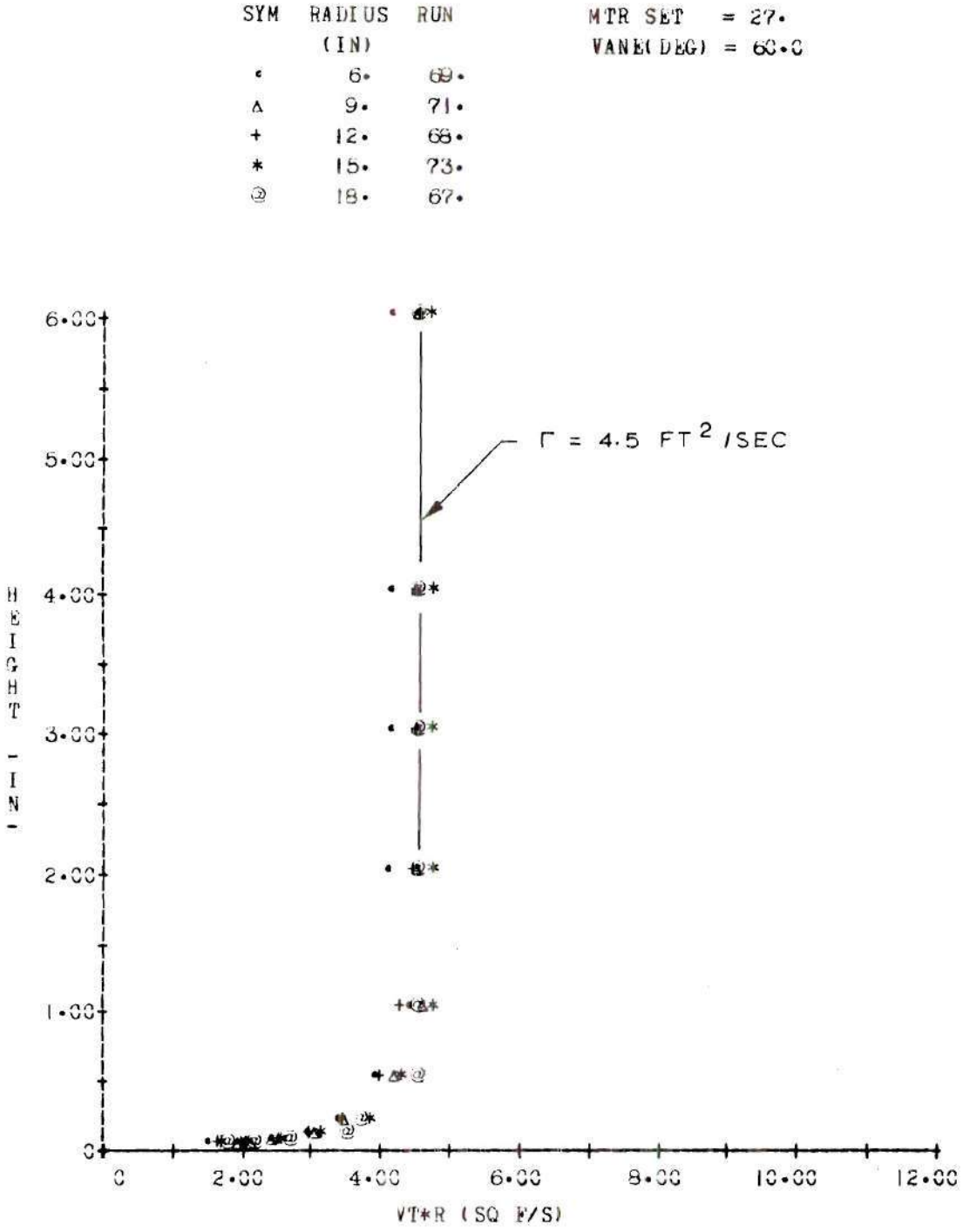

Figure 22. Local Circulation

Vane = 60.0°, Γ = 4.5 ft^2/sec.

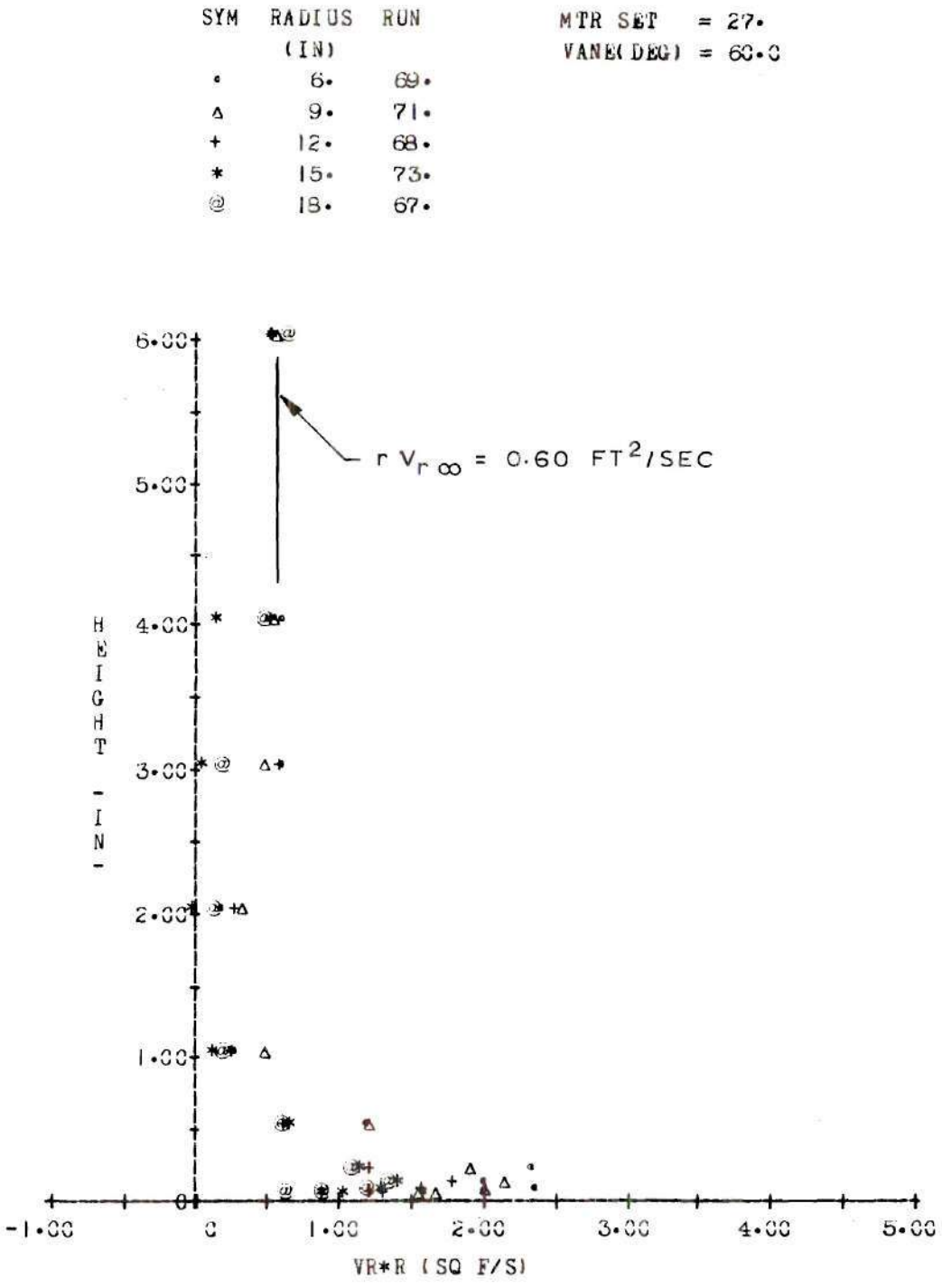

Figure 23. Local Radial Inflow

Vane = 60.0^{o}, $\Gamma = 4.5$ ft^2/sec.

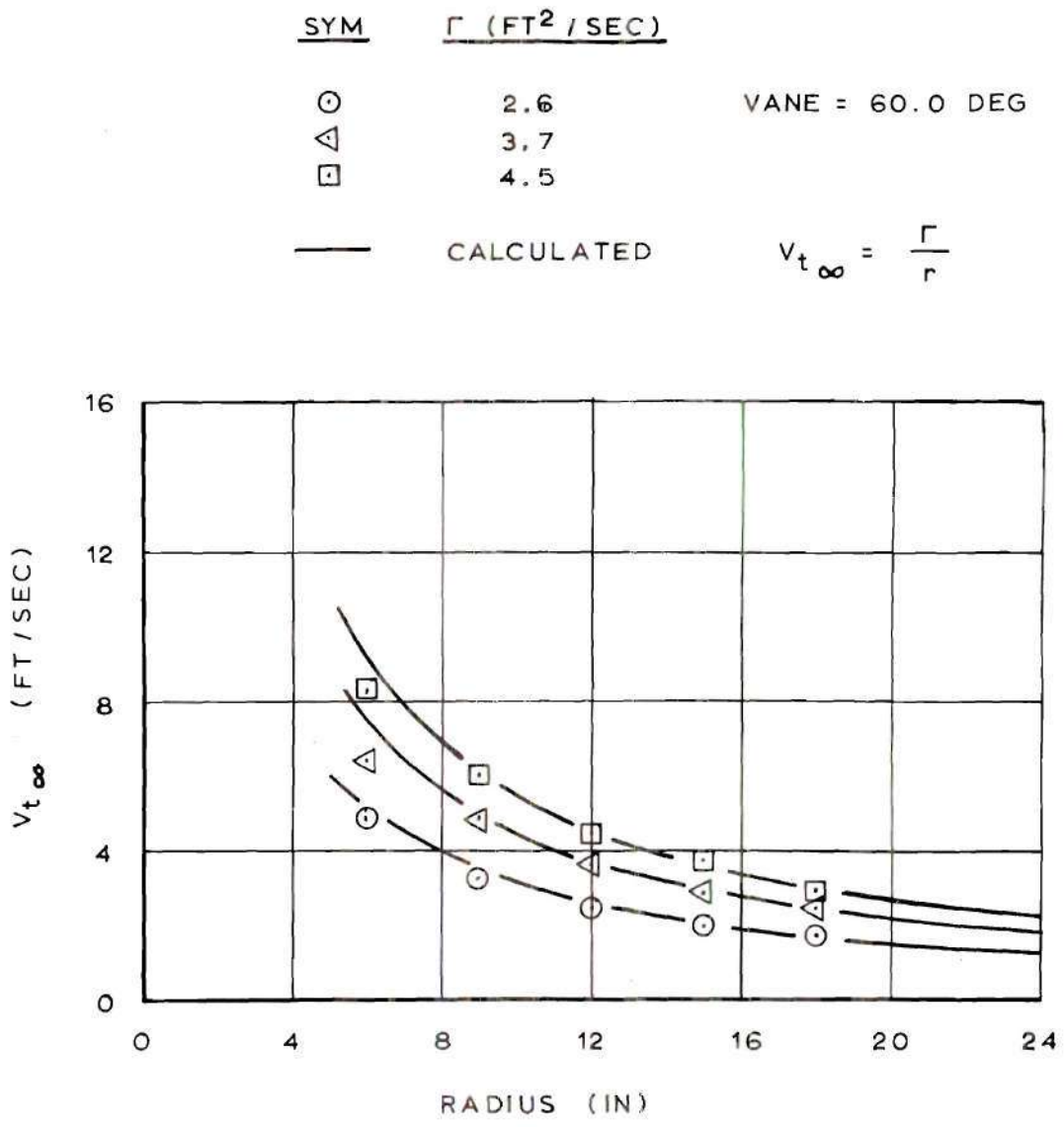

Figure 24. Freestream Tangential Velocity

Vane = 60.0 Deg.

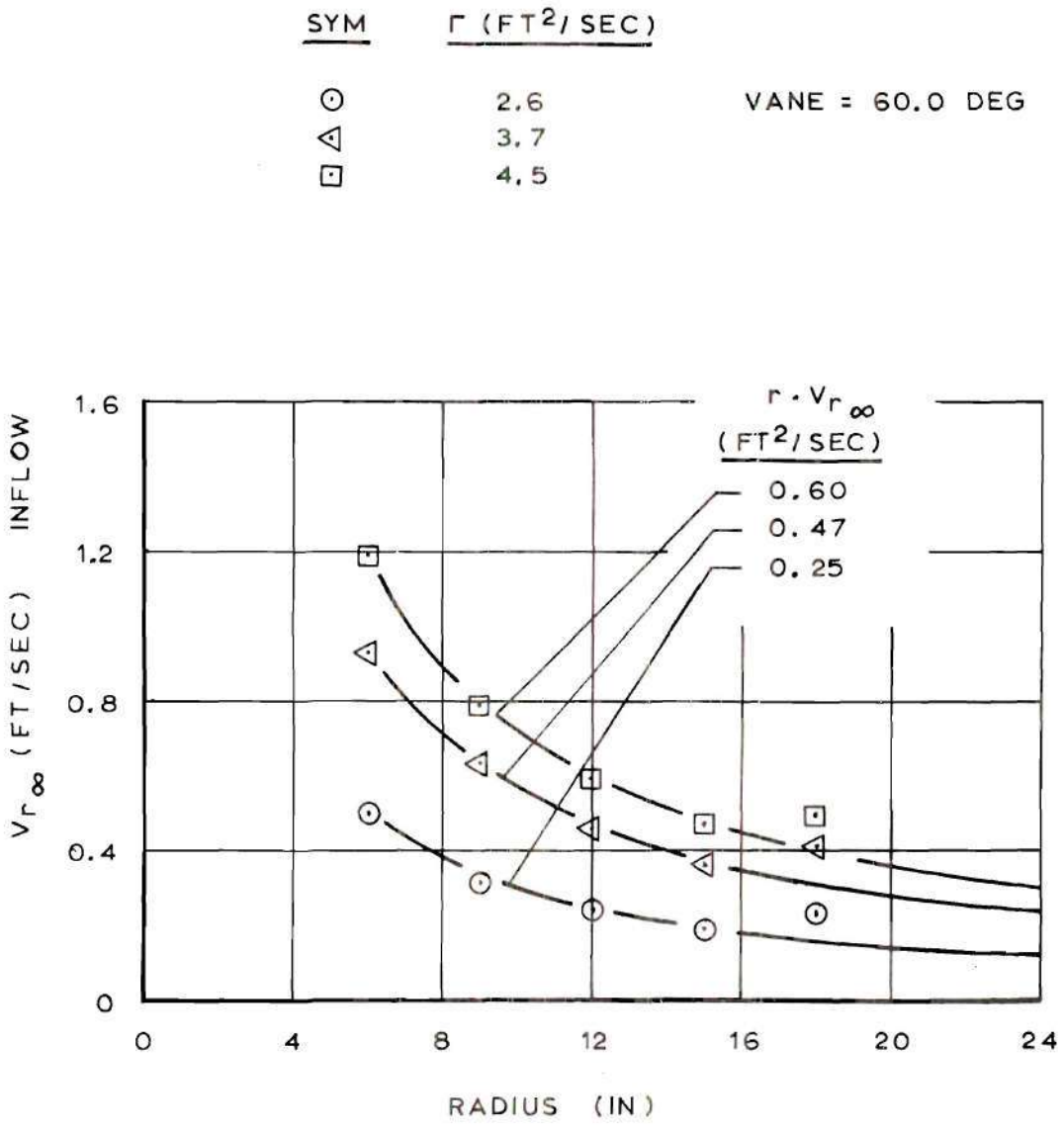

Figure 25. Freestream Radial Velocity

Vane = 60.0 Deg.

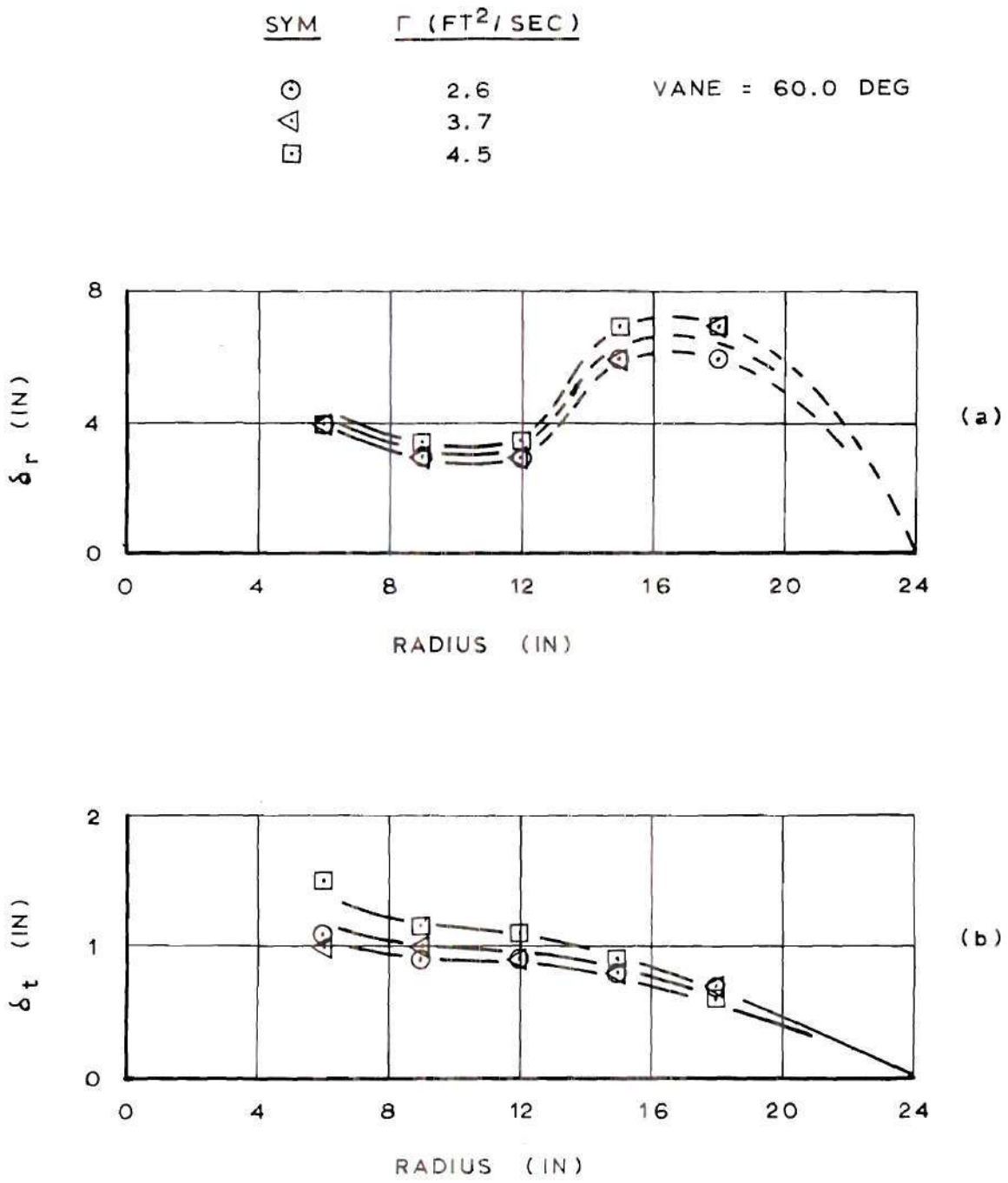

Figure 26. Radial and Tangential Velocity Boundary Layer Thickness

Vane = 60.0 Deg.

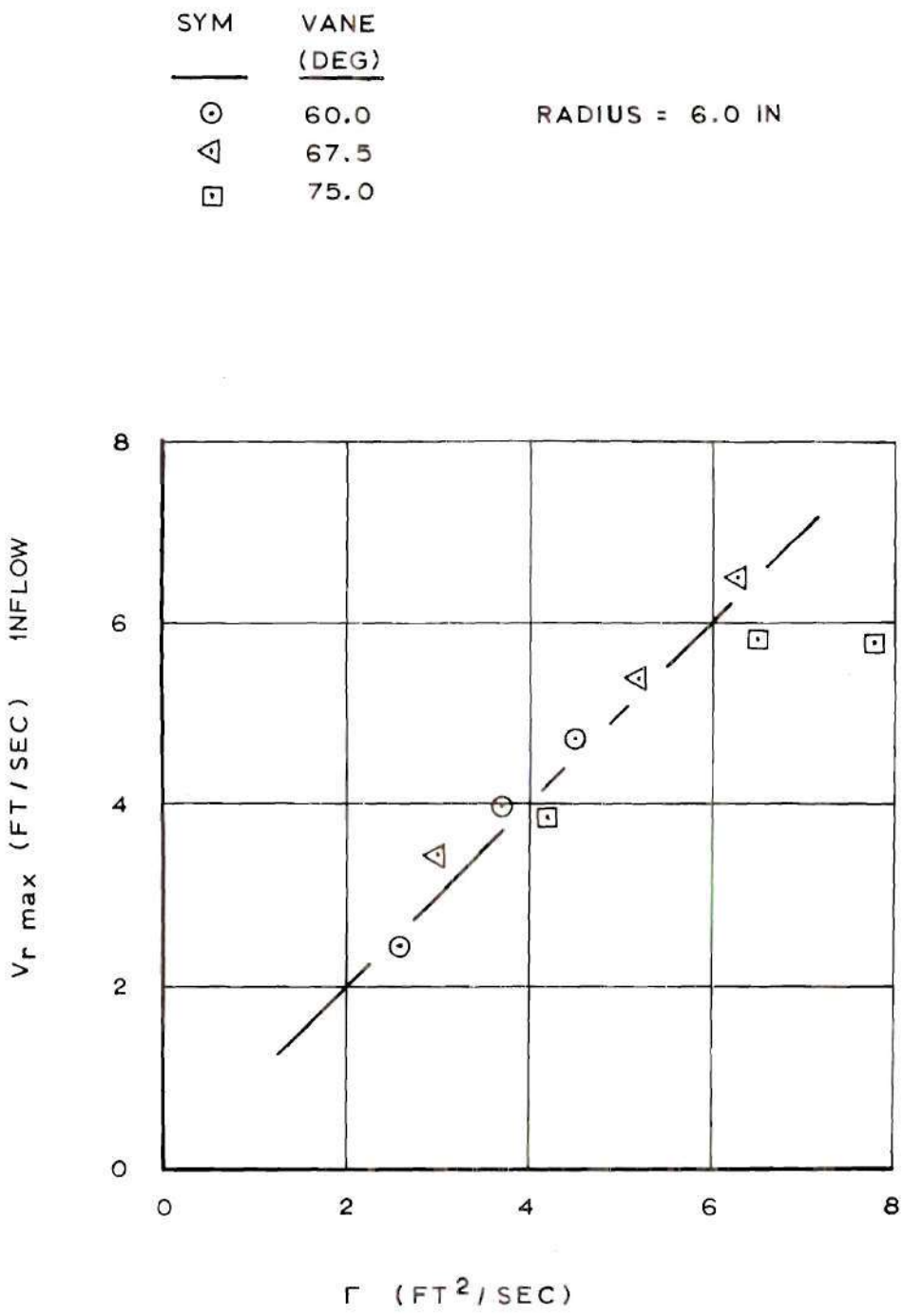

Figure 27. Maximum Radial Velocity Versus Freestream Circulation

Radius = 6.0 in.

	YING & CHANG	HUNTLEY
SYM	———	— — —
RADIUS (IN)	9.0	9.0
Γ (FT^2/SEC)	3.9	4.5
$V_{t\infty}$ (FT/SEC)	5.3	6.1
$V_{r\,max}$ (FT/SEC)	3.6	2.9
δ_r^* (IN)	-2.1	-0.32
δ_t^* (IN)	0.42	0.13
Θ_r (IN)	-63.	-2.5

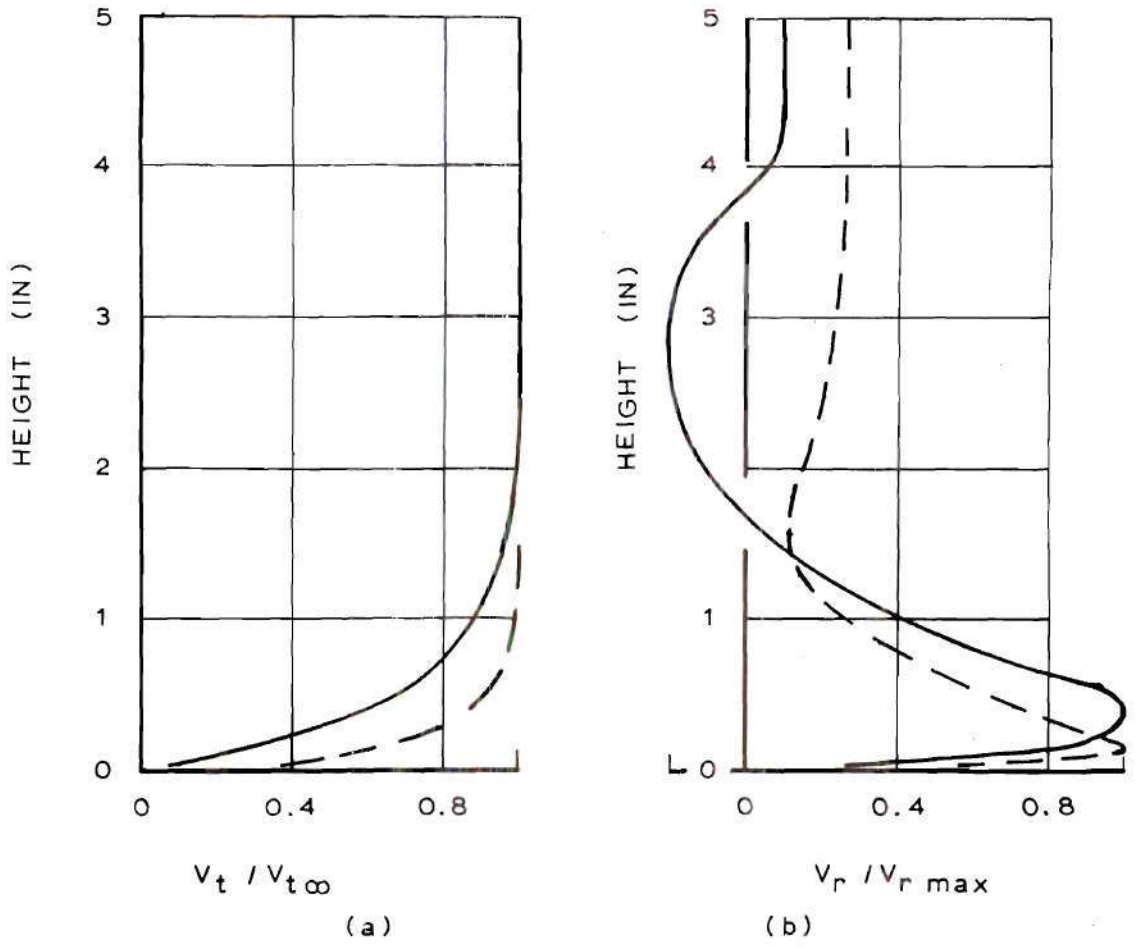

Figure 28. Ying and Chang Velocity Profile Comparison

Radius = 9 in.

	YING & CHANG	HUNTLEY
SYM	———	— — —
RADIUS (IN)	13.0	12.0
Γ (FT^2 / SEC)	3.9	4.5
$V_{t\infty}$ (FT / SEC)	3.6	4.5
$V_{r\ max}$ (FT / SEC)	2.2	1.8
δ_r^* (IN)	- 5.4	0.51
δ_t^* (IN)	0.39	0.21
Θ_r (IN)	- 100.	- 0.61

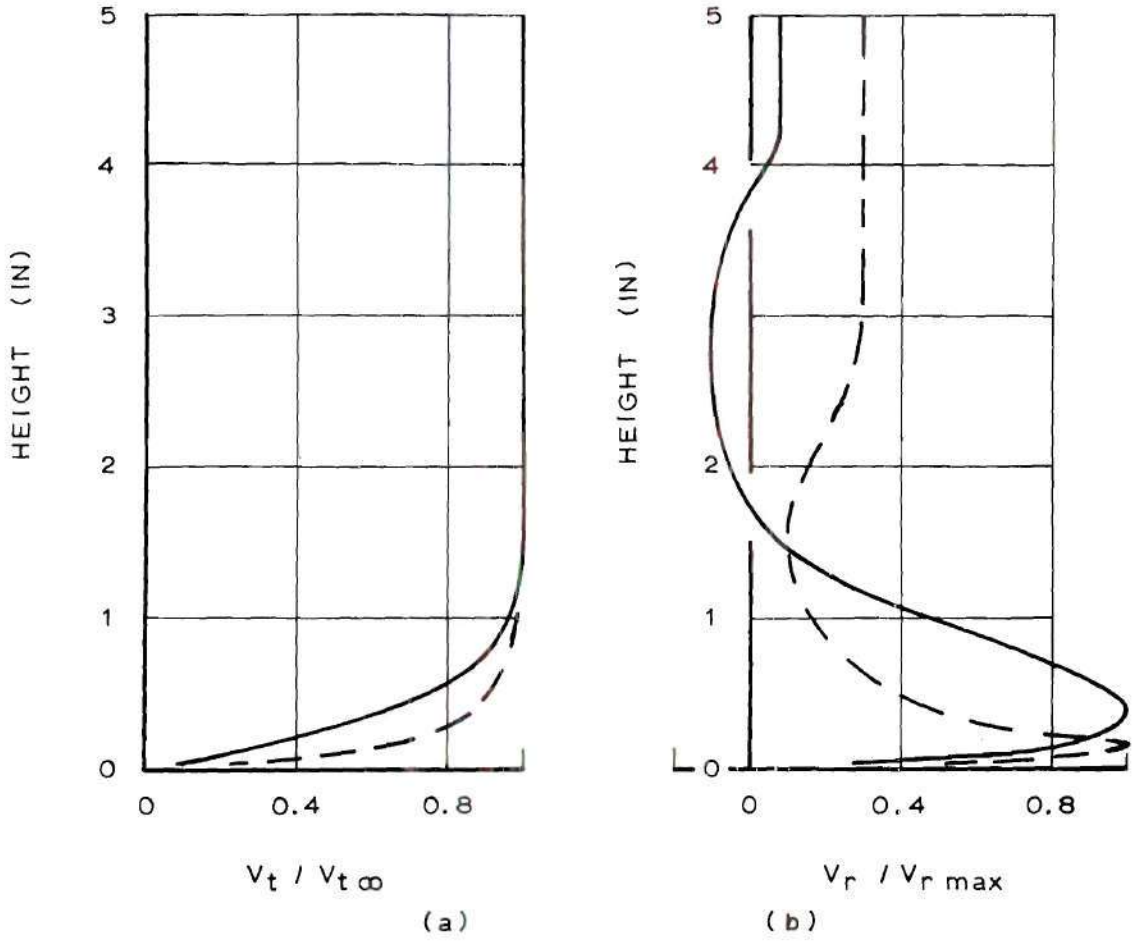

Figure 29. Ying and Chang Velocity Profile Comparison

Radius = 12.0 in.

the plots of velocity profiles at the height where the velocity profiles appear to reach ninety-nine percent of their freestream value.

One interesting result found by Ying and Chang (23) and confirmed by this experiment is that the maximum radial velocity varies linearly with circulation as shown in Figure 27 at the sample six inch radius.

Figures 28 and 29 show selected velocity profiles at two different radii compared with similar cases of experimental velocity profiles from Ying and Chang (23). Two significant differences appear. The boundary layer thicknesses measured in this work are less than those of Ying and Chang, and the freestream radial inflow of this work is higher.

Surface Shear Stress

Figures 30, 31, and 32 present the surface shear stress measured by the Preston tube. The direction of the shear stress, Φ, is calculated from the velocity direction profile with a second order least squares curve fit through the lower five points. Refer to Appendix C for the data reduction calculations.

The approximate uncertainty error in the Preston tube readings is ± 20 percent. This error was primarily caused by flow instabilities.

The inability of the electronic manometer used to sense pressure differences below 10^{-7} psi prevented shear stress measurements below about 10^{-6} psi.

The shear stress analysis is presented in the next chapter.

Law of the Wall

The vortex boundary layer is difficult to analyze in terms of the "law of the wall" because of its three-dimensional nature. But, because the tangential velocity

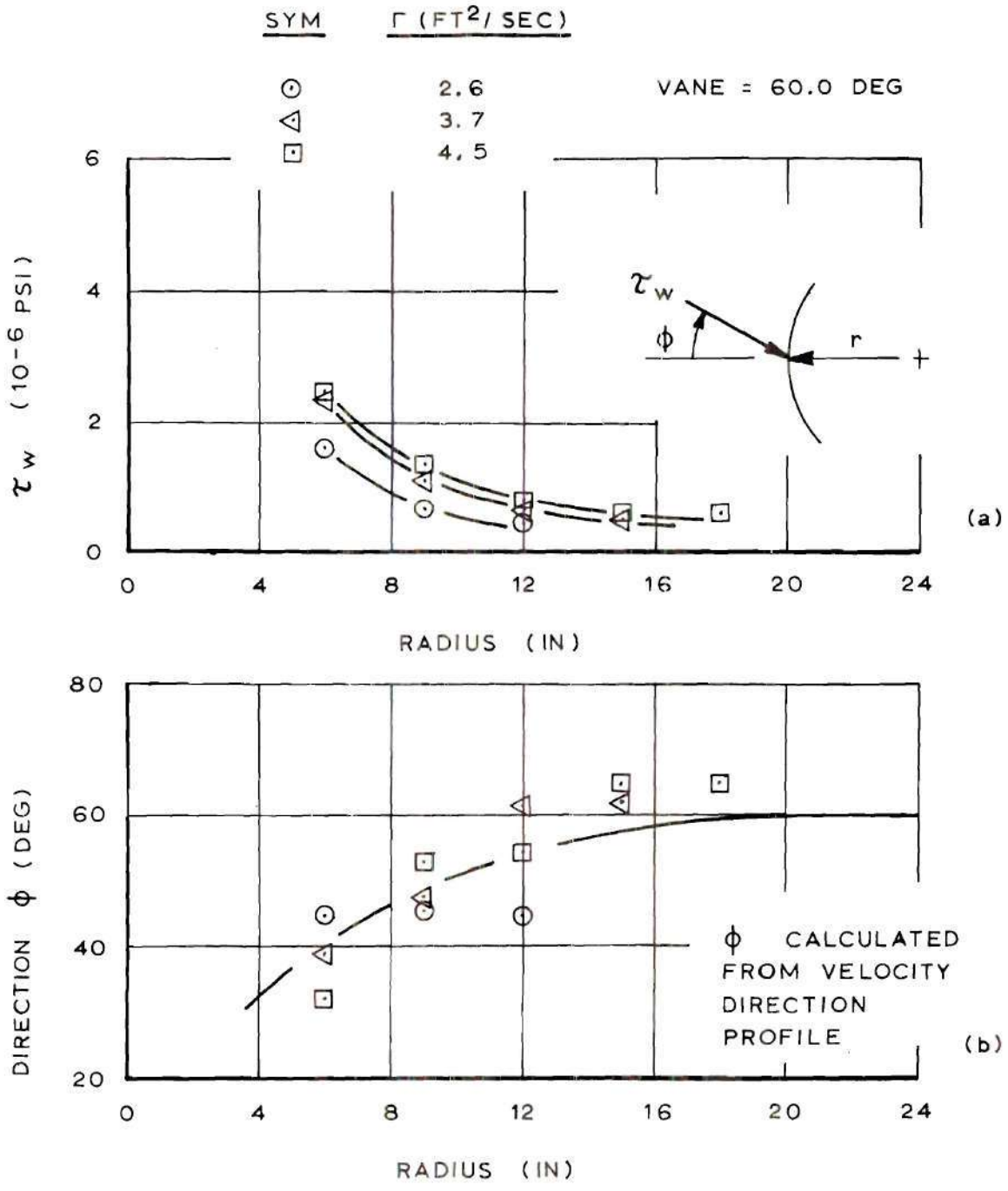

Figure 30. Magnitude and Direction of Surface Shear Stress

Vane = 60.0 Deg.

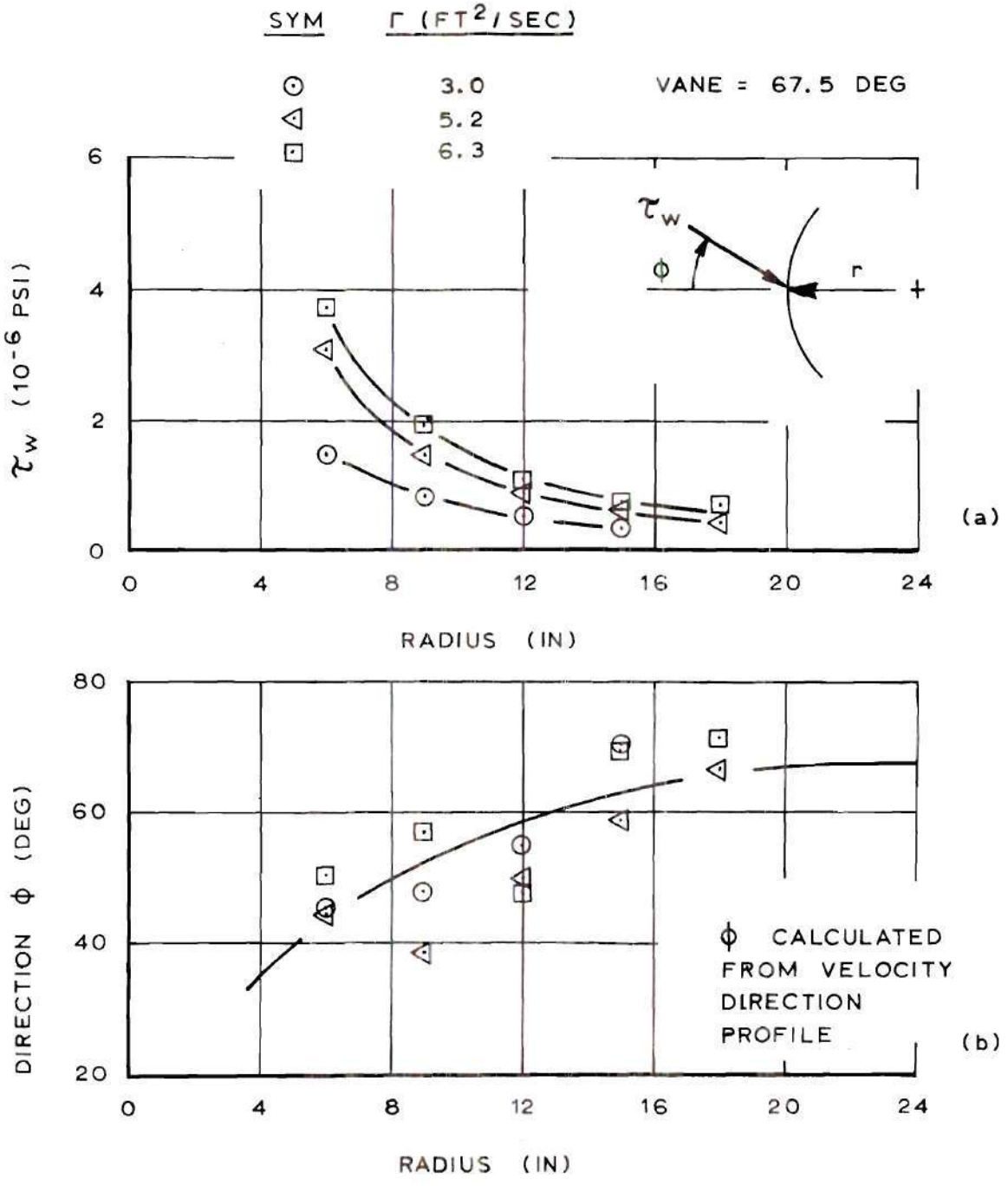

Figure 31. Magnitude and Direction of Surface Shear Stress

Vane = 67.5 Deg.

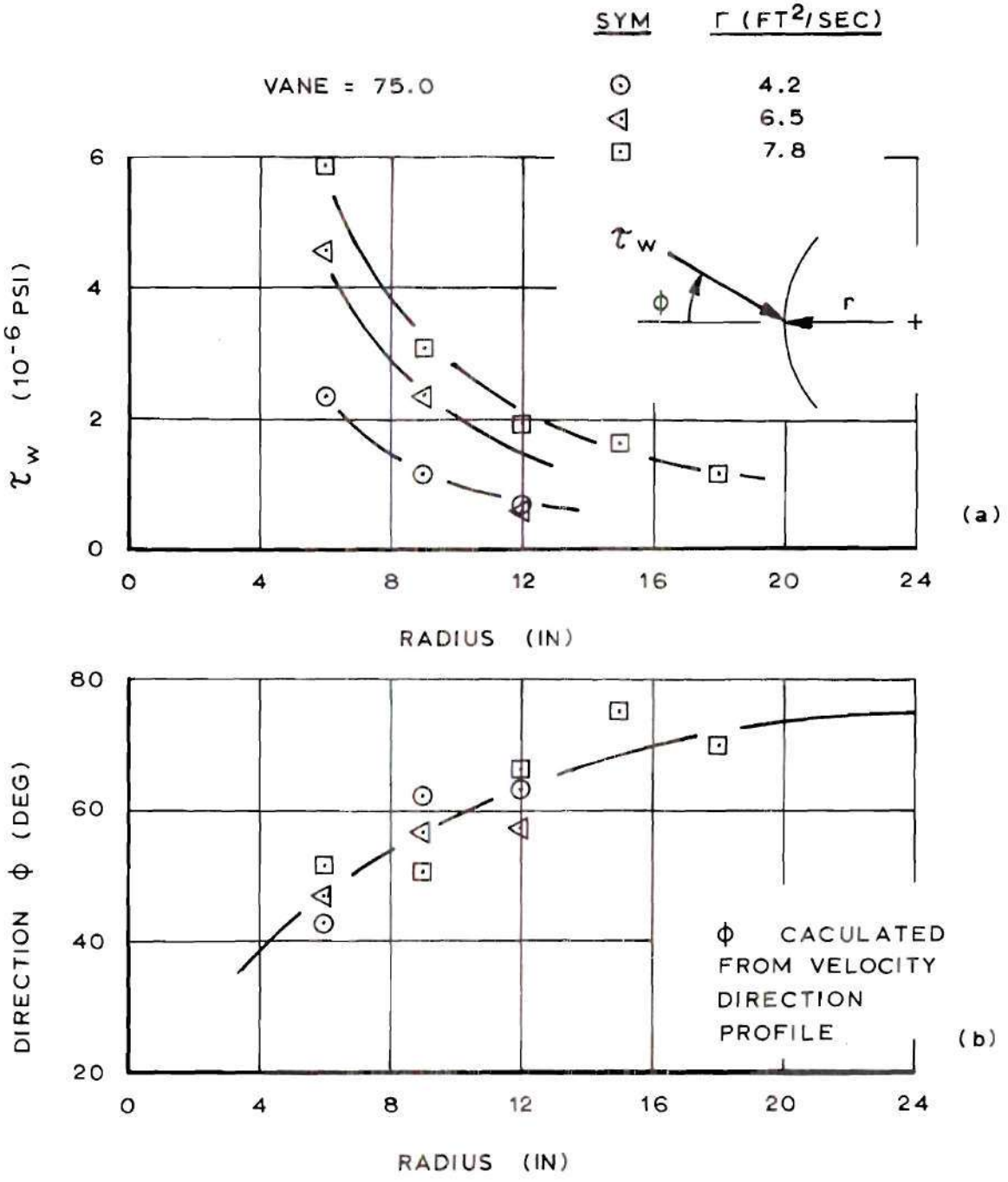

Figure 32. Magnitude and Direction of Surface Shear Stress

Vane = 75.0 Deg.

profile is similar to that of the two-dimensional boundary layer, it is presented here in terms of the "law of the wall" parameters, v_t/U_τ and $U_\tau z/\nu$, in Figures 33 and 34. The first, Figure 33, shows the velocity profile before the reference height correction, described in the Procedure section, was applied to it. The second, Figure 34, shows the velocity profile after the reference height correction was made. The reference height correction is shown to be justified. Recall that this correction was made by adjusting the reference height so that the surface shear stress calculated from the slope of the velocity profile at the surface agreed with that measured by the Preston tube. The slope of the velocity profile can be measured in the laminar sublayer, and the tangential velocity profile shows a very thick laminar sublayer ($z/\delta_t \lesssim 0.15$) compared to the flat plate two-dimensional velocity profile. The reference height correction adjusts the velocity profile so that it agrees, as it should, with the law of the wall in the laminar sublayer. Additionally, the velocity profiles appear to have individual logarithmic laws above the laminar sublayer.

Discussion

Generally, the tangential boundary layer development and results are good. Similarity to the flat plate two-dimensional velocity profile is established. The freestream tangential velocity describes the desired potential vortex. At the inner radius of six inches, the beginning of transition of the freestream velocity from a potential vortex to a rotational core can be seen.

The radial boundary layer is not as well developed as the tangential. It is developing over the outer half of the plate radius, from where it begins at the

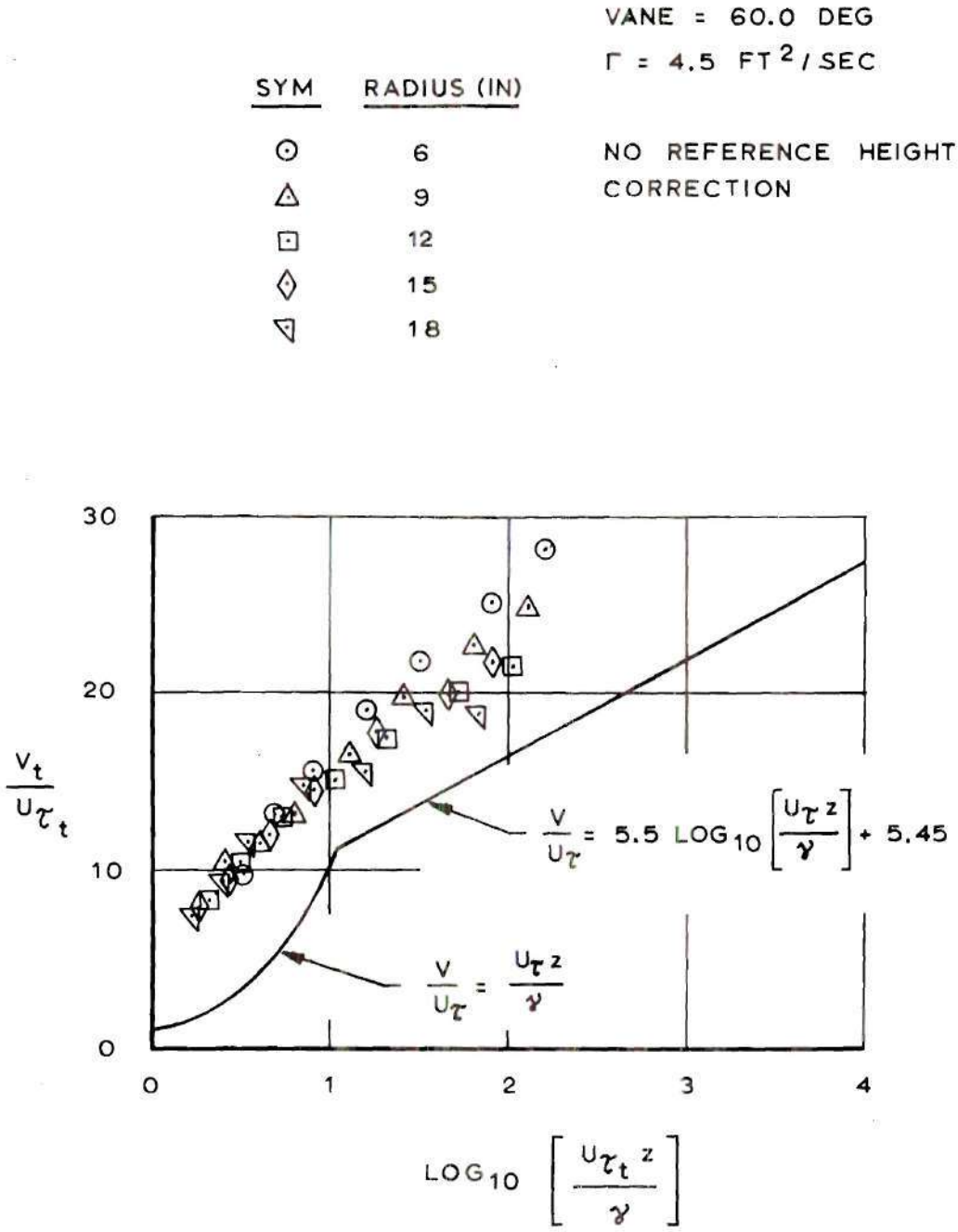

Figure 33. Tangential Velocity Profile Without The Height Correction Compared to the Law of the Wall.

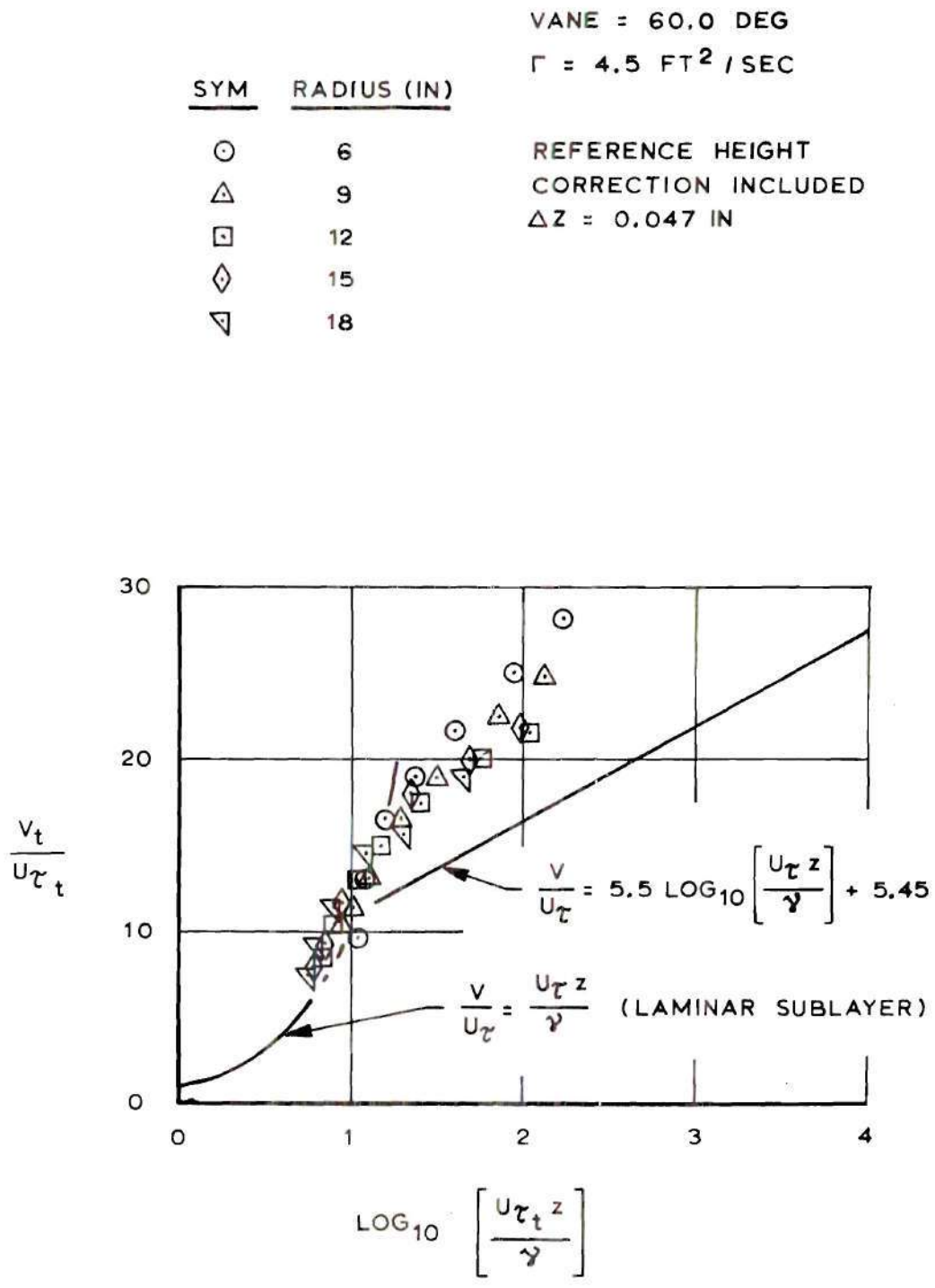

Figure 34. Tangential Velocity Profile with the Height Correction Compared to the Law of the Wall.

24 inch radius. Vertical velocity occurs in this region. The developed radial boundary layer with constant freestream radial inflow then exists from approximately the 12 inch radius to the six inch radius where it begins transition to the core and vertical flow begins again. Such a small section of the radius with the desired fully developed radial boundary layer is the most significant shortcoming of this research effort. Recommendations for better performance will be made in Chapter IV. The radial velocity profiles show the characteristic "S" shape caused by the increase of angular momentum with height, from zero at the surface to constant freestream Γ. They also show no similarity.

Repeatability and Error Analysis of Measured Velocity Profiles

Figures 35 and 36 show the repeatability of the velocity magnitude and direction. The velocity magnitude error band is ± 0.60 feet per second or ± 20 percent, whichever is smaller. The velocity direction error band is ± 5.0 degrees. The effect of the error bands on the radial and tangential velocity components is shown in the following example.

The tangential and radial velocities are

$$v_t = |\bar{v}| \sin \Phi \,, \tag{29}$$

and

$$v_r = |\bar{v}| \cos \Phi \,. \tag{30}$$

For this sample case use the typical values

$$|\bar{v}| = 4.0 \text{ ft/sec},$$

$$\Phi = 85. \text{ deg},$$

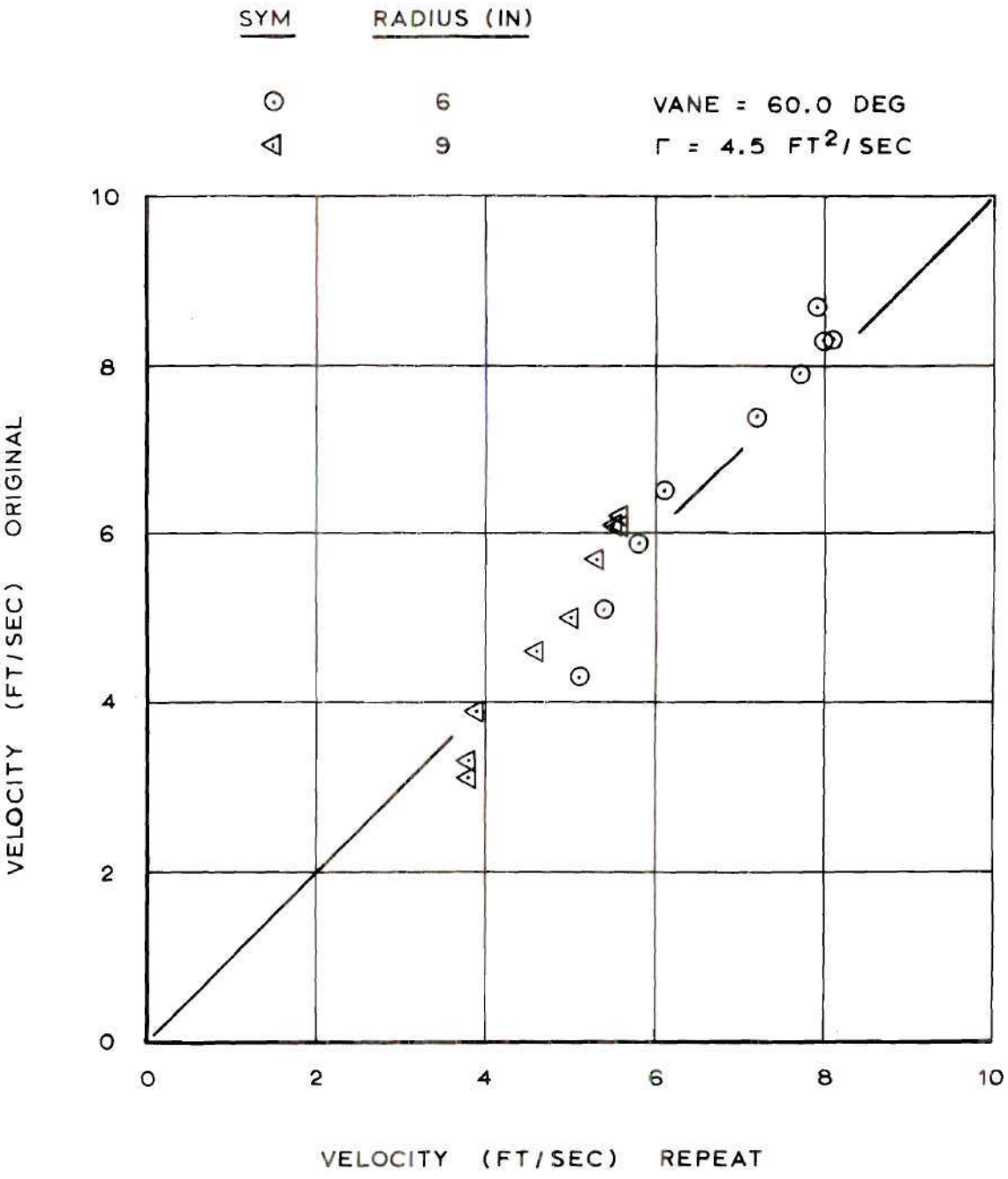

Figure 35. Velocity Magnitude Repeatability.

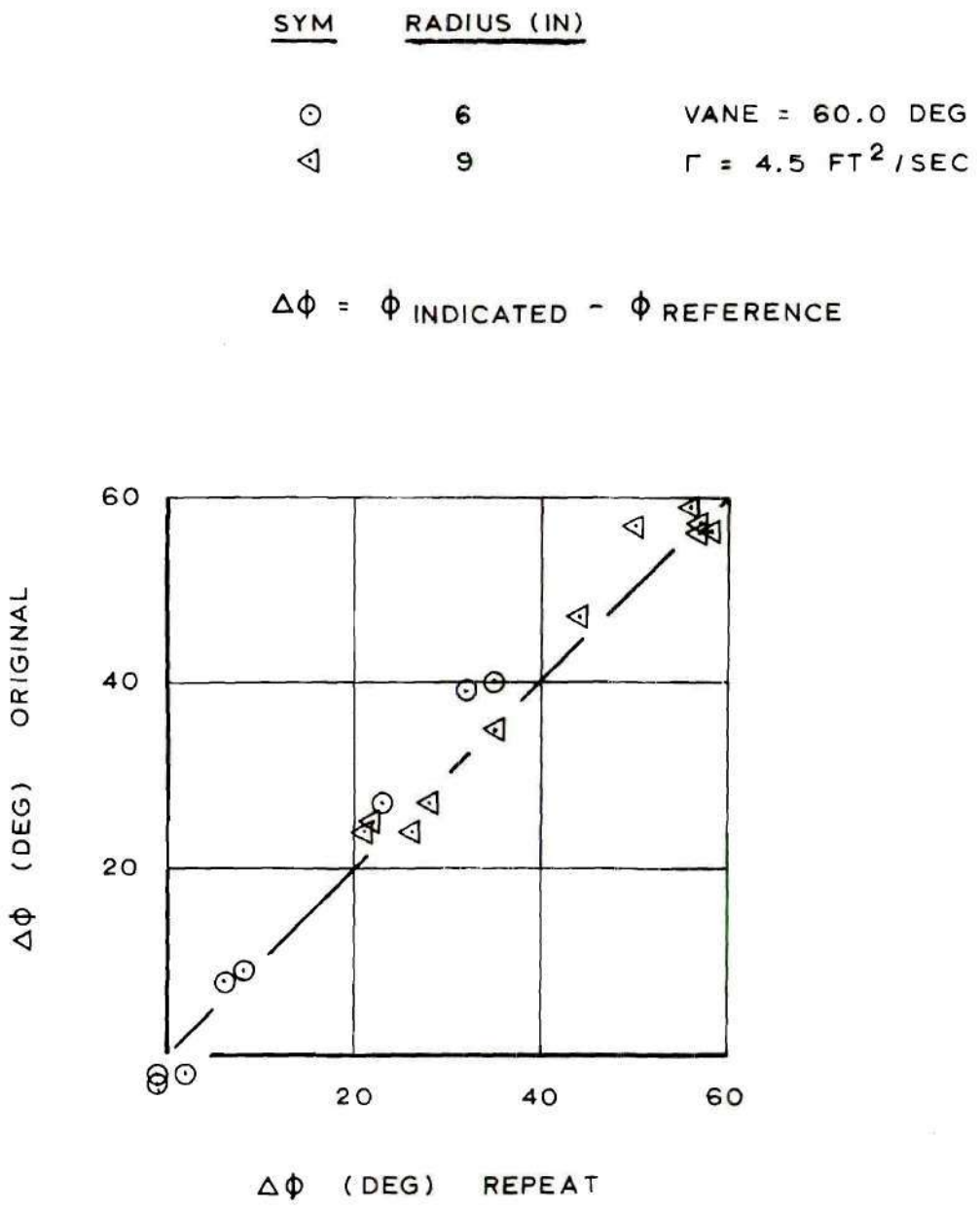

Figure 36. Velocity Direction Repeatability.

$$|\bar{v}|_{error} = \pm 0.6 \text{ ft/sec},$$

and

$$\Phi_{error} = \pm 5.0 \text{ deg.}$$

The worst possible combination of errors yield

$$v_{t\ min} = 3.3 \text{ ft/sec} ,$$

$$v_{t\ max} = 4.6 \text{ ft/sec} ,$$

$$v_{r\ min} = 0.0 \text{ ft/sec} ,$$

and

$$v_{r\ max} = 0.8 \text{ ft/sec} .$$

The principal reason for these large error bands is the flow instabilities, seen as oscillations of the core base location in a three inch diameter circle about its mean center position and oscillations in the strength (flow velocity) of the vortex. These effects were caused mainly by irregularities in the air supply provided by windows to an antisymmetric room. The steps taken to alleviate this problem have been discussed in other sections of this thesis, i.e., the operating procedures. Chapter IV discusses further possible helpful actions.

CHAPTER III

ANALYTICAL EFFORT

The momentum integral equations provide an analytical description of the vortex boundary layer. This chapter consists of a shear stress analysis to obtain the empirical surface shear stress relations suitable for use in the momentum integral equations and an evaluation of the momentum integral equations using the experimentally obtained characteristic thicknesses, δ_r^*, θ_r, δ_1, and δ_2, to check the accuracy of these test results.

Surface Shear Stress Analysis

The empirical laws describing the measured shear stress are evaluated in this section. The measured values of radial and tangential shear stress were calculated from the Preston tube measured surface shear stress magnitude and wall velocity angle in Figures 30, 31, and 32 by

$$\tau_{w_t} = \tau_w \sin \Phi \ , \tag{31}$$

and

$$\tau_{w_r} = \tau_w \cos \Phi \ . \tag{32}$$

Tangential Shear Stress

Because the tangential velocity profile similarity was the same as the flat plate two-dimensional velocity profile similarity, see Figure 20, the flat plate

two-dimensional shear law (21),

$$\tau_w = c_1 \rho v_\infty^2 \left[\frac{\nu}{v_\infty \delta}\right]^{\frac{1}{4}}, \tag{33}$$

with

$$c_1 = 0.0225 \quad , \tag{34}$$

$$v_\infty = v_{t\infty} \quad , \tag{35}$$

and

$$\delta = \delta_t \quad , \tag{36}$$

was used to describe the tangential shear stress, τ_{w_t}. The results in Figure 37 show this law describes τ_{w_t} when the constant,

$$c_1 = 0.0135,$$

is employed. The reduction from the flat plate shear law in c_1 is 40 percent.

Radial Shear Stress

The empirical radial shear stress law was found by assuming it was of the form,

$$\tau_{w_r} = c_2 \rho v_{r\infty}^2 \left[\frac{\delta v_{r\infty}}{\nu}\right]^n, \tag{37}$$

where c_2 and n are found from the experimental data shown in Figure 38 to be

$$n = -1.09 \quad , \tag{38}$$

and

$$c_2 = 310. \tag{39}$$

SYM	VANE (DEG)	Γ (FT^2/SEC)
⊙	60.0	2.6
◁	60.0	3.7
⊡	60.0	4.5
◇	67.5	3.0
▽	67.5	5.2
◡	67.5	6.3
⊙	75.0	4.2
◇	75.0	6.5
θ	75.0	7.8

$$\tau_{w_t}\ \text{CALC.} = C_1 \rho\, V_{t\infty}^2 \left[\frac{\gamma}{V_{t\infty}\,\delta_t}\right]^{1/4} \quad ; \quad C_1 = 0.0225$$

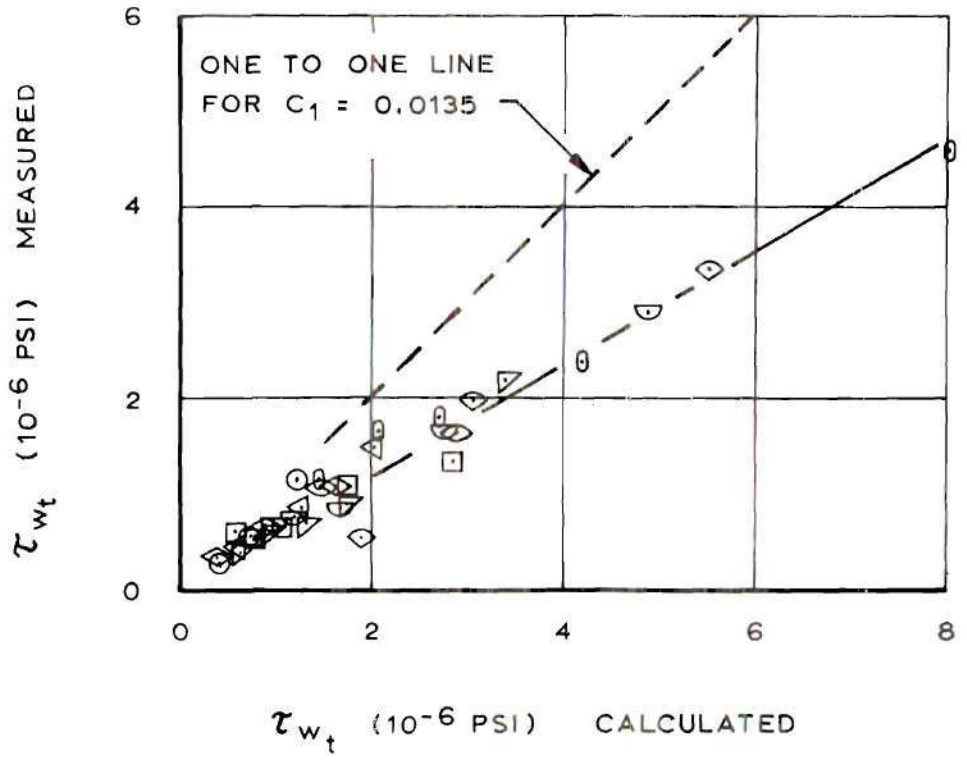

Figure 37. Tangential Shear Stress Correlation.

SYM	VANE (DEG)	Γ (FT^2/SEC)
⊙	60.0	2.6
△	60.0	3.7
□	60.0	4.5
◇	67.5	3.0
▽	67.5	5.2
⊙	67.5	6.3
⊙	75.0	4.2
◇	75.0	6.5
⊙	75.0	7.8

$$\frac{\tau_{w_r}}{\rho V_{r\infty}^2} = C_2 \left[\frac{\delta_r V_{r\infty}}{\nu}\right]^n$$

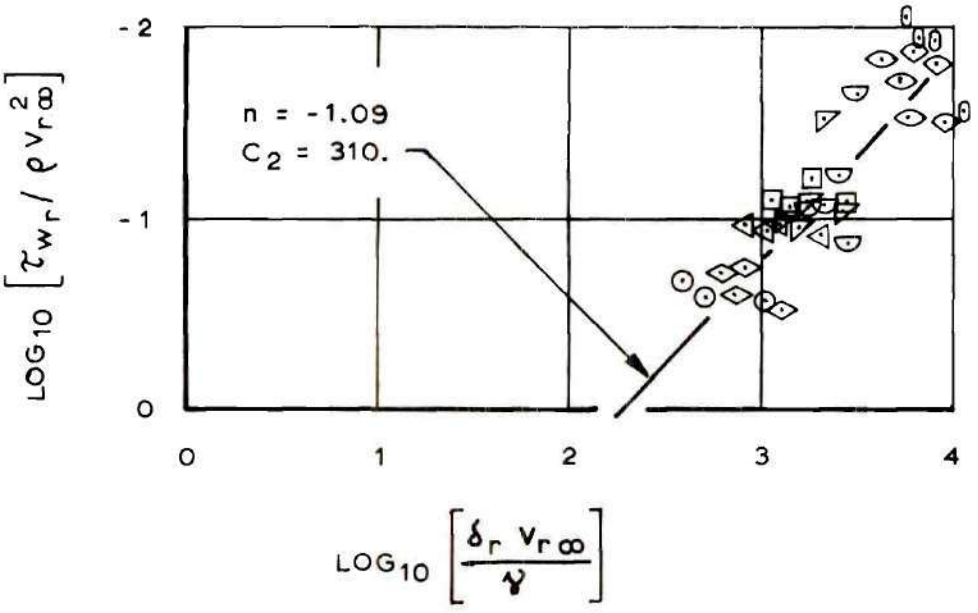

Figure 38. Radial Shear Stress Correlation.

SYM	VANE (DEG)	Γ (FT^2/SEC)
⊙	60.0	2.6
◁	60.0	3.7
⊡	60.0	4.5
◇	67.5	3.0
▽	67.5	5.2
◁	67.5	6.3
⊙	75.0	4.2
◇	75.0	6.5
0	75.0	7.8

$$\tau_{w_r} \text{ CALC.} = C_3 \rho V_{r\,max}^2 \left[\frac{\gamma}{(V_r \delta_r)_{max}}\right]^{1/4}$$

$$C_3 = 0.0225$$

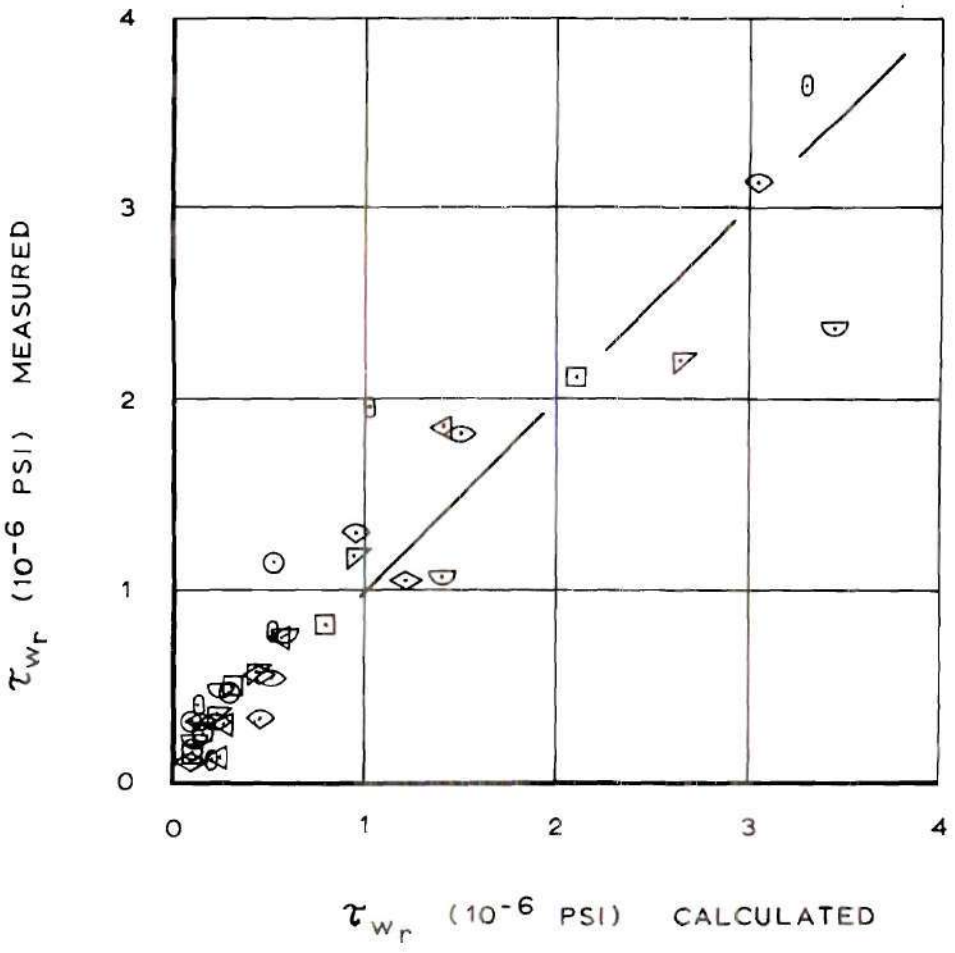

Figure 39. Radial Shear Stress Calculated from Maximum Velocity Conditions.

The above result has little relation to the two-dimensional flat plate shear law because of the use of the freestream conditions.

An interesting result occurs if the conditions at the maximum radial velocity are used in the calculation, as seen from Figure 39. The empirical flat plate law offers fairly good agreement with the measured data. This particular comparison was made because of the reasoning that the wall shear stress was not transmitted further to the boundary layer after τ_r went to zero when $\frac{\partial v_r}{\partial z}$ became zero.

The freestream empirical shear law is more important however, because the momentum integral analysis is based on the freestream conditions, δ_r and $v_{r\,\infty}$.

Momentum Integral Equation Analysis

This section consists of an evaluation of the momentum integral equations using the experimental data in order to check its accuracy and a simple error analysis linking the error in the experimental data to the error of the calculated momentum integral equations.

Evaluation

The momentum integral equations derived by Dr. Wolfgang Wulff are used to describe the boundary layer. Originally, Rott and Lewellen's momentum integral equations (20) were to be used, but they did not include the possibility of radial freestream velocity which does exist.

The momentum integral equations, which are derived and discussed in Appendix D, are

1) the radial momentum integral equation

$$\frac{d}{dr}\left(r\, v_{r\infty}^2\, \theta_r\right) + r v_{r\infty}\, \delta_r^* \frac{dv_{r\infty}}{dr} - v_{t\infty}^2\, \delta_1 + \frac{r}{\rho}\, \tau_{w_r} = 0 \quad , \tag{40}$$

where

$$\theta_r = \int_0^\infty \frac{v_r}{v_{r\infty}} \left(1 - \frac{v_r}{v_{r\infty}}\right) dz \quad , \tag{41}$$

$$\delta_1 = \int_0^\infty \left[1 - \left(\frac{v_t}{v_{t\infty}}\right)^2\right] dz \quad , \tag{42}$$

$$\text{and } \delta_r^* = \int_0^\infty \left(1 - \frac{v_r}{v_{r\infty}}\right) dz \quad , \tag{43}$$

2) and the angular momentum integral equation

$$\frac{d}{dr}\left(r^2 v_{r\infty}\, v_{t\infty}\, \delta_2\right) - r v_{t\infty} \frac{d}{dr}\left(r v_{r\infty} \delta_r^*\right) - \frac{r^2}{\rho}\, \tau_{w_t} = 0 \quad , \tag{44}$$

where

$$\delta_2 = \int_0^\infty \left(1 - \frac{v_r v_t}{v_{r\infty}\, v_{t\infty}}\right) dz \quad . \tag{45}$$

The variables δ_r^* and θ_r are the radial velocity thickness and radial momentum thickness respectively. In all the integrations the upper integration limit of ∞ may be replaced by δ_r or δ_t, the boundary layer thickness, since the integrand is

zero for $z > \delta$. Since $\delta_r \geq \delta_t$ for our data, δ_r is always used as the upper integration limit when evaluating these integrals.

The values of δ_r^*, δ_t^*, θ_r, δ_1, δ_2 and ΔQ for vane angle = 60.0 degrees are presented in Figures 40 to 42. The values for the other vane angles are in Appendix D. Previously undefined δ_t^* and ΔQ are the tangential velocity thickness and radial flow deficit in the boundary layer respectively where

$$\delta_t^* = \int_0^{\delta_t} \left(1 - \frac{v_t}{v_{t\,\infty}}\right) dz \tag{46}$$

and

$$\Delta Q = 2\pi r \int_0^{\delta_r} \left(v_r - v_{r\,\infty}\right) dz$$

$$= -2\pi r\, v_{r\,\infty}\, \delta_r^* \tag{47}$$

The integration calculations were performed in a digital computer program using an Aitken interpolation routine to calculate closely spaced values from the reduced data for a trapizoidal integration routine.

The radial and tangential momentum integral equations are evaluated for two typical test conditions,

$$\text{Vane angle} = 60.0 \text{ deg} \quad ,$$

$$\Gamma = 3.7 \text{ and } 4.5 \text{ ft}^2/\text{sec} \quad ,$$

and the calculations are presented in Tables 4 and 5 in Appendix D.

Due to errors in the balanced equations caused by inaccuracies in the

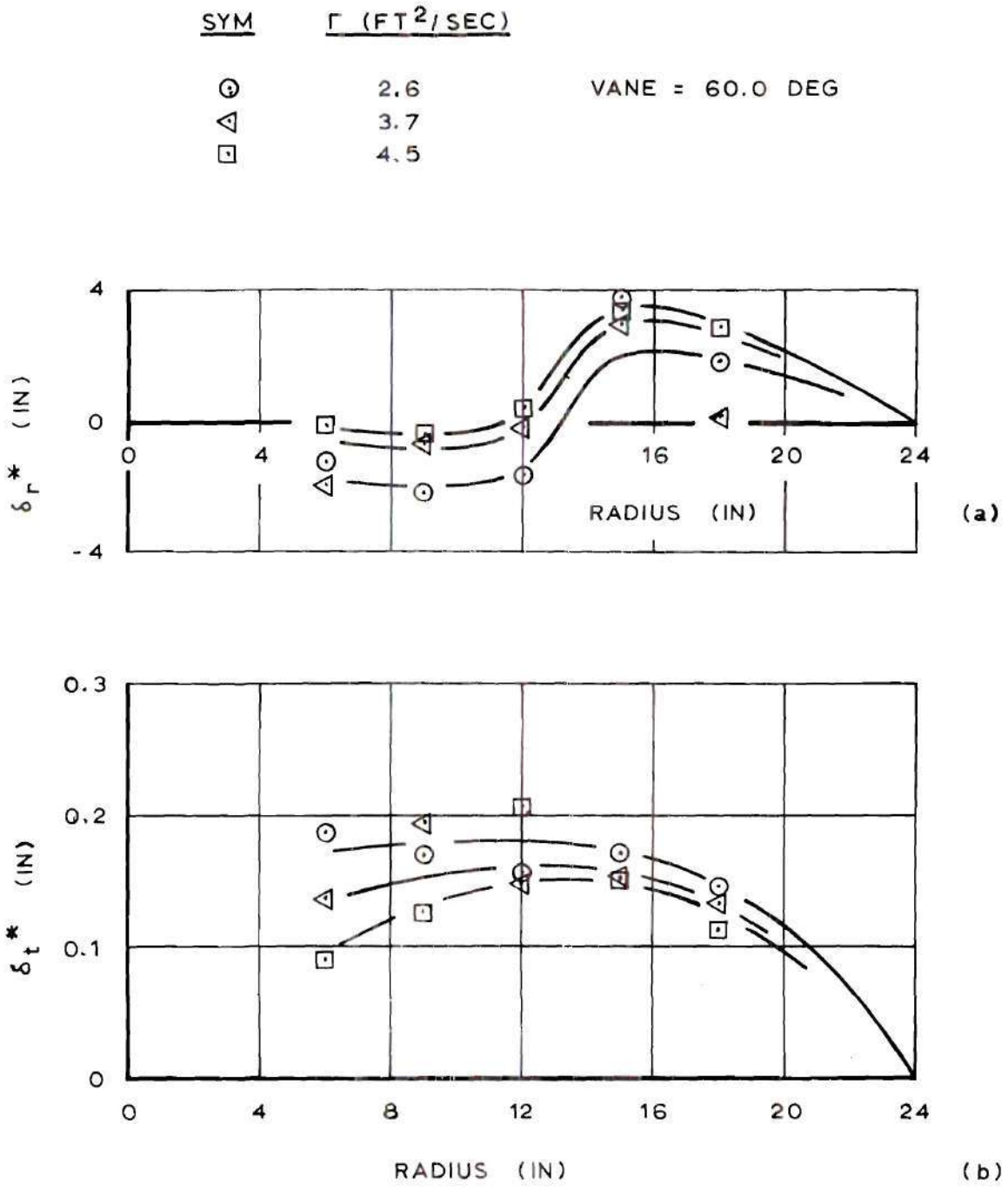

Figure 40. Radial and Tangential Velocity Displacement Thickness

Vane = 60.0 Deg.

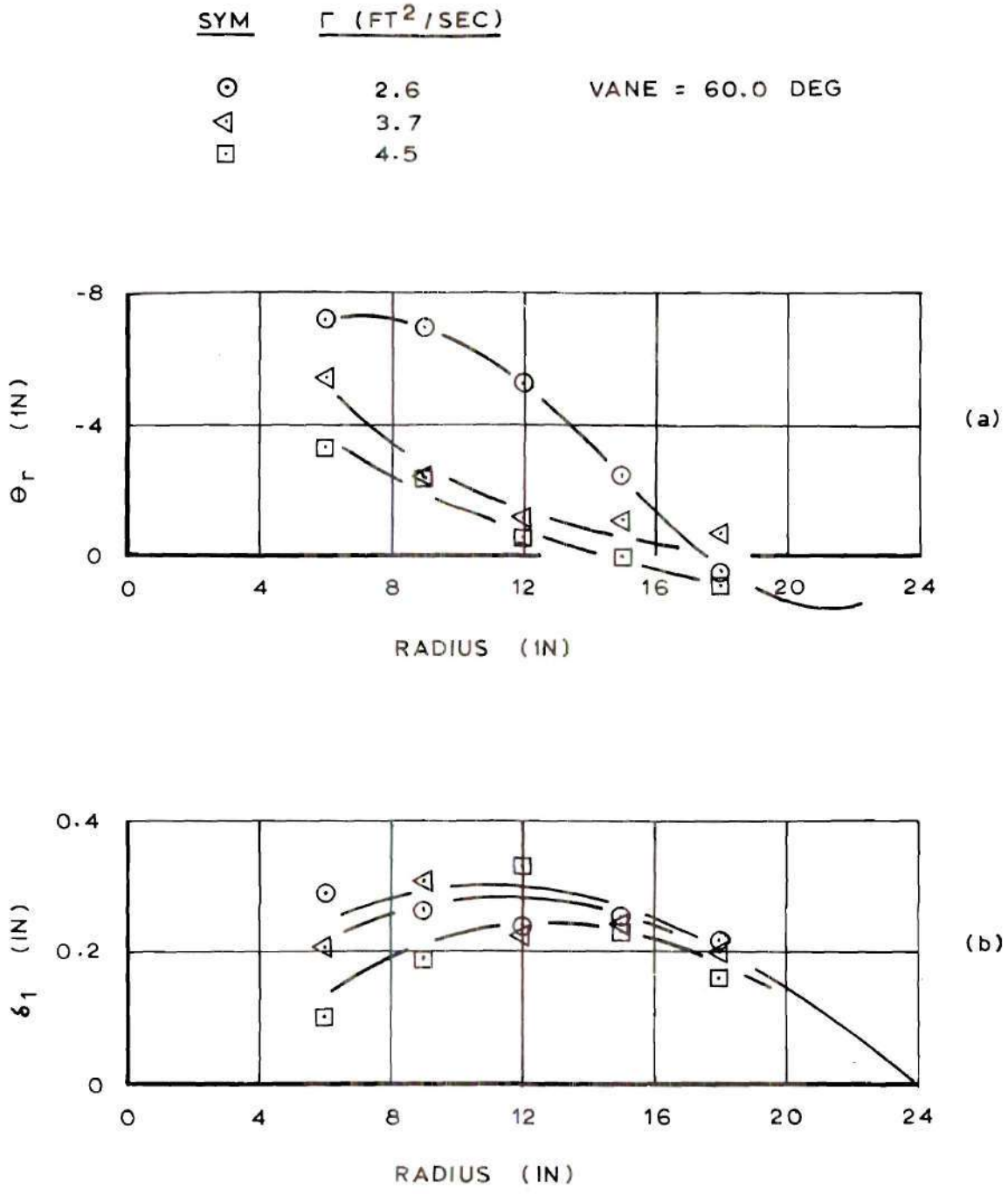

Figure 41. Radial Momentum Thickness and δ_1

Vane = 60.0 Deg.

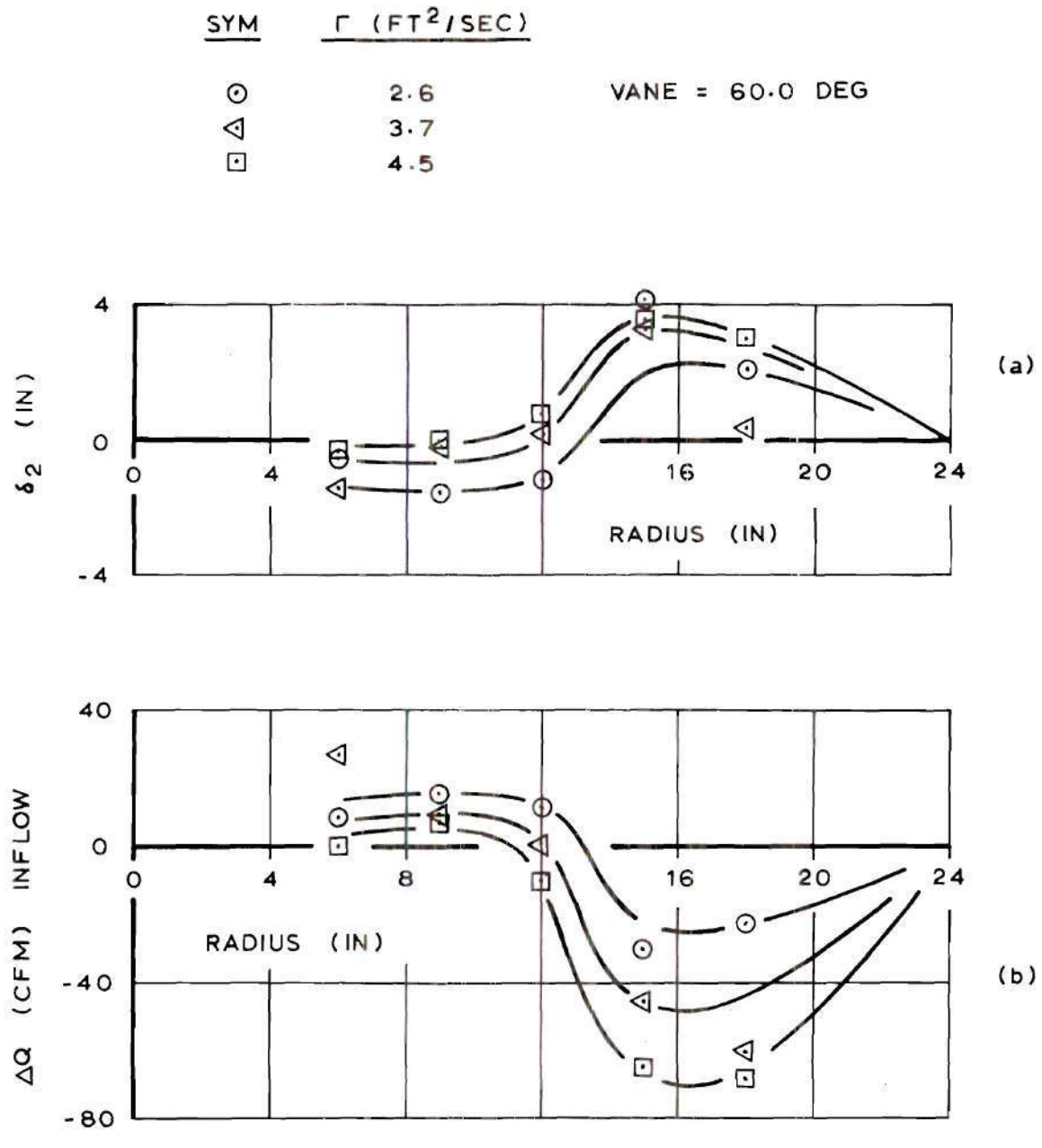

Figure 42. δ_2 and Radial Flow Increment

Vane = 60.0 Deg.

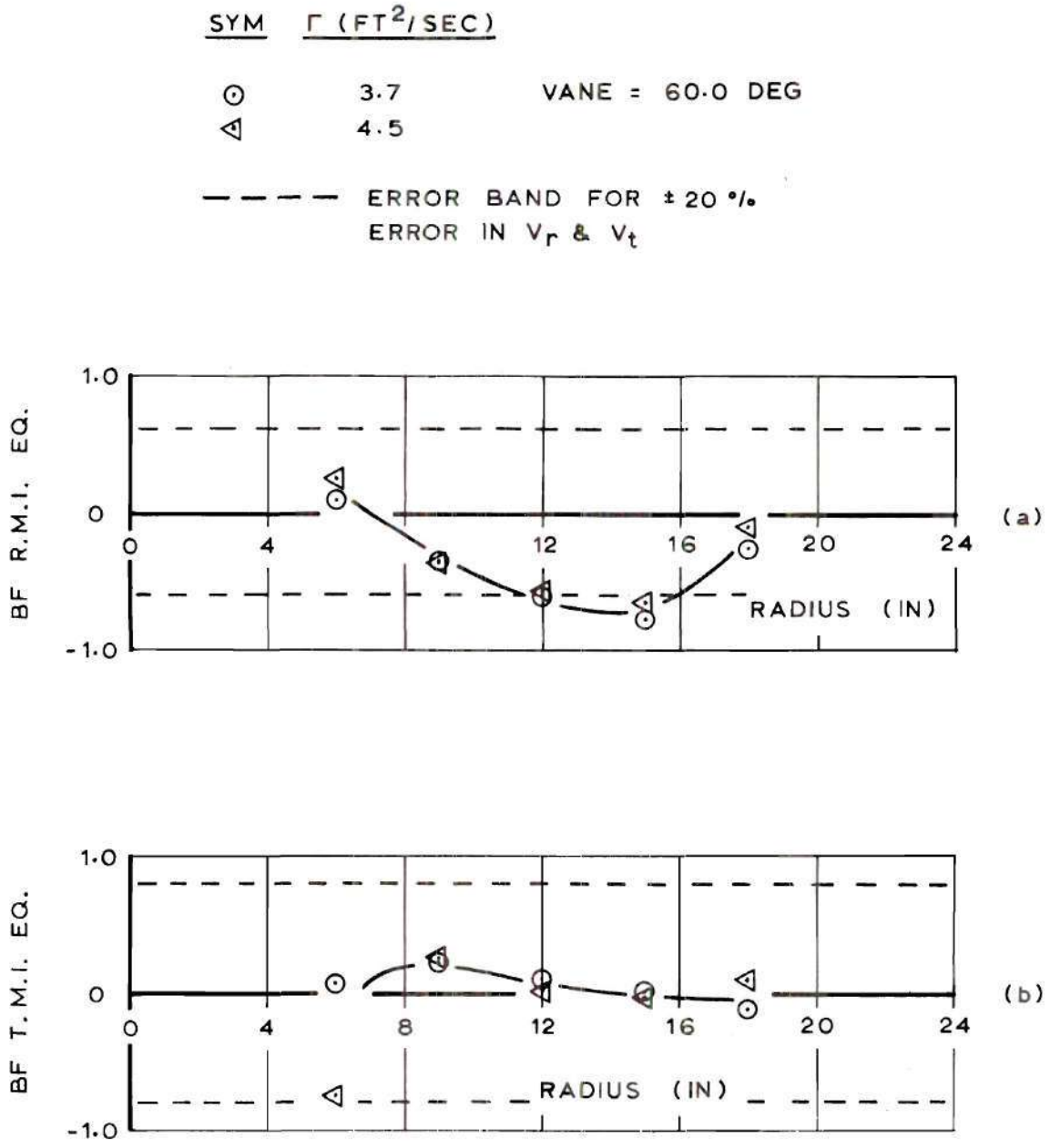

Figure 43. Balance Fraction Error of the Radial and Tangential Momentum Integral Equations.

variables used in the calculations, the results are presented in Figure 43 as the balance fraction,

$$BF = \frac{\text{balanced equation error}}{|\text{largest term in the equation}|} \quad . \tag{48}$$

The following section presents a simple error analysis applied to our results.

Simple Error Analysis of the Momentum Integral Equations

This analysis will attempt to show the relation between the error in the data used to calculate the momentum integral equation balance and the error in the balance. The balance fraction based on the error of the largest term in the balance equation will be evaluated assuming the error in the reduced data, v_t and v_r, is ± 20 percent. The actual error is not this simple, but this estimate is thought to be representative of the error in the test data. For the analysis the following simplified operation laws were used.

1) The error band of the result of multiplication and division is the addition of the individual error bands.
2) The error band of the result of addition and subtraction is the addition of the individual error bands.
3) The error band of the result of integration is division of the integral error band by two.
4) The error band of the result of differentiation is the multiplication by two of the error band of the differentiated value.

The resulting balance fraction for the radial momentum integral equation is between ± 0.60, and the balance fraction for the tangential momentum integral equation is

between $\pm$ 0.80. These values are shown on Figure 43 and, considering the simplicity of the analysis, adequately account for the experimental balance fraction values. Carrying this analysis one step further, and evaluating the balance fraction for an assumed reduced data error of $\pm$ 3 percent, which is thought to be the best obtainable; the resulting balance fractions for the radial and tangential momentum integral equations are $\pm$0.09 and $\pm$0.12 respectively. Thus this error analysis shows the order of magnitude of the improvement in the integral analysis if the accuracy of the measured data can be improved by approximately one order of magnitude.

CHAPTER IV

CONCLUSIONS AND RECOMMENDATIONS

Conclusions

The simulation of the vortex-surface boundary layer produced generally good results, but showed the need for increased flow stability to increase the accuracy of the measured data.

Freestream

Tangential Velocity. A potential vortex was established above the boundary layer.

Radial Velocity. Constant radial inflow existed above the boundary layer over a center section of the radius from six to twelve inches. Upward vertical flow existed elsewhere in combination with the radial inflow.

Boundary Layer

Tangential Velocity. The tangential velocity profile was well developed with the two-dimensional flat plate similarity of

$$\frac{v_t}{v_{t\,\infty}} = \left(\frac{z}{\delta_t}\right)^{\frac{1}{7}} . \tag{49}$$

Radial Velocity. The radial velocity profile was fully developed over only the six to twelve inch section of the radius. It was developing over the outer half of the plate radius from its beginning at the outer edge. No similarity was shown.

Shear Stress

Empirical surface shear stress laws were derived based on freestream conditions from the Preston tube measured surface shear. They are

$$\tau_{w_t} = 0.0135\, \rho v_{t\infty}^2 \left[\frac{\nu}{v_{t\infty}\delta_t}\right]^{\frac{1}{4}} . \tag{50}$$

and

$$\tau_{w_r} = 310.\ \rho v_{r\infty}^2 \left[\frac{\nu}{v_{r\infty}\delta_r}\right]^{1.09} . \tag{51}$$

Momentum Integral Analysis

The momentum integral equation analysis results showed that generally the data were not accurate enough to achieve balance in the equations.

Recommendations

Future researchers should work to increase flow stability, which may be done by increased air supply regulation (possibly with the use of more screens).

An effort should be made to achieve fully developed radial velocity profiles over a larger section of the radius. Vertical upflow at the beginning of the radial boundary layer should be reduced. These problems, along with the high freestream radial inflow are related to the fan and orifice used. A low head fan which requires a large orifice to pull large volumes of air through the vortex generator was used. The author believes that a high head fan with the head scaled to the pressure drop in a tornado core, combined with a smaller orifice would produce more favorable results. It would reduce the vertical flow outside the core and increase the

vertical flow in the core, thus increasing the mass supplied to the core by the radial boundary layer, and reducing the effect on its development of vertical velocity at the outer plate radius.

An examination should be made into increasing the accuracy of the instruments, for example, decreasing the V-probe angle to achieve greater angle sensitivity.

Further studies should include measurement of the flow above the boundary layer; an extension of the range of the test parameters, Γ and vane angle; and further testing of the vortex generator configuration, specifically, the height of the plastic shield, the number and arrangement of screens, the type of fan, and the orifice size.

APPENDIX A

VORTEX GENERATOR DETAILS

This appendix consists of the major drawings used to construct the vortex generator.

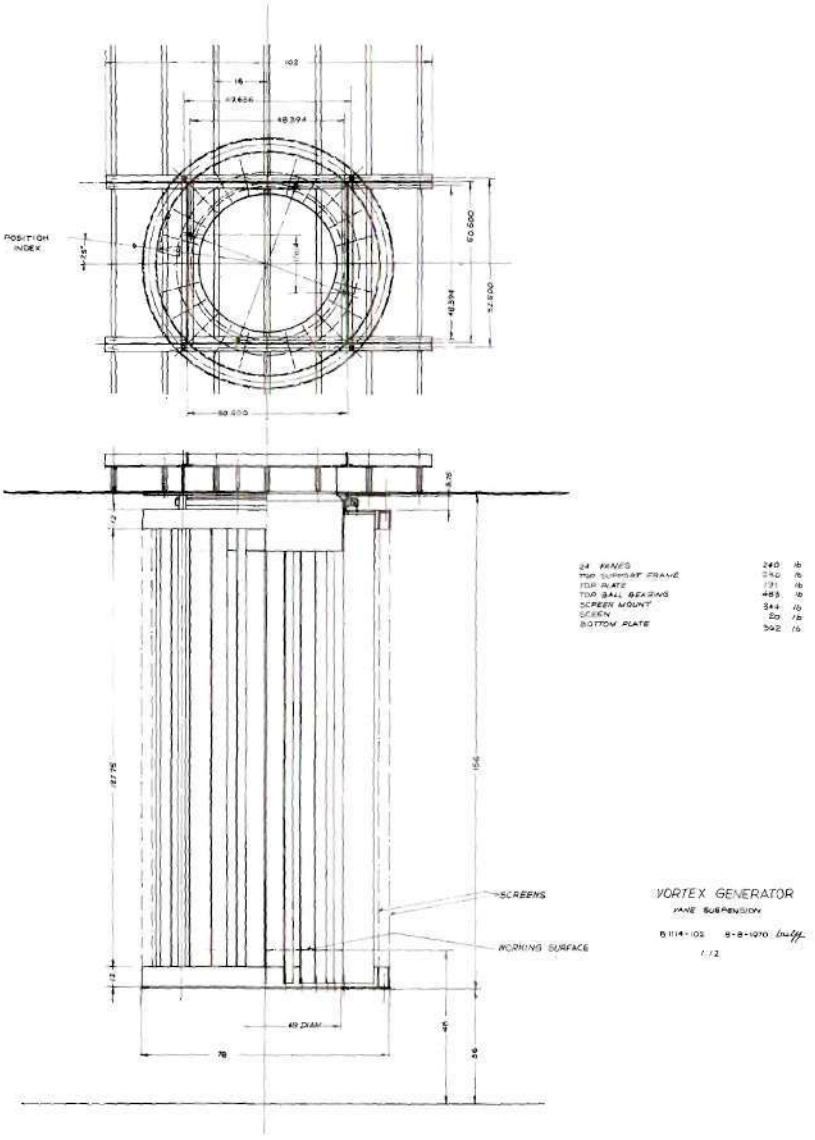

Figure 44. Vortex Generator.

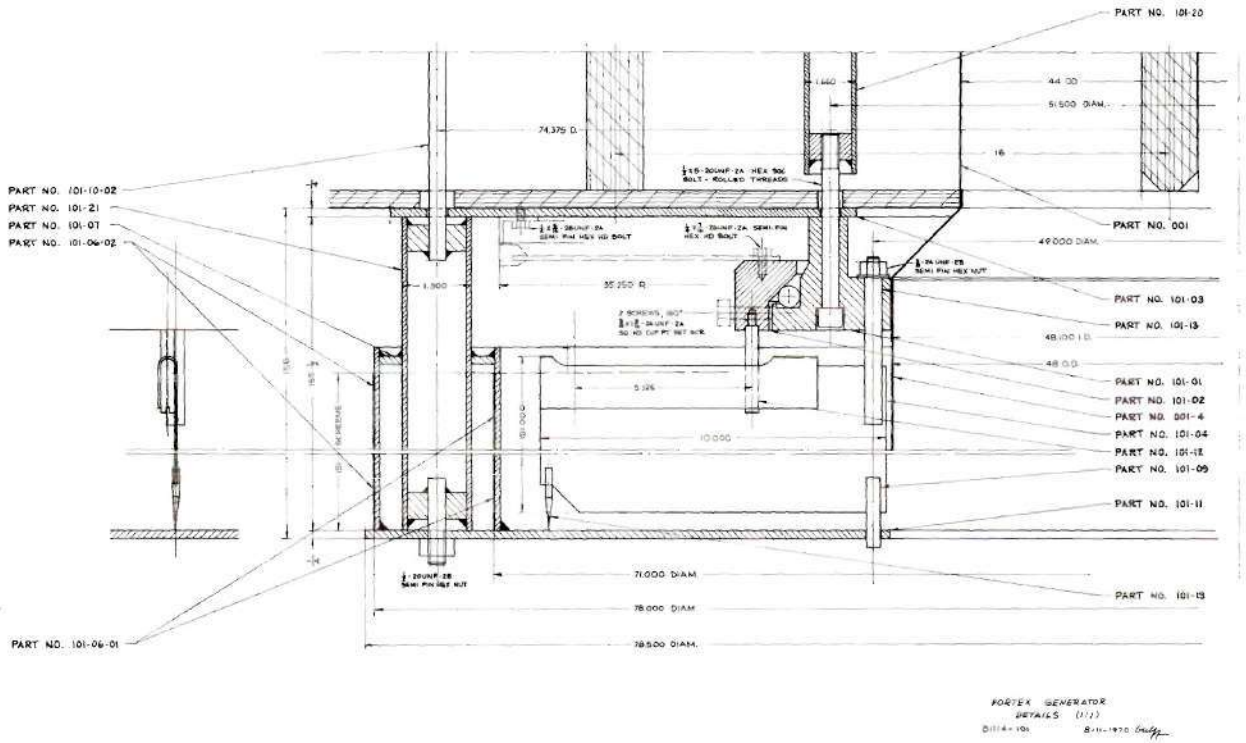

Figure 45. Vane Mounting--Sectional Side View.

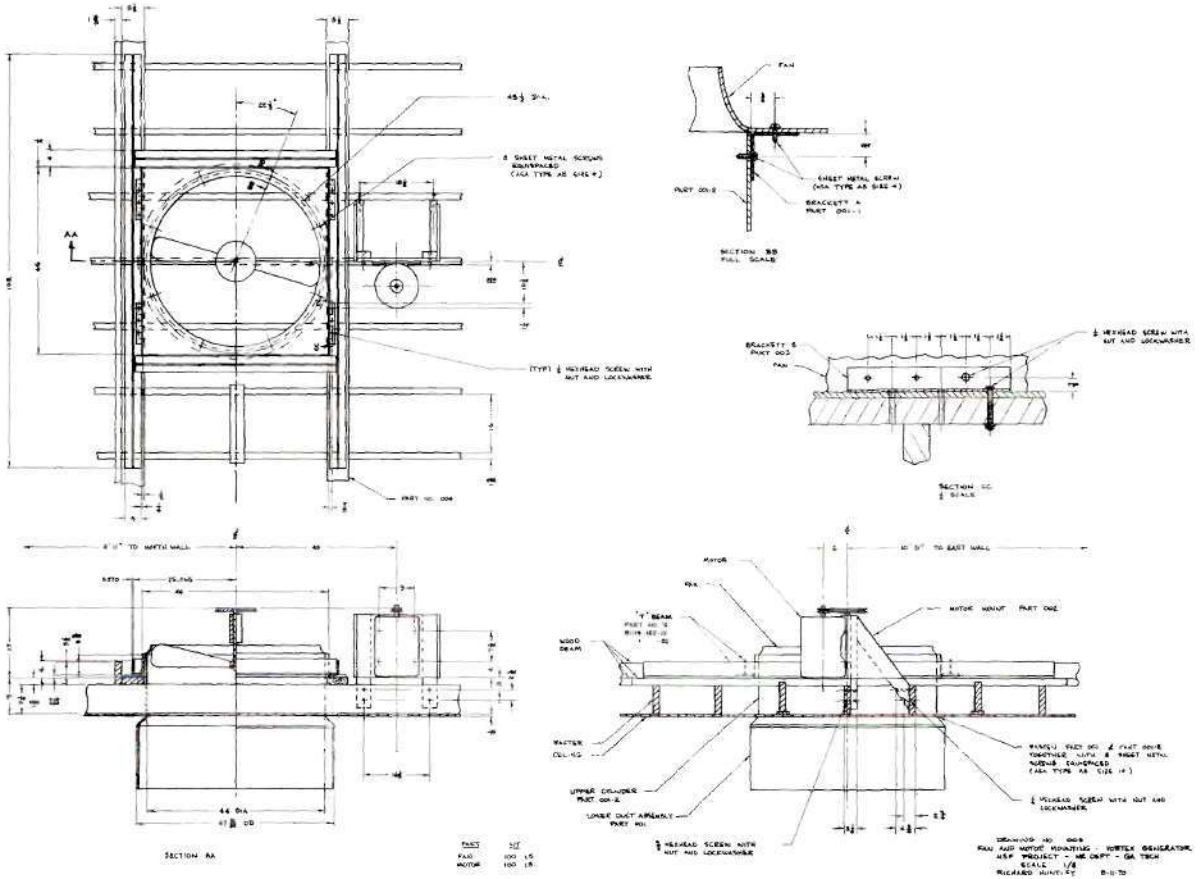

Figure 46. Fan Mounting.

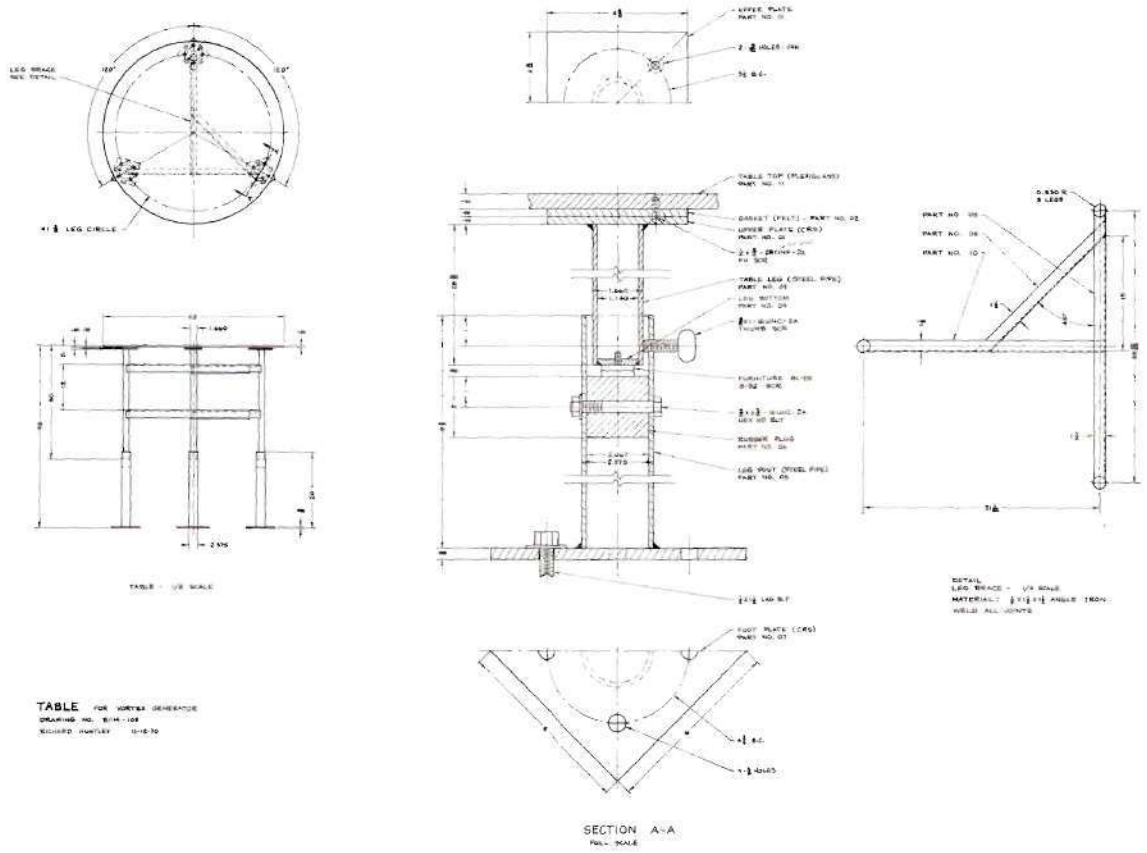

Figure 47. Table.

APPENDIX B

HOT WIRE ANEMOMETER DETAILS

An inexpensive, constant temperature, V-probe hot wire anemometer was constructed to measure the two-dimensional time mean velocity profile of the vortex-surface boundary layer. Its range of operation and general physical characteristics are described in the text. Essentially, it has a double resistance bridge, one bridge when balanced points the "V" in the velocity direction, and the other bridge when balanced indicates velocity magnitude with the current supplied to the bridge.

This appendix is divided into three major sections, the physical description, an analysis including circuit considerations and the predicted hot wire response, and the calibration.

Physical Description

The hot wire anemometer, shown in Figure 5, has the following components:

a) the probe, drawn in Figure 48;

b) a double bridge circuit, discussed earlier and shown in Figure 49, which can be separated for the calibration;

c) and the control circuit, shown in Figure 49, to balance the bridges and indicate the shunt voltage.

The probe was originally built with a thermocouple in it to measure ambient

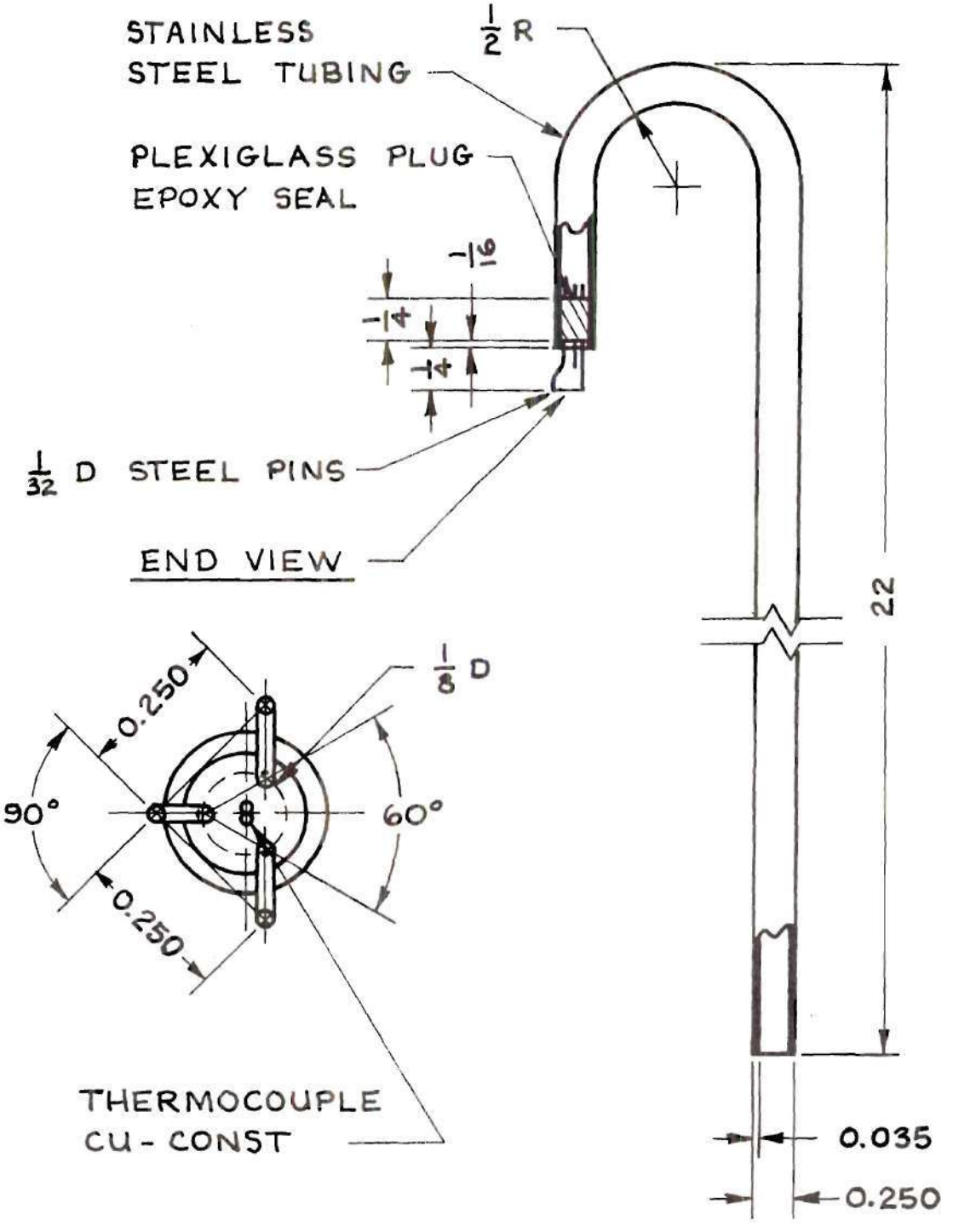

Figure 48. Hot Wire Anemometer V-Probe.

temperature; however, the heated wire interfered with the thermocouple reading, making it too difficult to calibrate, so a mercury thermometer, positioned at the beginning of the boundary layer, was used instead.

The 0.001 inch diameter wire was soldered to the steel pin tips using an acid flux, an indium alloy solder, and a conventional soldering gun.

All fixed resistors in the circuit are 1% wire wound, and the variable resistors are 5% wire wound.

The primary voltage supply is a regulated 12 volt direct current power supply.

Hot Wire Analysis

The purpose of this analysis is to support the construction and calibration. Specifically, the analysis contains.

1) initial considerations for the circuit, wire size, and resistance values used;
2) the detailed analysis determining the size of the direction bridge balance resistor;
3) the predicted hot wire response, including the velocity direction response, and the velocity magnitude sensitivity and response;
4) and the galvanometer filter used to obtain average voltage readings.

Initial Considerations

The circuit, see Figure 49, used is a modification of the hot wire anemometer in reference 11. The wire size, 0.001 inch diameter, was selected as a compromise between high damping, desirable to measure time mean velocity, and high wire to probe lead resistance. Other considerations which established the first estimate of the bridge resistances and voltage were

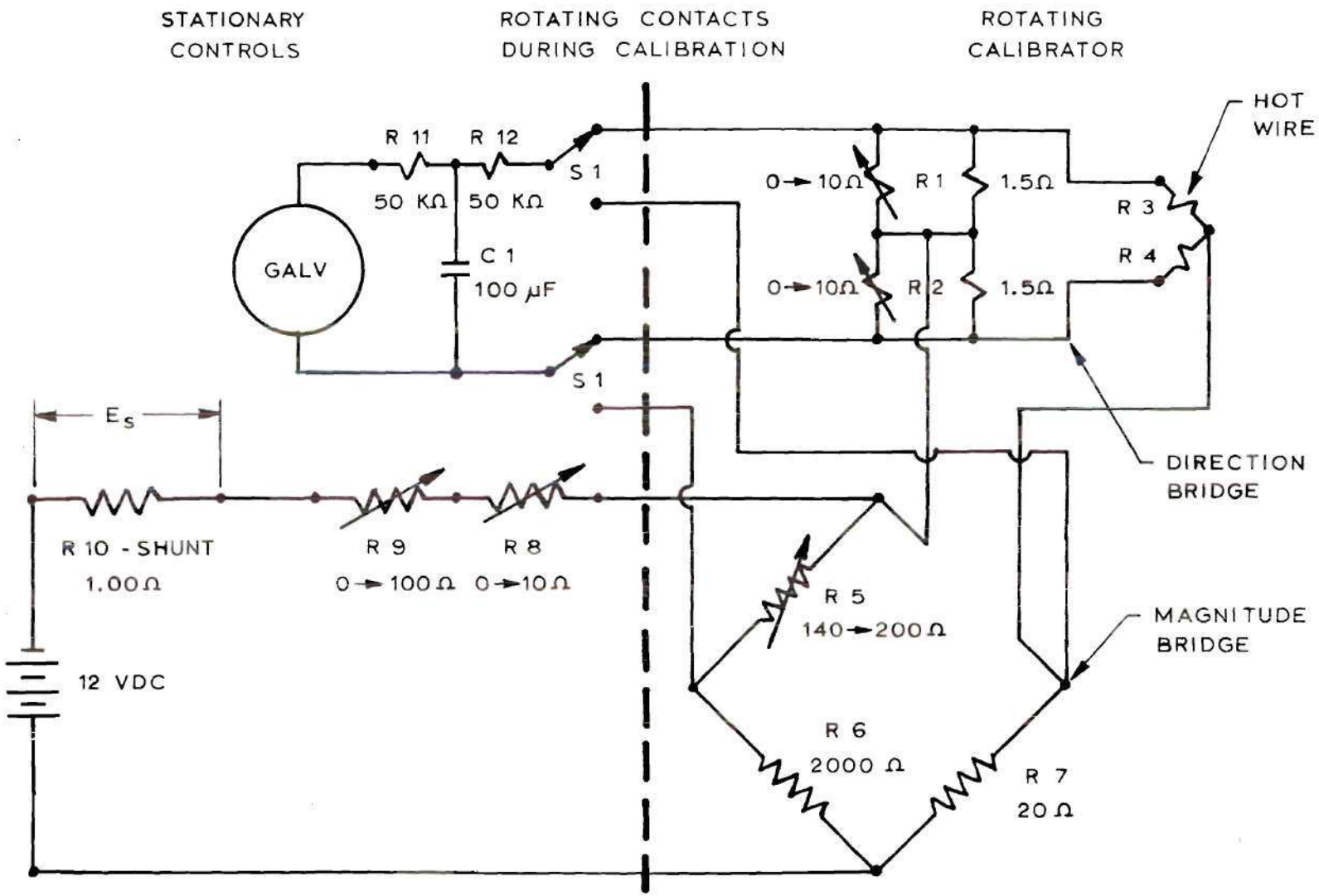

Figure 49. Hot Wire Anemometer Schematic.

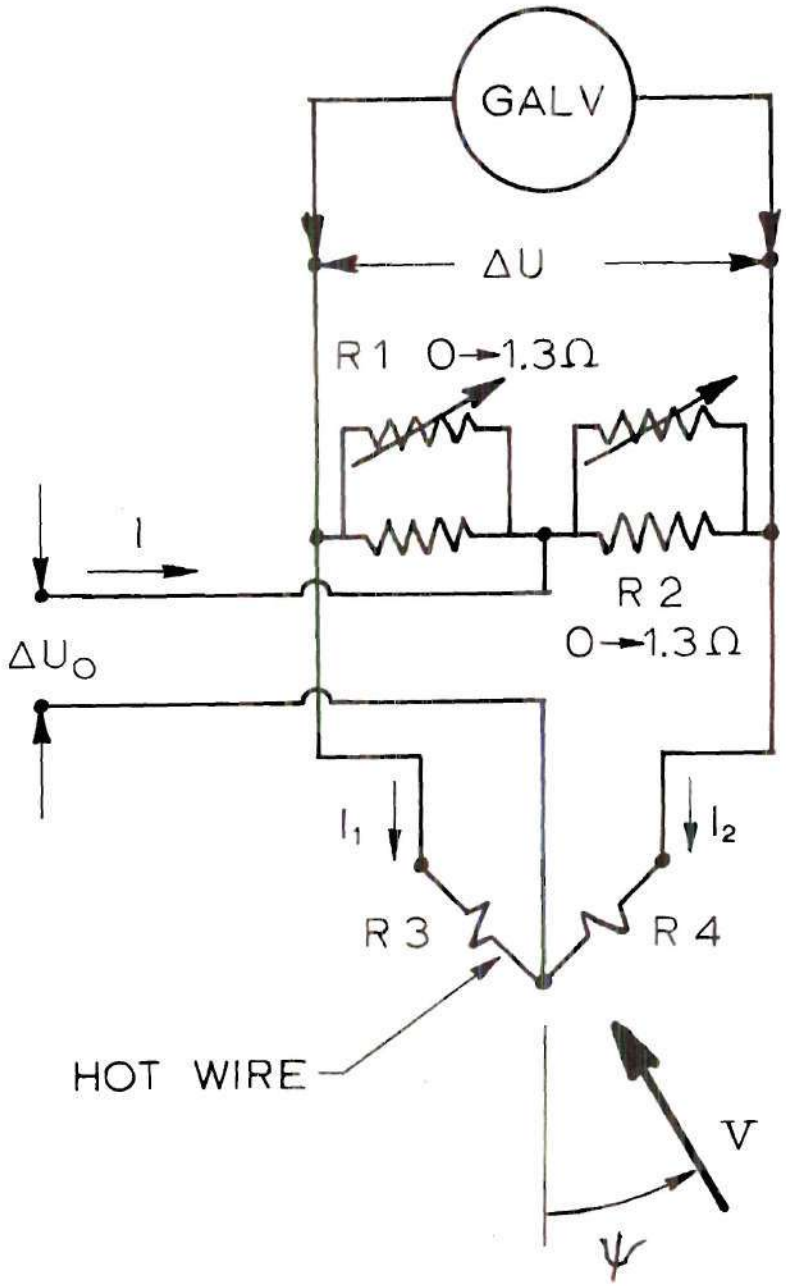

Figure 50. V-Probe Direction Bridge.

a) a wire length of approximately 0.25 inch for high L/d, and

b) a wire temperature approximately 150 degrees above ambient temperature to obtain the velocity sensitivity mentioned in the text.

Several small iterations of the circuit variables led to the final circuit in Figure 49. The final stages of analysis are included in the following pages.

Sizing of the Probe Balance Resistor in the Direction Bridge

Two resistances, R_1 and R_2, were needed in addition to the two hot wire resistances, R_3 and R_4, to complete the probe direction bridge, shown in Figure 50. They were made finely adjustable with a large variable resistor in parallel with a small fixed resistor, so small differences in the two hot wire resistances could be compensated.

The optimum of resistors R_1 and R_2 for maximum bridge sensitivity is calculated next.

The basic equations for the bridge in Figure 50 are

$$I = I_1 + I_2 \tag{B-1}$$

$$I_1(R_1 + R_3) = I_2(R_2 + R_4) \tag{B-2}$$

$$\Delta U_o = I(R_1 + R_3) \tag{B-3}$$

$$\Delta U = I_1 R_1 - I_2 R_2 \tag{B-4}$$

where ΔU is the bridge unbalance voltage, and ΔU_o is the bridge supply voltage. Since changes in velocity direction cause changes in hot wire resistance; for maximum directional sensitivity, find R_2 to maximize the sensitivity of $\frac{\Delta U}{\Delta U_o}$ with respect to R_4. The sensitivity of $\frac{\Delta U}{\Delta U_o}$ with respect to R_4 is

$$\frac{\partial}{\partial R_4}\left(\frac{\Delta U}{\Delta U_o}\right) = \frac{R_2}{(R_2+R_4)^2} \quad . \tag{B-5}$$

The optimum R_2 will be at

$$\frac{\partial}{\partial R_2}\left[\frac{\partial}{\partial R_4}\left(\frac{\Delta U}{\Delta U_o}\right)\right] = 0 \quad . \tag{B-6}$$

Solving equation B-6 gives

$$R_4 = R_2 \quad . \tag{B-7}$$

Similarly,

$$R_3 = R_1 \quad . \tag{B-8}$$

Thus R_1 and R_2 were chosen close to the size of R_3 and R_4. All are approximately 1.5 Ω.

The Estimated Hot Wire Velocity Direction Response

The objective of this section is to calculate the response of the direction bridge unbalance voltage, ΔU, to the velocity direction, Ψ, shown in Figures 50 and 51. The method used here will be to calculate the velocity direction sensitivity, $\partial(\Delta U)/\partial\Psi$, of the direction bridge. For the purpose of this analysis the unbalance voltage, $\Delta U = 0$, when the velocity direction, $\Psi = 0$.

The resistances R_3 and R_4 in Figures 50 and 51 are the two hot wires in the V-probe. Their resistance is a function of the normal ($\perp$) velocity component only,

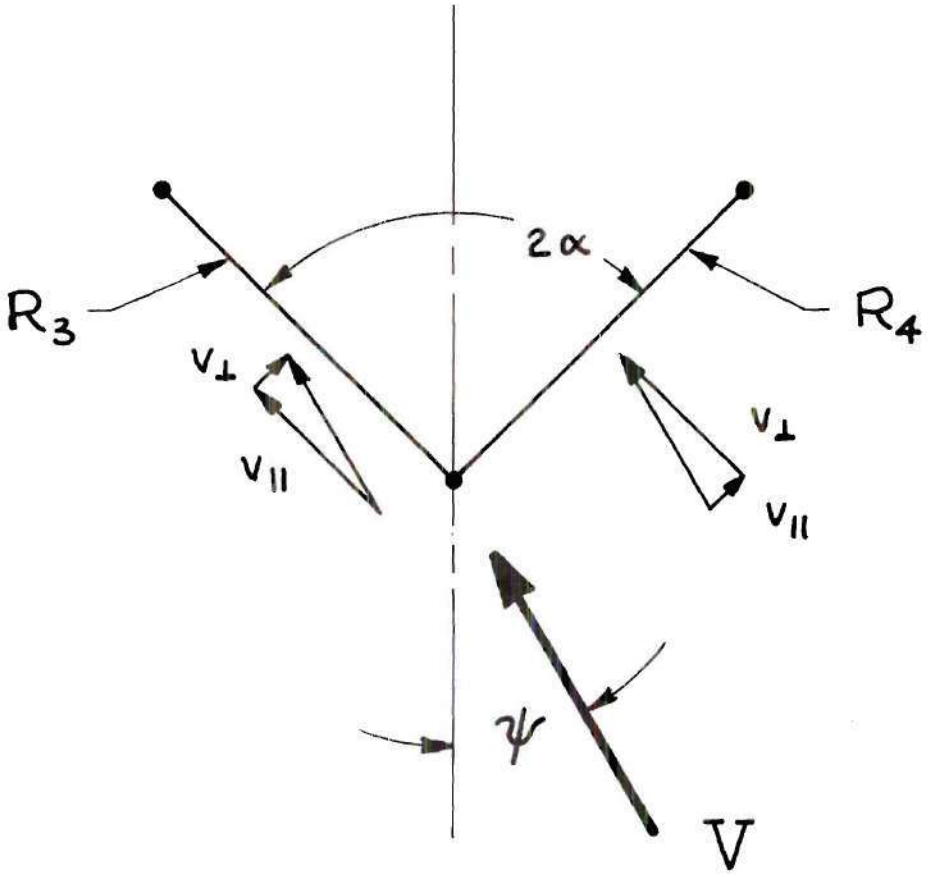

Figure 51. V-Probe Yaw Angle.

an assumption valid when the velocity is incident to the wire at angles greater than 15 degrees (12).

The significant velocity components are

$$v_{\perp 3} = V \sin(\alpha - \Psi) \quad , \tag{B-9}$$

and

$$v_{\perp 4} = V \sin(\alpha + \Psi) \quad . \tag{B-10}$$

From a circuit analysis of Figure 50,

$$\frac{\Delta U}{\Delta U_o} = \frac{R_1}{R_1+R_3} - \frac{R_2}{R_2+R_4} \quad . \tag{B-11}$$

The directional sensitivity is then

$$\frac{\partial}{\partial \Psi}\left(\frac{\Delta U}{\Delta U_o}\right) = -\frac{R_1}{(R_1+R_3)^2}\frac{\partial R_3}{\partial \Psi} + \frac{R_2}{(R_2+R_4)^2}\frac{\partial R_4}{\partial \Psi} \quad , \tag{B-12}$$

where

$$\frac{\partial R_3}{\partial \Psi} = -\frac{\partial R_3}{\partial v_{\perp 3}} V \cos(\alpha - \Psi) \quad , \tag{B-13}$$

and

$$\frac{\partial R_4}{\partial \Psi} = \frac{\partial R_4}{\partial v_{\perp 4}} V \cos(\alpha + \Psi) \quad . \tag{B-14}$$

To find $\frac{\partial R_3}{\partial v_{\perp 3}}$ and $\frac{\partial R_4}{\partial v_{\perp 4}}$,

assume convection heat transfer only and using Collis and Williams' relation (1),

$$\frac{I^2 R_w}{\pi L (T_w - T_\infty) k_f} \left(\frac{T_f}{T_\infty}\right)^{-0.17} = 0.24 + 0.56\, Re^{0.45} . \qquad \text{(B-15)}$$

Eliminating T_w in equation (B-15) with

$$T_w = T_o + \frac{1}{\alpha}\left(\frac{R_w}{R_o} - 1\right) , \qquad \text{(B-16)}$$

then

$$\frac{\partial R_w}{\partial v_\perp} = \frac{0.252}{A\,G} \left(\frac{d}{\nu_f}\right) \left(\frac{v_\perp d}{\nu_f}\right)^{-0.55} , \qquad \text{(B-17)}$$

with

$$G = \frac{R_w}{(B+CR_w)^2 (D+ER_w)^{0.17}} \left[(B+CR_w)\left(1 - \frac{0.17E}{D+ER_w}\right) - C\right] , \qquad \text{(B-18)}$$

$$A = \frac{I^2}{\pi L} , \quad B = T_o - T_\infty - \frac{1}{\alpha} , \quad C = \frac{1}{\alpha R_o} \qquad \text{(B-19a, b, c)}$$

$$D = \frac{1}{2T_\infty} \left(T_o + T_\infty - \frac{1}{\alpha}\right) , \quad E = \frac{1}{2T_\infty \alpha R_o} . \qquad \text{(B-19d, e)}$$

Notice that

$$A = A(I) , \qquad \text{(B-20)}$$

and

$$G = G(R_w) . \qquad \text{(B-21)}$$

Evaluating a particular case at

$V = 2$ ft/sec, $v_{\perp} = 1.4$ ft/sec.,

$\Psi = 0$,

$I = 0.1534$ amps,

$d = 0.0000832$ ft.,

$L = 0.174$ ft.,

$T_w = 328^{o}F = 788\ ^{o}R$,

$T_{\infty} = 85\ ^{o}F = 545^{o}R$,

$T_f = \dfrac{T_w + T_{\infty}}{2} = 666\ ^{o}R$,

$k_f = 0.0178$ BTU/(ft hr ^{o}F),

$\nu = 2.52 \times 10^{-4}$ ft^2/sec,

$T_o = 74.5\ ^{o}F = 534.5\ ^{o}R$,

$\alpha = 0.00312/^{o}F$,

$R_o = 1.105\ \Omega$,

$R_w = 1.989\ \Omega$,

results in

$$\frac{\partial R_w}{\partial v_{\perp}} = -0.123 \ \frac{\Omega}{\text{ft/sec}} \qquad \text{(B-22)}$$

The sensitivity from equation (B-12) becomes

$$\frac{\partial}{\partial \Psi}\left(\frac{\Delta U}{\Delta U_o}\right) = 0.114/\text{rad} \ , \qquad \text{(B-23)}$$

and for $\Delta U \approx 0.300$ volts,

$$\frac{\partial \Delta U}{\partial \Psi} = 0.598 \quad \frac{\text{millivolts}}{\text{deg.}} \tag{B-24}$$

This result is compared to the calibrated results on Figure 12 in the text.

Magnitude Bridge Sensitivity

In this analysis the sensitivity, $\frac{\partial}{\partial V}\left(\frac{\Delta U}{\Delta U_o}\right)$, of the magnitude bridge unbalance voltage, ΔU, to the velocity magnitude is calculated. Referring to Figure 52, first assume

$$R_{w_1} \approx R_{w_2} , \tag{B-25}$$

and

$$R_4 \approx R_5 , \tag{B-26}$$

So

$$R_p \approx \tfrac{1}{2}(R_{w_1} + R_4) . \tag{B-27}$$

The bridge sensitivity to velocity

$$\frac{\partial}{\partial V}\left(\frac{\Delta U}{\Delta U_o}\right) = \frac{\partial}{\partial R_p}\left(\frac{\Delta U}{\Delta U_o}\right) \frac{\partial R_p}{\partial V} . \tag{B-28}$$

The bridge circuit equations are

$$\Delta U_o = I_2(R_p + R_3) , \tag{B-29}$$

$$I_2(R_p + R_3) = I_1(R_1 + R_2) , \tag{B-30}$$

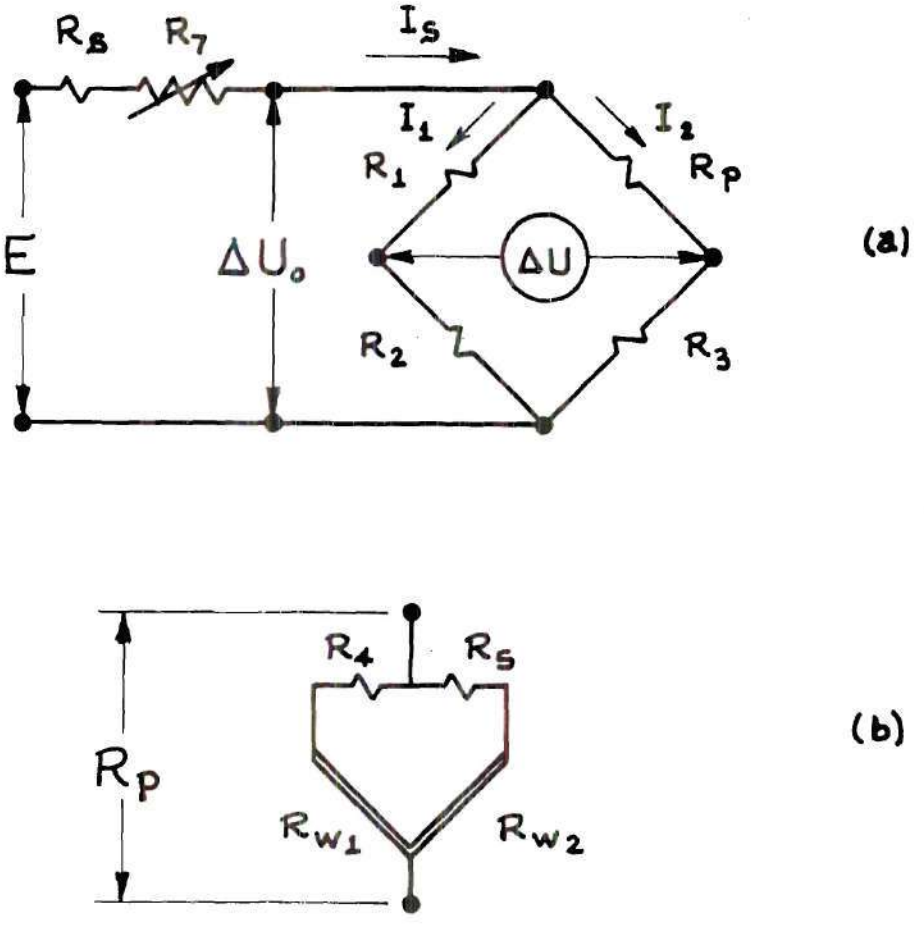

Figure 52. Hot Wire Bridge for Sensitivity Analysis.

$$\Delta U = I_2 R_p - I_1 R_1 \quad , \tag{B-31}$$

and

$$I_1 + I_2 = I_s \quad . \tag{B-32}$$

From equations (B-29) to (B-32)

$$\frac{\Delta U}{\Delta U_o} = \frac{R_p}{(R_p + R_3)} - \frac{R_1}{(R_1 + R_2)} \quad . \tag{B-33}$$

Then,

$$\frac{\partial}{\partial R_p}\left(\frac{\Delta U}{\Delta U_o}\right) = \frac{R_3}{(R_p + R_3)^2} \quad .$$

Using the resistance values from Figure 49 ,

$$\frac{\partial}{\partial R_p}\left(\frac{\Delta U}{\Delta U_o}\right) \approx 0.05/\,\Omega \quad , \tag{B-35}$$

and equation (B-22) of the sample case of the preceding section

$$\frac{\partial R_p}{\partial V} \approx -0.123 \ \frac{\Omega}{\text{ft/sec}} \quad .$$

Therefore,

$$\frac{\partial}{\partial V}\left(\frac{\Delta U}{\Delta U_o}\right) \approx -0.00615 \ \frac{1}{\text{ft/sec}} \quad . \tag{B-36}$$

The galvanometer used to balance the bridge has a sensitivity of $0.486 \ \frac{\text{mV}}{\text{mm}}$, and using a representative value for ΔU_o of six volts, the galvanometer sensitivity to

the velocity is about 7.8 $\frac{\text{cm}}{\text{ft/sec}}$. Since the galvanometer can be read to the nearest millimeter the velocity magnitude bridge is therefore sensitive to 0.01 ft/sec.

Velocity Magnitude Response Analysis Using a Digital Computer Program

The calculations for the velocity magnitude response analysis are done in digital computer program written in Fortran V for the Univac 1108 high speed digital computer.

The calculations predict a wide range of the probe response characteristics: the current-velocity-temperature relation, the heat transfer from the wire, the effect of conduction end losses, the damping, and the current sensitivity.

First, the equations which govern the calculations are presented, second the method of using these equations is given, and third the program listing and a sample of its output are presented.

Calculations. This section contains the equations for the calculations and some supporting analysis.

a) The solution to the current-velocity-temperature relation including end effects is now presented. The steady state energy balance for the model wire element in Figure 53 is, assuming constant resistance in the wire cross-section,

$$\frac{d^2\theta_w}{d\eta^2} - A\,\theta_w + B = 0 \quad , \tag{B-37}$$

where

$$\eta = \frac{x}{L} \quad , \tag{B-38}$$

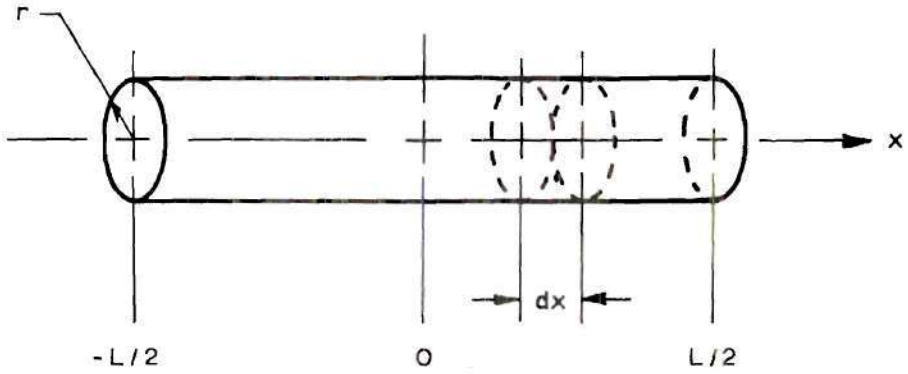

Figure 53. Hot Wire Analysis Model.

$$\theta_w = T_w - T_\infty \quad , \tag{B-39}$$

$$A = \frac{2L^2 h_f}{r k_w} \quad , \tag{B-40}$$

and

$$B = \frac{I^2 \bar{R}_w L}{\pi r^2 k_w} \quad . \tag{B-41}$$

T_w is the local wire temperature and T_∞ is the ambient fluid temperature. Assume the boundary conditions for the wire are a symmetric temperature distribution,

so,

$$@ \quad \eta = 0, \quad \frac{d\theta_w}{dy} = 0 \quad , \tag{B-42}$$

and that the end of wire is at ambient temperature since it is attached to the thick (compared to the wire diameter) steel support at ambient temperature,

so,

$$@ \ \eta = \pm 0.5, \ \theta_w = 0 \ . \tag{B-43}$$

Solving the above ordinary, second order, linear differential equation gives for the temperature distribution,

$$\theta_w = \frac{B}{A}\left[1 - \frac{\left(e^{\sqrt{A}\eta} + e^{-\sqrt{A}\eta}\right)}{\left(e^{\sqrt{A}/2} + e^{-\sqrt{A}/2}\right)}\right] \ . \tag{B-44}$$

The mean wire temperature is

$$\bar{\theta}_w = \frac{B}{A}\left[1 - \frac{2}{\sqrt{A}}\,\frac{\left(e^{\sqrt{A}/2} - e^{-\sqrt{A}/2}\right)}{\left(e^{\sqrt{A}/2} + e^{-\sqrt{A}/2}\right)}\right] . \qquad \text{(B-45)}$$

In solving these equations the mean wire temperature and velocity will be given, and the wire current is found from

$$I_w = \sqrt{\frac{|B|\pi r^2 k_w}{\bar{R}_w L}} , \qquad \text{(B-46)}$$

where B is calculated from equation (B-45).

b) The mean wire resistance as a function of the mean wire temperature,

for $$T_w = T_w(x) , \qquad \text{(B-47)}$$

and $$dR = \frac{\rho_r dx}{\pi r^2}\left[1 + \alpha(T_w - T_r)\right] , \qquad \text{(B-48)}$$

is $$\bar{R}_w = \int_{-L/2}^{L/2} dR . \qquad \text{(B-49)}$$

With the mean wire temperature,

$$\bar{T}_w = \frac{1}{L}\int_{-L/2}^{L/2} T_w\, dx , \qquad \text{(B-50)}$$

then the mean wire resistance is

$$\bar{R}_w = \bar{R}_r \left[1 + \alpha(\bar{T}_w - \bar{T}_r) \right] . \qquad \text{(B-51)}$$

c) The heat transfer from the wire is

(i) the conduction at both ends,

$$q_{cond} = 2\pi r^2 k_w \left. \frac{\partial T_w}{\partial x} \right|_{x = L/2} , \qquad \text{(B-52)}$$

with

$$\left. \frac{\partial T_w}{\partial x} \right|_{x=L/2} = \frac{B}{L\sqrt{A}} \left[\frac{-e^{\sqrt{A}/2} + e^{-\sqrt{A}/2}}{e^{\sqrt{A}/2} + e^{-\sqrt{A}/2}} \right] , \qquad \text{(B-53)}$$

(ii) the convection,

$$q_{conv} = 2\pi r L h_f (\bar{T}_w - T_\infty) , \qquad \text{(B-54)}$$

(iii) and the radiation,

$$q_{rad} = 2\pi r L \epsilon \sigma (\bar{T}_w^4 - T_\infty^4) , \qquad \text{(B-55)}$$

with $\epsilon = 1.0$.

$\bar{T}$ was obtained without including radiation. The radiation calculation is included only to show, as it does in the results, that radiation may be neglected in the analysis.

d) The heat generated by the wire is

$$q_{gen} = I^2 \bar{R}_w = q_{conv} + q_{cond} . \qquad \text{(B-56)}$$

e) The convection coefficients for infinite wires, in terms of the film temperature T_f, are for free convection from Holman (6),

$$Nu_f = (Pr_f\, Gr_f)^{1/12.5} , \tag{B-57}$$

for $$10^{-5} < Pr_f\, Gr_f < 1 ,$$

where

the Nusselt number, $$Nu_f = \frac{h_f d}{k_f} , \tag{B-58}$$

the Grashof number, $$Gr_f = \frac{g}{T_f} \frac{(T_w - T_\infty)}{\nu_f^2} d^3 , \tag{B-59}$$

the Prandtl number, $$Pr_f = \frac{\mu_f c_{Pf}}{k_f} , \tag{B-60}$$

and the film temperature, $$T_f = \frac{T_w + T_\infty}{2} ; \tag{B-61}$$

and for free convection from Collis and Williams (1),

$$Nu_f \left(\frac{T_f}{T_\infty}\right)^{-0.17} = 0.24 + 0.56\, (Re_f)^{0.45} , \tag{B-62}$$

for $$0.02 < Re_f < 44 , \tag{B-63}$$

where

the Reynolds number, $$Re_f = \frac{ud}{\nu_f} . \tag{B-64}$$

The air density using the equation of state is

$$\rho = \frac{P}{RT} \quad . \tag{B-65}$$

The thermal conductivity of air is a polynomial fit of data from reference 21,

$$k = 1.329 \times 10^{-4} + 3.190 \times 10^{-5} T$$

$$- 7.730 \times 10^{-9} T^2 \left[\frac{BTU}{ft\text{-}hr\text{-}^oF}\right] \quad , \tag{B-66}$$

for $400\ ^oR < T < 800\ ^oR$.

The air viscosity, from Sutherland's Law (21), is

$$\frac{\mu}{\mu_o} = \left(\frac{T}{T_o}\right)^{3/2} \frac{T_o + S_1}{T + S_1} \quad , \tag{B-67}$$

with

$$S_1 = 110\ ^oK \quad ,$$

$$\mu_o = 0.350 \times 10^{-6} \frac{lbf - sec}{ft^2} \quad ,$$

$$T_o = 0\ ^oC \quad .$$

f) The hot wire damping is found from the solution of the transient energy balance of a wire element, assuming convection heat transfer only, and an oscillatory ambient temperature.

It is

$$\xi = \frac{1}{\sqrt{1+(2\pi b)^2}} \quad , \tag{B-68}$$

where

$$b = \frac{\rho d_p \omega}{8\pi h_f} \quad , \tag{B-69}$$

and ω is the excitation frequency.

g) The current sensitivity is calculated by the finite difference technique, for example,

$$\left.\frac{\partial I}{\partial T_w}\right|_n = \frac{I_{n+1} - I_{n-1}}{T_{w_{n+1}} - T_{w_{n-1}}} \quad , \tag{B-70}$$

where

$$T_{w_{n+1}} = T_{w_n} + 0.5 \quad , \tag{B-71}$$

and

$$T_{w_{n-1}} = T_{w_n} - 0.5. \tag{B-72}$$

Similarly, $\frac{\partial I}{\partial T_\infty}$, $\frac{\partial I}{\partial V}$, and $\frac{\partial \bar{R}_w}{\partial T_w}$ were calculated.

h) The current, without conduction end losses, for convection alone is

$$I = \sqrt{q_{conv}/\bar{R}_w} \quad . \tag{B-73}$$

i) Another end loss correction taken from reference 12 was used as a check of the previously presented method of calculation. It is expressed as the fraction of heat lost due to conduction,

$$\zeta = \frac{1}{\sqrt{0.475}}\left(\frac{d}{L}\right)^{3/4}\left(\frac{k_w}{k_f}\right)^{1/2}\left(Re_{f,L}\right)^{-\frac{1}{4}}\left(1-t\right)^{\frac{1}{2}}, \qquad \text{(B-74)}$$

with $$t = \frac{\bar{T}_w - T_\infty}{\bar{T}_w + \alpha^{-1}}, \qquad \text{(B-75)}$$

and $$Re_{f,L} = \frac{uL}{\nu_f}. \qquad \text{(B-76)}$$

Method of Solution. The method of solution is to input a mean wire temperature, $\bar{T}_w$, an ambient fluid temperature, T_∞, and a probe velocity, V, and then solve for the wire current, I_w, and the other properties mentioned previously and shown in the sample output. The input probe velocity is reduced to a normal component,

$$v_n = V \cos(45^o), \qquad \text{(B-77)}$$

for the calculations. The current is calculated for one wire, then assuming the two wires in the v-probe are identical the current for the probe is calculated (since the two wires are in a parallel circuit),

$$I_p = 2I_w. \qquad \text{(B-78)}$$

The probe current (in amps) is assumed equal to the shunt voltage, E_s (in volts), because the shunt resistance, $R_s = 1.00\Omega$, and because, refer to Figure 49,

$$R_5 + R_6 >> R_p + R_7, \qquad \text{(B-79)}$$

so the shunt current is essentially the probe current.

Computer Program and Sample Output. The computer program with sample results for the hot wire analysis is shown in the following pages. The important results are discussed in the text.

The tabulated printed output page contains the significant input variables and the calculated results.

```
C
C      HOT WIRE CHARACTERISTICS PROGRAM
C
       DIMENSION ETA(10),THETA(10),TEMP1(10),VEL(10),TEMP2(10),
      1          RBAR(10)
       REAL MUF,KVISF,I1,I2,I3,I4,I5,I6,NUF,L
C
    1  READ(5,1000) ALPHA,TR,RESIST,WCOND,RADIUS,PR,L,PINF
 1000  FORMAT (6E10.4)
    2  WRITE(6,2000)
 2000  FORMAT ('1'26X'HOT  WIRE  CHARACTERISTICS'//)
    3  WRITE(6,2010) ALPHA,TR,RESIST,RADIUS,L,WCOND,PR,PINF
 2010  FORMAT (6X'ALPHA(1/DEGF)  = 'E10.4,9X'REF TEMP(DEGF) = 'E10.4/
      1         6X'RF RESIST(OHM) = 'E10.4/
      2         6X'RADIUS(FT)     = 'E10.4,9X'LENGTH(FT)      = 'E10.4/
      3         6X'TH COND(B/HFD) = 'E10.4,9X'PRANDTL NO      = 'E10.4/
      4         6X'ATM P(IN HG)   = 'E10.4)
    4  READ(5,1000,END=3000) TW,TINF,V
       WRITE(6,2020) TW,TINF,V
 2020  FORMAT (1X/6X'WIRE T(DEGF)   = 'E10.4,9X'AMB T(DEGF)     = 'E10.4/
      1          6X'PRB VEL(FT/S)  = 'E10.4)
       TINF = TINF+459.7
       TW = TW+459.7
       VN = V*COS(45/57.3)
       THBAR = TW-TINF
       RBAR1 = RESIST*(1.+ALPHA*(TW-459.7-TR))
       WRITE(6,2030) THBAR,RBAR1
 2030  FORMAT(1X/6X'THETA BR(DEGF) = 'E10.4,9X'MEAN R(OHMS)   = ,E10.4)
       TF = (TW+TINF)/2
       MUF = 0.350/10**6*(TF/492)**1.5*690./(TF+198)
       RHOF = 0.041206*PINF/TF
       KVISF= MUF/RHOF
       D = RADIUS*2
       REF = VN*D/KVISF
       GRF = 32.2/TF*THBAR/KVISF**2*D**3
       WRITE(6,2040) TF,MUF,RHOF,KVISF,REF,GRF
 2040  FORMAT (1X/6X'FILM T(DEGR)   = 'E10.4,9X'FLM VIS(PS/F2) = 'E10.4/
      1          6X'FL DEN(PS2/F4) = 'E10.4,9X'FL KVIS(F2/S)  = 'E10.4/
      2          6X'FL RE NO       = 'E10.4,9X'FL GR NO       = 'E10.4)
       IF(V.GT.0.) GO TO 5
       NUF = (PR*GRF)**0.08
       GO TO 6
    5  NUF = (0.240+0.56*REF**0.45)*(TF/TINF)**0.17
    6  FCOND = 1.329/10**4+3.190/10**5*TF-7.730/10**9*TF**2
       HF = NUF*FCOND/D
       WRITE(6,2050) NUF,FCOND,HF
 2050  FORMAT (1X/6X'NUSSELT NO     = 'E10.4,9X'FL COND(B/FHF) = 'E10.4/
      1          6X'FILM H(B/HF2F) = 'E10.4)
       A = 2*L**2*HF/RADIUS/WCOND
       SQA = SQRT(ABS(A))
       DENOM = EXP(SQA/2)+EXP(-SQA/2)
       B = THBAR*A/(1-2/SQA*(EXP(SQA/2)-EXP(-SQA/2))/DENOM)
       APR = 3.14159*RADIUS**2
       I1 = SQRT(ABS(B)/3.413*APR*WCOND/RBAR1/L)
       I2 = 2*I1
       WRITE(6,2060) I1,I2
```

```
2060 FORMAT (1X//6X'CURRENT(AMPS), HEAT TRANSFER, WIRE TEMP DIST,'/
    1            6X'AND SENSITIVITY WITH ESTIMATED COND END EFFECT'/
    2           6X'1 WIRE I       = 'E10.4,9X'2 WIRE(PRB) I  = 'E10.4)
     QCOND = -2*APR*WCOND*B/L/SQA*(-EXP(SQA/2)+EXP(-SQA/2))/DENOM
     QCONV = 2*3.14159*RADIUS*L*HF*THBAR
     QGEN = I1**2*RBAR1*3.413
     QRAD = 2*3.14159*RADIUS*L*0.1714/10**8*(TW**4-TINF**4)
     WRITE(6,2070) QCOND,QCONV,QGEN,QRAD
2070 FORMAT (1X/6X'Q COND(BTU/HR) = 'E10.4,9X'Q CONV(BTU/HR) = 'E10.4/
    1           6X'Q GEN(BTU/HR)  = 'E10.4,9X'Q RAD(BTU/HR)  = 'E10.4)
     WRITE(6,2090)
2090 FORMAT (/11X'ETA'6X'THETA WIRE'15X'FREQUENCY'3X'AMPLITUDE,/
    1         22X'(DEG F)'18X'(CPS)'5X'REDUCTION')
     RHOW = 0.322
     CP = 0.105
     DO 8 I=1,6
     ETA(I) = 0.1*(I-1)
     THETA(I) = B/A*(1-(EXP(SQA*ETA(I))+EXP(-SQA*ETA(I)))/DENOM)
     FREQ = 10**((I-1.)/2.)
     B2 = D*RHOW*CP*FREQ*3600/4/HF*1728
     AR = 1/SQRT(1+(2*3.14159*B2)**2)
   8 WRITE(6,2100) ETA(I),THETA(I),FREQ,AR
2100 FORMAT (5X,2E12.4,13X,2E12.4)
     DO 18 I=1,6
     IF(I-2) 11,11,12
  11 TEMP1(I)= I-1.5+TW
     TEMP2(I) = TINF
     VEL(I) = VN
     GO TO 15
  12 IF(I-4) 13,13,14
  13 TEMP1(I) = TW
     TEMP2(I) = I-3.5+TINF
     VEL(I) = VN
     GO TO 15
  14 TEMP1(I) = TW
     TEMP2(I) = TINF
     VEL(I) = (I-5.5+V)*COS(45/57.3)
  15 THBAR = TEMP1(I)-TEMP2(I)
     RBAR(I) = RESIST*(1+ALPHA*(TEMP1(I)-459.7-TR))
     TF = (TEMP1(I)+TEMP2(I))/2
     MUF = 0.350/10**6*(TF/492)**1.5*690./(TF+198)
     RHOF = 0.041206*PINF/TF
     KVISF = MUF/RHOF
     REF = VEL(I)*D/KVISF
     GRF = 32.2/TF*THBAR/KVISF**2*D**3
     IF(V.GT.0.) GO TO 16
     NUF = (PR*GRF)**0.08
     GO TO 17
  16 NUF = (0.240+0.56*REF**0.45)*(TF/TINF)**0.17
     FCOND = 1.329/10**4+3.190/10**5*TF-7.730/10**9*TF**2
  17 HF = NUF*FCOND/D
     QCONV = 2*3.14159*RADIUS*L*HF*THBAR
     A = 2*L**2*HF/RADIUS/WCOND
     SQA = SQRT(ABS(A))
     DENOM = EXP(SQA/2)+EXP(-SQA/2)
     B = THBAR*A/(1-2/SQA*(EXP(SQA/2)-EXP(-SQA/2))/DENOM)
  18 THETA(I) = SQRT(ABS(B)/3.413*APR*WCOND/RBAR/L)
```

```
      DIDTW = (THETA(2)-THETA(1))/(TEMP1(2)-TEMP1(1))
      DIDTA = (THETA(4)-THETA(3))/(TEMP2(4)-TEMP2(3))
      DIDV = THETA(6)-THETA(5)
      DRWDTW = RBAR(2)-RBAR(1)
      DIDTW2 = 2*DIDTW
      DIDTA2 = 2*DIDTA
      DIDV2 = 2*DIDV
      WRITE(6,2140) DIDTW2,DIDV2,DIDTA2,DRWDTW
 2140 FORMAT (1X/6X'DERIVATIVES OF CURRENT (SENSITIVITY)'/
     1            6X'DIDTW2(A/DF)    = 'E10.4,9X'DIDV2(A/F/S)    = 'E10.4/
     2            6X'DIDTA2(A/DF)    = 'E10.4,9X'DRWDTW(OHM/DF) = 'E10.4)
      I3 = SQRT(QCONV/RBAR1/3.413)
      I4 = 2*I3
      WRITE(6,2080) I3,I4
 2080 FORMAT (1X/6X'CURRENT(AMPS) WITH NO END LOSS'/
     1            6X'1 WIRE I        = 'E10.4,9X'2 WIRE(PRB) I   = 'E10.4)
      REFL = REF*L/D
      T = THBAR/(TW-459.7+1/ALPHA)
      R1 = WCOND/FCOND
      IF(V.GT.0.) GO TO 9
      ZETA = 0.1
      GO TO 10
    9 ZETA = 1/0.475**0.5*(D/L)**0.75*R1**0.5/REFL**0.25*(1-T)**0.5
   10 WRITE(6,2120) REFL,T,ZETA
 2120 FORMAT (1X/6X'CURRENT(AMPS) WITH TN2117 COND END EFFECT'/
     1            6X'REFL            = 'E10.4,9X'W COND/FL-COND = 'E10.4/
     2            6X'ZETA(LOSS FRAC)= 'E10.4)
      I5 = SQRT(QCONV/RBAR1/3.413*(1+ZETA))
      I6 = 2*I5
      WRITE(6,2130) I5,I6
 2130 FORMAT (6X'1 WIRE I       = 'E10.4,9X'2 WIRE(PRB) I   = 'E10.4)
      GO TO 2
 3000 STOP
      END
```

HOT WIRE CHARACTERISTICS

ALPHA(1/)DEGF)	=	.2270-02	REF TEMP(DEGF)	=	.3200+02
OF RESIST(OHMS)	=	.1100+01			
RADIUS(FT)	=	.4160-04	LENGTH(FT)	=	.1850-01
TH COND(B/HFD)	=	.4750+02	PRANDTL NO	=	.7100+00
ATM P(IN HG)	=	.3000+02			
WIRE T(DEGF)	=	.2660+03	AMB T(DEGF)	=	.7000+02
PRB VEL(FT/S)	=	.0000			
THETA BR(DEGF)	=	.1960+03	MEAN R(OHMS)	=	.1787+01
FILM T(DEGR)	=	.6277+03	FLM VIS(PS/F2)	=	.4215-06
FL DEN(PS2/F4)	=	.1969-02	FL KVIS(F2/S)	=	.2140-03
FL RE NO	=	.0000	FL GR NO	=	.1264-03
NUSSELT NO	=	.4745+00	FL COND(B/FHF)	=	.1711-01
FILM H(B/HF2F)	=	.9759+02			

CURRENT(AMPS), HEAT TRANSFER, WIRE TEMP DIST,
AND SENSITIVITY WITH ESTIMATED COND END EFFECT

1 WIRE I	=	.1518+00	2 WIRE(PRB) I	=	.3036+00
Q COND(BTU/HR)	=	.4806-01	Q CONV(BTU/HR)	=	.9249-01
Q GEN(BTU/HR)	=	.1405+00	Q RAD(BTU/HR)	=	.1646-02

ETA	THETA WIRE (DEG F)	FREQUENCY (CPS)	AMPLITUDE REDUCTION
.0000	.2654+03	.1000+01	.9625+00
.1000+00	.2598+03	.3162+01	.7467+00
.2000+00	.2409+03	.1000+02	.3346+00
.3000+00	.2022+03	.3162+02	.1116+00
.4000+00	.1302+03	.1000+03	.3548-01
.5000+00	.8876-05	.3162+03	.1123-01

DERIVATIVES OF CURRENT (SENSITIVITY)

DIDTW2(A/DF)	=	.7887-03	DIDV2(A/F/S)	=	.0000
DIDTA2(A/DF)	=	-.8537-03	DRWDTW(OHM/DF)	=	.2937-02

CURRENT(AMPS) WITH NO END LOSS

1 WIRE I	=	.1231+00	2 WIRE(PRB) I	=	.2463+00

CURRENT(AMPS) WITH TN2117 COND END EFFECT

REFL	=	.3056+02	W COND/FL-COND	=	.3060+00
ZETA(LOSS FRAC)	=	.1000+00			
1 WIRE I	=	.1291+00	2 WIRE(PRB) I	=	.2583+00

HOT WIRE CHARACTERISTICS

ALPHA(1/DEGF) =	.2670-02	REF TEMP(DEGF) =	.3200+02
RF RESIST(OHM) =	.1100+01		
RADIUS(FT) =	.4160-04	LENGTH(FT) =	.1850-01
TH COND(B/HFD) =	.4750+02	PRANDTL NO =	.7100+00
ATM P(IN HG) =	.3000+02		
WIRE T(DEGF) =	.2660+03	AMB T(DEGF) =	.7000+02
PRB VEL(FT/S) =	.5000+01		
THETA BR(DEGF) =	.1960+03	MEAN R(OHMS) =	.1787+01
FILM T(DEGR) =	.6277+03	FLM VIS(PS/F2) =	.4215-06
FL DEN(PS2/F4) =	.1969-02	FL KVIS(F2/S) =	.2140-03
FL RE NO =	.1375+01	FL GR NO =	.1264-03
NUSSELT NO =	.9121+00	FL COND(B/FHF) =	.1711-01
FILM H(B/HF2F) =	.1876+03		

CURRENT(AMPS), HEAT TRANSFER, WIRE TEMP DIST,
AND SENSITIVITY WITH ESTIMATED COND END EFFECT

1 WIRE I =	.1969+00	2 WIRE(PRB) I =	.3937+00
Q COND(BTU/HR) =	.5462-01	Q CONV(BTU/HR) =	.1778+00
Q GEN(BTU/HR) =	.2364+00	Q RAD(BTU/HR) =	.1646-02

ETA	THETA WIRE (DEG F)	FREQUENCY (CPS)	AMPLITUDE REDUCTION
.0000	.2514+03	.1000+01	.9894+00
.1000+00	.2482+03	.3162+01	.9073+00
.2000+00	.2365+03	.1000+02	.5637+00
.3000+00	.2082+03	.3162+02	.2110+00
.4000+00	.1441+03	.1000+03	.6809-01
.5000+00	.1553-04	.3162+03	.2158-01

DERIVATIVES OF CURRENT (SENSITIVITY)

DIDTW2(A/DF) =	.1059-02	DIDV2(A/F/S) =	.1083-01
DIDTA2(A/DF) =	-.9506-03	DRWDTW(OHM/DF) =	.2937-02

CURRENT(AMPS) WITH NO END LOSS

1 WIRE I =	.1734+00	2 WIRE(PRB) I =	.3469+00

CURRENT(AMPS) WITH TN2117 COND END EFFECT

REFL =	.3362+03	W COND/FL-COND =	.3060+00
ZETA(LOSS FRAC) =	.2583+00		
1 WIRE I =	.1945+00	2 WIRE(PRB) I =	.3891+00

Galvanometer and Filter

A simple low pass filter is attached to the galvanometer, to dampen oscillations which made the bridges difficult to balance. Also resistances were added in series to the galvanometer to reduce its sensitivity, see Figure 54, with

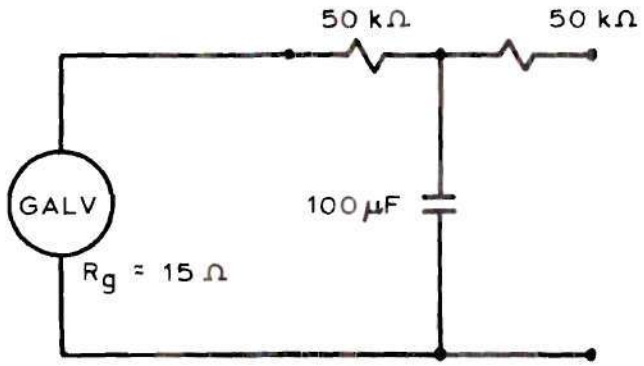

Figure 54. Galvanometer and Filter.

these results:

a) galvanometer sensitivity (above) is 0.212 $\frac{\mu V}{mm}$,

b) galvanometer sensitivity with 100 KΩ series resistance is 0.486 $\frac{mV}{mm}$,

c) filter time constant $\tau = RC = 5$ seconds.

Calibration

To use the hot wire anemometer, the calibration of the velocity as a function of ambient temperature and shunt voltage for a fixed wire temperature, and the

velocity reference angle with respect to the probe axis, Ψ_o, were needed. This section presents the method of calibration, and the final results are presented in the text.

Reference Line for Probe Angle

The probe reference line was defined as the intersection of a plane perpendicular to the probe shaft and the plane parallel to and intersecting the center of the "U" shaped bend in the probe shaft shown in Figure 48. Ideally this reference line would coincide with the velocity vector when the direction bridge is balanced.

The angle between the velocity vector and the probe reference line was determined in a small wind tunnel by rotating the probe into the velocity vector until its direction bridge was balanced. The error between the probe reference line and the velocity vector was the velocity reference angle. The wind tunnel was one-dimensional with a $3\frac{1}{2}$ x $3\frac{1}{2}$ inch cross section. The probe direction was the angle between the probe reference line and the wind tunnel wall, measured in the horizontal plane.

The results of the velocity reference angle calibration are presented in Figure 12 in the text. Table 2 presents a sample of the calibration data.

To assure accurate transfer of the probe reference line when taking data in the vortex generator, a reference pointer was mounted on the shaft of the probe. It was aligned using parallel blocks on a flat surface.

Velocity Magnitude

To calibrate the velocity versus shunt voltage and ambient temperature, a three foot radius, variable speed, horizontally rotating arm, shown in Figures 8

and 55, was built.

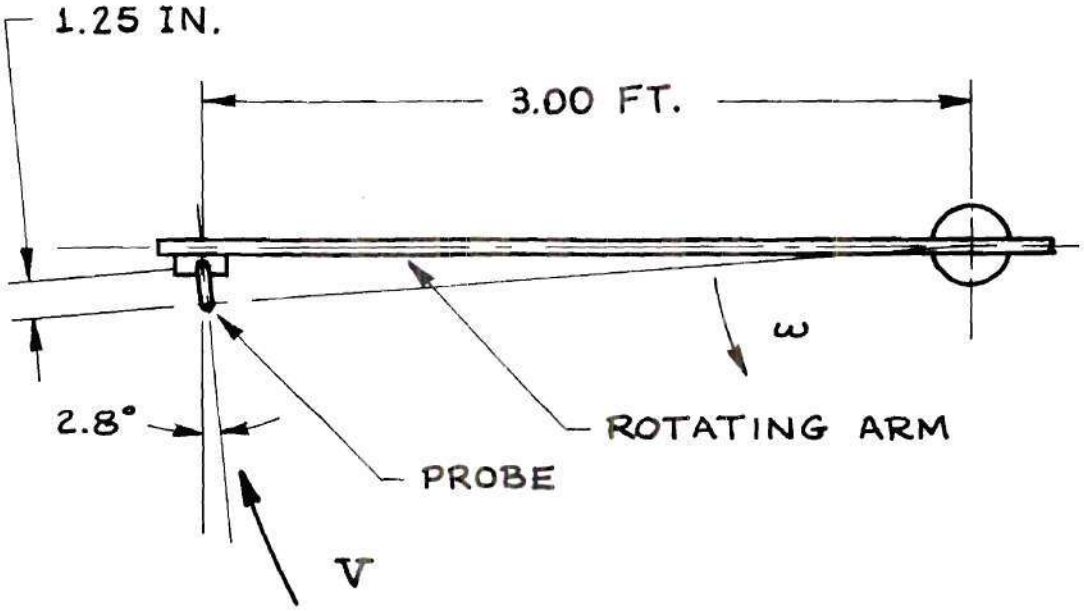

Figure 55. Probe Velocity Calibration Mounting.

The probe was mounted on the rotating arm pointing inward 2.8 degrees from the tangent in order to have the velocity direction at the "V"coincident with the probe reference angle during calibration. The probe was calibrated at several velocities and ambient temperatures. Table 3 shows a sample of the recorded data. The final results are presented in the text.

Table 2. Sample Hot Wire Velocity Direction Calibration

Run Using Small Wind Tunnel

(Run 55, September 29, 1971)

Data Pt.	T_r (^oF)	E_s (Volts)	Fan Setting	ΔU (mV)	Ψ (deg)	Vel. (ft/sec)
1	88.0	0.2584	0	0	0	0
2		0.3415	50	+0.7	0	4.18
3				+3.0	+5.0	
4				+5.5	+10.0	
5				+10.9	+20.0	
6				+16.2	+30.0	
7				+ 1.0	0	
8				- 1.0	- 5.0	
9				- 3.3	-10.0	
10				- 8.5	-20.0	
11				-14.5	-30.0	
12	88.0	0.3415	50	+ 0.9	0	4.18

Table 3. Sample Hot Wire Velocity Magnitude Calibration

Run on Rotating Arm.

(Run 44, September 9, 1971)

Data Pt.	Mtr. Set	Arm Cyc.	Sec.	V (ft/sec)	E_s (volts)	T_r (°F)
1	0	0		0	0.2615	85.0
2	16	-				
3	20	3.00	34.8	1.62	0.3076	88.0
4	30	10.00	52.1	3.62	0.3363	88.1
5	40	15.0	48.3	5.86	0.3582	88.2
6	50	25.0	56.0	8.41	0.3775	88.3
7	60	35.0	59.1	11.14	0.3942	88.3
8	70	50.0	64.4	14.62	0.4107	88.4
9	60	40.0	64.9	11.61	0.3961	88.5
10	50	30.0	65.2	8.66	0.3783	88.6
11	40	20.0	62.8	6.01	0.3591	88.7
12	30	10.0	51.4	3.67	0.3365	89.0
13	20	5.0	48.6	1.94	0.3120	89.2
14	0	0		0	0.2589	89.4

APPENDIX C

DATA REDUCTION DETAILS

This appendix is composed of the calculations, including the digital computer program, used to reduce the measured data to velocity profiles and surface shear stress, the plotted velocity profiles of the tests not presented in the text, and the plotted freestream velocities and boundary layer thicknesses of the tests not presented in the text.

Data Reduction Programs

The vortex generator data reduction programs consist of three programs and several supporting subroutines. The principal program, called the Vortex Generator Data Reduction Program, reduces the input recorded data to surface shear stresses and velocity profiles and outputs the results into semi-permanent computer storage. The second program, called the Write Program, reads the reduced data from storage and prints it at either a remote terminal or at a batch printer which prints large volumes of printed output faster than the remote terminal. The third program, called the Plot Program, reads the reduced data from storage and makes specified plots of the velocity profiles at the Mechanical Engineering Department's remote plotting terminal. The programs are written in Fortran V and are run on the Univac 1108 computer. The program calculations and program listing with sample output follow.

Vortex Generator Data Reduction Program Operations

From the input measured data for each test, namely,

Φ_o - the probe reference angle,

r_1 - the radius at the probe shaft location,

z - the probe "V" height,

$\Phi_i(r_1, z)$ - the indicated velocity direction,

$V_s(r_1, z)$ - the indicated hot wire shunt voltage,

$T_r(r_1, z)$ - the ambient temperature, and

Δp - the Preston tube pressure differential,

the following significant data are calculated,

$\Phi(r_1, z)$ - the velocity direction,

$V(r_1, z)$ - the velocity magnitude,

$v_r(r_1, z)$ - the radial velocity (+ inward),

$v_t(r_1, z)$ - the tangential velocity (+ clockwise) , and

$\tau_w(r_1)$ - the surface shear stress.

This task is performed in three subroutines called

1) Subroutine VPDR which calculates the velocity magnitude, direction, and components at the true radius with respect to the vortex center,

2) Subroutine PTAU which calculates the surface shear stress magnitude using the Preston tube pressure difference, and

3) Subroutine VTAU which calculates the surface shear stress magnitude and direction using the velocity magnitude and direction profiles.

These program units are discussed next.

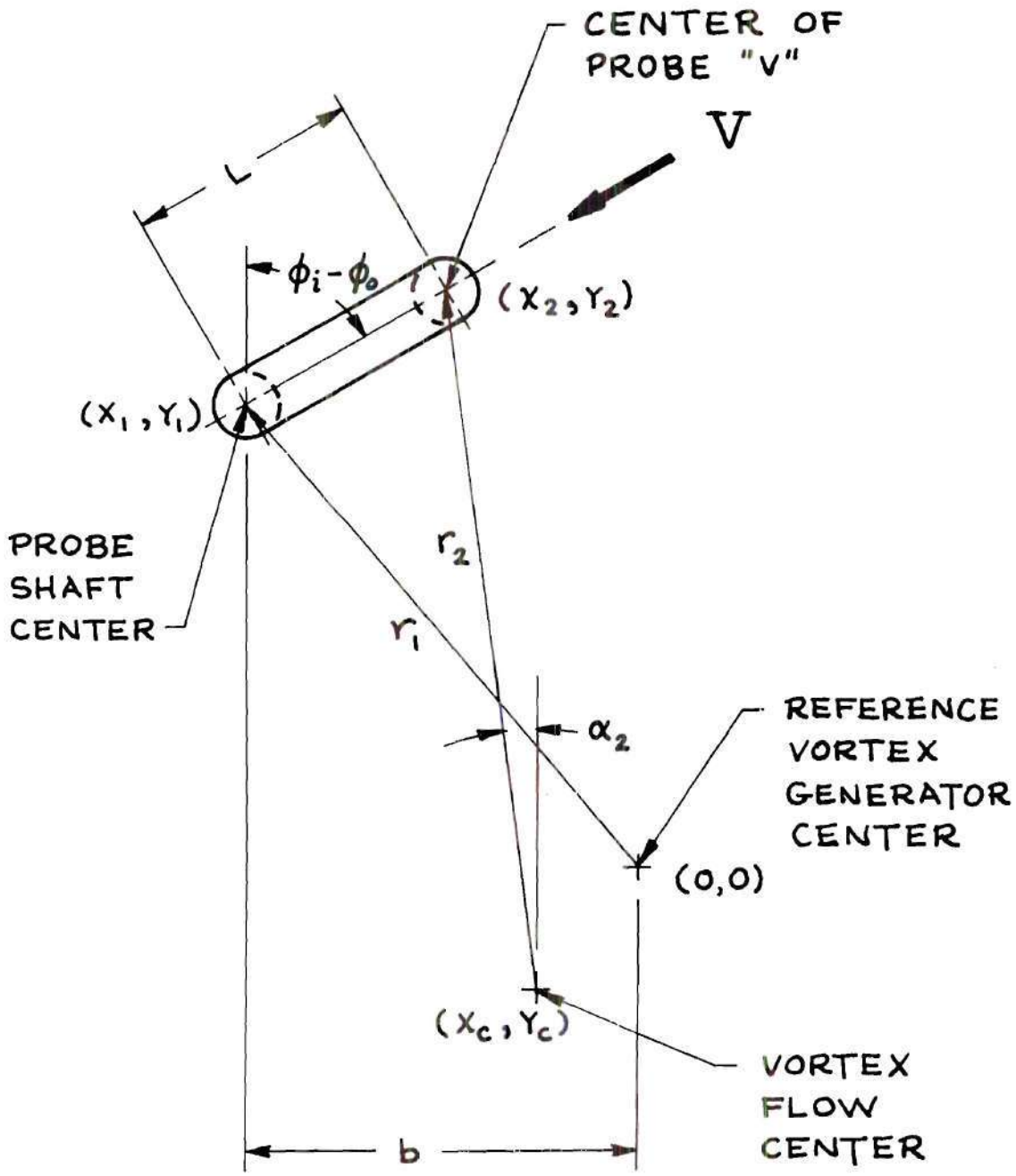

Figure 56. Geometry in Data Reduction for Probe Position with Respect to the True Vortex Axis.

The input data first goes into Subroutine VPDR to calculate $V(r_2, z)$, $\Phi(r_2, z)$, $v_r(r_2, z)$, $v_t(r_2, z)$, and r_2 where r_2 is the true radius with respect to the vortex center The following calculations are performed.

1) The position and velocity direction are calculated, including corrections for the probe "U" bend in the shaft and for a vortex flow center different from the reference vortex generator center. The equations for the calculations, refer to Figure 56, are

$$x_1 = -b \quad , \tag{C-1}$$

$$y_1 = \sqrt{r_1^2 - b^2} \quad , \tag{C-2}$$

$$x_2 = -b + L \sin(\Phi_i - \Phi_o) \, , \tag{C-3}$$

$$y_2 = y_1 + L \cos(\Phi_i - \Phi_o) \, , \tag{C-4}$$

$$r_2 = \sqrt{(x_2 + x_c)^2 + (y_2 + y_c)^2} \quad , \tag{C-5}$$

$$\alpha_2 = \tan^{-1} \left| \frac{-x_2 + x_c}{y_2 - y_c} \right| \quad , \tag{C-6}$$

$$\Phi = \Phi_i - \Phi_o + \alpha_2 \, . \tag{C-7}$$

2) The velocity magnitude is calculated using the equation derived from the calibration, refer to Figure 11,

$$E_s \Big|_{T=80} = E_s \left| \left(\frac{T_w - 80}{T_w - T} \right)^{0.61} \right|_T \quad , \tag{C-8}$$

$$V = \sum_{i=1}^{7} c_i \left[\frac{E_s\Big|_{T=80} - 0.266}{10} \right]^i . \qquad \text{(C-9)}$$

The volocity components are calculated from

$$v_r = V \sin \Phi , \qquad \text{(C10)}$$

and

$$v_t = V \cos \Phi . \qquad \text{(C-11)}$$

When the calculations are returned to the main program, the velocities are recalculated at the reference radius, r_1, by interpolation from the set of velocities at r_2 returned by Subroutine VPDR.

The Subroutine PTAU calculates the surface shear stress magnitude, $\tau_w(r_1)$, using the Preston tube pressure difference, Δp. The equations used come from Patel's calibration (17).

with $$x^* = \log_{10}\left[\Delta p \frac{d^2}{4\rho\nu^2} \right] , \qquad \text{(C-12)}$$

for $$0 \leq x^* \leq 2.9 ,$$

$$y^* = \tfrac{1}{2} x^* + 0.037 , \qquad \text{(C-13)}$$

for $$2.9 \leq x^* < 5.6 ,$$

$$y^* = 0.8287 - 0.1381 x^* + 0.1437 x^{*2} - 0.0060 x^{*3} , \qquad \text{(C-14)}$$

and for $$5.6 \leq x^* < 7.6$$

$$x^* = y^* + 2 \log_{10}(1.95\, y^* + 4.10) \quad . \tag{C-15}$$

The last equation is solved using a Newton-Ralphson iterative technique.

Then,

$$\tau_w = \frac{4\rho\nu^2}{d^2} \left[a \log_{10} y^*\right] \quad . \tag{C-16}$$

The Subroutine VTAU calculates the surface shear stress magnitude and direction using the velocity magnitude and direction profiles.

1) The surface shear stress is

$$\tau_w = \mu \left.\frac{\partial V}{\partial z}\right|_{z=0} \quad . \tag{C-17}$$

The velocity slope is calculated by inserting $V(z=0) = 0$ in the velocity profile and fitting a third order least squares curve through the bottom five points of the velocity profile. Thus

$$V(z) = \sum_{i=1}^{4} a_i z^{i-1} \quad , \tag{C-18}$$

and

$$\left.\frac{\partial V}{\partial z}\right|_{z=0} = a_2 \quad . \tag{C-19}$$

2) The surface shear stress direction is calculated by fitting a second order least squares curve through the lowest five points of the velocity direction profile,

so,

$$\Phi(z) = \sum_{i=1}^{3} a_i z^{i-1} . \qquad \text{(C-20)}$$

Then,

$$\Phi(0) = a_1 . \qquad \text{(C-21)}$$

Program Listing and Sample Output

A listing of the entire set of the data reduction programs and a sample of the printed output are presented. Later figures show the plotted output.

```
C
C      VORTEX GENERATOR DATA REDUCTION
C
       DIMENSION COMT1(18),Z(7,39),PHI(7,39),VS(7,39),
      1TR(7,39),V(7,39),VR(7,39),VT(7,39),R2(7,39),VT2(39),
      2VR2(39),R22(39),
      3R1(10),RUN(10),VT3(7,20),VR3(7,20),VTOV(7,20),VROV(7,20),
      4P(10),DP(10),D1(20),VRR(7,20),VTR(7,20),PHII(7,20),
      5D2(20),D3(20),D4(20),PHIO(10),PRTAU(10),VETAU(10),PHIT(10),
      6N2(20),VRRI(7,20),QR(7,20)
C
C      READ DATA - CALCULATE VELOCITIES, DIRECTIONS,
C      AND TRUE RADII.
C
    1  READ(5,1000,END=3000) N1
C      N1 IS THE NUMBER OF RUNS
 1000  FORMAT (2I2)
       READ(5,1010) COMT1
 1010  FORMAT (18A4)
       READ(5,1020) AMST,VANE
       READ(5,1020) XC,YC
       DO 3 I=1,N1
       READ(5,1000) N2(I)
C      N2 IS THE NUMBER OF DATA POINTS PER RUN
       READ(5,1020) RUN(I),R1(I),PHIO(I),DP(I)
 1020  FORMAT (5F10.5)
       N3=N2(I)
       DO 3 J=1,N3
       READ(5,1020) (Z(I,J),PHII(I,J),VS(I,J),TR(I,J))
       Z(I,J)=Z(I,J)+0.030
    3  CALL VPDR(R1(I),PHIO(I),PHII(I,J),VS(I,J),TR(I,J),XC,YC,
      1          V(I,J),PHI(I,J),VR(I,J),VT(I,J),R2(I,J))
C
C      RADIUS CORRECTION -  TO GET RADIUS CORRECTION,
C      ALL RUNS MUST HAVE THE SAME NO. OF DATA POINTS AT THE
C      SAME HEIGHTS, AND THERE MUST BE 2 RUNS OR MORE ARRANGED
C      IN MONOTONICALLY INCREASING RADII.
C
       IF(N1.EQ.1) GO TO 7
       DO 4 I=1,N1
       IF(I.EQ.N1) GO TO 4
       IF(N2(I)-N2(I+1)) 7,4,7
    4  CONTINUE
       N3=N2(1)
       DO 6 J=1,N3
       DO 5 I=1,N1
       K=I
       IF(I.EQ.1) K=2
       IF(R2(K,J).LE.R2(K-1,J)) GO TO 7
       R22(I)=R2(I,J)
       VT2(I)=VT(I,J)
    5  VR2(I)=VR(I,J)
       N4=N1
       IF(N4.GT.3) N4=3
       DO 6 I=1,N1
       VT3(I,J)=AITINT(R22,VT2,N1,R1(I),N4,P)
```

```
    6 VR3(I,J)=AITINT(R22,VR2,N1,R1(I),N4,P)
      GO TO 9
    7 WRITE(6,2070)
 2070 FORMAT (1X'DATA IS NOT CORRECTED FOR RADIUS')
      DO 8 I=1,N1
      N3=N2(I)
      DO 8 J=1,N3
      VT3(I,J)=VT(I,J)
    8 VR3(I,J)=VR(I,J)
C
C     GET MAX VELOCITIES, CALCULATE NONDIMENSIONAL VELOCITIES
C     AND SKIN FRICTION.
C
    9 DO 12 I=1,N1
      N3=N2(I)
      VR3M=VR3(I,1)
      DO 10 K=2,N3
   10 IF(VR3M.LT.VR3(I,K)) VR3M=VR3(I,K)
      DO 11 J=1,N3
      VTOV(I,J)=VT3(I,J)/VT3(I,N3)
      VROV(I,J)=VR3(I,J)/VR3M
      D1(J)=PHI(I,J)
      D2(J)=SQRT(VT3(I,J)**2+VR3(I,J)**2)
      D3(J)=Z(I,J)
      VRR(I,J)=VR3(I,J)*R1(I)/12.
      D4(J)=VRR(I,J)
   11 VTR(I,J)=VT3(I,J)*R1(I)/12.
      PRTAU(I)=PTAU(DP(I),TR(I,1))
      CALL VTAU(D3,D2,D1,N3,TR(I,1),VETAU(I),PHIT(I))
      IF(Z(I,1).LE.0.) GO TO 15
      N3=N3+1
      DO 16 J=N3,2,-1
      D3(J)=D3(J-1)
   16 D4(J)=D4(J-1)
      D3(1)=0.
      D4(1)=0.
   15 DO 12 J=1,N3
      VRRI(I,J)=TRAP1(D3,D4,J)/12.
      QR(I,J)=2*3.14159*60.*VRRI(I,J)
      IF(Z(I,1).GT.0.AND.J.GT.1) VRRI(I,J-1)=VRRI(I,J)
   12 IF(Z(I,1).GT.0.AND.J.GT.1) QR(I,J-1)=QR(I,J)
C
C     OUTPUT OF DATA
C
      WRITE(3,2000) N1
 2000 FORMAT (I2)
      WRITE(3,2010) COMT1
 2010 FORMAT (18A4)
      WRITE(3,2020) AMST,VANE
      WRITE(3,2020) XC,YC
      DO 13 I=1,N1
      WRITE(3,2000) N2(I)
      N3=N2(I)
      WRITE(3,2020) RUN(I),R1(I),PHIO(I),DP(I)
 2020 FORMAT (4E12.4)
      WRITE(3,2030) PRTAU(I),VETAU(I),PHIT(I)
      WRITE(3,2030) (Z(I,J),PHII(I,J),VS(I,J),TR(I,J),J=1,N3)
```

```
2030 FORMAT (4E12.4)
     WRITE(3,2040) (PHI(I,J),V(I,J),VR(I,J),VT(I,J),TR(I,J),
    1               R2(I,J),J=1,N3)
2040 FORMAT (6E12.4)
     WRITE(3,2030) (VT3(I,J),VR3(I,J),VTOV(I,J),VROV(I,J),J=1,N3)
  13 WRITE(3,2030) (VRR(I,J),VTR(I,J),VRRI(I,J),QR(I,J),J=1,N3)
     GO TO 1
3000 ENDFILE 3
     STOP
     END
```

```
C
C      WRITE PROGRAM FOR VORTEX GENERATOR DATA REDUCTION
C      PROGRAM, READS FROM FILE AND WRITES AT PRINTER
C
       DIMENSION COMT1(18),N2(20),RUN(20),R1(20),PHIO(20),DP(20),
      1PRTAU(20),VETAU(20),PHIT(20),Z(7,20),PHII(7,20),VS(7,20),
      2R2(7,20),PHI(7,20),V(7,20),VR(7,20),VT(7,20),TR(7,20),VT3(7,20),
      3VR3(7,20),VTOV(7,20),VROV(7,20),VRR(7,20),VTR(7,20),VRRI(7,20),
      4QR(7,20)
C
       READ(5,1000) NR
C      NR - 00 - REMOTE PRINTOUT
C         - 01 - BATCH PRINTOUT
       READ(3,1000) N1
 1000  FORMAT (I2)
       READ(3,1010) COMT1
 1010  FORMAT (18A4)
       READ(3,1020) AMST,VANE
       READ(3,1020) XC,YC
       DO 1 I=1,N1
       READ(3,1000) N2(I)
       N3=N2(I)
       READ(3,1020) RUN(I),R1(I),PHIO(1),DP(I)
 1020  FORMAT (4E12.4)
       READ(3,1030) PRTAU(I),VETAU(I),PHIT(I)
 1030  FORMAT (4E12.4)
       READ(3,1030) (Z(I,J),PHII(I,J),VS(I,J),TR(I,J),J=1,N3)
       READ(3,1040) (PHI(I,J),V(I,J),VR(I,J),VT(I,J),TR(I,J),
      1              R2(I,J),J=1,N3)
 1040  FORMAT (6E12.4)
       READ(3,1030) (VT3(I,J),VR3(I,J),VTOV(I,J),VROV(I,J),J=1,N3)
    1  READ(3,1030) (VRR(I,J),VTR(I,J),VRRI(I,J),QR(I,J),J=1,N3)
C
       DO 3 I=1,N1
       IF(NR.GT.0) GO TO 2
       WRITE(6,2000)
 2000  FORMAT (1X'ADVANCE TO NEW PAGE, TYPE CR')
       READ(5,1050) CH
 1050  FORMAT (1A6)
    2  N3=N2(I)
       WRITE(6,2010) COMT1
 2010  FORMAT ('1'25X'VORTEX GENERATOR'//18A4)
       WRITE(6,2080) XC,YC
 2080  FORMAT (1X/5X'CENTER OF FLOW WRT GENERATOR CENTER'/
      1         5X'XC = 'F5.2,5X'YC = 'F5.2)
       WRITE(6,2020) RUN(I),R1(I),PHIO(I)
 2020  FORMAT (1X/9X'RUN NO  'F4.0,8X'RADIUS(IN) =  'F4.1,
      18X'PHIO(DEG) =  'F4.1)
       WRITE(6,2030) DP(I),PRTAU(I),VETAU(I),PHIT(I)
 2030  FORMAT (8X'PRESTON DP(PSI) ='F13.4,4X'PREST TAUW(PSI) = 'E10.4/
      1         8X'VEL PRF TAUW(PSI) = 'E10.4,4X'TAUW ANGLE(DEG) = 'E10.4)
       WRITE(6,2040) (Z(I,J),PHII(I,J),VS(I,J),TR(I,J),J=1,N3)
 2040  FORMAT (1X/4X'HEIGHT'5X'IND ANGLE'3X'SHUNT VLT'3X'ROOM TEMP'/
      15X'(IN)'9X'(DEG)'6X'(VOLTS)'5X'(DEG F)'/(4E12.4))
       WRITE(6,2050) (Z(I,J),PHI(I,J),V(I,J),VR(I,J),VT(I,J),
      1R2(I,J),J=1,N3)
```

```
2050 FORMAT (1X/4X'HEIGHT'6X'VEL DIR'5X'VELOCITY'4X'RAD VEL'
    15X'TAN VEL'5X'TRUE RAD'/5X'(IN)'6X'(DEG FROM'4X'(FT/SEC)'
    24X'(FT/SEC)'4X'(FT/SEC)'6X'(IN)'/17X'RAD IN)'/(6E12.4))
     WRITE(6,2060) (Z(I,J),VT3(I,J),VR3(I,J),VTOV(I,J),
    1VROV(I,J),J=1,N3)
2060 FORMAT (1X/5X'CORRECTED FOR RADIUS'/
    14X'HEIGHT'6X'TAN VEL'5X'RAD VEL'4X'VT/VT-INF'3X'VR/VR-MAX'/
    215X'(FT/SEC)'4X'(FT/SEC)'/(5E12.4))
   3 WRITE(6,2070) (Z(I,J),VTR(I,J),VRR(I,J),VRRI(I,J),
    1QR(I,J),J=1,N3)
2070 FORMAT ('1'4X'HEIGHT'8X'VT*R'8X'VR*R'6X'INT VR*R'6X'Q IN'/
    1       5X'(IN)'7X'(SQ F/S)'4X'(SQ F/S)'3X'(CUB FT/S)'4X'(CFM)'/
    2       (5E12.4))
     END
```

```
C
C      PLOT PROGRAM FOR VORTEX GENERATOR DATA REDUCTION
C      PROGRAM, READS FROM FILE AND PLOTS AT PRINTER
C
       DIMENSION COMT1(18),N2(20),RUN(20),R1(20),PHIO(20),DP(20),
      1PRTAU(20),VETAU(20),PHIT(20),Z(7,20),PHII(7,20),VS(7,20),
      2R2(7,20),PHI(7,20),V(7,20),VR(7,20),VT(7,20),TR(7,20),VT3(7,20),
      3VR3(7,20),VTOV(7,20),VROV(7,20),VRR(7,20),VTR(7,20),VRRI(7,20),
      4QR(7,20),VTLAB(10),VRLAB(10),ZLAB(10),VOVLAB(10),UOULAB(10)
      5,NC(10),VTRLAB(10),VRRLAB(10)
       DATA VTLAB/'TAN VEL (FT/SEC)'/,
      1      VRLAB/'RAD VEL (FT/SEC)'/,
      2       ZLAB/'HEIGHT -IN-'/,
      3     VOVLAB/'VT/(VT-INF)'/,
      4     UOULAB/'VR/(VR-MAX)'/,
      5     VTRLAB/'VT*R (SQ F/S)'/,
      6     VRRLAB/'VR*R (SQ F/S)'/
C
       READ(5,1050) (NC(I),I=1,6)
C      FOR PLOTS DESIRED, INPUT NC = 01
C      FOR PLOTS NOT DESIRED, INPUT NC = 00
 1050 FORMAT (10I2)
       READ(3,1000) N1
 1000 FORMAT (I2)
       READ(3,1010) COMT1
 1010 FORMAT (18A4)
       READ(3,1020) AMST,VANE
       READ(3,1020) XC,YC
       DO 1 I=1,N1
       READ(3,1000) N2(I)
       N3=N2(I)
       READ(3,1020) RUN(I),R1(I),PHIO(I),DP(I)
 1020 FORMAT (4E12.4)
       READ(3,1030) PRTAU(I),VETAU(I),PHIT(I)
 1030 FORMAT (4E12.4)
       READ(3,1030) (Z(I,J),PHII(I,J),VS(I,J),TR(I,J),J=1,N3)
       READ(3,1040) (PHI(I,J),V(I,J),VR(I,J),VT(I,J),TR(I,J),
      1              R2(I,J),J=1,N3)
 1040 FORMAT (6E12.4)
       READ(3,1030) (VT3(I,J),VR3(I,J),VTOV(I,J),VROV(I,J),J=1,N3)
    1  READ(3,1030) (VRR(I,J),VTR(I,J),VRRI(I,J),QR(I,J),J=1,N3)
C
       RUN(19)=AMST
       RUN(20)=VANE
       IF(NC(1).LE.0) GO TO 2
       CALL PLOT(VT3,Z,N1,N2,R1,RUN,0.,0.,0.,0.,0.,0.,2.4,1.2,
      1          VTLAB,ZLAB)
    2  IF(NC(2).LE.0) GO TO 3
       CALL PLOT(VR3,Z,N1,N2,R1,RUN,0.,0.,0.833,0.,-2.,0.,2.4,1.2,
      1          VRLAB,ZLAB)
    3  IF(NC(3).LE.0) GO TO 4
       CALL PLOT(VTOV,Z,N1,N2,R1,RUN,0.,0.,0.,0.,0.,0.,0.24,
      1          1.2,VOVLAB,ZLAB)
    4  IF(NC(4).LE.0) GO TO 5
       CALL PLOT(VROV,Z,N1,N2,R1,RUN,0.,0.,0.833,0.,-0.2,0.,0.24,
      1          1.2,UOULAB,ZLAB)
```

```
5 IF(NC(5).LE.0) GO TO 6
  CALL PLOT (VTR,Z,N1,N2,R1,RUN,0.,0.,0.,0.,0.,0.,
 1           2.4,1.2,VTRLAB,ZLAB)
6 IF(NC(6).LE.0) GO TO 7
  CALL PLOT (VRR,Z,N1,N2,R1,RUN,0.,0.,0.833,0.,-1.,0.,
 1           1.2,1.2,VRRLAB,ZLAB)
7 CONTINUE
  END
```

```
      SUBROUTINE PLOT(X,Y,N1,N2,RAD,RUN,BSFX,BXFY,BYFX,BYFY,
     1XMIN,YMIN,XSCALE,YSCALE,IXTITL,IYTITL)
C
C     PLOT ROUTINE FOR VELOCITY PROFILES
C
C     X - X ARRAY, N1 RUNS BY N2 DATA POINTS
C     Y - Y ARRAY
C     RAD,RUN - RADII AND RUNS OF N1 DIMENSION
C     BXFX,BXFY,BYFX,BYFY - BEGINING OF X-AXIS AND Y-AXIS
C     XMIN,YMIN - MINIMUM VALUES OF X AND Y AXIS
C     XSCALE,YSCALE - SCALE OF X AND Y AXIS (UNITS/INCH)
C     IXTITL,IYTITL - TITLES OF X AND Y AXIS
C
      DIMENSION X(7,20),Y(7,20),RAD(10),RUN(20),N2(20),
     1IXTITL(10),IYTITL(10),X2(20),Y2(20),ISYM(10)
      DATA ISYM(1),ISYM(2),ISYM(3),ISYM(4),ISYM(5),ISYM(6),
     1ISYM(7)/'&','\','+','*','.','X','Y'/
      WRITE(6,2010)
 2010 FORMAT (1X'ADVANCE TO NEW PAGE, TYPE CR')
      READ(5,1000) CH
 1000 FORMAT (1A6)
      DO 2 I=1,N1
      IF(I.EQ.1) WRITE(6,2000) RUN(19),RUN(20)
 2000 FORMAT (25X'SYM  RADIUS  RUN'10X'MTR SET   = 'F3.0/
     1         31X'(IN)'16X'VANE(DEG) = 'F4.1)
    2 WRITE(6,2020) ISYM(I),RAD(I),RUN(I)
 2020 FORMAT (26X,1A1,5X,F3.0,3X,F4.0)
      CALL TGPLOT(5.5,0)
      CALL TGORIG(0.8,0.)
      CALL TGAXIS(BXFX,BXFY,5.,XMIN,XSCALE,4,12,2,IXTITL)
      CALL TGAXIS(BYFX,BYFY,5.,YMIN,YSCALE,1,12,2,IYTITL)
      DO 6 I=1,N1
      N3=N2(I)
      DO 4 J=1,N3
      X2(J)=X(I,J)
    4 Y2(J)=Y(I,J)
    6 CALL TGCURV(X2,Y2,N3,XMIN,YMIN,XSCALE,YSCALE,ISYM(I),1)
      CALL TGEND
      RETURN
      END
```

```
      SUBROUTINE VPDR(R1,PHIO,PHII,VS,TR,XC,YC,V,PHI,
     1                VR,VT,R2)
C
C     VORTEX GENERATOR VELOCITY PROFILE DATA REDUCTION
C
      DIMENSION C(10)
      DATA C(1),C(2),C(3),C(4),C(5),C(6),C(7),C(8)/
     10.,.1831063E+01,.5135996E+01,-.9386128E+01,
     2.1342887E+02,-.5632328E+01,-.3675746,.5568272
     3/ETA,TRF,TW,B,RL/0.61,80.,264.,5.125,1.25/
      RPD=3.14159/180.
      Y1=SQRT(R1**2-B**2)
      A1=ATAN((B+XC)/(Y1-YC))/RPD
      PHIP=PHII-PHIO
      X2=B-RL*SIN(PHIP*RPD)
      Y2=Y1+RL*COS(PHIP*RPD)
      R2=SQRT((X2+XC)**2+(Y2-YC)**2)
      A2=ATAN((X2+XC)/(Y2-YC))/RPD
      PHI=PHIP+A2
      DT1=TW-TR
      DT2=TW-TRF
      V=0.
      VS2=VS*(DT2/DT1)**ETA
      DO 1 I=1,8
    1 V=V+C(I)*((VS2-0.266)*10)**(I-1)
      VT=V*SIN(PHI*RPD)
      VR=V*COS(PHI*RPD)
      RETURN
      END
```

```
      FUNCTION PTAU(DP,T)
C
C     CALCULATION OF SKIN FRICTION (PSI) USING PRESTON TUBE
C     DELTA P (PSI)
C
      TDR(X)=X+459.688
      DEN(X)=0.041206*29.92/X
      VIS(X)=0.3170*X**1.5*734.7/(X+216.)/10**10
      IF(DP.LE.0) GO TO 6
      OD=0.0625
      F=OD**2*DEN(TDR(T))/4/VIS(TDR(T))**2
      XSTAR=ALOG10(DP*F)
      IF(XSTAR.LE.2.9) YSTAR=XSTAR/2+0.037
      IF(XSTAR.GT.2.9.AND.XSTAR.LT.5.6)
     1YSTAR=0.8287-0.1381*XSTAR+0.1437*XSTAR**2-0.0060*XSTAR**3
      IF(XSTAR-5.6) 5,1,1
    1 YSTAR=XSTAR/2
      IF(XSTAR.LE.0) YSTAR=1.
      N=0
    2 EL=YSTAR
      A=1.95*YSTAR+4.10
      DXDY=1+3.9*0.43429448/A
      YSTAR=YSTAR-(YSTAR+2*ALOG10(A)-XSTAR)/DXDY
      N=N+1
      IF(ABS(YSTAR-EL)-1/10**5) 5,5,3
    3 IF(N-20) 2,2,4
    4 WRITE(6,2000)
 2000 FORMAT (1X'NUMBER OF ITERATIONS IN PTAU EXCEEDED 20')
    5 PTAU=10**YSTAR/F
      RETURN
    6 PTAU=0.
      RETURN
      END
```

```
      SUBROUTINE VTAU(Z,V,PHI,N,T,TAU,PHIP)
C
C     CALCULATION OF SKIN FRICTION, TAU, (PSI) AND DIRECTION,
C     PHIP, (DEG) FROM THE VELOCITY AND ANGLE PROFILES
C
      DIMENSION Z(20),V(20),W(20),T1(20),T2(20),T3(20),C(20),
     1Z2(20),V2(20),PHI(20),A(20),ALPHA(20),BETA(20)
      TDR(X)=X+459.688
      VIS(X)=0.3170*X**1.5*734.7/(X+216.)/10**10
      N1=N
      IF(V(1)-0.) 1,3,1
    1 DO 2 I=N1,1,-1
      Z2(I+1)=Z(I)
    2 V2(I+1)=V(I)
      Z2(1)=0.
      V2(1)=0.
      N1=N1+1
      GO TO 5
    3 DO 4 I=1,N1
      V2(I)=V(I)
    4 Z2(I)=Z(I)
    5 IF(N1.LE.1) GO TO 6
      IF(N1.GT.5) N1=5
      N2=N1-1
      IF(N2.GT.3) N2=3
      CALL ORTHLS(Z2,V2,W,N1,0,0,C,ALPHA,BETA,N2,T1,T2,T3,IND1)
      CALL COEFS(0,C,ALPHA,BETA,N2,A,T1,T2,T3,IND2)
      TAU=VIS(TDR(T))*A(2)/12.
      N1=N
      IF(N1.GT.5) N1=5
      N2=N1-1
      IF(N2.GT.2) N2=2
      CALL ORTHLS(Z,PHI,W,N1,0,0,C,ALPHA,BETA,N2,T1,T2,T3,IND1)
      CALL COEFS(0,C,ALPHA,BETA,N2,A,T1,T2,T3,IND2)
      PHIP=A(1)
      RETURN
    6 WRITE(6,2000)
 2000 FORMAT (1X'INPUT DATA INSUFFICIENT TO CALCULATE TAU')
      TAU=0.
      PHIP=0.
      RETURN
      END
```

```
      FUNCTION TRAP1(X,Y,N)
C
C     TRAPIZOIDAL INTEGRATION OF Y OVER X.  Y AND X
C     ARE MATCHING ARRAYS OF N POINTS.  X IS INCREASING.
C
      DIMENSION X(N),Y(N)
      TRAP1=0.
      IF(N.EQ.1) GO TO 2
      DO 1 I=2,N
    1 TRAP1=TRAP1+(X(I)-X(I-1))*(Y(I)+Y(I-1))/2
    2 RETURN
      END
```

VORTEX GENERATOR

MOTOR 27 BLADE 60 QF = 12,700 CFM

CENTER OF FLOW WRT GENERATOR CENTER
XC = .00 YC = .00

RUN NO 69. RADIUS(IN) = 6.0 PHI0(DEG) = 64.0
PRESTON DP(PSI) = .7500-04 PREST TAUW(PSI) = .2499-05
VEL PRF TAUW(PSI) = .6232-06 TAUW ANGLE(DEG) = .3204+02

HEIGHT (IN)	IND ANGLE (DEG)	SHUNT VLT (VOLTS)	ROOM TEMP (DEG F)
.6700-01	.6000+02	.3538+00	.7820+02
.7700-01	.6100+02	.3640+00	.7820+02
.9700-01	.6100+02	.3720+00	.7820+02
.1470+00	.7100+02	.3774+00	.7830+02
.2470+00	.7200+02	.3845+00	.7830+02
.5470+00	.9000+02	.3874+00	.7830+02
.1047+01	.1040+03	.3936+00	.7830+02
.2047+01	.1050+03	.3900+00	.7830+02
.3047+01	.9900+02	.3900+00	.7830+02
.4047+01	.9900+02	.3900+00	.7830+02
.6047+01	.1000+03	.3900+00	.7830+02

HEIGHT (IN)	VEL DIR (DEG FROM RAD IN)	VELOCITY (FT/SEC)	RAD VEL (FT/SEC)	TAN VEL (FT/SEC)	TRUE RAD (IN)
.6700-01	.4604+02	.4117+01	.2858+01	.2964+01	.6800+01
.7700-01	.4692+02	.5115+01	.3494+01	.3735+01	.6784+01
.9700-01	.4692+02	.6002+01	.4100+01	.4384+01	.6784+01
.1470+00	.5575+02	.6670+01	.3754+01	.5514+01	.6614+01
.2470+00	.5665+02	.7595+01	.4176+01	.6344+01	.6596+01
.5470+00	.7317+02	.7994+01	.2315+01	.7652+01	.6242+01
.1047+01	.8666+02	.8891+01	.5174+00	.8876+01	.5942+01
.2047+01	.8765+02	.8363+01	.3424+00	.8356+01	.5920+01
.3047+01	.8177+02	.8363+01	.1197+01	.8277+01	.6050+01
.4047+01	.8177+02	.8363+01	.1197+01	.8277+01	.6050+01
.6047+01	.8274+02	.8363+01	.1057+01	.8296+01	.6028+01

CORRECTED FOR RADIUS

HEIGHT	TAN VEL (FT/SEC)	RAD VEL (FT/SEC)	VT/VT-INF	VR/VR-MAX
.6700-01	.3043+01	.3175+01	.3656+00	.6727+00
.7700-01	.4110+01	.4020+01	.4939+00	.8518+00
.9700-01	.4886+01	.4719+01	.5872+00	.1000+01
.1470+00	.5940+01	.3979+01	.7139+00	.8432+00
.2470+00	.6845+01	.4647+01	.8225+00	.9847+00
.5470+00	.7852+01	.2363+01	.9436+00	.5008+00
.1047+01	.8818+01	.5258+00	.1060+01	.1114+00
.2047+01	.8288+01	.3488+00	.9960+00	.7390-01
.3047+01	.8320+01	.1210+01	.9999+00	.2565+00
.4047+01	.8323+01	.1207+01	.1000+01	.2557+00
.6047+01	.8321+01	.1060+01	.1000+01	.2246+00

HEIGHT (IN)	VT*R (SQ F/S)	VR*R (SQ F/S)	INT VR*R (CUB FT/S)	Q IN (CFM)
.6700-01	.1521+01	.1587+01	.4431-02	.1671+01
.7700-01	.2055+01	.2010+01	.5930-02	.2236+01
.9700-01	.2443+01	.2360+01	.9572-02	.3608+01
.1470+00	.2970+01	.1990+01	.1863-01	.7024+01
.2470+00	.3422+01	.2324+01	.3660-01	.1380+02
.5470+00	.3926+01	.1182+01	.8042-01	.3032+02
.1047+01	.4409+01	.2629+00	.1105+00	.4166+02
.2047+01	.4144+01	.1744+00	.1287+00	.4853+02
.3047+01	.4160+01	.6052+00	.1612+00	.6078+02
.4047+01	.4161+01	.6033+00	.2116+00	.7976+02
.6047+01	.4161+01	.5299+00	.3060+00	.1154+03

Supplementary Velocity Profiles and Related Data

The velocity profiles, freestream velocities, and boundary layer thicknesses were presented in the text for only sample test conditions. The data for the remaining test results are presented here in Figures 57 to 78.

The velocity profiles were plotted using the Mechanical Engineering Department's remote (computer) plotting terminal.

The velocity profiles are presented first, then the freestream velocities, and finally the boundary layer thicknesses.

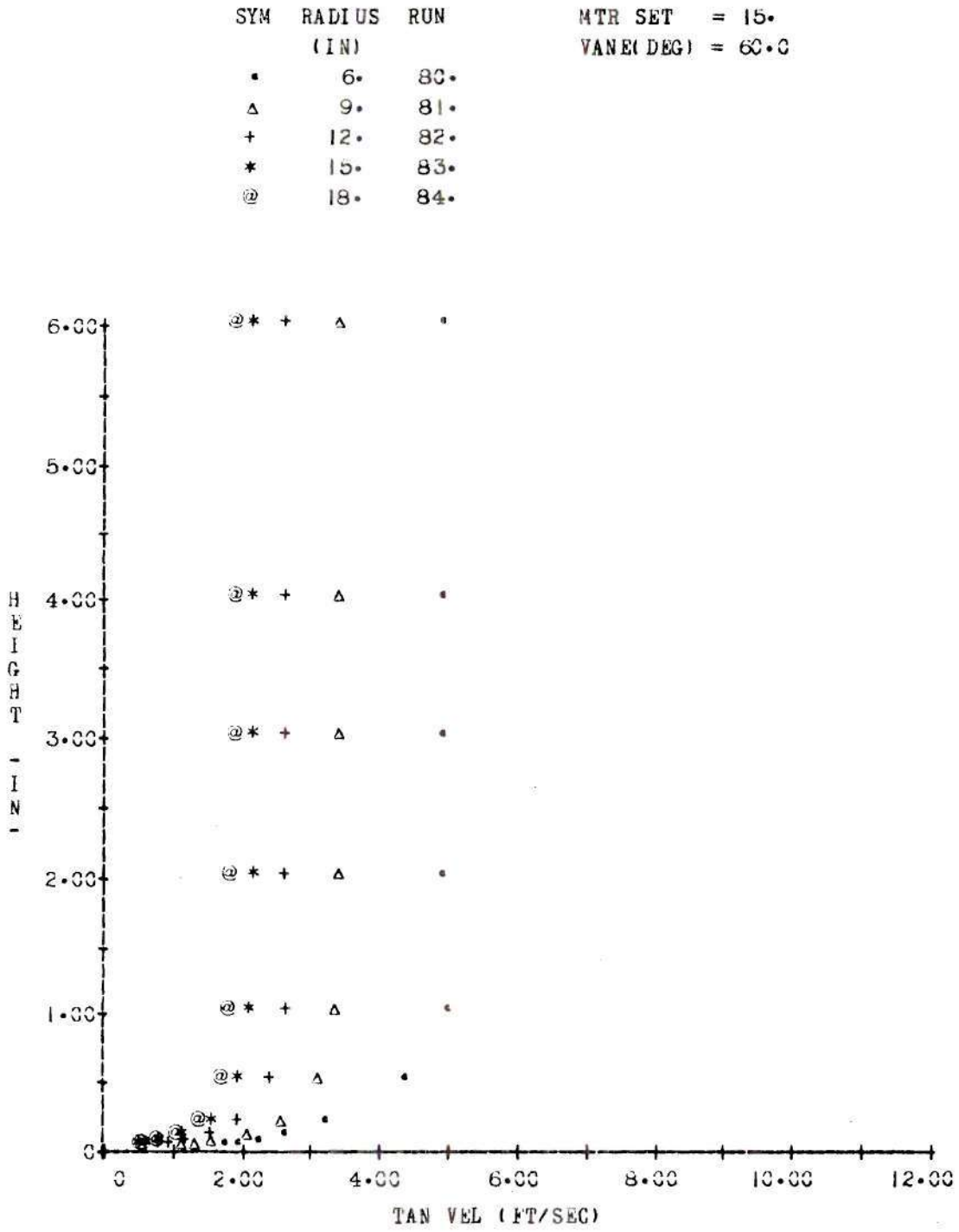

Figure 57. Tangential Velocity Profiles

Vane = 60.0^{o}, $\Gamma = 2.6\ ft^2/sec.$

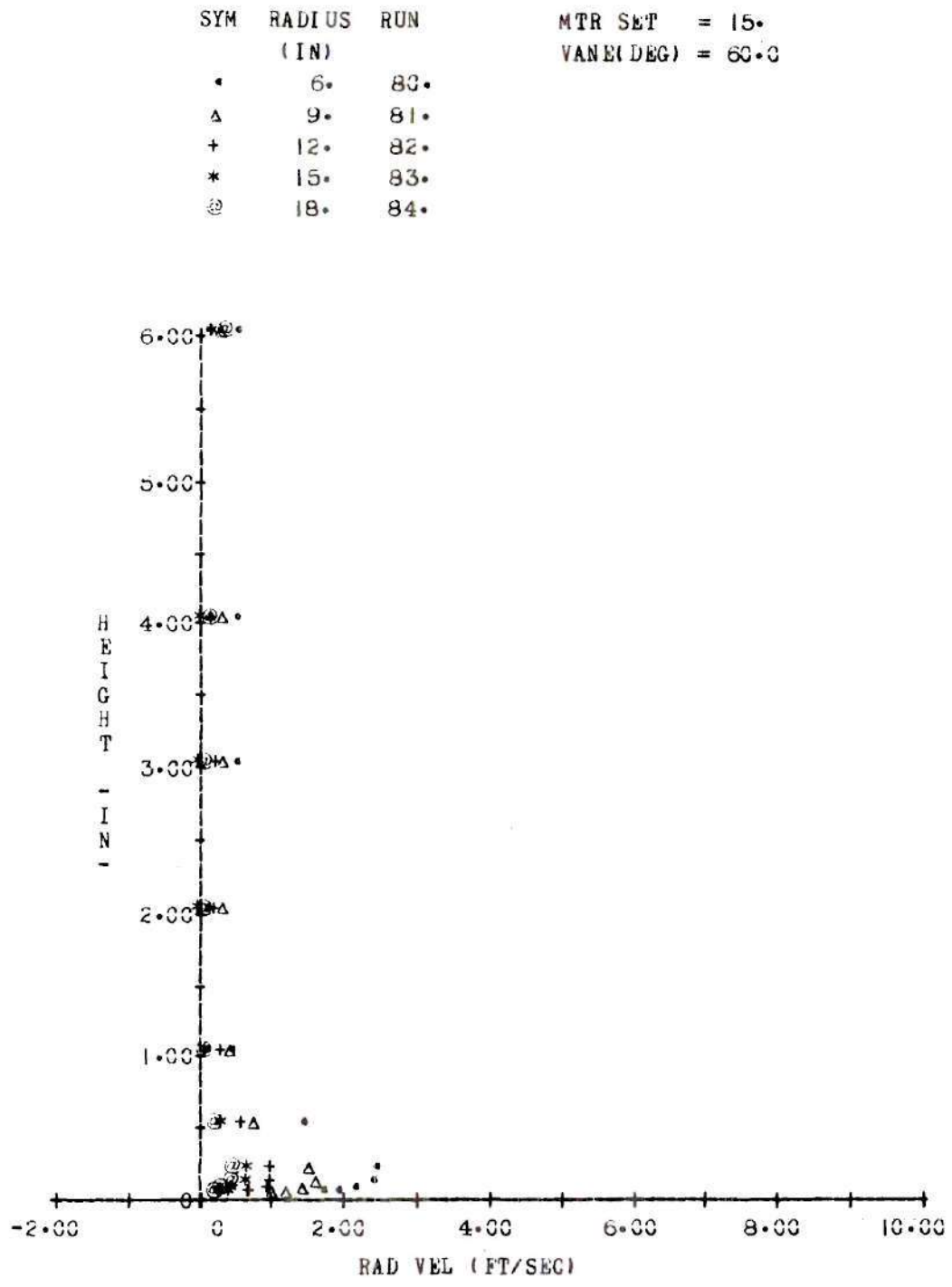

Figure 58. Radial Velocity Profiles (Inflow)

Vane = 60.0°, $\Gamma = 2.6\ ft^2/sec.$

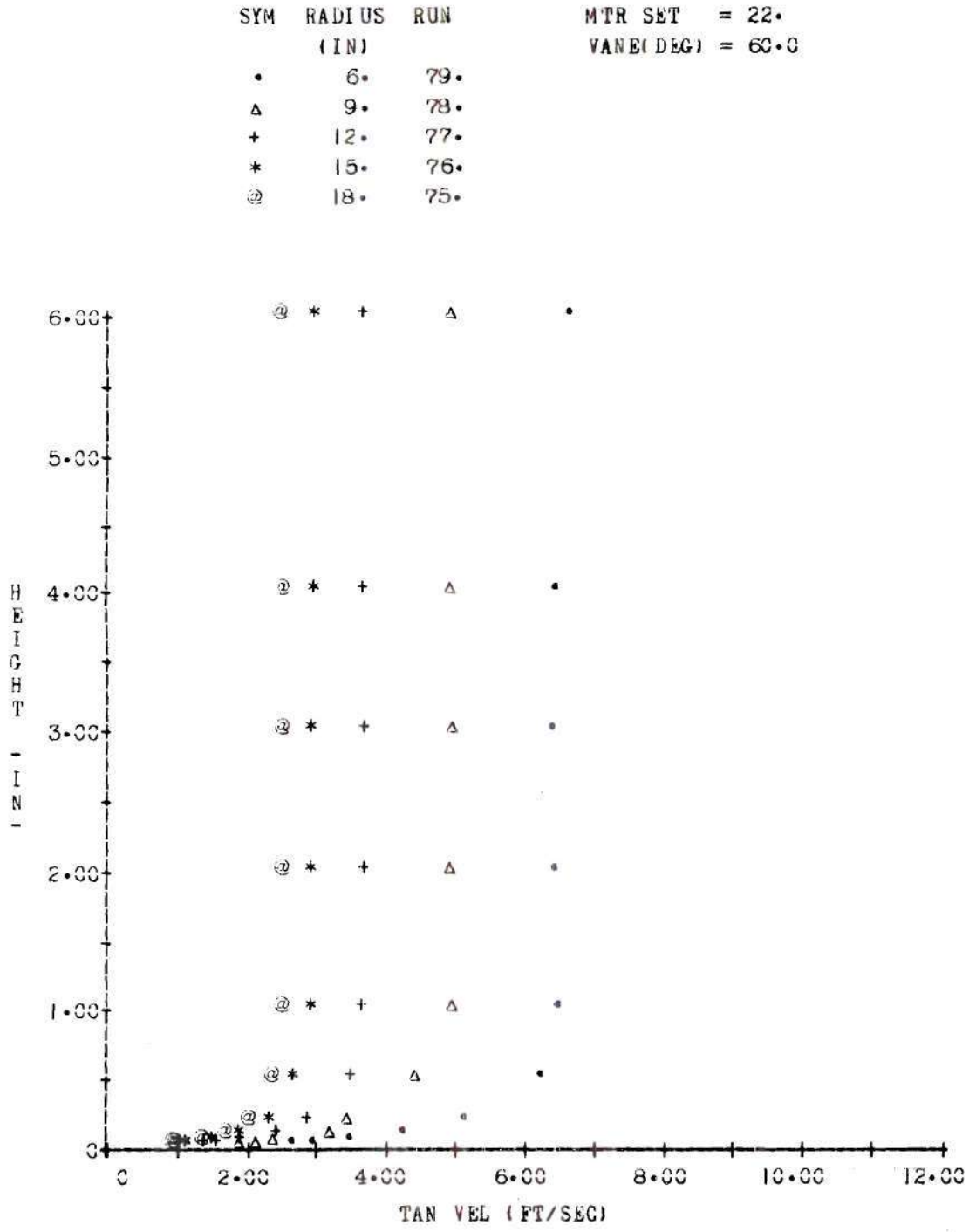

Figure 59. Tangential Velocity Profiles

Vane = 60.0°, $\Gamma = 3.7\ ft^2/sec.$

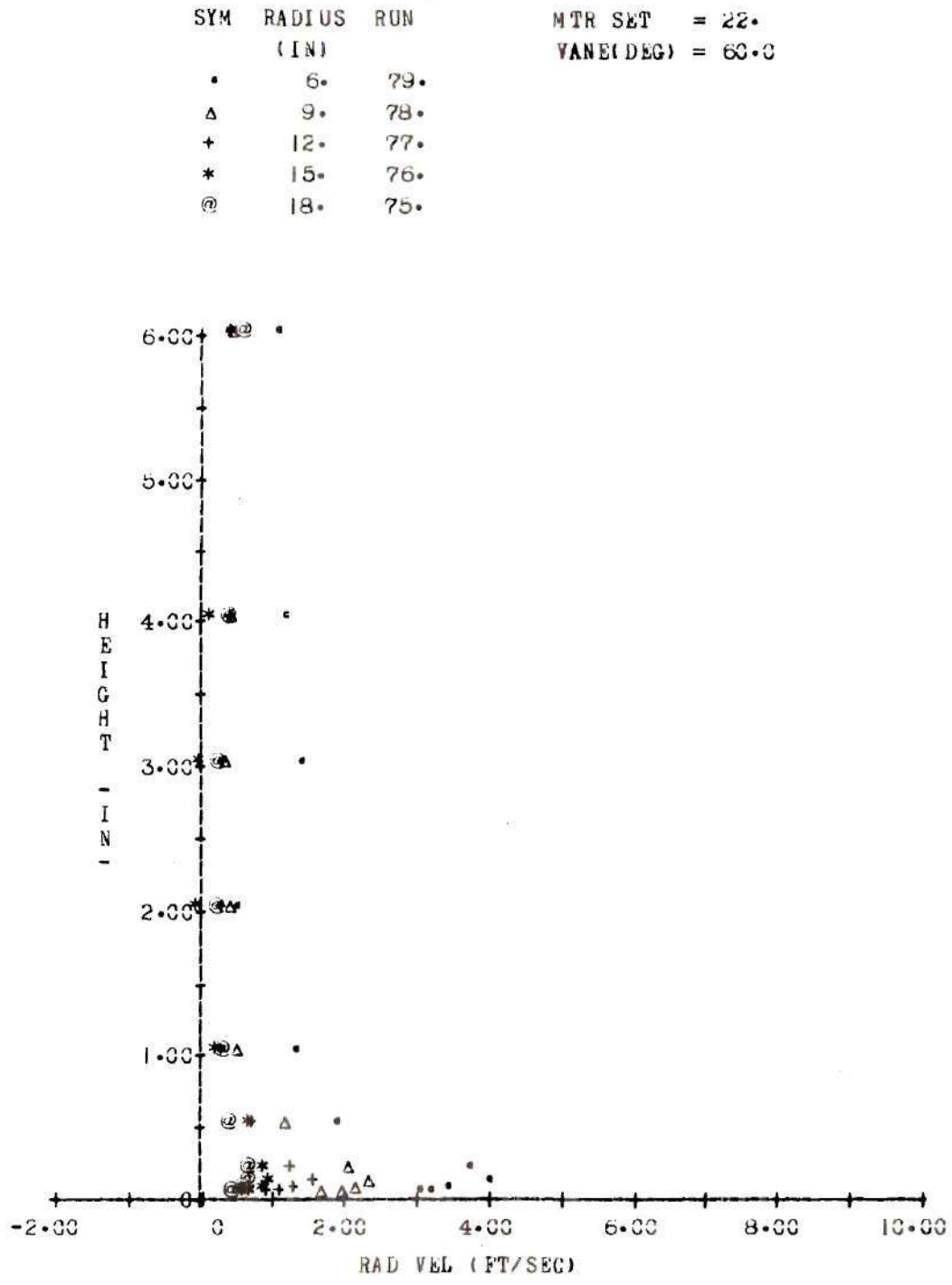

Figure 60. Radial Velocity Profiles (Inflow)

Vane = 60.0^{o}, $\Gamma = 3.7\ ft^2/sec.$

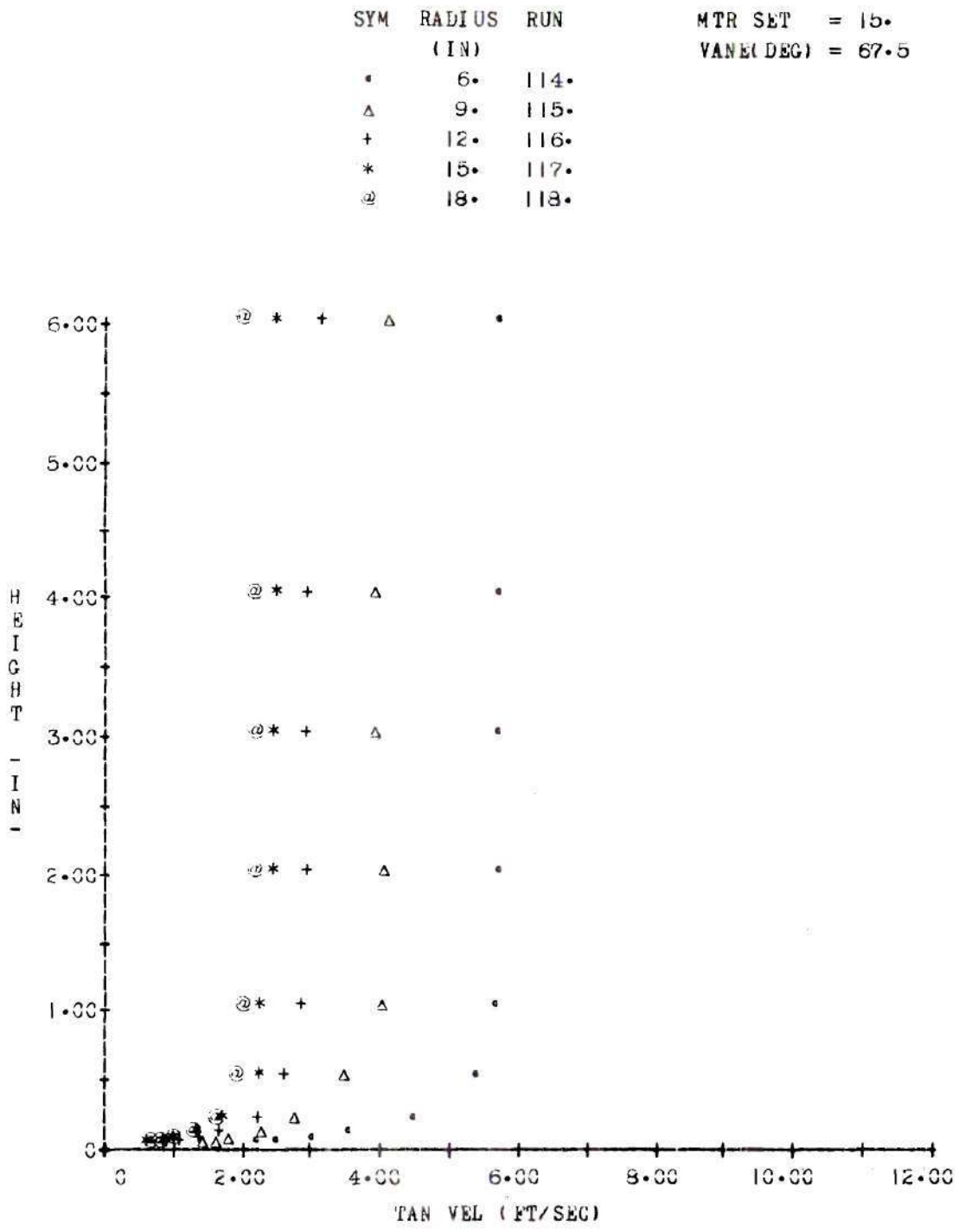

Figure 61. Tangential Velocity Profiles

Vane = 67.5^{o}, $\Gamma = 3.0\ ft^{2}/sec.$

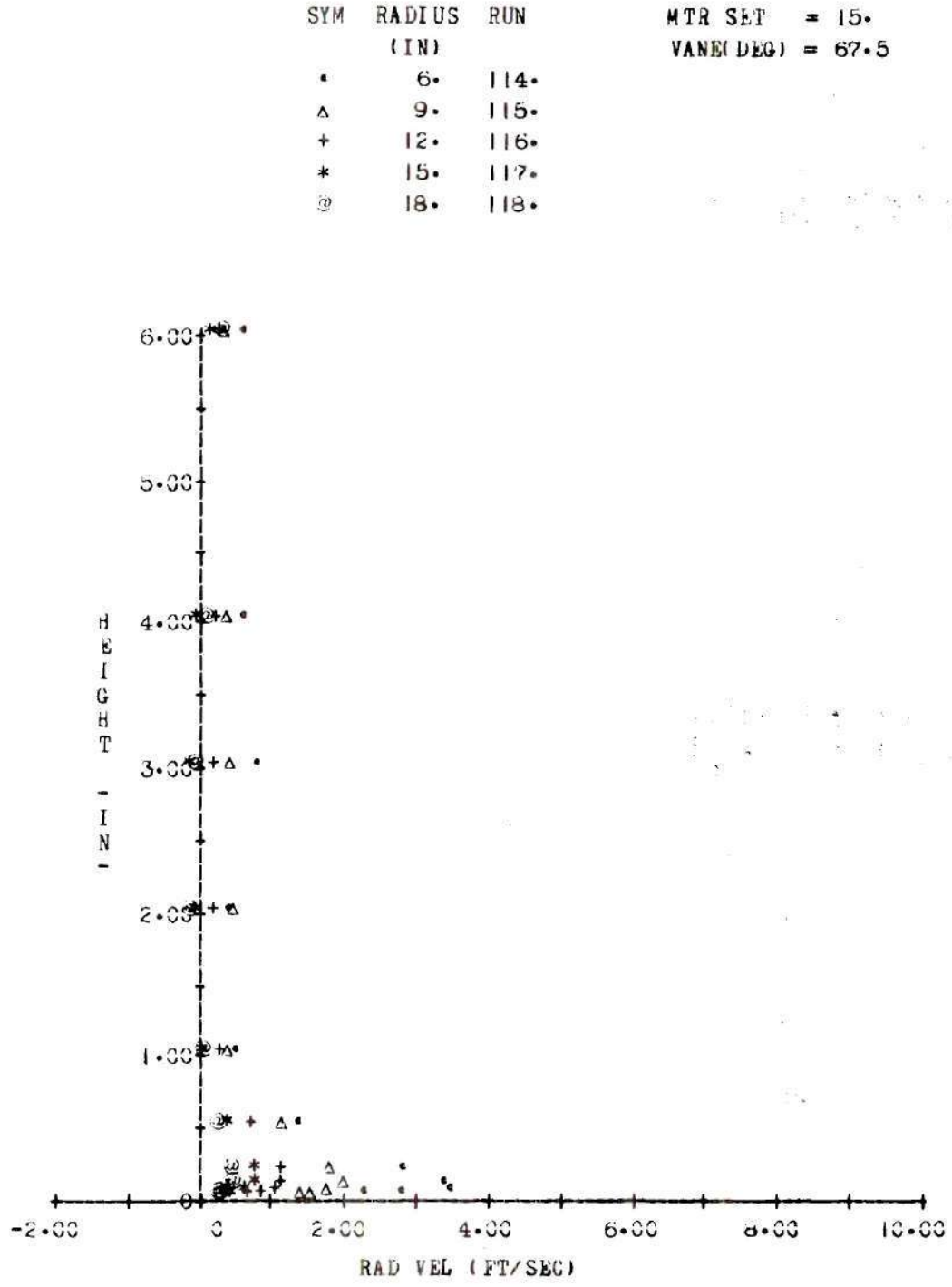

Figure 62. Radial Velocity Profiles (Inflow)

Vane = 67.5^{o}, $\Gamma = 3.0\ ft^{2}/sec.$

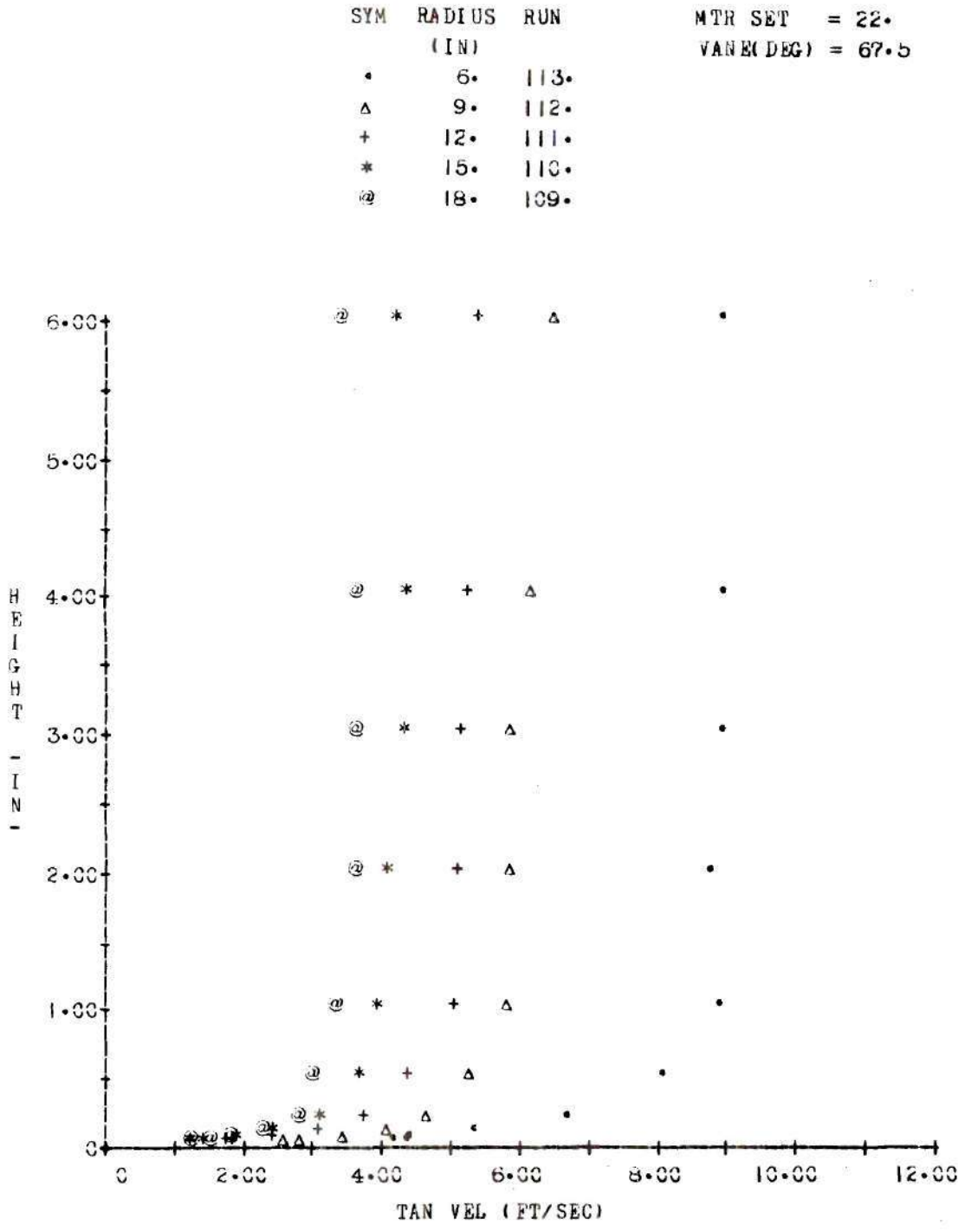

Figure 63. Tangential Velocity Profiles

Vane = 67.5^{o}, $\Gamma = 5.2\ ft^{2}/sec.$

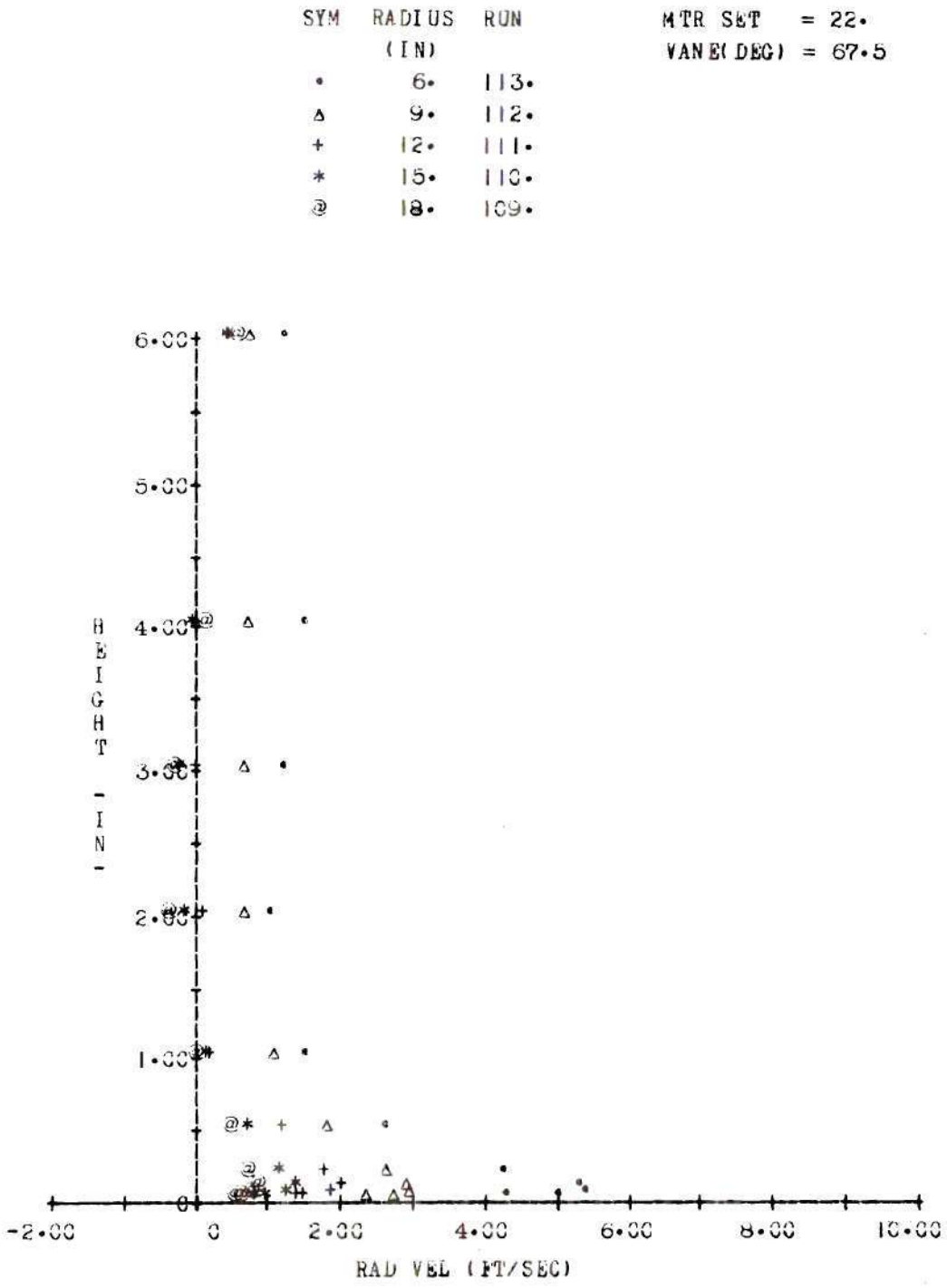

Figure 64. Radial Velocity Profiles (Inflow)

Vane = 67.5^{o}, $\Gamma = 5.2\ ft^2/sec.$

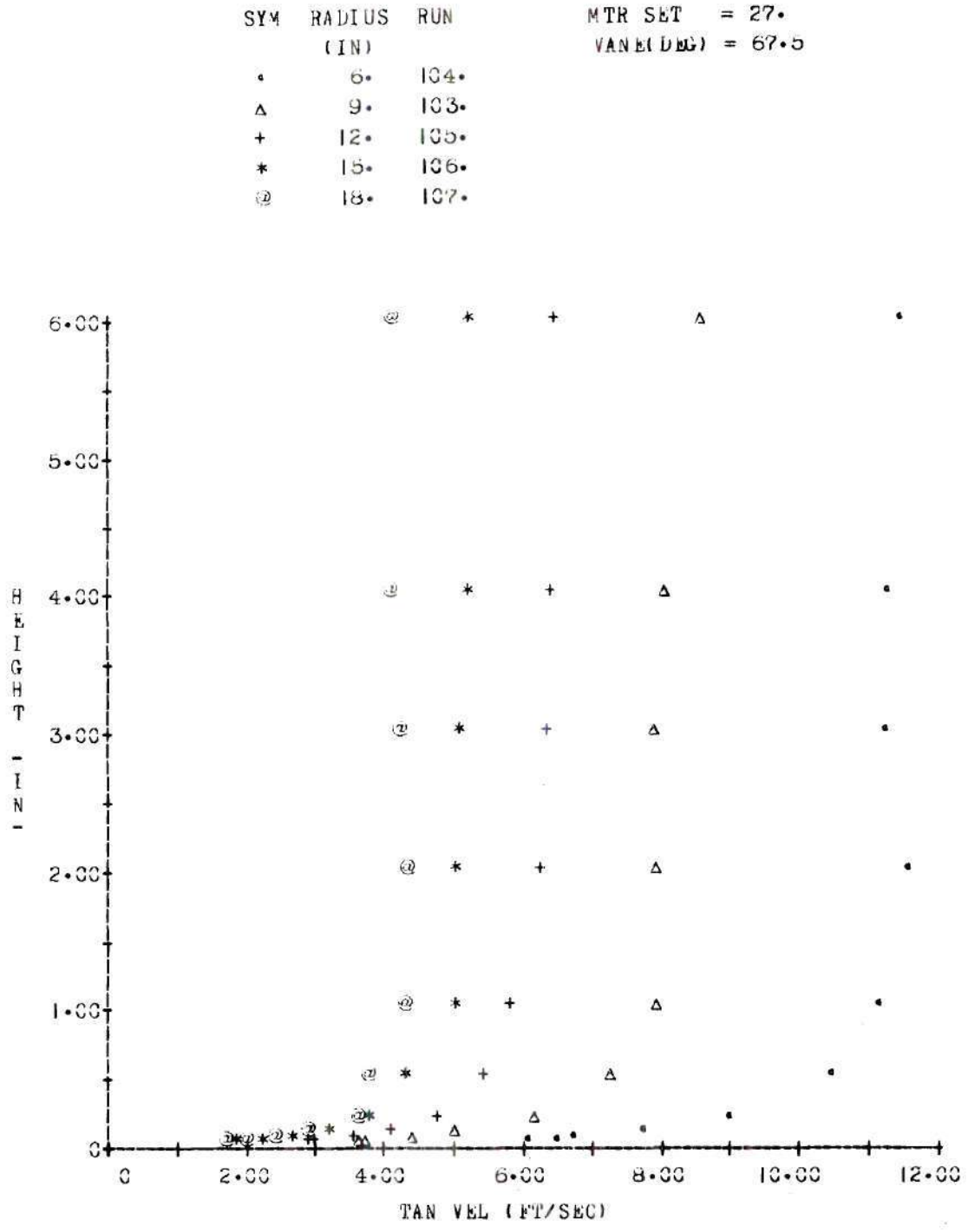

Figure 65. Tangential Velocity Profiles

Vane = 67.5^{o}, $\Gamma = 6.3\ ft^2/sec.$

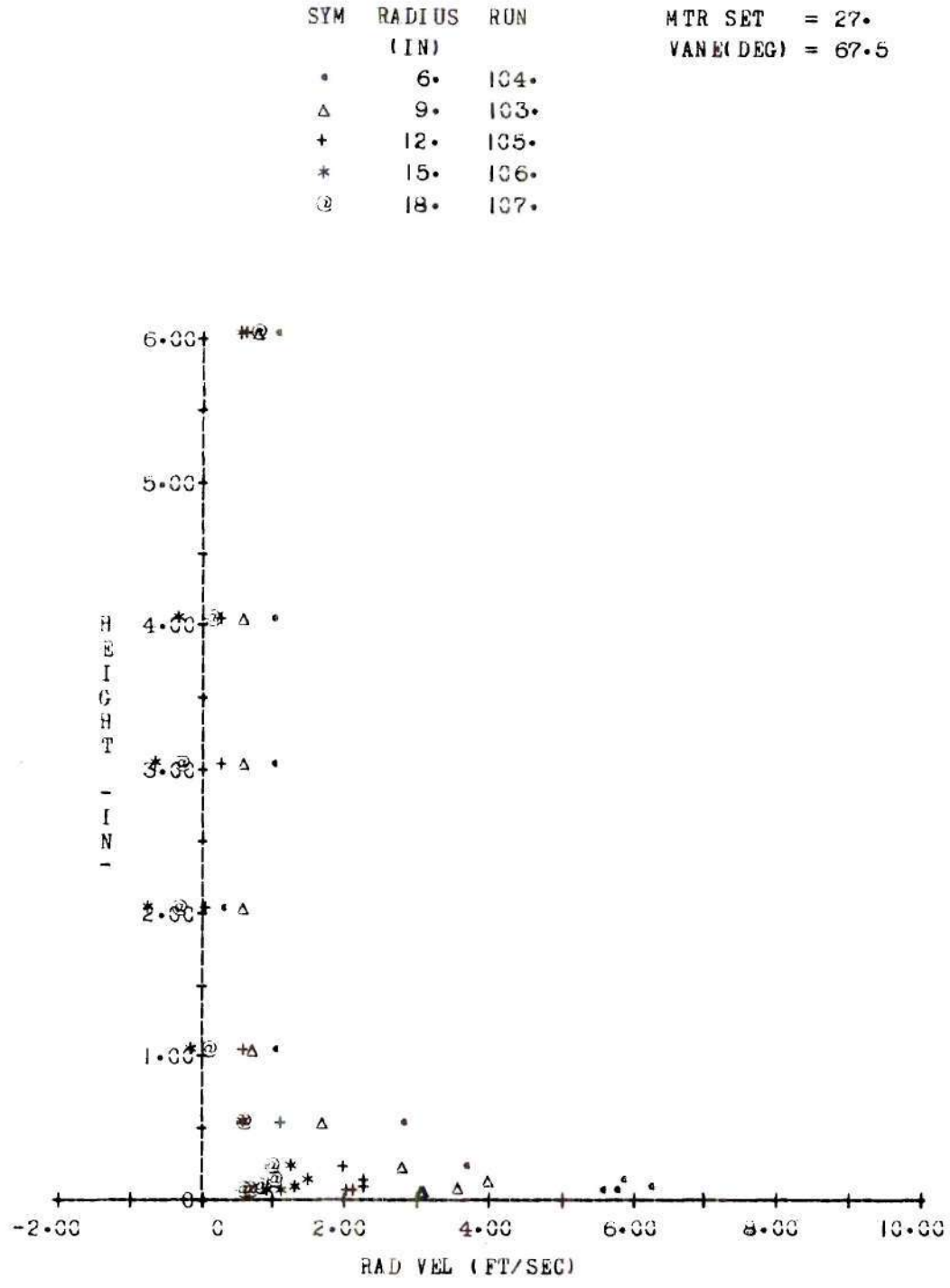

Figure 66. Radial Velocity Profiles (Inflow)

Vane = 67.5^{o}, $\Gamma = 6.3\ ft^{2}/sec.$

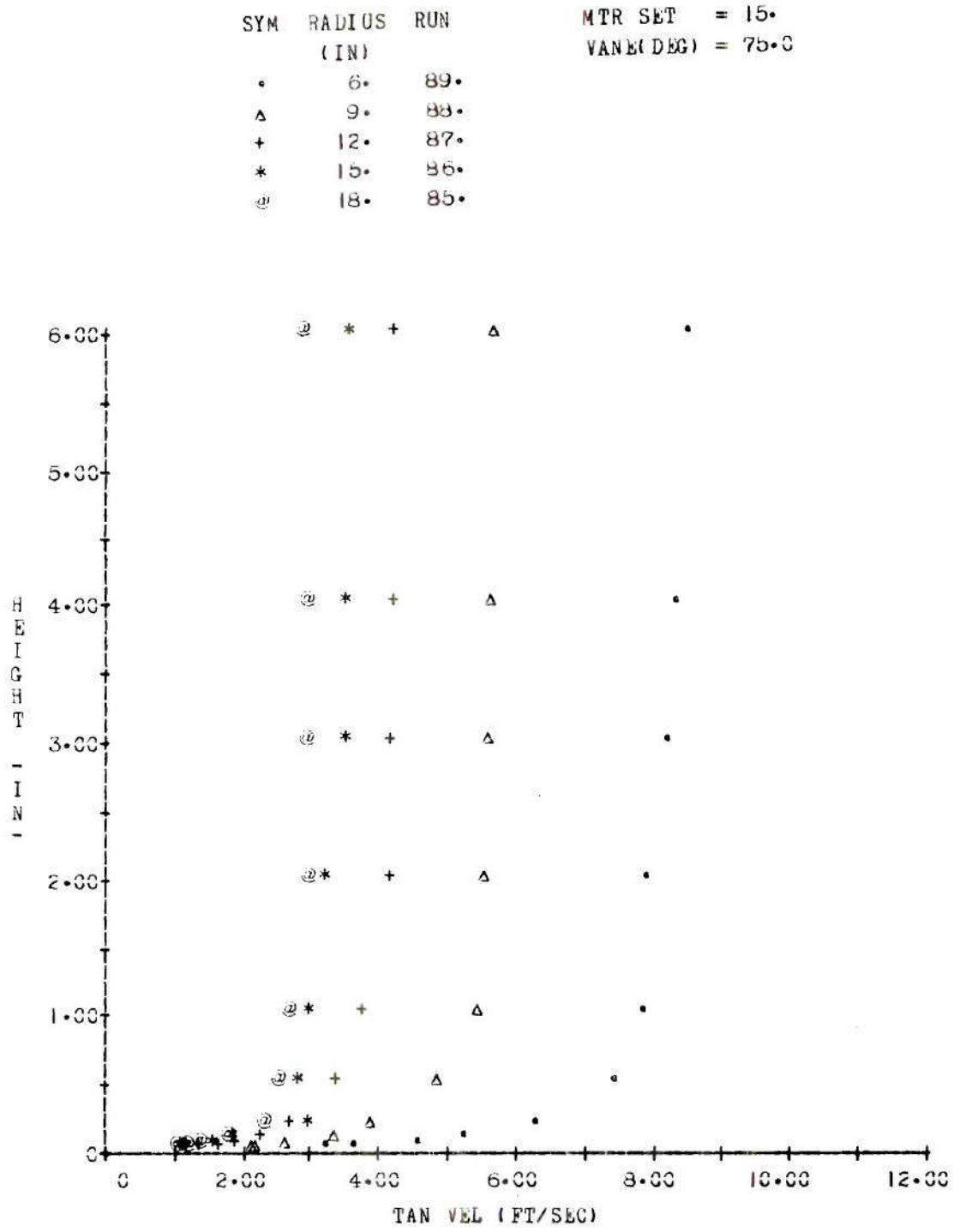

Figure 67. Tangential Velocity Profiles

Vane = 75.0^{o}, $\Gamma = 4.2\ ft^2/sec.$

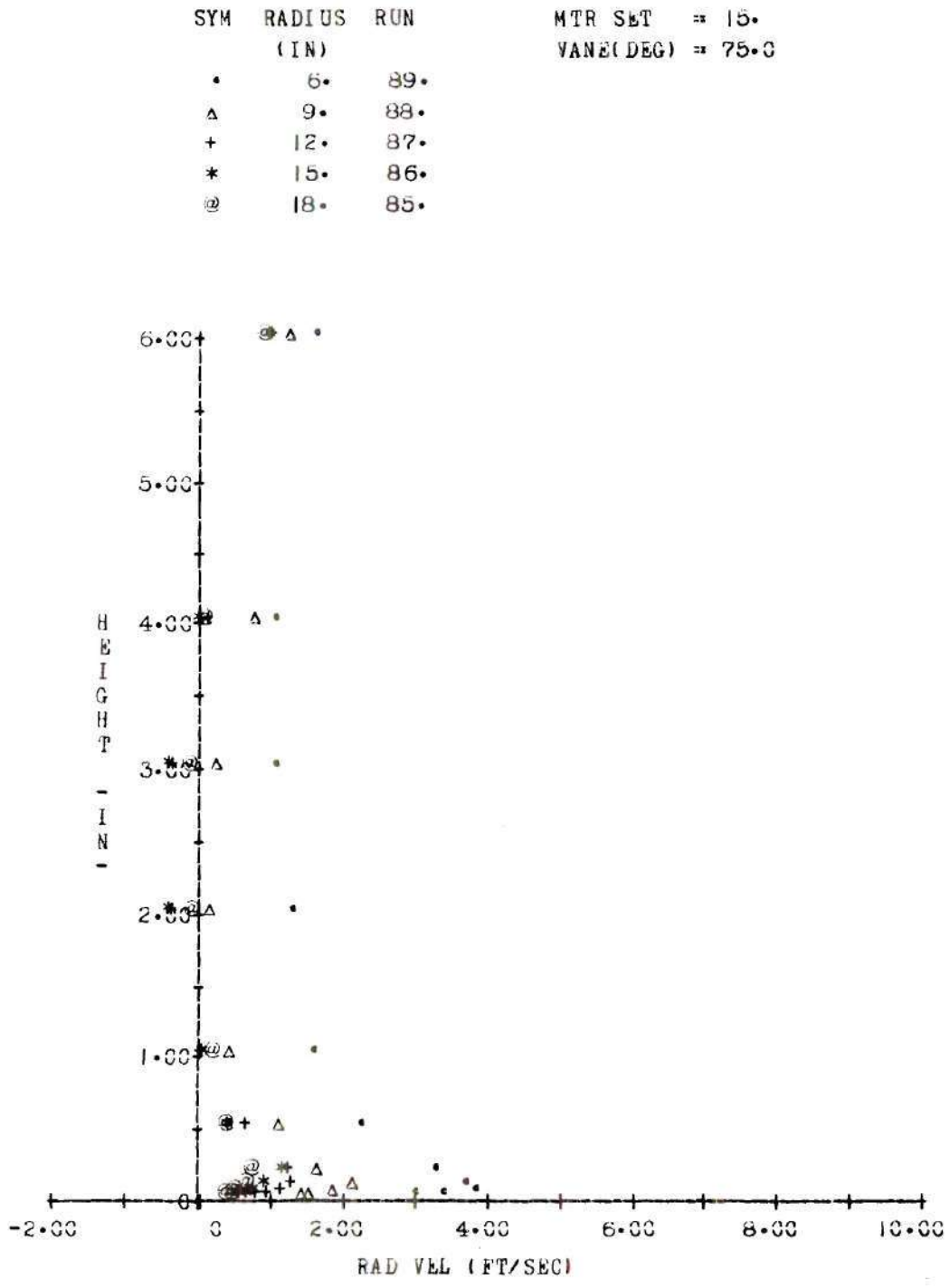

Figure 68. Radial Velocity Profiles (Inflow)

Vane = 75.0°, Γ = 4.2 ft^2/sec.

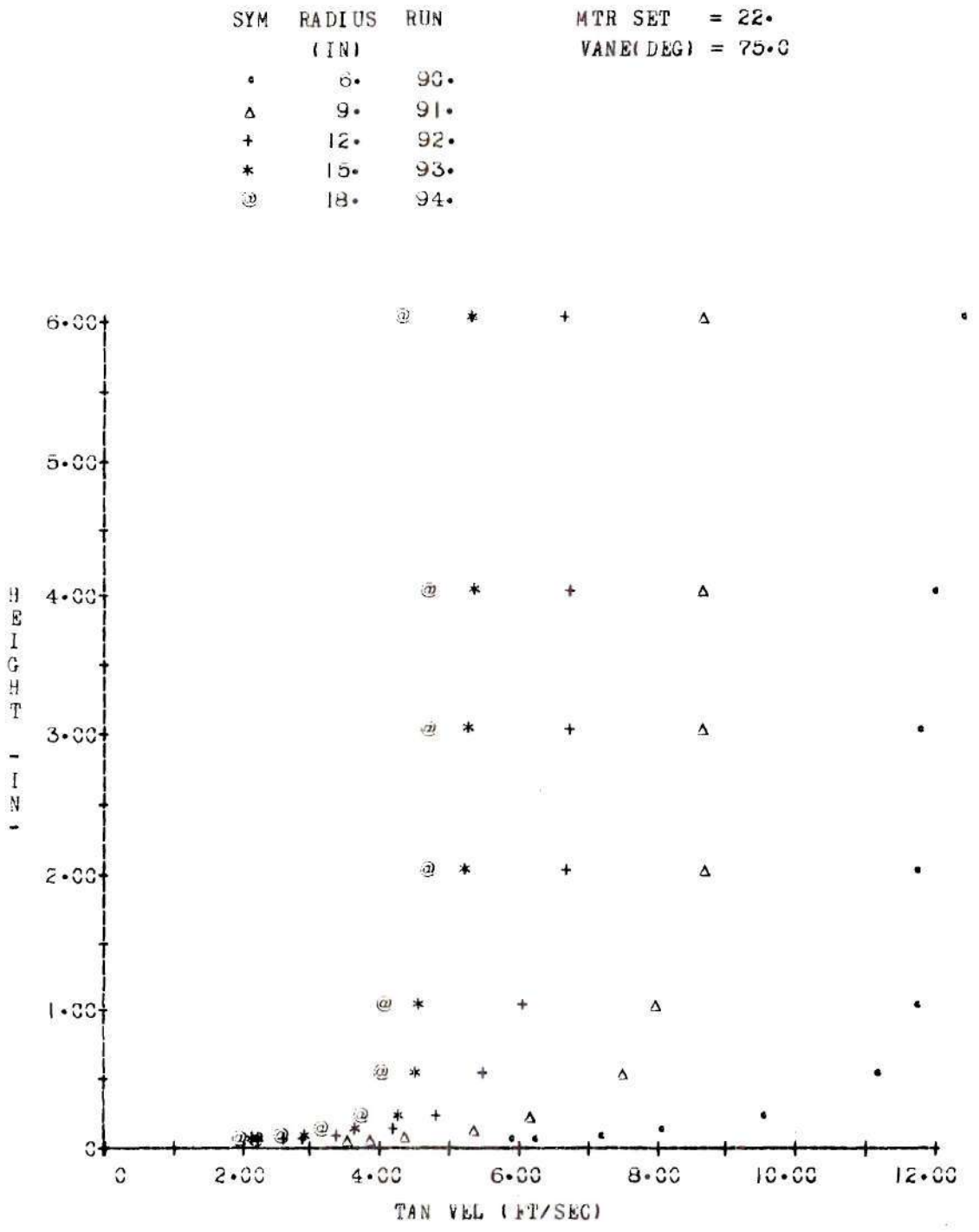

Figure 69. Tangential Velocity Profiles

Vane = 75.0^{o}, $\Gamma = 6.5\ ft^2/sec.$

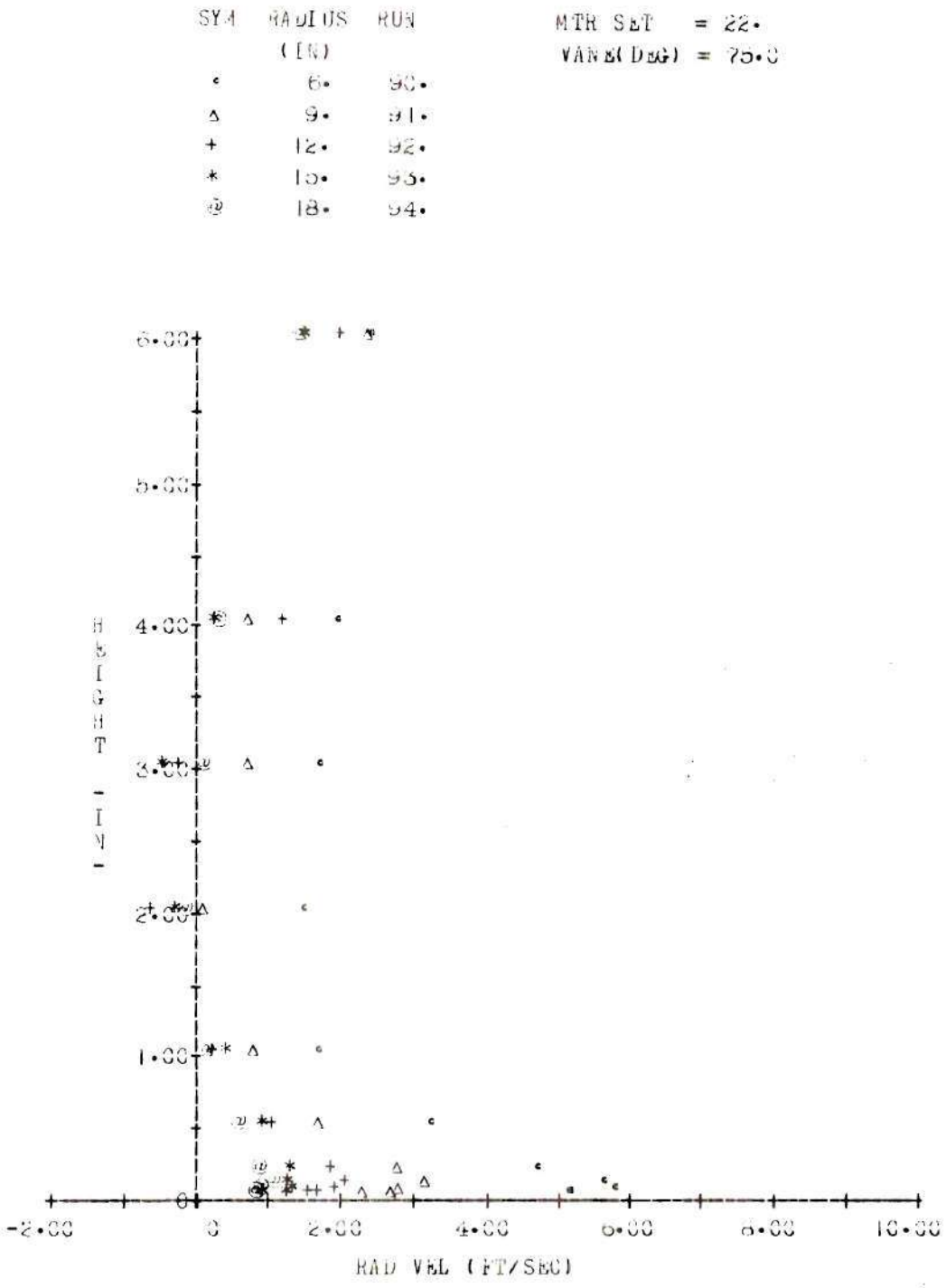

Figure 70. Radial Velocity Profiles (Inflow)

Vane = 75.0°, $\Gamma = 6.5\ ft^2/sec.$

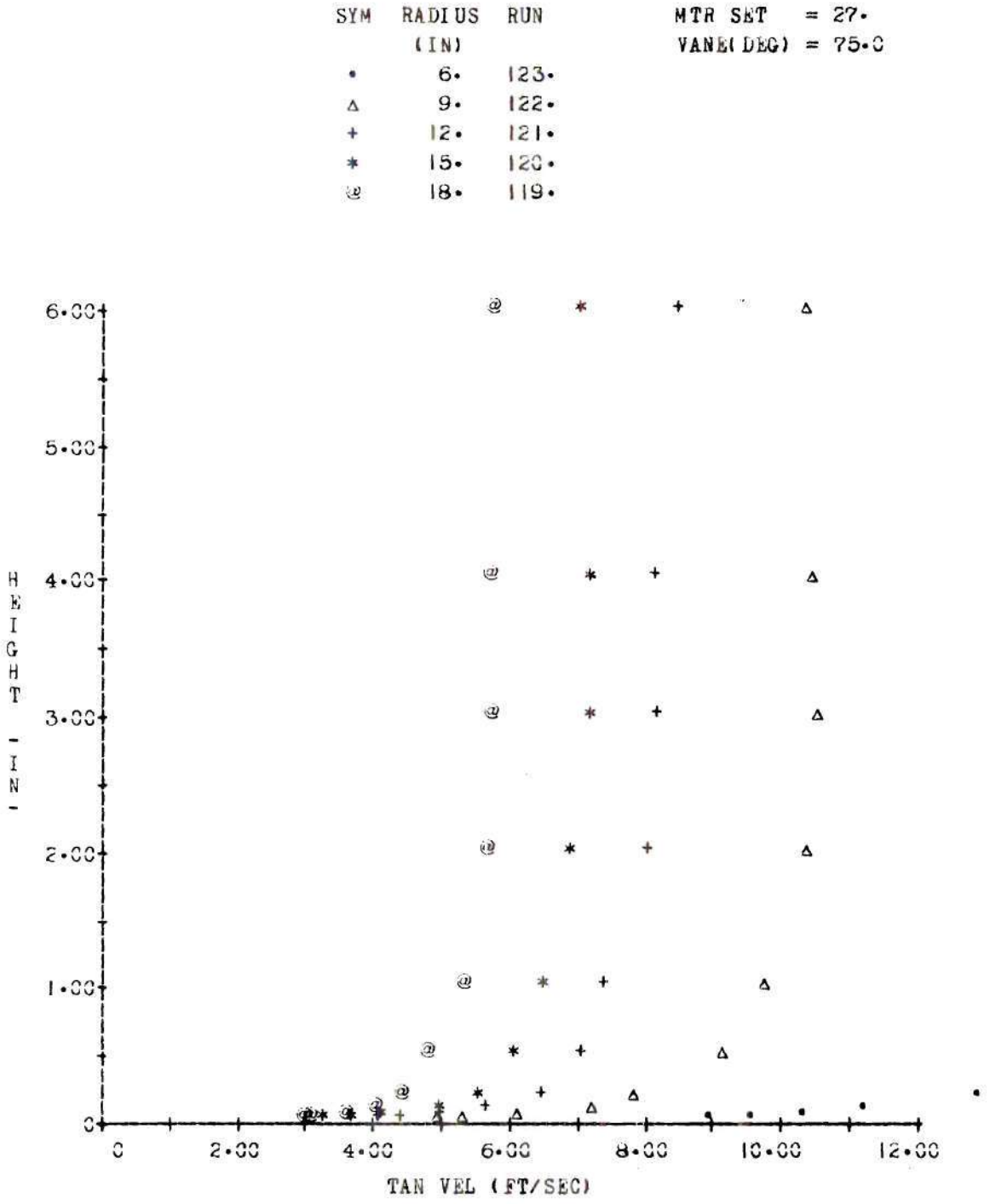

Figure 71. Tangential Velocity Profiles

Vane = 75.0°, Γ = 7.8 ft^2/sec.

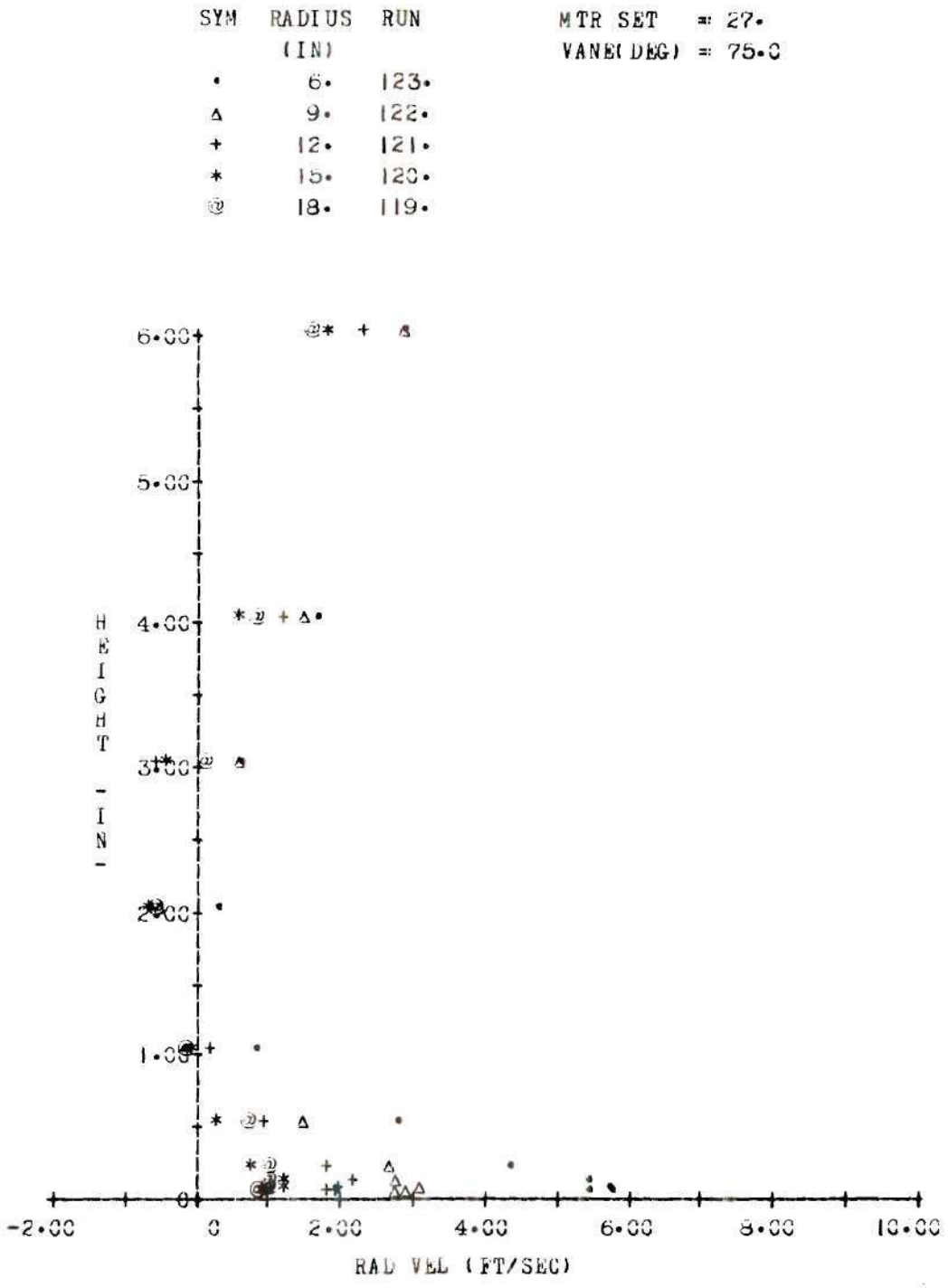

Figure 72. Radial Velocity Profiles (Inflow)

Vane = 75.0^{o}, $\Gamma = 7.8\ ft^2/sec.$

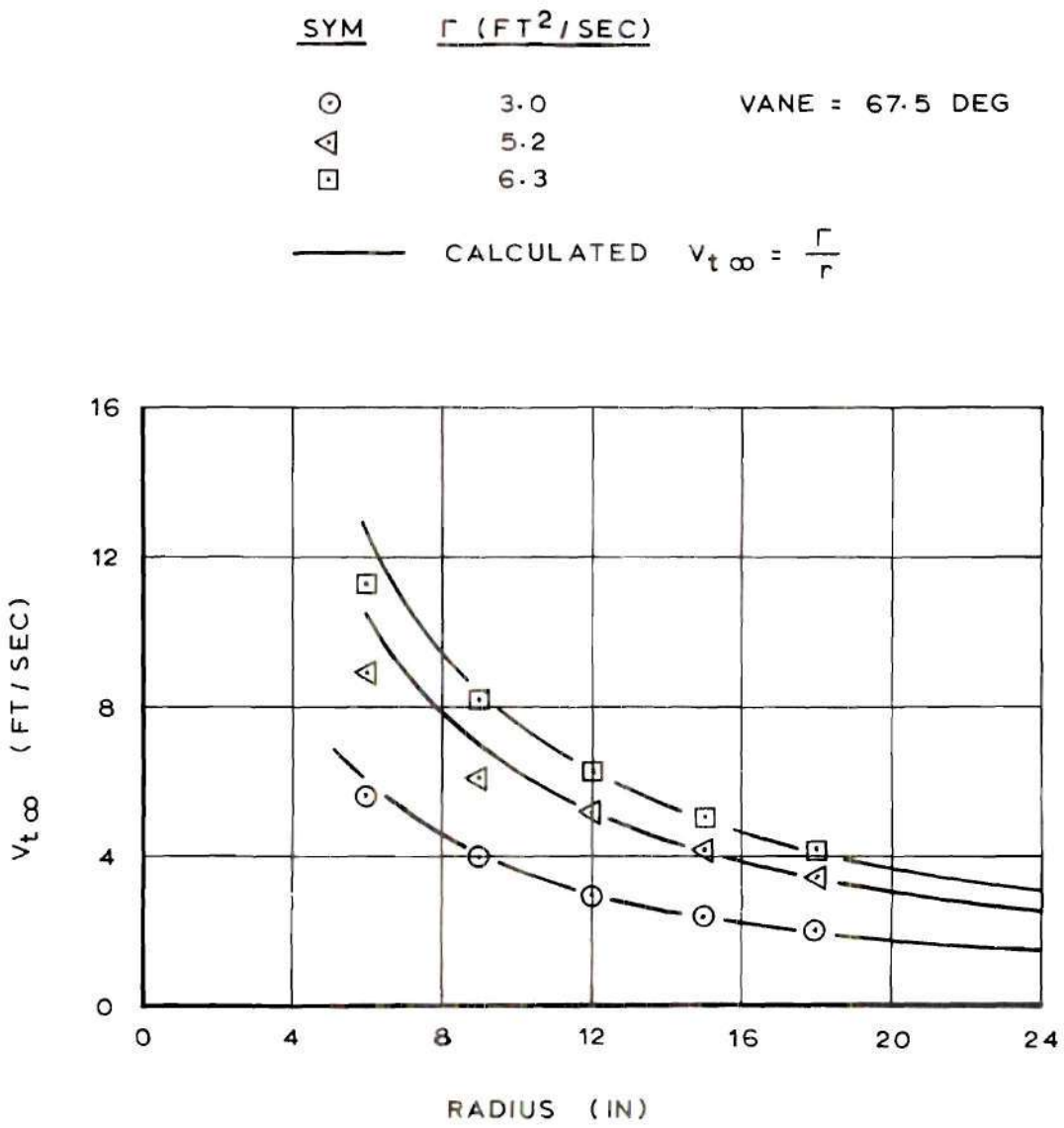

Figure 73. Freestream Tangential Velocity

Vane = 67.5 Deg.

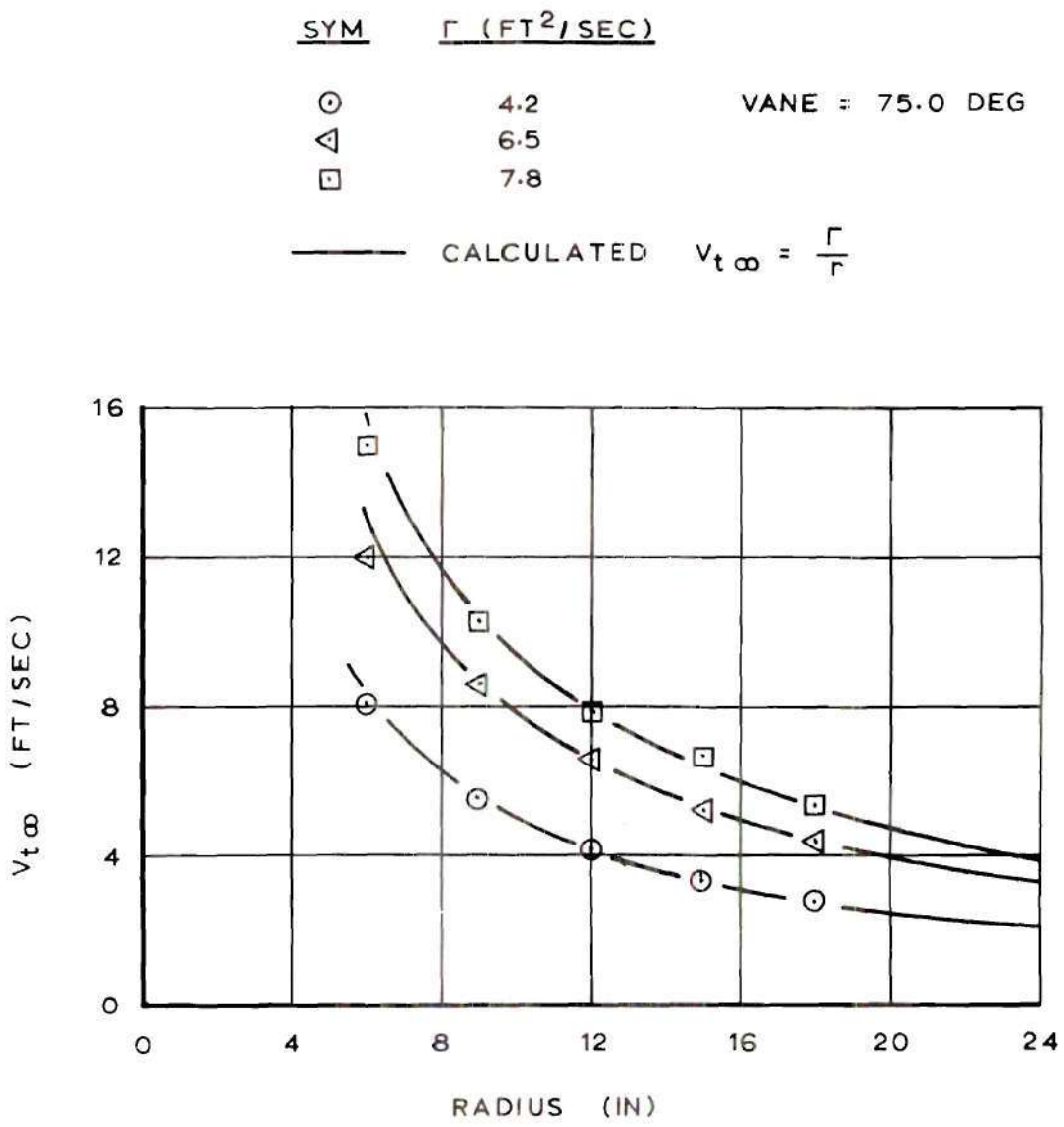

Figure 74. Freestream Tangential Velocity

Vane = 75.0 Deg.

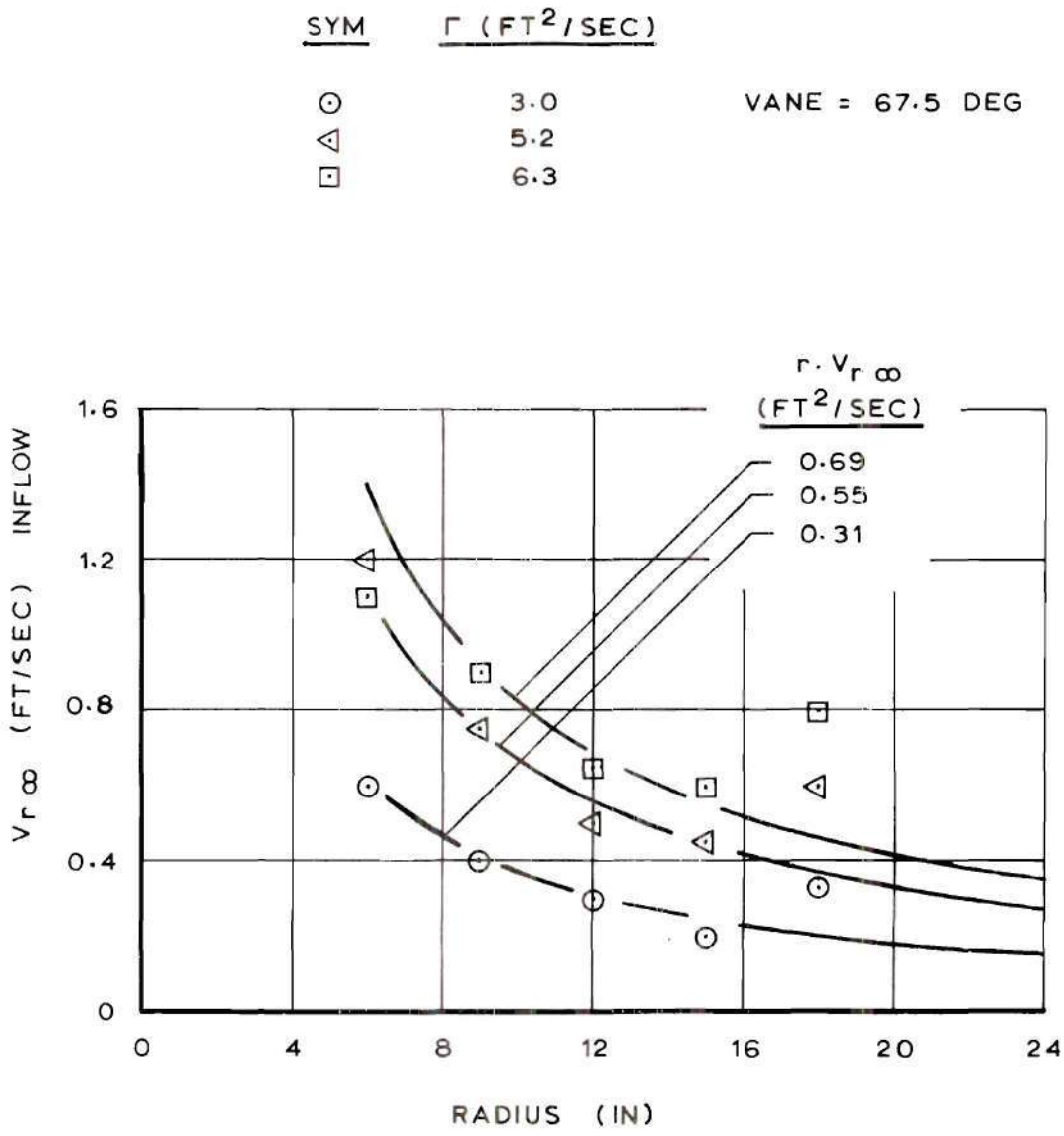

Figure 75. Freestream Radial Velocity

Vane = 67.5 Deg.

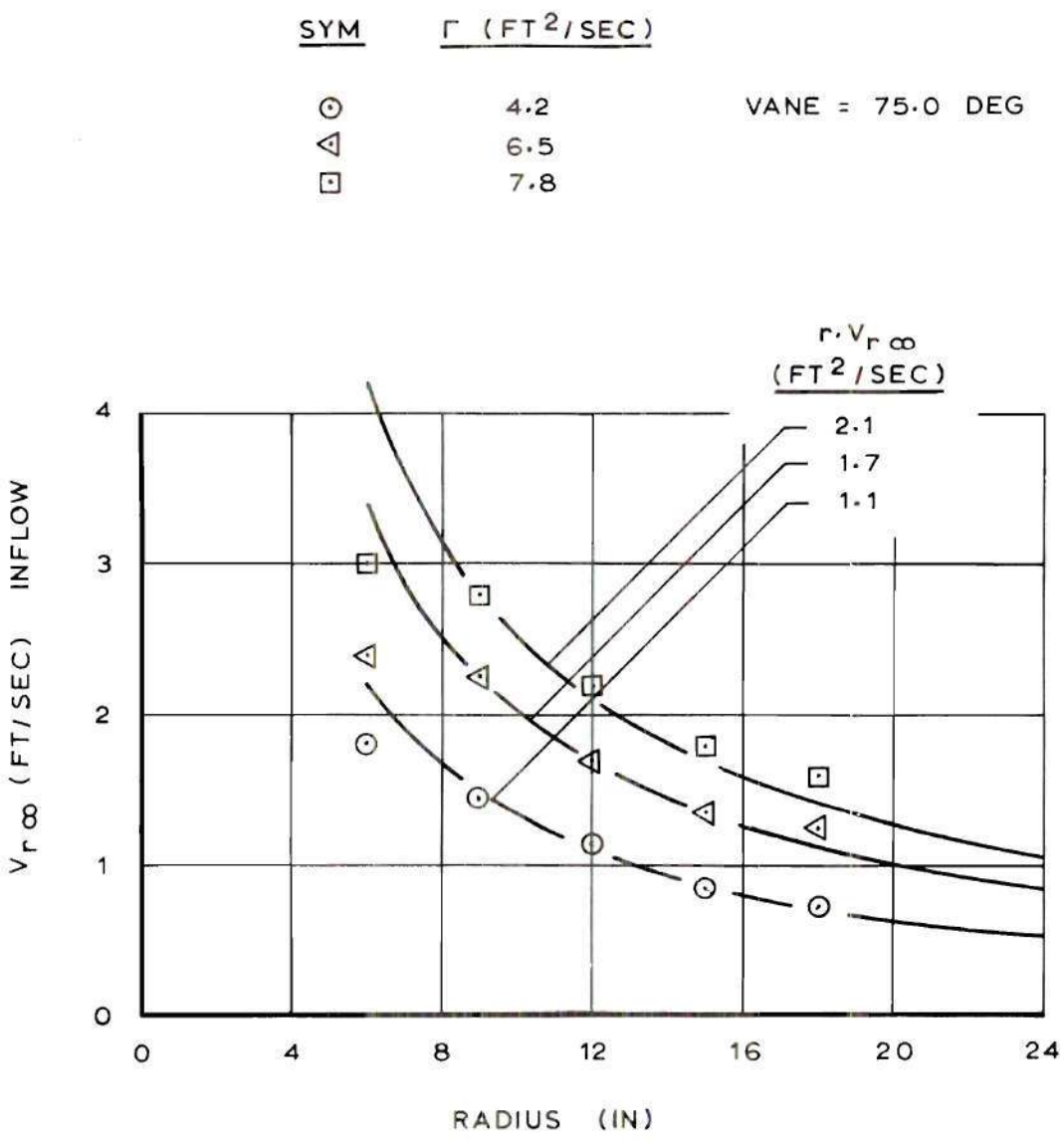

Figure 76. Freestream Radial Velocity

Vane = 75.0 Deg.

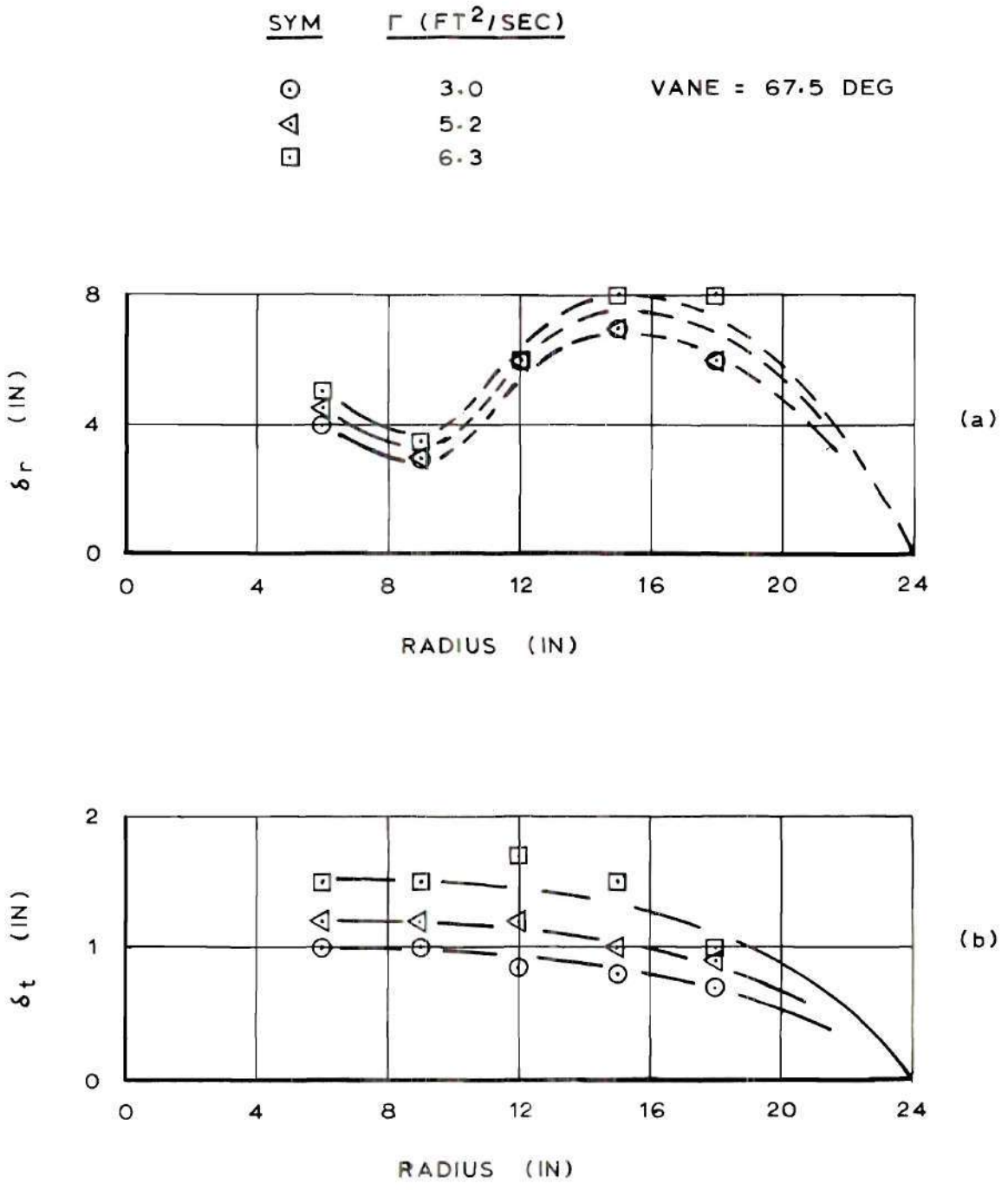

Figure 77. Radial and Tangential Velocity Boundary Layer Thickness

Vane = 67.5 Deg.

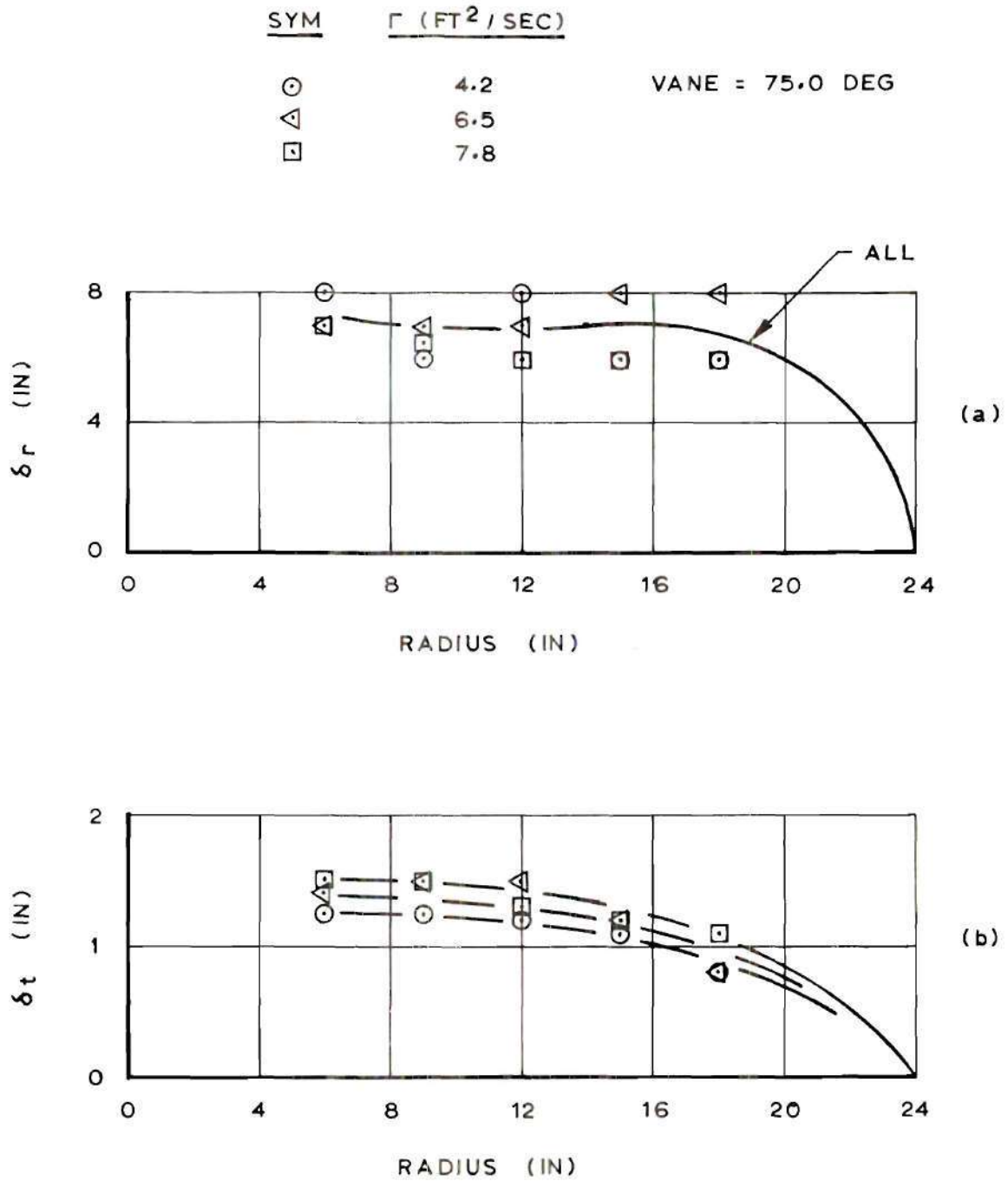

Figure 78. Radial and Tangential Velocity Boundary Layer Thickness

Vane = 75.0 Deg.

APPENDIX D

MOMENTUM INTEGRAL EQUATIONS DERIVATION AND SUPPORTING ANALYSIS

The momentum integral equations provide a mathematical description of the boundary layer. This appendix presents their derivation from the Navier-Stokes momentum equations. It also contains the supplementary details of the analysis of these equations presented in Chapter III.

Derivation of Momentum Integral Equations

Nomenclature

For the derivation of the momentum integral equations the following nomenclature is used.

u - Radial velocity.

v - Tangential velocity.

w - Vertical velocity.

U - Freestream radial velocity.

V - Freestream tangential velocity.

Radial Momentum Integral Equation

The Navier-Stokes radial momentum equation (21) for axisymmetric flow, neglecting the shear term $2\mu \frac{\partial}{\partial r}\left[\frac{\partial w}{\partial z}\right]$ since it is small compared to the other shear terms, is

$$u\frac{\partial u}{\partial r} + w\frac{\partial u}{\partial z} - \frac{v^2}{r} = -\frac{1}{\rho}\frac{\partial p}{\partial r} + \frac{1}{\rho}\frac{\partial \tau_{rz}}{\partial z} \quad . \tag{D-1}$$

Outside the boundary layer

$$u = U \quad , \tag{D-2}$$

$$v = V \quad , \tag{D-3}$$

$$U\frac{dU}{dr} - \frac{V^2}{r} = -\frac{1}{\rho}\frac{dp}{dr} \quad . \tag{D-4}$$

Recognizing that the vertical pressure gradient is of the order ρg and negligibly small through the boundary layer, and substituting equation (D-4) into equation (D-1) gives

$$ru\frac{\partial u}{\partial r} + rw\frac{\partial u}{\partial z} - v^2 = rU\frac{dU}{dr} - V^2 + \frac{r}{\rho}\frac{\partial \tau_{rz}}{\partial z} \quad . \tag{D-5}$$

Using the continuity equation

$$\frac{\partial}{\partial z}(ruw) = -\frac{\partial (ru)}{\partial r} + rw\frac{\partial u}{\partial z} \quad , \tag{D-6}$$

equation (D-5) becomes

$$\frac{\partial}{\partial r}(ru^2) + \frac{\partial}{\partial z}(ruw) + V^2\left[1 - \left(\frac{v}{V}\right)^2\right] - rU\frac{dU}{dr}$$

$$= \frac{r}{\rho}\frac{\partial \tau_{rz}}{\partial z} \quad . \tag{D-7}$$

Integrating equation (D-7) over constant height, h, gives

$$\int_o^h \left[\frac{\partial}{\partial r}(ru^2) - rU \frac{dU}{dr} \right] dz + u(h) \int_o^h \frac{\partial(rw)}{\partial z} dz$$

$$+ V^2 \int_o^h \left[1 - \left(\frac{v}{V} \right)^2 \right] dz = \frac{r}{\rho} \tau_{rz} \Big|_o^h \quad . \tag{D-8}$$

Applying Leibnitz's Rule, with $\frac{dh}{dr} = 0$, to equation (D-8) gives

$$\frac{d}{dr} \int_o^h (ru^2)\, dz - rU \frac{dU}{dr} \int_o^h dz - u(h) \frac{d}{dr} \int_o^h (ru)\, dz$$

$$+ V^2 \int_o^h \left[1 - \left(\frac{v}{V} \right)^2 \right] dz = \frac{r}{\rho} \tau_{rz} \Big|_o^h \quad . \tag{D-9}$$

Since,

$$\frac{d}{dr} \left\{ u(h) \int_o^h (ru)dz \right\} = u(h) \frac{d}{dr} \int_o^h rudz + \frac{du(h)}{dr} \int_o^h rudz \, , \tag{D-10}$$

equation (D-9) becomes

$$\frac{d}{dr}\int_o^h ru[u-u(h)]\,dz - \int_o^h r\left[U\frac{dU}{dr} - \frac{udu(h)}{dr}\right]dz$$

$$+ V^2\int_o^h\left[1-\left(\frac{v}{V}\right)^2\right]dz = \frac{r}{\rho}\,\tau_{rz}\Big|_o^h \quad . \tag{D-11}$$

Letting $h \to \infty$, $u(h) \to U$, and $\tau_{rz}(h) \to 0$, equation (D-11) becomes

$$\frac{d}{dr}\left\{rU^2\int_o^\infty \frac{u}{U}\left(1-\frac{u}{U}\right)dz\right\} + r\,U\frac{dU}{dr}\int_o^\infty\left(1-\frac{u}{U}\right)dz$$

$$- V^2\int_o^\infty\left[1-\left(\frac{v}{V}\right)^2\right]dz = \frac{r}{\rho}\,\tau_{rz}(0) \quad . \tag{D-12}$$

Let:

$$\theta_r = \delta_r\int_o^\infty \frac{u}{U}\left(1-\frac{u}{U}\right)d\eta = \delta_r\,\lambda_1 \ , \tag{D-13}$$

$$\delta_r^* = \delta_r\int_o^\infty\left(1-\frac{u}{U}\right)d\eta = \delta_r\lambda_2 \ , \tag{D-14}$$

and

$$\delta_1 = \delta_t\int_o^\infty\left[1-\left(\frac{v}{V}\right)^2\right]d\xi = \delta_t\,\lambda_3 \ , \tag{D-15}$$

where $\eta = z/\delta_r$, and $\xi = z/\delta_t$.

Equation (D-12) becomes

$$\frac{d}{dr}\left\{r\,U^2\theta_r\right\} + r\,U\delta_r^*\frac{dU}{dr} - V^2\delta_1 = \frac{r}{\rho}\tau_{rz}(0) \quad . \tag{D-16}$$

Angular Momentum Integral Equation

The Navier-Stokes angular momentum equation (21) for axisymmetric flow is

$$u\frac{\partial u}{\partial r} + w\frac{\partial v}{\partial z} + \frac{uv}{r} = \frac{1}{\rho}\left[\frac{\partial(r^2\tau_{zt})}{\partial z} + r^2\left(\frac{1}{r}\frac{\partial(r\,\tau_{rt})}{\partial r} + \frac{\tau_{rt}}{r}\right)\right] . \tag{D-17}$$

Outside the boundary layer

$$u = U \ , \tag{D-18}$$

$$v = V \ , \tag{D-19}$$

$$\frac{\partial u}{\partial z} = \frac{\partial v}{\partial z} = 0 \ , \tag{D-20}$$

$$\frac{\partial}{\partial r}(r^2UV) - r\,V\frac{\partial(rU)}{\partial r} = \frac{r^2}{\rho}\left[\frac{1}{r}\frac{\partial(r\,\tau_{rt})}{\partial r} + \frac{\tau_{rt}}{r}\right] \quad . \tag{D-21}$$

Since,

$$\frac{1}{r}\frac{\partial}{\partial r}(ruv) = u\frac{\partial v}{\partial r} + v\left(\frac{u}{r} - \frac{\partial u}{\partial r}\right) \ , \tag{D-22}$$

and from the continuity equation

$$\frac{\partial w}{\partial z} = -\frac{1}{r}\frac{\partial(ru)}{\partial r} \ , \tag{D-23}$$

then

$$\frac{1}{r}\frac{\partial}{\partial r}(r\,u\,v) = -v\,\frac{\partial w}{\partial z} + u\,\frac{\partial v}{\partial r} \quad . \tag{D-24}$$

Substituting equations (D-21) and (D-24) into equation (D-17) gives

$$\frac{\partial}{\partial r}(r^2\,u\,v) + \frac{\partial}{\partial z}(r^2\,v\,w) - \frac{\partial}{\partial r}(r^2 UV) + rV\frac{\partial}{\partial r}(rU) = \frac{r^2}{\rho}\frac{\partial \tau_{zt}}{\partial z} \quad . \tag{D-25}$$

Integrating equation (D-25) over constant height, h, gives

$$\int_o^h \frac{\partial}{\partial r}\left[r^2(uv - UV)\right]dz + r\,v(h)\int_o^h \frac{\partial(rw)}{\partial z}\,dz$$

$$+ \int_o^h rV\frac{\partial}{\partial r}(rU)\,dz = \frac{r^2}{\rho}\tau_{zt}\Big|_o^h \quad . \tag{D-26}$$

Applying Leibnitz's Rule, with $\frac{dh}{dr} = 0$, to equation (D-26) gives

$$\frac{d}{dr}\left[\int_o^h r^2(uv - UV)\,dz\right] - rv(h)\frac{d}{dr}\left[\int_o^h ru\,dz\right]$$

$$+ rV\frac{d}{dr}\left[\int_o^h rU dz\right] = \frac{r^2}{o}\tau_{zt}\Big|_o^h \quad . \tag{D-27}$$

Let $h \to \infty$ with $v(h) \to V$, and $\tau_{zt}(h) \to 0$, equation (D-27) becomes

$$\frac{d}{dr}\left\{r^2\, UV \int_o^\infty \left(1 - \frac{uv}{UV}\right) dz\right\} - r\,V \frac{d}{dr}\left\{rU \int_o^\infty \left(1 - \frac{u}{U}\right) dz\right\}$$

$$= \frac{r^2}{\rho}\, \tau_{zt}(0) \quad . \tag{D-28}$$

Use $$\frac{v}{V} = (\xi)^{1/7} \quad ,$$

and let

$$\delta_2 = \delta_r \int_o^1 \left[1 - \frac{u}{U}(\xi)^{\frac{1}{7}} \left(\frac{\delta_r}{\delta_t}\right)^{\frac{1}{7}}\right] d\eta = \delta_r\, \eta - \delta_r \left(\frac{\delta_r}{\delta_t}\right)^{\frac{1}{7}} \lambda_4 \quad , \tag{D-29}$$

and

$$\delta_r^* = \delta_r \int_o^\infty \left(1 - \frac{u}{U}\right) d\eta = \delta_r\, \lambda_2 , \tag{D-30}$$

where $$\eta = \frac{z}{\delta_r} \quad , \text{ and } \quad \xi = \frac{z}{\delta_t} \quad .$$

Equation (D-28) becomes

$$\frac{d}{dr}(r^2 UV \delta_2) - r\,V \frac{d}{dr}(rU \delta_r^*) = \frac{r^2}{\rho}\, \tau_{zt}(0) \quad . \tag{D-31}$$

Summary

There are four profile parameters, δ_r^*, θ_r, δ_1, and δ_2, which together with the free stream velocities and the wall shear stress, determine the boundary layer flow.

Alternately, equations (D-16) and (D-31) determine δ_r and δ_t in terms of freestream velocities U(r), and V(r), and the universal velocity profile parameters, λ_1, λ_2, λ_3, and λ_4 in equations (D-13), (D-14), (D-15), and (D-29). The initial conditions for the solution are $\delta_r = 0$ and $\delta_t = 0$ at the plate radius, r = R, where the boundary layer begins. The radial volumetric flow rate in the boundary layer can be obtained by

$$Q = 2\pi r U \delta_r \int_0^1 \frac{u}{U} d\eta \ . \qquad \text{(D-32)}$$

Supplementary Data of Momentum Integral Analysis

In this section, in Figures 79 to 84, the values of the characteristic parameters, δ_r^*, δ_t^*, θ_r, δ_1, δ_2, and ΔQ, are presented for the test conditions not covered in Chapter III. Also, Tables 4 and 5 present the calculation of the radial and tangential momentum integral equations for the analysis in Chapter III.

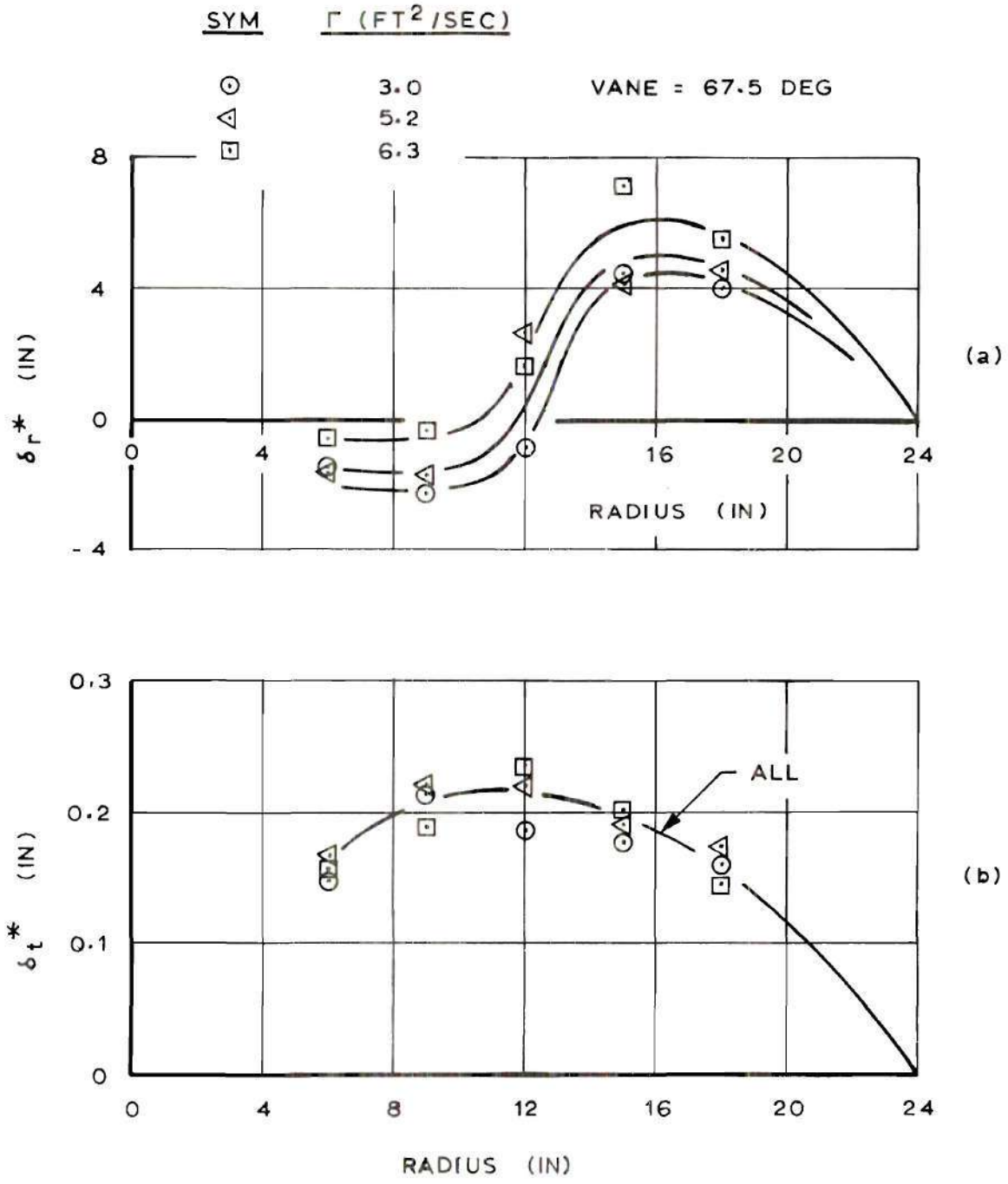

Figure 79. Radial and Tangential Velocity Displacement Thickness

Vane = 67.5 Deg.

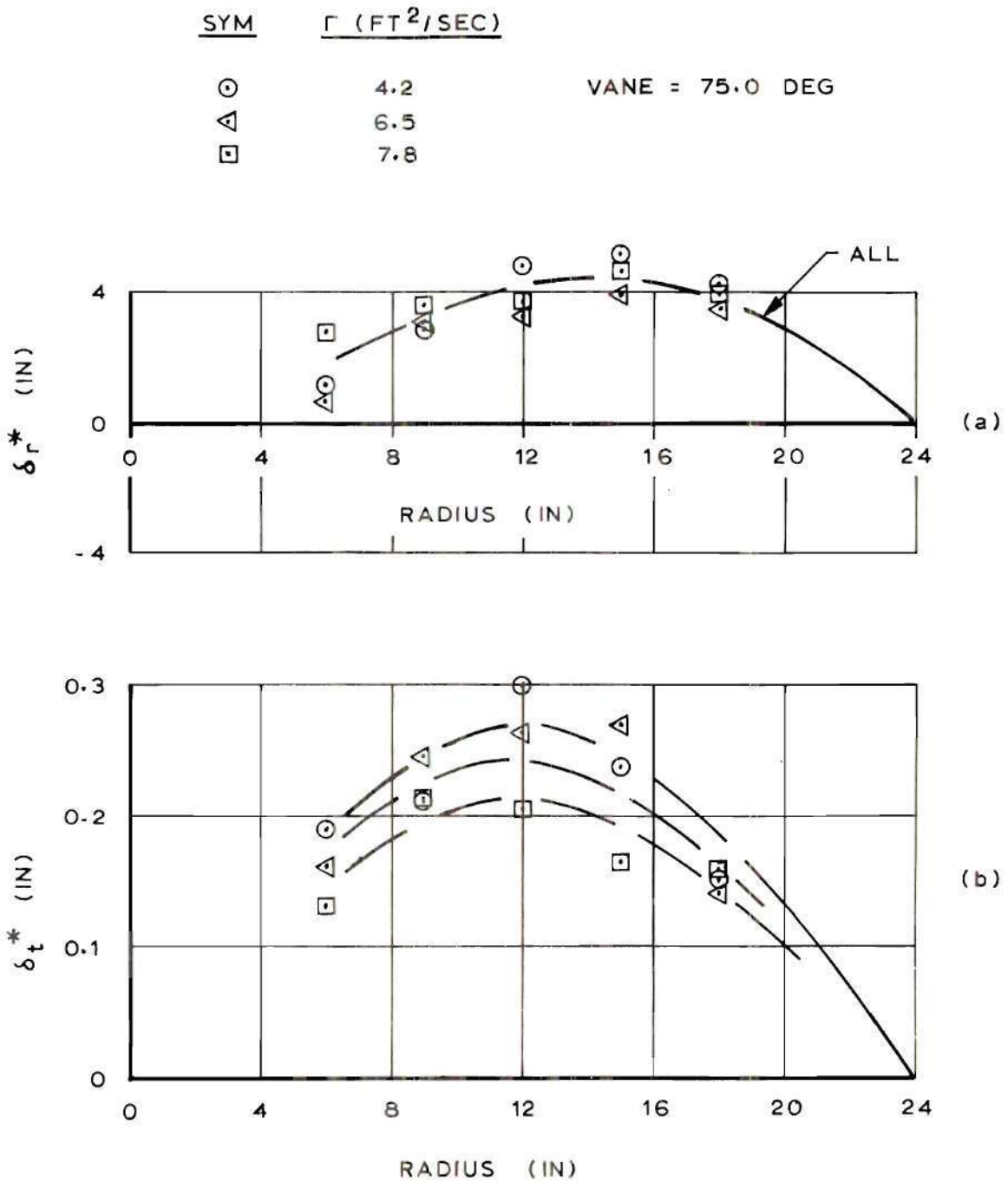

Figure 80. Radial and Tangential Velocity Displacement Thickness

Vane = 75.0 Deg.

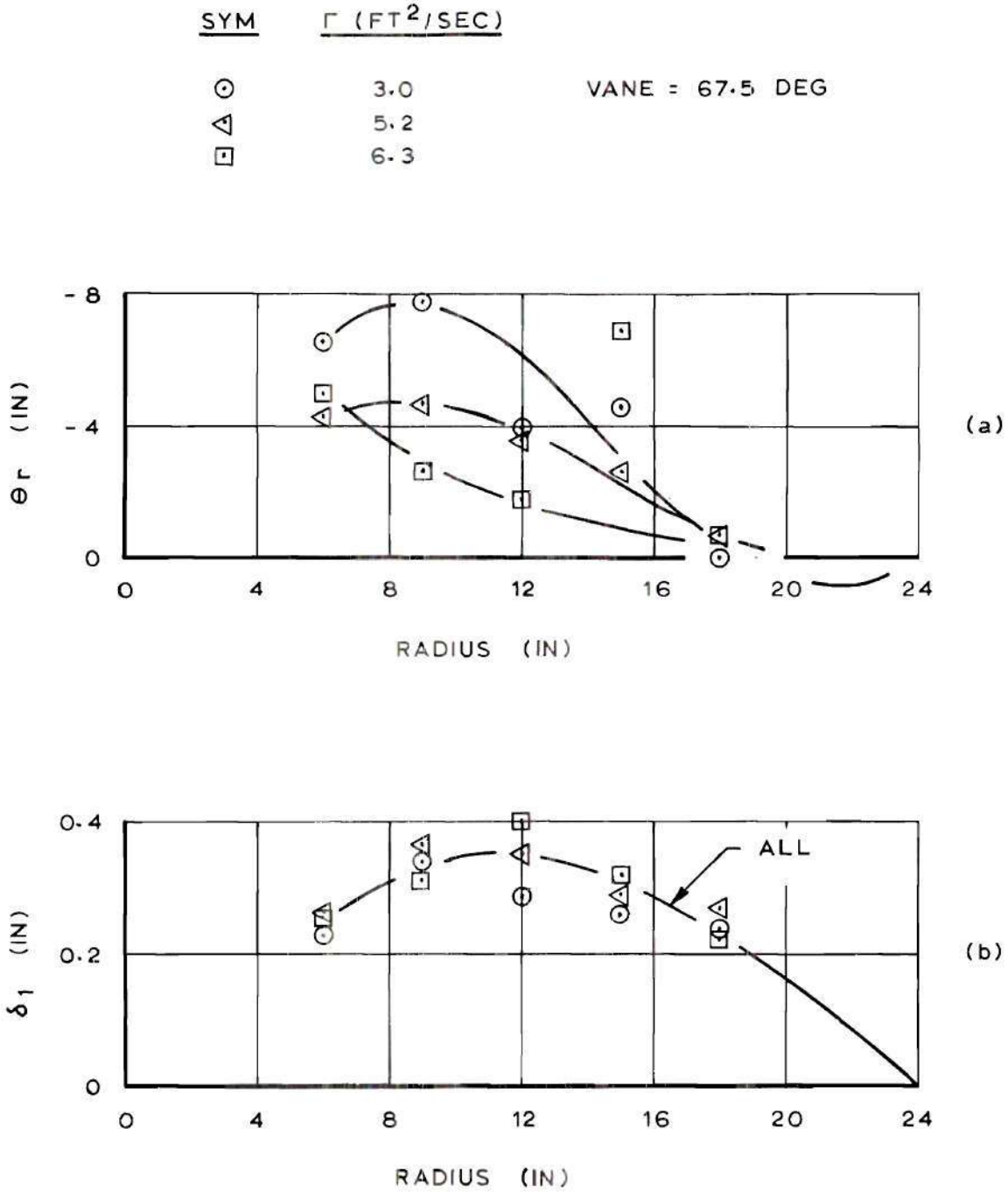

Figure 81. Radial Momentum Thickness and δ_1

Vane = 67.5 Deg.

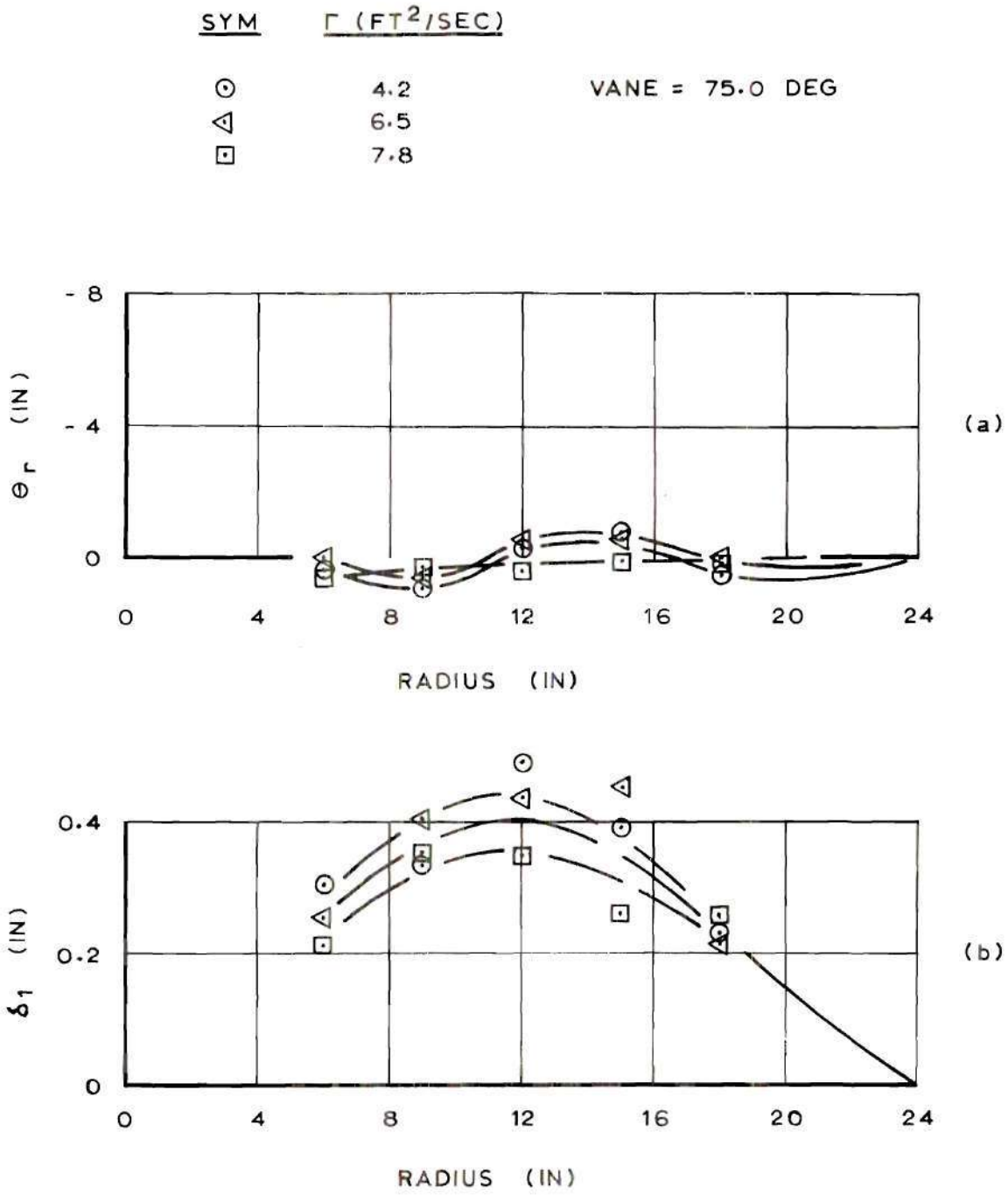

Figure 82. Radial Momentum Thickness and δ_1

Vane = 75.0 Deg.

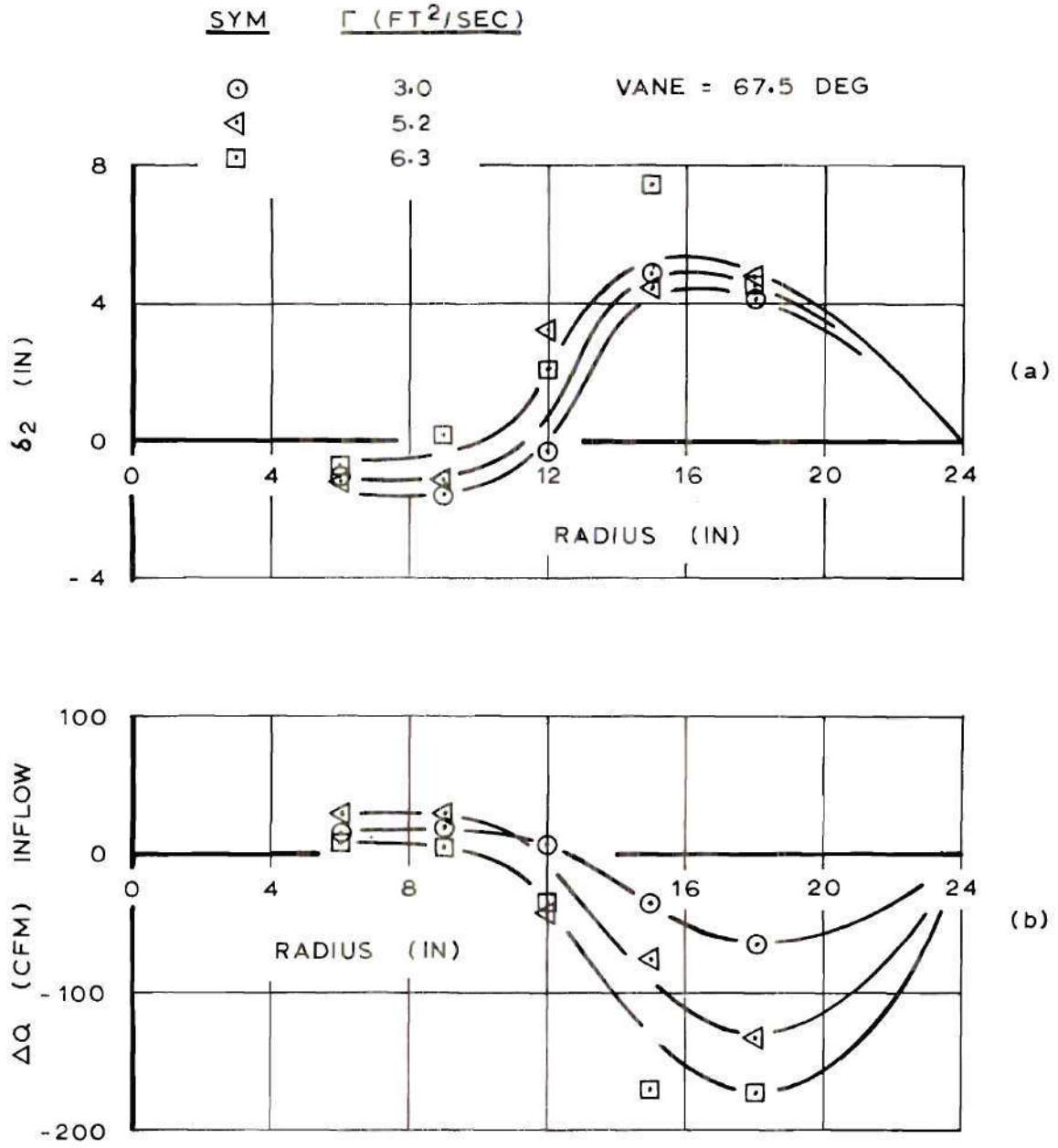

Figure 83. δ_2 and Radial Flow Increment

Vane = 67.5 Deg.

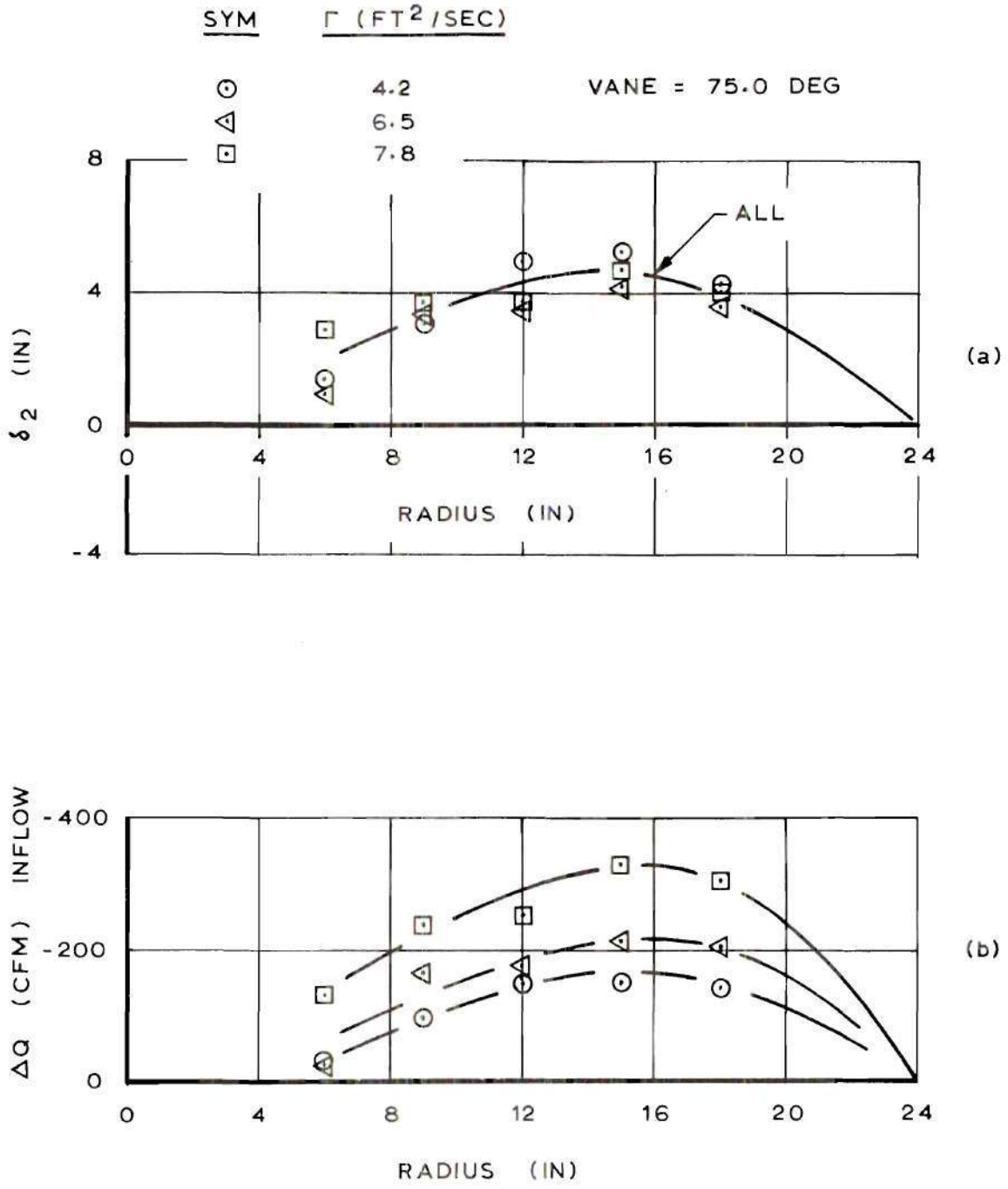

Figure 84. δ_2 and Radial Flow Increment

Vane = 75.0 Deg.

Table 4. Calculated Radial Momentum Integral Equation

Test: Vane = 60.0 deg

Γ = 3.7 ft^2/sec

Radius (in)	① $\frac{d}{dr}\left(r v_{r\infty} \theta_r\right)$ (ft^3/sec^2)	② $rv_{r\infty}\delta^*_r \frac{dv_{r\infty}}{dr}$ (ft^3/sec^2)	③ $v^2_{t\infty}\delta_1$ (ft^3/sec^2)
6	0.747	0.039	0.762
9	0.300	0.025	0.551
12	0.105	0.002	0.320
15	0.045	-0.023	0.188
18	0.010	0.050	0.104

Radius (in)	④ $\frac{r}{\rho}\tau_{w_r}$ (ft^3/sec^2)	⑤ Balance ① + ② - ③ + ④ (ft^3/sec^2)	BF ⑤ / |Largest Term|
6	0.054	0.078	0.102
9	0.036	-0.190	-0.345
12	0.024	-0.190	-0.594
15	0.019	-0.147	-0.783
18	0.017	-0.027	-0.260

Table 4 (Continued)

Test: Vane = 60, 0 deg

Γ = 4.5 ft^2/sec

Radius (in)	① $\frac{d}{dr}\left(r v_{r\infty} \theta_r\right)$ (ft^3/sec^2)	② $r v_{r\infty} \delta_r^* \frac{dv_{r\infty}}{dr}$ (ft^3/sec^2)	③ $v_{t\infty}^2 \delta_1$ (ft^3/sec^2)
6	0.927	0.012	0.747
9	0.350	0.016	0.640
12	0.165	-0.015	0.422
15	0.110	-0.038	0.276
18	0.050	0.049	0.135

Radius (in)	④ $\frac{r}{\rho}\tau_{w_r}$ (ft^3/sec^2)	Balance ① + ② - ③ + ④ (ft^3/sec^2)	BF ⑤ / |Largest Term|
6	0.057	0.249	0.268
9	0.041	-0.233	-0.364
12	0.029	-0.243	-0.575
15	0.024	-0.180	-0.652
18	0.023	-0.013	-0.096

Table 5. Calculated Tangential Momentum Integral Equation

Test: Vane = 60.0 deg

Γ = 3.7 ft^2/sec

Radius	① $\frac{d}{dr}\left(r^2 v_{r\infty} v_{t\infty} \delta_2\right)$	② $r v_{t\infty} \frac{d}{dr}\left(r v_{r\infty} \delta_r^*\right)$	③ $\frac{r^2}{\rho}\tau_{w_t}$
(in)	(ft^4/sec^2)	(ft^4/sec^2)	(ft^4/sec^2)
6	-0.04	-0.02	-0.023
9	0.02	0.04	-0.029
12	1.00	0.92	-0.034
15	1.58	1.60	-0.040
18	-0.68	-0.56	-0.045

Radius	④ Balance ① - ② - ③	BF ④ ÷ |Largest term|
(in)	(ft^4/sec^2)	
6	0.003	0.075
9	0.009	0.225
12	0.114	0.114
15	0.020	0.012
18	-0.075	-0.110

Table 5 (Continued)

Test: Vane = 60.0 deg

Γ = 4.5 ft^2/sec

Radius	① $\frac{d}{dr}\left(r^2 v_{r\infty} v_{t\infty} \delta_2\right)$	② $r v_{t\infty} \frac{d}{dr}\left(r v_{r\infty} \delta_r^*\right)$	③ $\frac{r^2}{\rho} \tau_{w_t}$
(in)	(ft^4/sec^2)	(ft^4/sec^2)	(ft^4/sec^2)
6	-0.10	0	-0.026
9	0.04	0.06	-0.035
12	1.56	1.58	-0.041
15	1.71	1.79	-0.048
18	-1.00	-0.96	-0.057

Radius	④ Balance ① - ② - ③	BF ④ ÷ |Largest Term|
(in)	(ft^4/sec^2)	
6	-0.074	-0.740
9	0.015	0.250
12	0.021	0.013
15	-0.032	-0.019
18	0.097	0.097

BIBLIOGRAPHY

1. Collis and Williams, 1959, "Two Dimensional Convection from Heated Wires at Low Reynolds Numbers," J. of Fluid Mechanics, Vol. 6

2. Dhawan, S., 1952, Direct Measurement of Skin Friction, NACA TN 2567

3. East, L. F., 1966, Measurement of Skin Friction at Low Subsonic Speeds by the Razor Blade Technique, A.R.C. R&M No. 3525

4. Greenspan, H. P., 1968, The Theory of Rotating Fluids, Cambridge University Press

5. Head, M. R., and Rechenberg, I., 1962, "The Preston Tube as a Means of Measuring Skin Friction," J. of Fluid Mechanics, Vol. 14, Pt. 1.

6. Holman, J. P., 1963, Heat Transfer, McGraw-Hill Book Co.

7. Julich, E. Achenbach, 1971, "Experimentelle Bestimmung der Impulsverlustdicke beim querangeströmten Kreiszylinder," Wärme-und Stoffübertragung, Bd. 4, S. 18-24

8. Kidd, G. J., Jr. and Farris, G. J., 1968, "Potential Vortex Flow Adjacent to a Stationary Surface," J. of Applied Mechanics, June 1968

9. King, W. S., and Lewellen, W. S., 1964, "Boundary-Layer Similarity Solutions for Rotating Flows with and without Magnetic Interaction," The Physics of Fluids, Vol. 7, No. 10

10. Kuo, H. L., 1971, "Axisymmetric Flows in the Boundary Layer of a Maintained Vortex," J. of the Atmospheric Sciences, Vol. 28

11. Lee, S. L., 1966, "Axisymmetric Turbulent Swirling Natural-Convection Plume," J. of Applied Mechanics, APM No. 66-APM-X

12. Lowell, H. H., 1950, Design and Applications of Hot-Wire Anemometers for Steady-State Measurements at Transonic and Supersonic Airspeeds, NACA TN 2117

13. Ludwieg, H., 1950, Instrument for Measuring the Wall Shearing Stress of Turbulent Boundary Layers, NACA TM 1284

14. Morton, B. R., 1970, "The Physics of Fire Whirls," Fire Research Abstracts and Reviews

15. Nielson, H. J., 1969, Origin and Properties of Fire Whirls, Final Technical Report, IITRI Project J6129 (Illinois Institute)

16. Pankhurst, R. C., and Holder, D. W., 1952, Wind Tunnel Technique, Sir Isaac Pitman & Sons Ltd., London

17. Patel, V. C., 1965, "Calibration of the Preston Tube and Limitations on its Use in Pressure Gradients," J. of Fluid Mechanics, Vol. 23, Part 1

18. Preston, J. H., 1954, "The Determination of Turbulent Skin Friction by Means of Pitot Tubes," J. of the Royal Aeronautical Society, Vol. 58

19. Rechenberg, I., 1963, "Messung der Turbulenten Unterschubspannung," Z. Flugwiss. 11, Heft 11

20. Rott, N. and Lewellen, W. S., 1964, "Boundary Layers in Rotating Flows," Applied Mechanics Proc. 11th International Congress, Muenchen

21. Schlichting, H., 1968, Boundary Layer Theory, McGraw-Hill Inc.

22. Schwiderski, E. W., 1969, "On the Axisymmetric Vortex Flow Over a Flat Surface," J. of Applied Mechanics, Sept. 1969

23. Ying, S. J. and Chang, C. C., 1970, "Exploratory Model Study of Tornado-Like Vortex Dynamics," J. of Atmospheric Sciences, Vol. 27, No. 1